

AD

USAAVLABS TECHNICAL REPORT 66-81

**20-HOUR FOLLOW-ON FLIGHT TEST PROGRAM,
XV-9A HOT CYCLE RESEARCH AIRCRAFT**

Summary Report on Task 1

By

**G. W. Pieper
N. B. Hirsh**

December 1966

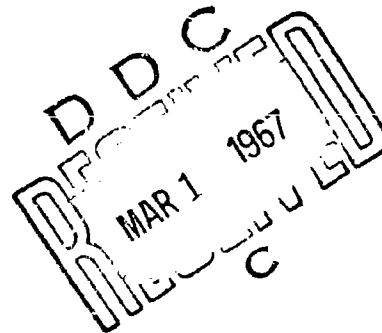
**U. S. ARMY AVIATION MATERIEL LABORATORIES
FORT EUSTIS, VIRGINIA**

**CONTRACT DA 44-177-AMC-225(T)
HUGHES TOOL COMPANY
AIRCRAFT DIVISION
CULVER CITY, CALIFORNIA**

*Distribution of this
document is unlimited*



ARCHIVE COPY



Disclaimers

The findings in this report are not to be construed as an official Department of the Army position unless so designated by other authorized documents.

When Government drawings, specifications, or other data are used for any purpose other than in connection with a definitely related Government procurement operation, the United States Government thereby incurs no responsibility nor any obligation whatsoever; and the fact that the Government may have formulated, furnished, or in any way supplied the said drawings, specifications, or other data is not to be regarded by implication or otherwise as in any manner licensing the holder or any other person or corporation, or conveying any rights or permission, to manufacture, use, or sell any patented invention that may in any way be related thereto.

Trade names cited in this report do not constitute an official endorsement or approval of the use of such commercial hardware or software.

Disposition Instructions

Destroy this report when no longer needed. Do not return it to originator.

ACCESSION FOR	
CFST:	WHITE SECTION TO
DDC	SUBSECTION TO
UNANNOUNCED	<i>Per statement in file</i>
JUSTIFICATION	
BY <i>Am</i>	
DISTRIBUTION AVAILABILITY CODES	
DIST.	AVAIL. AND OR SPECIAL
1	



DEPARTMENT OF THE ARMY
U. S. ARMY AVIATION MATERIEL LABORATORIES
FORT EUSTIS, VIRGINIA 23604

This report has been prepared by Hughes Tool Company-Aircraft Division, under the provision of Contract DA 44-177-AMC-225(T) Task I, to present in summary form the results of the XV-9A Hot Cycle 20-Hour Flight Test Program.

The report is published for the dissemination of information and the reporting of program results.

Task 1M131001D15701
Contract DA 44-177-AMC-225(T)
USAAVLABS Technical Report 66-81

December 1966

20-HOUR FOLLOW-ON FLIGHT TEST PROGRAM,
XV-9A HOT CYCLE RESEARCH AIRCRAFT

Summary Report on Task I

HTC-AD 66-4

by

C. W. Pieper
N. B. Hirsh

172 660

Prepared by

Hughes Tool Company - Aircraft Division
Culver City, California

for

U. S. ARMY AVIATION MATERIEL LABORATORIES
FORT EUSTIS, VIRGINIA

Distribution of this
document is unlimited

ABSTRACT

This report summarizes the results of Task I under Contract DA 44-177-AMC-225(T). Hughes Tool Company - Aircraft Division conducted a 20-hour follow-on flight test program on the XV-9A Hot Cycle Research Aircraft to provide additional technical data for evaluation of Hot Cycle propulsion system performance and operating characteristics.

During the tests, performed from 30 April 1965 through 26 August 1965, the performance, structural qualities, and stability and control of the Hot Cycle rotor and propulsion system were evaluated in greater depth than that practical during the initial 15-hour flight test program. The 20 hours of flight testing involved expansion of flight envelope and included evaluation of aircraft and rotor system performance, flight loads, cooling, and flying qualities in various flight modes. At the conclusion of flight testing, a ground test of the tethered rotor system was performed, followed by a teardown inspection of the aircraft. The teardown inspection was completed on 23 December 1965.

FOREWORD

This report was prepared in accordance with Contract DA 44-177-AMC-225(T) with the U.S. Army Aviation Materiel Laboratories. The contract became effective on 17 March 1965. Work on Task I was completed on 23 December 1965. The report summarizes the 20-hour follow-on flight test program of the XV-9A Hot Cycle Research Aircraft, U.S. Serial Number 64-15107.

The work was accomplished by Hughes Tool Company - Aircraft Division in Culver City, California, under the direction of Mr. H.O. Nay, Director of Aeronautical Engineering, and under the direct supervision of Mr. C.R. Smith, Manager, Hot Cycle Department. This report was prepared by C.W. Pieper and N.B. Hirsh.

Task II, under the above contract, concerns the preliminary design of a rotor system for a Hot Cycle heavy-lift helicopter. This work will be reported under separate cover.

CONTENTS

	<u>Page</u>
ABSTRACT	iii
FOREWORD	v
LIST OF ILLUSTRATIONS	ix
LIST OF TABLES	xiv
LIST OF SYMBOLS	xv
SUMMARY	1
RESULTS	4
RECOMMENDATIONS	6
DESCRIPTION OF TEST AIRCRAFT	7
Weight Summary	7
Performance	7
Rotor Characteristics	7
Rotor Speed	8
Powerplant	8
Overall Dimensions	8
Empennage	11
Maximum Control Displacements	11
FLIGHT TESTS	12
Inspection and Maintenance Period	12
Summary of Testing	13
Flight Test Procedures	18
Flight Test Results	20
ROTOR SYSTEM TETHER TESTS	103
Introduction	103
Test Setup	103
Test Procedure	106
Test Instrumentation	106
Test Results	108
Application of Tether Test Results to Rotor Performance	120
TEARDOWN INSPECTION	122
Introduction	122
Rotor System Leakage Tests	122
Inspection Procedure	123

	<u>Page</u>
REFERENCES	142
DISTRIBUTION	144
APPENDIXES	
I. Description of Test Instrumentation	145
II. Rotor Blade Fatigue Life Computation	152
III. Results of Simulated Hot Cycle Spar Tests With Thermal Gradients Between Spar and Doubler	161
IV. Description of Tasks Accomplished During Inspection and Maintenance Period	174
V. Rotor Control System Rod End Fatigue Test	182
VI. Configuration and Change Log	185
VII. Aircraft Weight and Balance Data - XV-9A 15107	190
VIII. Pilot's Comments and Qualitative Evaluation of the XV-9A	191
IX. Propulsion System Performance Test Data and Corrections	202

ILLUSTRATIONS

<u>Figure</u>		<u>Page</u>
1	XV-9A Hot Cycle Research Aircraft	1
2	General Arrangement, XV-9A Hot Cycle Research Aircraft	9
3	Cyclic Spar Axial Load at Station 90.75 Versus True Airspeed	21
4	Cyclic Hub Plate Stress Versus True Airspeed	21
5	Cyclic Flapwise Bending Moment at Station 100 Versus True Airspeed	22
6	Cyclic Flapwise Bending Moment at Station 75.4 Versus True Airspeed	22
7	Cyclic Shaft Bending Moment Versus True Airspeed	23
8	Cyclic Shear Load at Station 23 Versus True Airspeed	23
9	Cyclic Pitch Link Load Versus True Airspeed	24
10	V-n Diagram	24
11	Peak Cyclic Spar Axial Load at Station 90.75 Versus Load Factor	25
12	Peak Cyclic Hub Plate Stress Versus Load Factor	26
13	Peak Cyclic Flapwise Bending Moment at Station 100 Versus Load Factor	26
14	Peak Cyclic Flapwise Bending Moment at Station 75.4 Versus Load Factor	27
15	Peak Cyclic Shaft Bending Moment Versus Load Factor	27
16	Peak Cyclic Shear Load at Station 23 Versus Load Factor	28
17	Peak Cyclic Pitch Link Load Versus Load Factor	28
18	Blade Spar Cyclic Axial Load Spectrum, Flight 26	29
19	Blade Spar Axial Load Spectrum, Flight 31	31
20	Blade Spar Cyclic Axial Load Spectrum, Flight 35	32
21	Blade Spar Cyclic Axial Load Spectrum, Flight 43	33

<u>Figure</u>		<u>Page</u>
22	Cyclic Chordwise Bending Moment Versus Blade Radius . . .	35
23	Cyclic Flapwise Bending Moment Versus Blade Radius . . .	36
24	Pitch Link Load Versus Tip Mach Number - Blue Blade . . .	37
25	Maximum Rotor Operating Temperatures	39
26	Maximum Fuselage Operating Temperatures	41
27	Temperature Versus Pressure, Engine S/N 027	43
28	Temperature Versus Pressure, Engine S/N 026	44
29	Temperature Versus Pressure, Engine S/N 101	45
30	Engine Temperature Relationship, Engine S/N 027	46
31	Engine Temperature Relationship, Engine S/N 026	47
32	Engine Temperature Relationship, Engine S/N 101	48
33	T_{T5}/θ Versus Percent $N_G/\sqrt{\theta}$, Engine S/N 026	49
34	T_{T5}/θ Versus Percent $N_G/\sqrt{\theta}$, Engine S/N 101	50
35	T_{T5}/θ Versus Percent $N_G/\sqrt{\theta}$, Engine S/N 027	51
36	Engine Discharge Temperature Versus Pressure	52
37	Observed Specific Fuel Consumption	54
38	Comparison of Specific Fuel Consumption Versus Referred Rotor Horsepower	55
39	Temperature Rise Versus Fuel Air Ratio	56
40	Level Flight Horsepower Required Versus True Airspeed, 3,500-Foot Altitude, Standard Day	57
41	Level Flight Horsepower Required Versus True Airspeed, 6,000-Foot Altitude, Standard Day	57
42	Level Flight Horsepower Required Versus True Airspeed, Sea Level, Standard Day	58
43	Fuel Flow Versus True Airspeed, 3,500-Foot Altitude, Standard Day	59
44	Fuel Flow Versus True Airspeed, 6,000-Foot Altitude, Standard Day	60
45	Fuel Flow Versus True Airspeed, Sea Level, Standard Day	61

<u>Figure</u>		<u>Page</u>
46	Maximum Airspeed for Full-Up Collective Pitch	61
47	Airspeed Calibration - Photopanel	62
48	Rate of Climb	65
49	Autorotational Rate of Descent	65
50	Thrust Coefficient Versus Torque Coefficient, Hover IGE	66
51	Thrust Coefficient Versus Torque Coefficient, Hover OGE	66
52	Gross Weight Versus Rotor Horsepower, Hover IGE . . .	67
53	Gross Weight Versus Rotor Horsepower, Hover OGE . . .	67
54	Referred Rotor Horsepower Available Versus Turbine Discharge Temperature	69
55	Hover Performance, IGE	70
56	Hover Performance, OGE	71
57	Single-Engine Flight	73
58	Rotor Horsepower Versus Airspeed - Single-Engine Flight	75
59	Aircraft Response to a Forward Longitudinal Step Input in Hover	76
60	Aircraft Response to a Left Lateral Input in Hover	77
61	Aircraft Response to a Left Pedal Step Input in Hover . .	78
62	Aircraft Response to a Right Pedal Step Input in Hover . .	80
63	Aircraft Response to a Forward Longitudinal Pulse Input in Hover	82
64	Aircraft Response to a Left Lateral Pulse Input in Hover	83
65	Control Positions in Sideward Flight	84
66	Rearward Flight Longitudinal Cyclic Control Position Versus Speed	85
67	Level Flight Control Position Versus Airspeed	86
68	Speed Stability	87

<u>Figure</u>		<u>Page</u>
69	Static Directional Stability in Level Flight	87
70	Tuft Behavior in Cruise Flight	90
71	Aircraft Response to a Left Lateral Step Input in Level Flight	92
72	Aircraft Response to an Aft Longitudinal Pulse Input in Level Flight	94
73	Aircraft Response to a Left Lateral Pulse Input in Level Flight	95
74	Aircraft Response to a Right Pedal Pulse Input in Level Flight	96
75	Control Position Versus Airspeed in Climb	97
76	Static Directional Stability in Climb	99
77	Static Directional Stability in Descent	100
78	Typical Vibratory Accelerations at Center of Gravity Versus True Airspeed	102
79	Typical Vibratory Accelerations at Pilot's Seat Versus True Airspeed	102
80	Tether Test Blade Orientation	104
81	Tether Test Setup	105
82	Tether Test Velocity Coefficient	111
83	Tether Test Flow Coefficient	112
84	Tether Test Thrust Coefficient	113
85	Tether Test Blade Duct Friction Factor Determination	114
86	Duct System Pressure Variation	116
87	Rotor System Pressure Ratio Versus Rotor RPM - Flight and Tether Tests	117
88	Rotor System Pressure Ratio Versus Rotor RPM - Flight Test	118
89	Engine Accessory Drive Couplings	125
90	Rotating Seal, Inner	127
91	Rotating Seal, Outer	128

<u>Figure</u>		<u>Page</u>
92	Spar to Segment Bolts	130
93	Blade Retention Straps and Bolts	131
94	Articulating Duct, Hub to Blade	134
95	Flexure Ten, Yellow Blade, Station 203.5	136
96	Hot Gas Rotor Ducting, Yellow Blade	137
97	Servo Actuator Components	139
98	Rod Ends and Self-Aligning Bearings	140
99	Instrumentation Schematic	146
100	Cyclic Spar to Segment Bolt Bearing Stresses Versus Load Cycles	153
101	Bolt Hole Stress Concentration Factor	154
102	Spar-to-Segment-Bolt Load Versus Bolt Slope	156
103	Bolt Loads - Spar to Segment Cyclic Load Versus Steady Load	157
104	S-N Curve, Spars - Chordwise Bending Stress	158
105	Typical Doubler in Milled Out Area and Thermocouples . .	162
106	Fatigue Test Specimen	163
107	Overall View of Cold Specimen Setup (Room Temperature)	164
108	Overall View of Heated Specimen Setup	165
109	Closeup of Cold Specimen	166
110	Closeup of Heated Specimen	167
111	View of Side "A" of Specimens After Test Failures in 1 and 3	170
112	View of Side "B" of Specimens After Test Failure in Specimen 2	171
113	Typical Pins Removed From Doublers - Note Impres- sions From Spar Laminations	172
114	Rod End Specimen Installed in Fatigue Test Machine	183
115	Rod End Specimen Test Setup	184
116	Weight Coordinates	190

TABLES

<u>Table</u>	<u>Page</u>
I. Flight Test Operations Summary	14
II. Number of Cycles of Blade Spar Axial Load Greater Than $\pm 7,000$ Pounds	30
III. Hover Ceiling, IGE	72
IV. Hover Ceiling, OGE	72
V. Control Power	79
VI. Rotor System Tether Test Summary	107
VII. Rotor System Tether Test Instrumentation Parameters	107
VIII. Tether Test Data Summary - Twin-Engine	109
IX. Tether Test Data Summary - Single-Engine	110
X. Blade Tip Cascade Areas	119
XI. Propulsion System Leakage Measurement in Square inches	123
XII. Rotor Blade Life	159
XIII. Fatigue Test Results	169
XIV. Airplane Weighing Record	190
XV. Observed and Corrected Fuel Flow and Rotor and Gas Horsepower	203

LIST OF SYMBOLS

A	Area	sq in.
A_e	Nozzle exit area	sq in.
A_{π}	Parasite drag area	sq ft
$^{\circ}\text{C}$	Degrees centigrade	degrees
C_F	Nozzle thrust coefficient	
C_L	Lift coefficient	
C_P	Specific heat (at constant pressure)	BTU/lb $^{\circ}\text{F}$
C_Q	Torque coefficient	
C_T	Nozzle thrust coefficient	
C_V	Nozzle velocity coefficient	
C_v	Specific heat (at constant volume)	BTU/lb $^{\circ}\text{F}$
C_W	Nozzle flow coefficient	
C_T/σ	Thrust coefficient/solidity ratio	
f	Blade duct friction factor	
F	Thrust	lb
\bar{F}	Average thrust	lb
$^{\circ}\text{F}$	Degrees Fahrenheit	degrees
F_c	Coriolis force	lb
F_j	Jet thrust	lb
F_N	Net thrust ($F_j - F_c$)	lb
F/A	Fuel/air ratio	
GW	Gross weight	lb
h_D	Density altitude	ft
h_p	Pressure altitude	ft
i_H	Incidence of horizontal stabilizer	degrees
IAS	Indicated airspeed	knots
IGE	In ground effect	
M_T	Nozzle exit Mach number	

\overline{M}	Blade duct Mach number	
n	Aircraft load factor	g's
N_f	Rotor governor shaft rpm	percent
N_G	Engine rpm	percent
N_R	Main rotor rpm	percent
OGE	Out of ground effect	
\overline{P}	Pressure	psia
P	Average pressure	psia
PLA	Engine fuel control power lever angle	degrees
PPF	Profile power factor	
P_S	Static pressure	psia
P_T	Total pressure	psia
$P_{T1,2,3}$	Total pressure at station designation	psia
P_0	Ambient pressure	psia
QT	Qualification flight rated engine	
R	Universal gas constant	
$^{\circ}R$	Degrees Rankine	degrees
RHP	Rotor horsepower	
T	Temperature	degrees
T_T	Total temperature	degrees
$T_{T1,2,3}$	Total temperature at station designation	degrees
T_{t_e}	Total temperature, nozzle exit	degrees
TAS	True airspeed	knots
V_j	Jet velocity	fps
V_T	Rotor tip speed	fps
W	Aircraft weight	lb
W	Mass flow	lb/sec
W_a	Airflow	lb/sec
W_f	Fuel flow	lb/hr
$W_{1,2,3}$	Mass flow at station designation	lb/sec

YT	Preliminary flight rated engine	
Z/D	Rotor height/rotor diameter ratio	
γ	Ratio of specific heats (C_p/C_v)	
γ_e	Ratio of specific heats at nozzle exit	
δ	Relative absolute pressure (P/P_0)	
ρ	Density	slug/ft ³
ρ_0	Density of ambient air at sea level standard conditions	slug/ft ³
θ	Relative absolute temperature (T/T_0)	
$\theta_{0.75}$	Collective pitch angle at 75-percent blade radius	degrees
μ	Rotor advance ratio, forward speed/tip speed	
σ	Blade solidity ratio - total blade area/rotor disc area	
ϕ	Bank angle	degrees
Sub _{1, 2, 3}	Station designations	
ΔT	Ideal temperature drop for given ratio of gas pressure to ambient pressure	degrees

STATION DESIGNATIONS

0	Ambient
2	Engine compressor inlet face
3	Engine compressor discharge
4	Engine turbine inlet
5	Engine turbine discharge
7	Engine exhaust (forward face of diverter valve)
8	Blade root - articulating duct
9	Blade-tip cascade inlet
9 $\frac{1}{2}$	Blade-tip centerline
10	Cascade exit

SUMMARY

This report presents the results of the XV-9A Hot Cycle Research Aircraft 20-hour follow-on flight test program and, in addition, presents the results of the rotor system tether test and of the teardown inspection. The XV-9A (see Figure 1) was designed and constructed by Hughes Tool Company - Aircraft Division under contract to the United States Army Aviation Materiel Laboratories (USAAVLABS), Fort Eustis, Virginia, to perform research flight testing of the Hughes Hot Cycle propulsion system. The Hot Cycle propulsion system provides power to the rotor by means of high-energy gas flow ejected from nozzles located at the tip of each rotor blade, producing tangential thrust on the blade and driving torque for the lifting rotor.



Figure 1. XV-9A Hot Cycle Research Aircraft.

Initial flight testing of the XV-9A aircraft under Contract DA 44-177-AMC-877(T) was conducted from November 1964 through February 1965 and consisted of approximately 15 hours of flight. Results of this testing were reported in Reference 1.

The 20-hour follow-on flight test program was flown to provide additional technical data for further evaluation of both the Hot Cycle propulsion system performance and operating characteristics, structural loads and temperatures, flight envelope expansion, and single-engine operation and the XV-9A flying qualities during hover, climb, level flight, and autorotational descents.

The aircraft was extensively instrumented for measurement of structural loads, temperatures, performance, vibration, control positions, rates, and attitudes prior to the start of flight tests. The instrumentation systems that produced these data were calibrated prior to the start of testing and, where appropriate, recalibrated during the course of the test program to ensure maximum accuracy of results. For a description of the test aircraft, refer to the section that follows. A description of the test instrumentation systems is given in Appendix I.

Flight testing was accomplished at the Hughes Culver City facility and at Edwards Air Force Base. Within the allowable flight envelope of the aircraft, all normal helicopter flight modes were evaluated. These included lift-off to hover, steady hovering flight both in and out of ground effect, hovering turns, sideward and rearward flight, climb, level flight, single-engine rotor flight, minimum-power descents, approach to hover, and landing.

Flight testing was accomplished by the contractor during the period 30 April through 26 August 1965. The initial portion of the flight test program consisted of shakedown and checkout flights at the contractor's facility in Culver City, California. After satisfactory shakedown flights, the aircraft was flown to Edwards Air Force Base, California, where the majority of the testing was accomplished.

During the flight test program, 23 flights were flown with a total of 19 hours 32 minutes of flight time. The aircraft was flown to Culver City from Edwards Air Force Base following successful completion of flight testing.

At the conclusion of flight testing, a rotor system tether test was accomplished. During this test, the rotor system was restrained by a horizontal thrust-measuring apparatus. Engine and rotor system temperatures and pressures were observed and recorded.

Subsequent to rotor system tether testing, a teardown inspection of the aircraft was accomplished for the purpose of determining the effect of 35 hours of flight. No significant discrepancies were noted.

During the course of the flight test program, several supporting fatigue tests of rotor system components were run. As a result of this testing, a revised rotor blade spar service life of 1,590 hours is predicted. Results of testing and fatigue life analysis are included in this report as Appendixes II and III, respectively.

RESULTS

The objective of the XV-9A Hot Cycle Research Aircraft, to obtain basic flight research data on the Hot Cycle Rotor System, has been accomplished by the completion of the 20-hour follow-on flight test program. This program has obtained data on structural loads, performance, stability, control, vibration, and operating characteristics at various flight speeds, altitudes, rotor speeds, center-of-gravity locations, gross weights, and load factors within the allowable flight envelope of the aircraft.

The measured performance of the Hot Cycle propulsion system in hover, climb, and level flight was determined to be in agreement with the predicted performance, based on the actual parasite drag and blade profile power factor of the XV-9A aircraft. Data are presented for the observed XV-9A performance with YT-64 engines, and further analysis and data are shown for predicted XV-9A performance, based on aircraft drag and rotor blade improvements and the use of fully qualified current production T-64 engines.

The aircraft performance in forward flight, climb, and hover was limited by the available collective pitch rather than power. This control system limitation is applicable to this particular rotor, originally designed as a ground test unit.

The performance of the gas reaction yaw control system was generally satisfactory. However, it was detrimental to overall Hot Cycle system performance for conditions where maximum rotor power was desired. This deleterious effect is primarily due to the increase in exit area seen by the engines when the yaw valve is open.

In hover, the control power in pitch and roll was found to be adequate to meet the specific control response requirements of MIL-H-8501A. Comparison of the measured control response with theoretical predictions shows good agreement, indicating that the XV-9A free-floating hub rotor control power characteristics can be predicted by theory. This was also true of the theoretical calculations of rotor damping in roll (forward flight), which showed good agreement with measured roll damping.

Maximum level flight speed at forward and mid center of gravity was 120 knots, which was limited by available collective pitch travel. Sufficient power and longitudinal control margin existed for a speed of approximately 130 knots.

Speed stability was found to be neutral in level flight. Improvement in speed stability could be obtained by increasing the nose-down stabilizer incidence at the expense of reduced forward stick margin at higher speeds.

The XV-9A has neutral effective dihedral in level flight. The static directional stability in level flight was found to be approximately neutral. The primary reason for the rather low directional stability was attributed to the V-tail operating in the region of low dynamic pressure created by the large flow separation at the rotor hub-pylon junction. A drag cleanup in this area would improve the stability, both directionally and laterally.

Structural loads in critical components were determined for all flight conditions and, in general, these loads are shown to be in accordance with the structural design criteria. The rotor blade cyclic chordwise bending moments (span axial loads) were found to be higher than desired for the maximum speed level flight condition and during some pilot-induced conditions.

Analysis of predicted blade service life based on an actual flight loads frequency spectrum and post-flight fatigue testing shows a blade fatigue life of 1,590 hours (refer to page 159).

The autorotational capability of the Hot Cycle rotor was determined during minimum power descents. Full autorotative landings were not accomplished because of control system limitations and directional stability characteristics.

Rotor speed-governing characteristics for hover and level flight were satisfactory and engine matching was accomplished by engine power levers. The concept of two gas generators with mixed exhaust flow powering a Hot Cycle rotor was determined to be satisfactory with certain engine control system refinements.

The results of rotor blade tether tests verified that the theoretical analysis of Hot Cycle system performance is essentially correct. The tether test data indicated that rotor performance can be improved by some refinement of the blade-tip cascade nozzles. These data also confirmed the theoretical duct friction factor of 0.003.

The rotor system leakage test and teardown inspection conducted following completion of flight and ground tests revealed no significant change in system leakage or wear in critical components.

RECOMMENDATIONS

Based on the flight test results obtained during the 20-hour follow-on program and on the previous 15-hour flight test program, the following recommendations are submitted:

1. Conduct a structural development test program to accumulate design criteria necessary for development of advanced Hot Cycle rotor systems having an increased service life of rotor components subject to vibratory loads. Particular emphasis would be given to the blade spars, their attachment configuration, blade ducting, seals, hot gas valves, bellows, and insulating techniques.
2. Extend the scope of the Task II rotor system preliminary design effort to include an extensive preliminary design of the complete aircraft. Included in this expanded effort would be a comprehensive aircraft preliminary design with special emphasis given to operational, performance, weight, and structural characteristics.
3. Initiate expanded design studies of the benefits and penalties associated with increasing the cruise speed and range capabilities of Hot Cycle helicopters through the use of compounding by the addition of wings and cruise fans.
4. Conduct a study of the rotor power management systems to develop parameters necessary for design of the mechanical portion of the system, and for development of fuel control and rotor governing system requirements. This study should consider single- and multiple-engine aircraft that would utilize 1970 state-of-the-art engines. The study should also consider the benefits and penalties associated with either combining the exhaust of multiple gas generators or maintaining separate exhaust flow through the use of concentric ducting.

DESCRIPTION OF TEST AIRCRAFT

The XV-9A Hot Cycle Research Aircraft is a helicopter having a three-bladed Hot Cycle pressure jet rotor driven by high-energy gases produced by two General Electric YT-64 gas generators. The exhaust gas flow produced by the YT-64 gas generators is ducted through J-85 diverter valves, transition ducts, hub, and blade ducts to blade-tip cascade nozzles that produce the rotor driving torque.

A general arrangement drawing of the aircraft follows (Figure 2). A detailed description of the aircraft structure, systems, characteristics, and design criteria is given in Reference 3.

WEIGHT SUMMARY

	<u>Pounds</u>
Empty weight	8,656
Design minimum gross weight	10,000
Design gross weight	15,300
Design alternate overload gross weight (external load)	25,500
Aircraft weight with zero fuel, crew, and normal instrumentation (actual)	10,645
Fuel (maximum)	3,200
Ballast (internal)	1,455

PERFORMANCE (Design Objectives)

<u>Condition</u>	<u>Gross Weight (lb)</u>	<u>Altitude and Temperature</u>	<u>Speed (kn)</u>
Maximum Speed	15,300	Sea Level Standard	140
Maximum Speed	10,000	Sea Level Standard	150

ROTOR CHARACTERISTICS

Number of blades	3
Rotor radius	27.6 feet
Blade area (3 blades)	217.5 square feet
Disc area	2,392.0 square feet
Rotor solidity	0.091
Blade chord	31.5 inches
Blade airfoil	NACA 0018

Blade twist	-8 degrees
Hot gas ducts	
Number of ducts per blade	2
Total duct area per blade	54.8 square inches
Blade-tip cascade area per blade (closure valve open)	37.5 square inches

ROTOR SPEED

	<u>rpm</u>	<u>V_T</u> <u>(fps)</u>
Design operational power-on or power-off	243 (100-percent N _R)	700
Design minimum, power-on or power-off	225	648
Design maximum, power-on (red line)	255	734
Design maximum, power-off (red line)	255	734
Rotor speed, limit, power-on or power-off	295	848

POWERPLANT

2 YT 64-6 Gas Generators

	T (deg R)	T (deg F)	Pressure Ratio	Pressure (psig)	Gas Flow (lb/sec)
SLS Normal Rated	1,499	1,039	2.61	23.6	23.8
SLS Military Rated	1,577	1,117	2.83	26.9	25.0

OVERALL DIMENSIONS

	<u>Feet</u>
Aircraft length (rotor turning)	59.70
Fuselage length	44.17
Tread of main wheels	11.00
Height (to top of rotor hub)	12.40
Width (across lateral pylons)	12.20

10'-4"
(124")

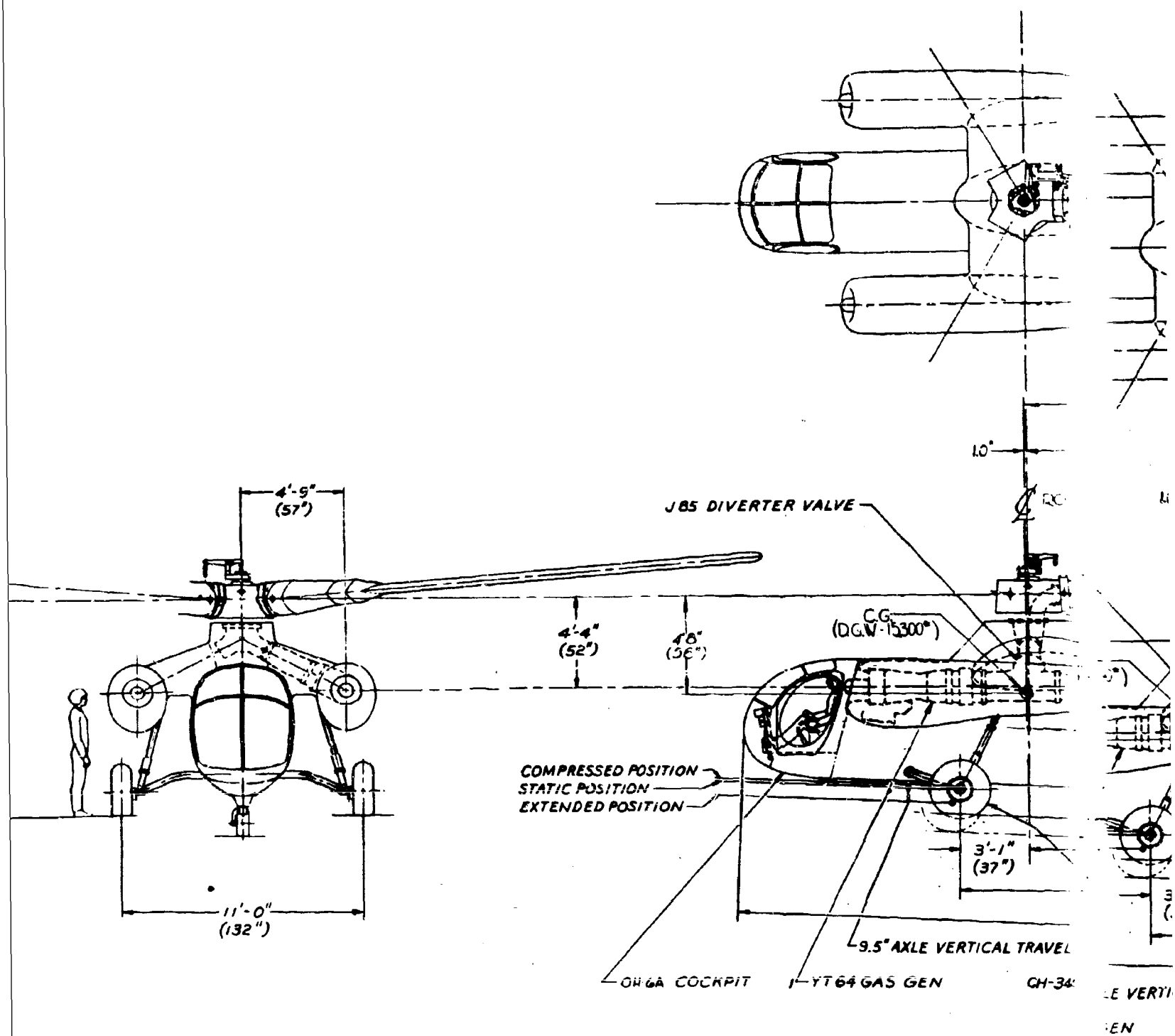
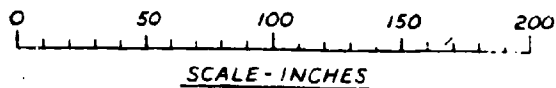
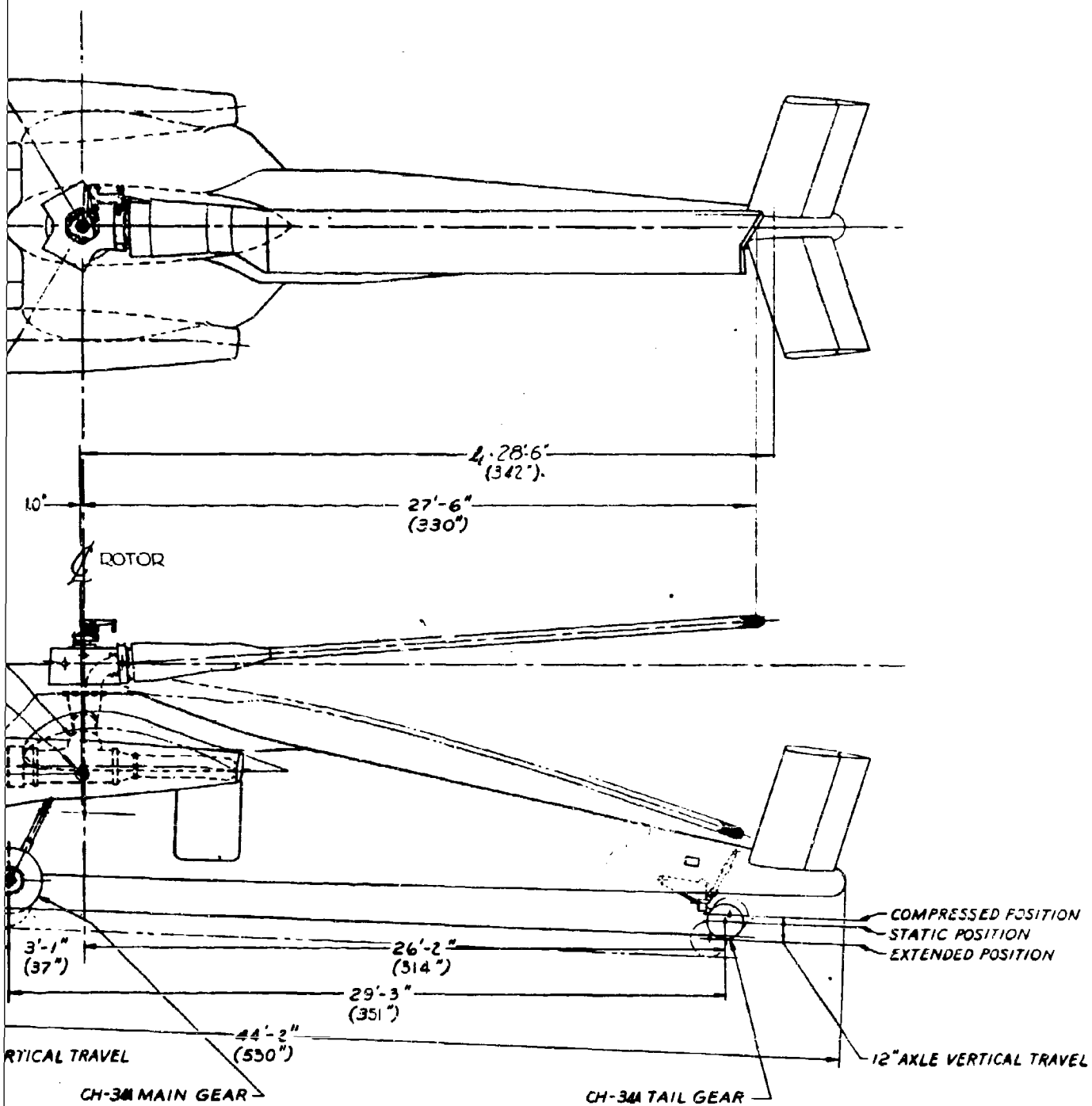


Figure 2. General Arrangement, KV-9A Hot Cycle R



ot Cycle Research Aircraft.

EMPENNAGE

Area (total)	54.0 square feet
Dihedral	45.0 degrees
Sweep	7.5 degrees
Incidence (referenced to rotor shaft)	1.0 degree
Chord	± 5 -degree adjustment
Span	3.50 feet
Aspect ratio (geometric)	15.40 feet
Airfoil	4.35
Rudder chord (37.5 percent, including overhang)	NACA 0012
Rudder span	1.31 feet
Rudder area	15.40 feet
Rudder deflection	19.90 square feet
	± 20.0 degrees

MAXIMUM CONTROL DISPLACEMENTS

Cyclic control	
Longitudinal cyclic pitch	± 10 degrees
Longitudinal cyclic stick travel	11 inches
Lateral cyclic pitch	± 7 degrees
Lateral cyclic pitch stick travel	10 inches
Collective	
Collective-pitch travel	12 degrees
Collective-stick travel	7.5 inches
Rudder pedal (from neutral)	
Full left	3.0 inches
Full right	3.0 inches

FLIGHT TESTS

INSPECTION AND MAINTENANCE PERIOD

The flight test program was preceded by an inspection and maintenance period to prepare the aircraft and its test instrumentation for additional testing following the initial flight testing conducted under Contract DA 44-177-AMC-877(T). The tasks and changes accomplished during the inspection and maintenance period are described in detail in Appendix IV. The major items accomplished were as follows:

1. Disassembly of the rotor blades; inspection of the blade spars, blade segments, ducts, retention straps, root-end flexures; and replacement of spar-to-segment attachment bolts
2. Inspection of the rotor-hub structure and ducting
3. Inspection of the fuselage, empennage, power module, and landing gear
4. Inspection of the engines, diverter valves, propulsion controls, and propulsion-system ducting
5. Replacement of engine S/N 027 with engine S/N 101
6. Removal and inspection of the rotor hydraulic power-control actuators
7. Replacement of 3/32-inch-diameter rudder cables with 1/4-inch-diameter cables
8. Rerigging of rudders to 7 degrees right with neutral yaw-control valve
9. Installation of nacelle to fuselage stiffening struts (these were later removed after flight 23 as a result of 3-per-rev vibration problems)
10. Removal, inspection, and recalibration of instrumentation and test equipment
11. Reinstallation of rotor-blade strain gages and recalibration of the blue-blade assembly in a static test fixture

SUMMARY OF TESTING

Flight testing consisted of an initial checkout and shakedown phase at Culver City, California, a ferry flight to Edwards Air Force Base, California, flight tests at Edwards AFB, and a ferry flight back to Culver City at the termination of those tests. A summary of all ground and flight operations is shown in Table I.

Shakedown and checkout of the aircraft prior to ferry to Edwards AFB consisted of seven flights to functionally check out the aircraft, its systems, and its test instrumentation and to resolve vibratory problems connected with fuselage/engine nacelle resonance characteristics. The overall vibration level was made acceptable by removal of the fuselage to the nacelle stiffening struts, by installation of a tie-cable between the stabilizer tips, and by placement of detuning ballast weights at the fuselage nose and tail and at each engine nacelle.

Rotor blade cyclic loads were carefully analyzed during the shakedown period, as a result of failures that had occurred in the specimen blade spars during the blade root-end fatigue test program (Reference 4). A flight loads spectrum obtained during flight 26 (which included flight maneuvers at altitudes up to 5,000 feet) yielded blade cyclic loads that were considered to be representative of conditions to be encountered in the ensuing flight test program.

Following analysis and review of these data, it was determined that the blade-spar fatigue life was adequate to complete the flight test program as planned, provided precautions were taken in the form of additional blade stress instrumentation, visual inspection, and the reduction and analysis of blade stress data following each flight. In this manner, the blade-life load spectrum was continuously evaluated during the course of flight testing to ensure safety of flight at all times. A detailed discussion of the rotor-blade fatigue life is presented in Appendix II. Supporting test data are presented in Appendix III.

As a result of an increase in rotor control loads anticipated for the expanded flight envelope of the follow-on flight test program, a fatigue test of a typical rotor control system rod end was accomplished. The results of this fatigue test are included as Appendix V.

The XV-9A was ferried to Edwards AFB, California, on 9 June 1965. The flight was made at an altitude of 5,000 to 6,000 feet at 70-knot IAS. Flight testing at Edwards AFB consisted of 15 flights, during which the majority of the test data for this follow-on program were obtained.

TABLE I
FLIGHT TEST OPERATIONS SUMMARY
(U. S. Army 15107)

Flight Number	Date	Purpose	Operating Times (hr)			
			Engine 1	Engine 2	Rotor	Flight
			(S/N 101-3A)	(S/N 026-1B)		
Ground Run	4-16-65	Engine and rotor shakedown; rotor tracking checkout; systems checkout	0:49	0:44	0:25	-
Ground Run	4-20-65	Rotor tracking and balance; engine operating data; single-engine rotor operation	0:59	0:58	0:36	-
Ground Run	4-21-65	Rotor tracking and balance; Ng governing checkout	1:01	1:02	0:46	-
Ground Run	4-22-65	Rotor tracking and balance	0:32	0:39	0:21	-
Ground Run	4-23-65	Rotor balance; engine acceleration checks	1:16	1:29	0:47	-
Ground Run	4-26-65	Rotor balance with tie-down cables installed	0:33	0:39	0:13	-
Ground Run	4-27-65	Rotor balance; engine acceleration characteristics	1:14	1:20	0:51	-
Ground Run	4-28-65	Ground instability test; rotor governing setup; engine-rotor acceleration data	1:24	1:29	1:13	-
22	4-30-65	Hovering flight checkout; ground run rotor track and balance; electrical failure simulation	1:21	1:34	0:52	0:18
Ground Run	5-3-65	Rotor balance and tracking; engine idle adjustment; engine-rotor operating data to $\theta_{0.75} = 10^\circ$	1:03	1:08	0:44	-
23	5-4-65	Functional flight test; ground run rotor balance and tracking; engine-rotor acceleration data	1:24	1:33	1:10	0:39
Ground Run	5-6-65	Scheduled flight 24, vibration investigation; aborted due to engine 1 fuel control malfunction	0:08	0:11	-	-
Ground Run	5-7-65	Engine 1 fuel control checkout; fuel control S/N 22284 installed (from engine S/N 010-4)	0:42	-	-	-
Ground Run	5-10-65	Engine 1 fuel control checkout; fuel control S/N 23249 installed (from engine S/N 027-1A)	0:42	-	-	-
Ground Run	5-11-65	Engine 1 functional checkout with fuel control S/N 23249	1:46	0:51	0:39	-
Ground Run	5-12-65	Engine 1 functional checkout; variable geometry rigging and density adjustment	0:36	0:10	-	-
Ground Run	5-13-65	Tie-down run; engine-rotor operating characteristics at $\theta_{0.75} = 10^\circ$; emergency shutdown evaluation; rotor governing system deactivation checkout	1:05	1:10	0:50	-
24	5-17-65	Vibration investigation; flight 24A with basic configuration; flight 24 B and C with 11-lb stabilizer weights installed; flight 24D with 18-lb stabilizer weights installed	1:39	1:56	1:23	0:45

TABLE I (Continued)

Flight Number	Date	Purpose	Operating Times (hr)			
			Engine 1	Engine 2	Rotor	Flight
25	5-18-65	Vibration investigation; flight 25C with 7-lb stabilizer weights and tail normal; flight 25A with 40-lb tail weights and 18-lb stabilizer weights; flight 25B with 30-lb tail weights and 11-lb stabilizer weights	1:25	1:31	1:13	0:40
26	5-21-65	Malibu test area; climb to 5,000 feet; level flight at 5,000 and 3,000 feet and at 50-, 60-, and 70-kn IAS	1:13	1:16	1:09	0:55
Ground Run	5-24-65	Engine operating data; over-board; cleaned compressor, engine 2; engine 2 variable geometry rigging; single-engine rotor operation	1:02	1:20	0:41	-
Ground Run	5-25-65	Engine topping check at $\theta_{0.75} = 10.5^\circ$ (maximum) with 99 percent N_R	0:25	0:30	0:12	-
27	5-26-65	Blade loads; effect of cg variation; flight 27A at fwd cg and flight 27B at aft cg; level flight at 80-kn and 20° banked turns	0:45	0:49	0:37	0:22
(Removed engine 101-1A and installed engine 027-1A in left nacelle)						
(S/N 027-1A)						
Ground Run	6-4-65	Functional checkout, engine 027-1A; tie-down run and topping check to rotor	1:18	0:28	0:24	-
28	6-4-65	Vibration investigation; stabilizer tie-cable installed; functional test flight with engine 027-1A installed	0:39	0:41	0:26	0:16
29	6-9-65	Ferry flight to Edwards Air Force Base; climb to 5,000-foot cruise altitude	1:47	1:39	1:30	1:10
Ground Run	6-16-65	Engine leak check; fuel manifold change	0:05	0:07	-	-
30	6-17-65	Hover evaluation at Edwards AFB; level flight at 3,200 ft and at 50-, 60-, 75-, and 95-kn; sideslips; directional and lateral pulses; 55- and 75-kn run-on landings	1:46	1:46	1:39	1:23
31	6-22-65	Sawtooth climbs at 40-, 60-, and 70-kn and at 3,500 to 4,500 ft; level flight at 5,500 ft and at 73.5 kn; climb 3,000 ft to 6,000 ft; level flight at 6,500 ft and at 50 kn	1:36	1:34	1:10	1:00

TABLE I (Continued)

Flight Number	Date	Purpose	Operating Times (hr)			
			Engine 1	Engine 2	Rotor	Flight
32	6-24-65	Check climb to 6,500 ft-hp at 55 kn; level flight at 6,500 ft-hp and at 50-, 61-, 70-, and 81-kn IAS; level flight at 3,200 ft-hp; 1.2 g symmetrical pull-up at 60 kn; level flight at 3,200 ft and at 95-kn IAS	1:46	1:44	1:38	1:16
33	6-28-65	Hover performance at $N_R = 100$ percent; hover stability with cyclic pulses and step inputs	1:09	1:09	1:03	0:48
34	6-30-65	Functional checkout, warning light system; flight plan not accomplished due to warning light malfunction	0:44	0:45	0:29	0:06
Ground Run	7-1-65	Functional checkout, warning light system and flight control system dither	0:17	0:16	0:09	-
35	7-2-65	Climb to 7,500 ft; speed stability at 45 to 65 in; speed-power at 7,500 ft and at 50-, 60-, and 75-kn IAS; sawtooth climbs and descents; speed-power at 3,200 ft	1:52	1:54	1:47	1:25
36	7-7-65	Speed-power at 5,500 ft density altitude and at 97- and 100-percent N_R ; pacer aircraft airspeed calibration (T-37); speed stability with mid-cg, symmetrical pull-ups	1:34	1:37	1:29	1:11
37	7-9-65	Climb to 6,000 ft with fwd cg; longitudinal controllability, climb and descent; directional characteristics, descent	0:57	0:57	0:51	0:39
38	7-13-65	Hover performance at $N_R = 100$ percent; airspeed calibration, OH-6A pacer at 42 to 95-kn IAS; climb to 8,500 ft; level flight at 8,500 ft and at 50-, 60-, and 70-kn IAS	1:53	1:53	1:46	1:22
39	7-15-65	Climb to 8,050 ft; single-engine rotor operation during descent; longitudinal controllability with aft cg	1:24	1:24	1:15	0:45
(Removed engine 026-1B and installed engine 101-3A in right nacelle)						
(S/N 101-3A)						
Ground Run	7-26-65	Functional checkout and variable geometry tracking, engine S/N 101-3A; topping and acceleration checks; fuel control S/N 22626 installed	0:28	1:21	0:21	-

TABLE I (Continued)

Flight Number	Date	Purpose	Operating Times (hr)			
			Engine 1	Engine 2	Rotor	Flight
40	7-27-65	Climb to 8,600 ft; single-engine descent with Engine 1 overboard	1:05	1:02	0:52	0:25
41	7-29-65	Hover performance, IGE with $N_R = 97, 100$ and 103 percent; hover turns to 90° with 1- and 2-inch pedal deflection; chase aircraft aborted flight	1:03	0:57	0:52	0:27
Ground Run	7-30-65	Functional checkout of diverter-valve operation and of diverter-valve position switches	0:18	0:11	0:06	-
Ground Run	8-2-65	Flight plan discontinued due to diverter-valve 1 position indicating light malfunction	0:16	0:12	0:04	-
Ground Run	8-4-65	Functional checkout, diverter-valve 1	0:16	0:10	0:06	-
42	8-5-65	Climb to 10,000 ft; speed-power at 10,000 ft and at 55 kn; single-engine descent with engine 2 overboard to 4,100 ft; hover performance at 97, 100, and 103 percent N_R	1:36	1:33	1:28	0:53
43	8-12-65	Hover performance, OGE; symmetrical pull-ups at 60-kn and at 3,500 ft; descent from 6,000 ft; hover performance IGE	2:37	2:29	2:17	1:33
Ground Run	8-18-65	Functional checkout of revised bolt installation on rear spar outboard hole	0:22	0:20	0:15	0:04
Ground Run	8-25-65	Functional checkout, replaced blue-blade tip segment; rebalanced rotor	0:31	0:27	0:19	0:03
44	8-26-65	Ferry flight to Culver City; speed-power, 6,500 ft at 95 percent N_R	1:27	1:21	1:15	1:07
Ground Run	9-1-65	Diverter-valve leakage test	0:33	0:36	0:34	-
Program Total			29:39	33:53	39:23	19:32
Prior Total			0:00	31:38	45:22	15:42
Cumulative Total			29:39	65:31	84:45	35:14

The significant portions of the test data and their analyses are presented in the section titled Flight Test Results.

FLIGHT TEST PROCEDURES

The aircraft was extensively instrumented for measurement of engine and rotor performance, structural blade loads and temperatures, aircraft rates and attitudes, control positions, and flight parameters. Continuous data records were taken during flight. All instrumentation was calibrated prior to the start of the program, and check calibrations were accomplished at periodic intervals during the program to ensure maximum accuracy of test data. Instrumentation calibration was accomplished again after completion of the test program.

The XV-9A flight operations at Edwards AFB were based at the Army Aviation Test Activity (ATA) hangar. Chase aircraft support was supplied by ATA, and all flights were accompanied by a chase aircraft (normally a helicopter) with aerial photo coverage provided by Hughes personnel. Crash and fire protection was supplied by Edwards AFB personnel.

Flights were scheduled on a weekly basis in accordance with Edwards AFB flight test preparations procedures. The normal flight schedule was for two flights per week of more than 1-hour duration each. Flights were scheduled during early morning hours because of the more favorable atmospheric conditions for testing. A typical daily flight test activity was as follows:

0430	Crew reports
0600	Engine start
0615	Takeoff
0730	Land
0740	Engine shutdown
0945	Flight data, test logs, and instrumentation setup and status sheets sent to Culver City via liaison aircraft
1300	Postflight debriefing and planning meeting, Culver City

All flight test operations were preceded by a standard preflight inspection of the airframe, rotor, engines, and systems to ensure safety of flight and proper operation of the aircraft. Postflight inspection of the entire aircraft, systems, and test instrumentation was accomplished. The rotor blade spars were inspected at blade station 91 after each flight to ensure continued structural integrity. This inspection was necessitated by the occurrence of a fatigue crack on the (specimen) spars at

this location on the blade root-end fatigue test specimen (Reference 4). No discrepancies were found in this area during the course of the program.

Preflight and postflight inspection signoff sheets were used to guide maintenance personnel and to provide recorded verification of completed items. All work items accomplished on the aircraft between flights were entered on work sheets that described the task to be done and provided a record of all changes and maintenance performed on the aircraft. These items were authorized by the engineer in charge and were signed off and stamped by the inspector to denote completion. A configuration and change log is included as Appendix VI.

Two-way radio communication between the XV-9A and ground personnel was maintained during all flight operations, for monitoring and coordinating test operations. A flight test log was kept for each flight test operation, to document operating time and pilot observations and to facilitate data reduction.

Data handling was expedited by means of a liaison aircraft - a single-engine Cessna 210 - that was operated between Edwards AFB and the contractor's facility at Culver City. The flight data, consisting of undeveloped oscillograph rolls and photo panel film, Brown recorder rolls, instrumentation setup and status sheets, and the flight test log were assembled at Edwards AFB immediately following each test flight and were flown to Culver City, where data processing and reduction were accomplished. Transcription of the pilot's comments from the airborne tape recorder was accomplished at Edwards AFB following each flight.

The aircraft's weight and center of gravity were determined by actual weighing of the in-flight configuration at the beginning and at the end of the flight test period at Edwards AFB. The final weight and balance check was accomplished at the Weights Hangar at Edwards AFB. The aircraft weight and balance sheets showing the actual weighing results are included in Appendix VII. Correlation with previous weighing at Culver City was satisfactory.

The in-flight center of gravity and gross weight were computed from fuel quantity readings taken at each data point and at frequent intervals during flight. Center-of-gravity control was accomplished by means of pilot management of the individual fuel quantities in the forward and aft fuel cells during flight. This procedure was accomplished by crossfeeding both engines from either the forward or the aft fuel cell until the desired center of gravity was attained.

FLIGHT TEST RESULTS

The aircraft was evaluated and test data were recorded for evaluation of Hot Cycle system performance, structural loads and temperatures, stability and control characteristics and vibration levels for the following flight conditions:

1. Engine and rotor start
2. Rotor acceleration
3. Taxi and ground handling
4. Hovering
 - a. Steady hover, IGE and OGE
 - b. Hover turns
5. Transition to forward flight
6. Approach to hover
7. Climb
8. Level flight,
9. Level flight turns at 20- and 30-degree bank angle
10. Single-engine rotor flight
11. Symmetrical pull-ups
12. Sideward flight to right and left
13. Rearward flight
14. Descents, normal and minimum-power
15. Landing

The flight test results are presented in following paragraphs. In addition, a qualitative evaluation of the aircraft is presented in Appendix VIII. Because of the large volume of flight test data recorded, only the significant portions are presented. All other flight test data are on file at the contractor's facility.

Structural Data

Load levels observed during the 20-hour flight test program on the XV-9A were essentially the same as those observed during the 15-hour flight test program (Reference 1) for comparable speeds, altitudes, and load factors. The loads reported on the following pages cover flight to higher speeds, higher altitudes, and higher load factors than those shown in Reference 1.

Figures 3 through 9 present the variation of the significant structural cyclic loads with increasing airspeed in stabilized level flight.

Figure 10 is the V-n diagram for the XV-9A at sea level and at a gross weight of 13,000 pounds. Since the data points shown on this figure were

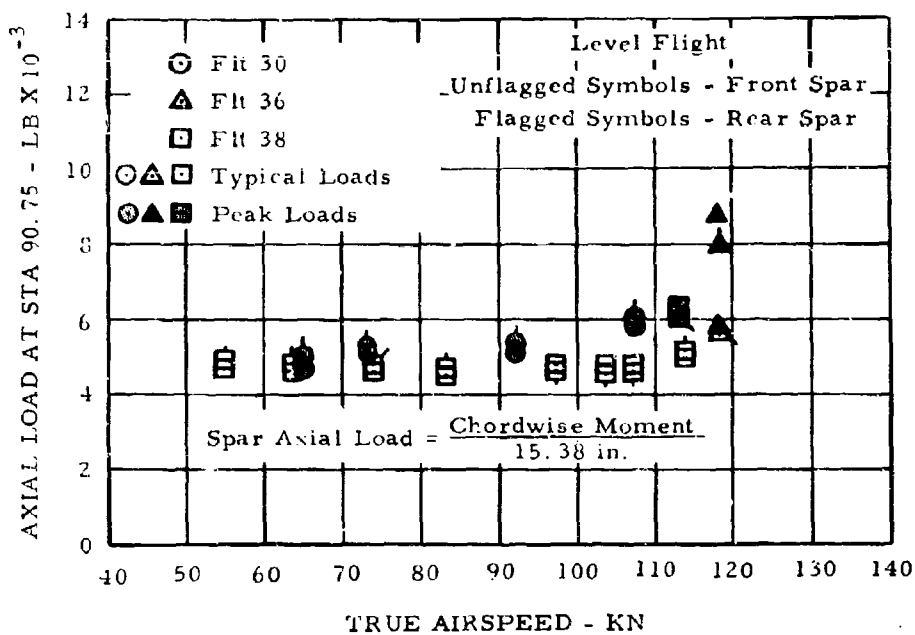


Figure 3. Cyclic Spar Axial Load at Station 90.75 Versus True Airspeed.

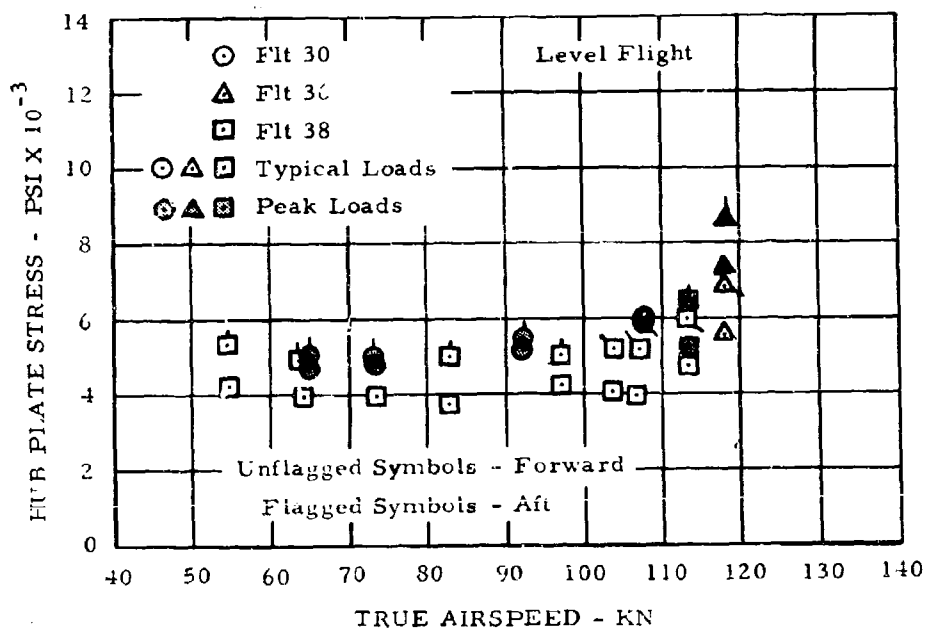


Figure 4. Cyclic Hub Plate Stress Versus True Airspeed.

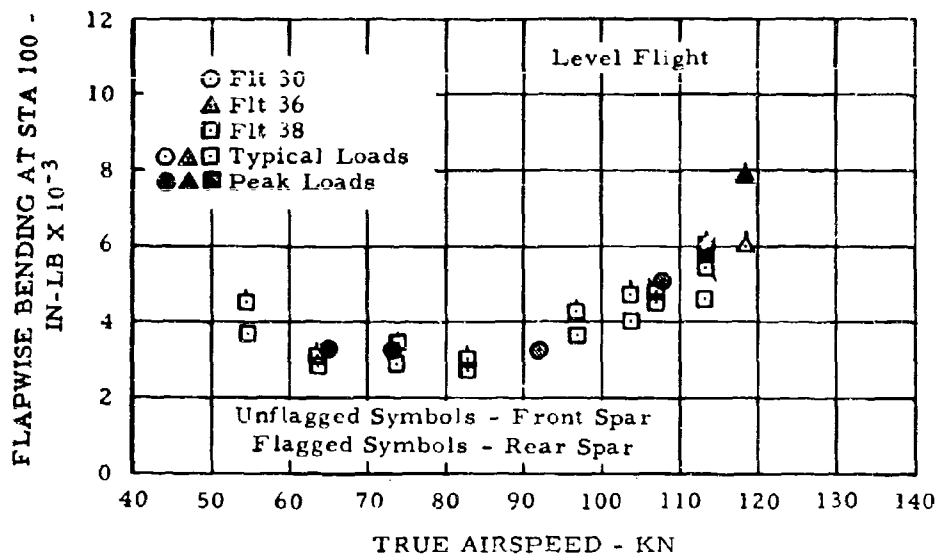


Figure 5. Cyclic Flapwise Bending Moment at Station 100 Versus True Airspeed.

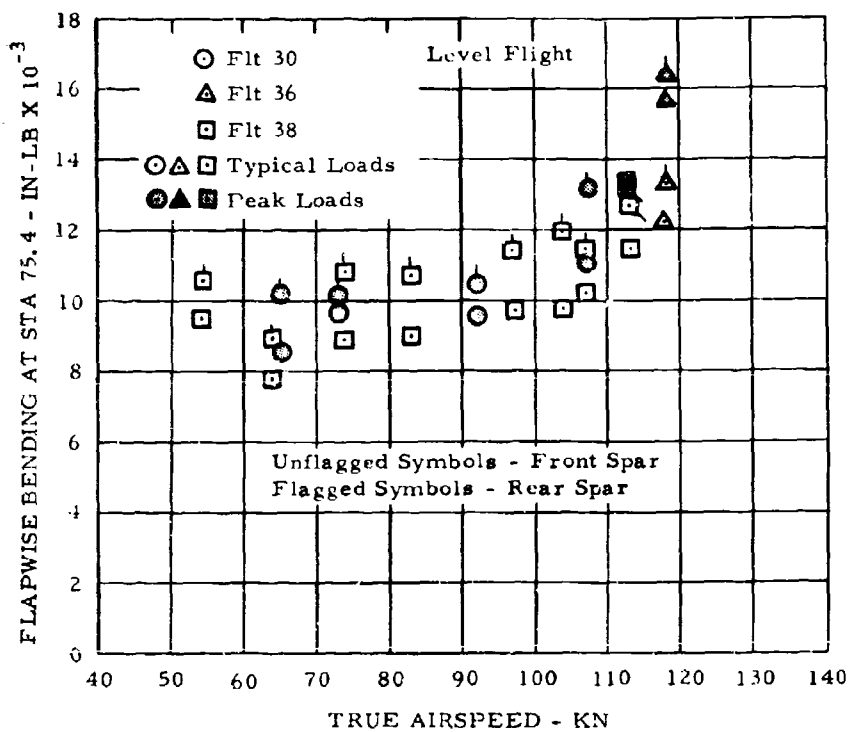


Figure 6. Cyclic Flapwise Bending Moment at Station 75.4 Versus True Airspeed.

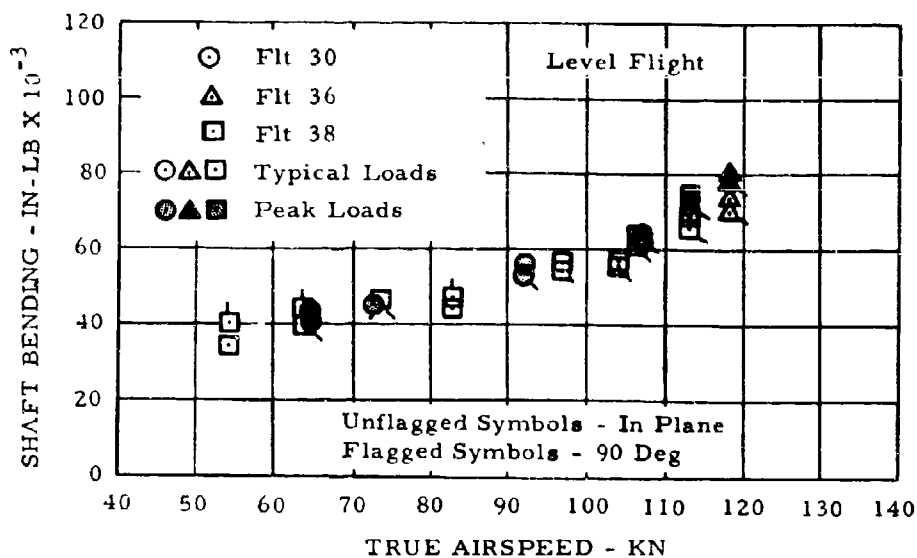


Figure 7. Cyclic Shaft Bending Moment Versus True Airspeed.

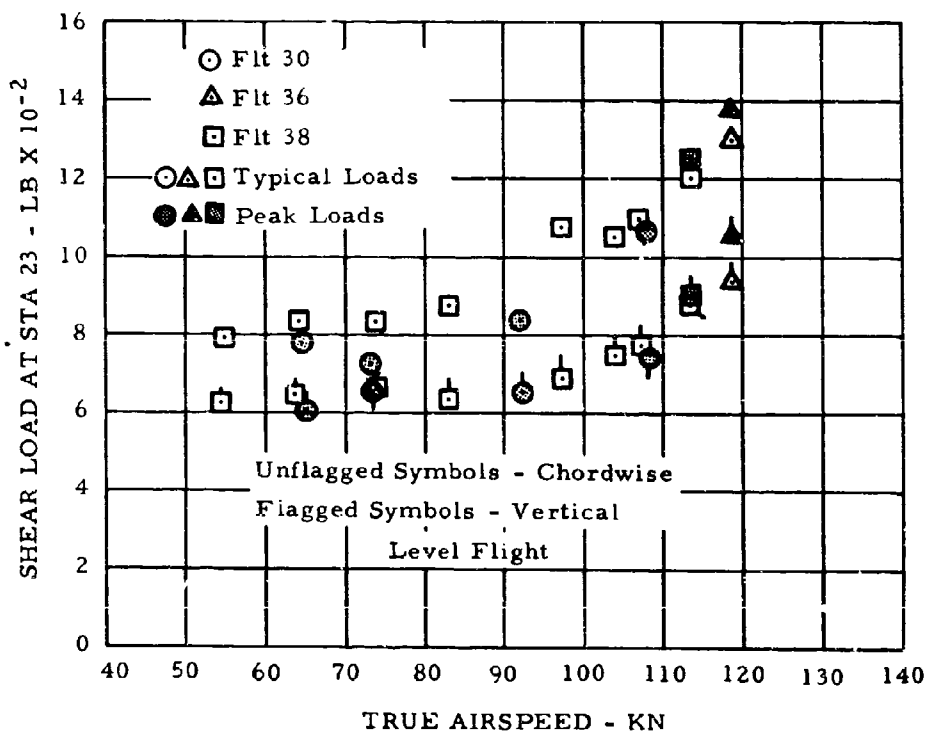


Figure 8. Cyclic Shear Load at Station 23 Versus True Airspeed.

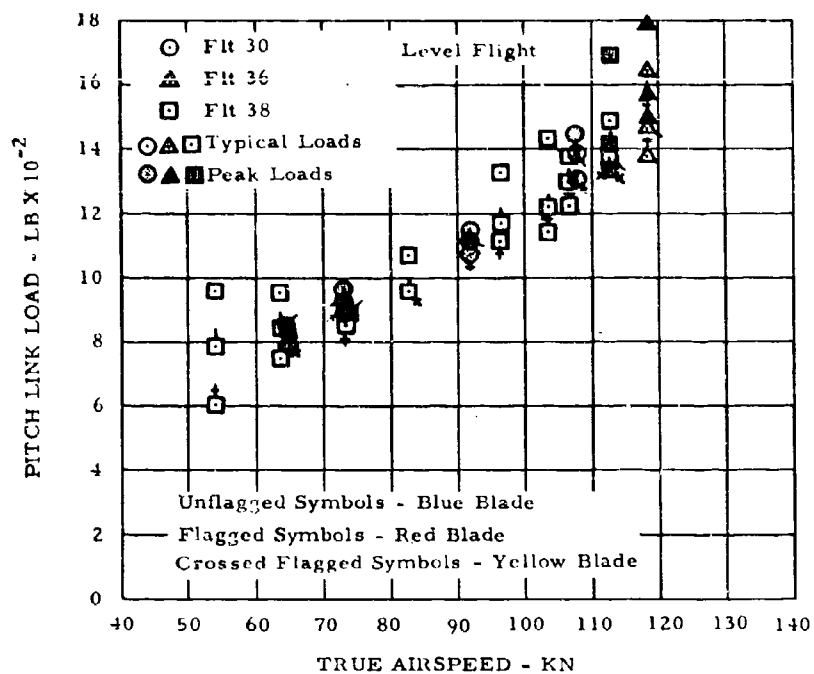


Figure 9. Cyclic Pitch Link Load Versus True Airspeed.

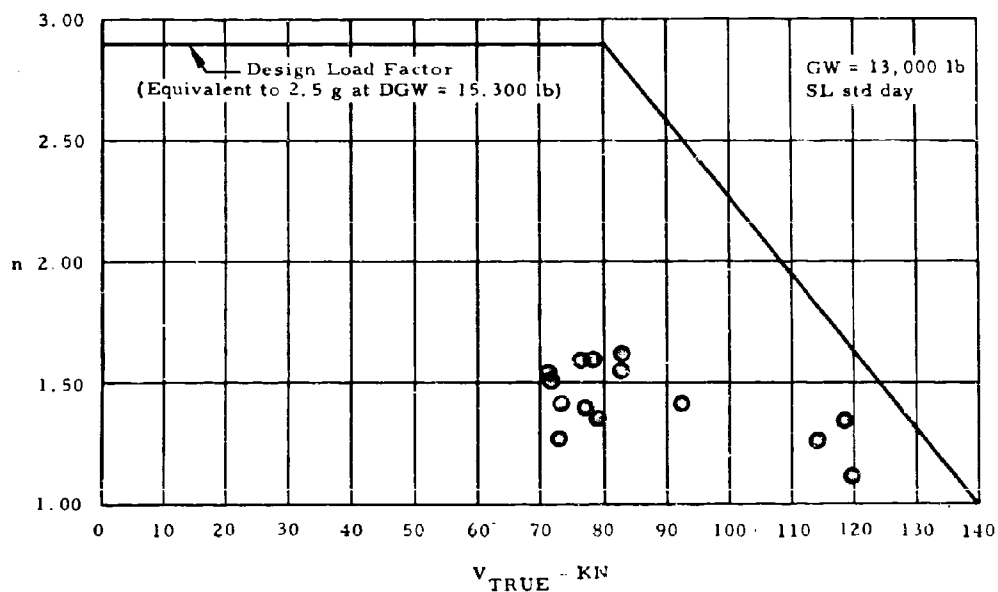


Figure 10. V-n Diagram.

obtained at various altitudes and gross weights, the points were corrected on a C_T/σ basis to sea level standard and to 13,000-pound gross weight by means of the equation

$$n \text{ (sea level std, 13,000 lb)} = \frac{n \text{ (measured)} \times W \text{ (at time of test)}}{13,000 (\rho/\rho_0)}$$

(No correction for rotor speed is necessary, inasmuch as all tests were conducted at approximately 100-percent rotor speed.)

The cyclic blade loads were observed to increase appreciably in the air-speed range from 110 to 120 knots where the collective pitch required approached and reached maximum (9.8 degrees). Lower cyclic blade loads in this region would be expected to result from parasite drag reduction and improved blade profile power factor, as discussed in the Performance section of this report.

Figures 11 through 17 present the variation of the significant structural cyclic loads with increasing load factor during maneuvers at approximately 70- to 80-knot airspeed, including pull-ups and turns. The load factors used on these plots are corrected to sea level and to 13,000-pound gross weight by the preceding equation. The flapwise bending loads show an increase at 1.6-g adjusted load factor. Otherwise, there is a small effect of load factor on cyclic loads.

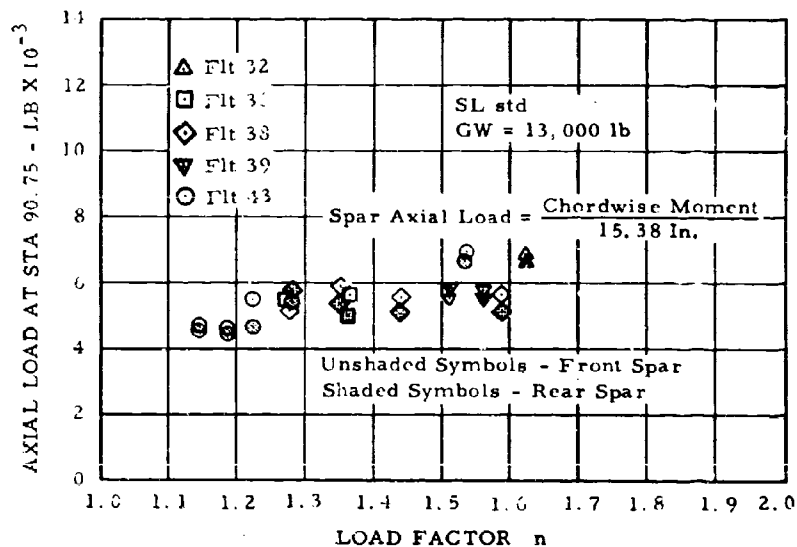


Figure 11. Peak Cyclic Spar Axial Load at Station 90.75 Versus Load Factor.

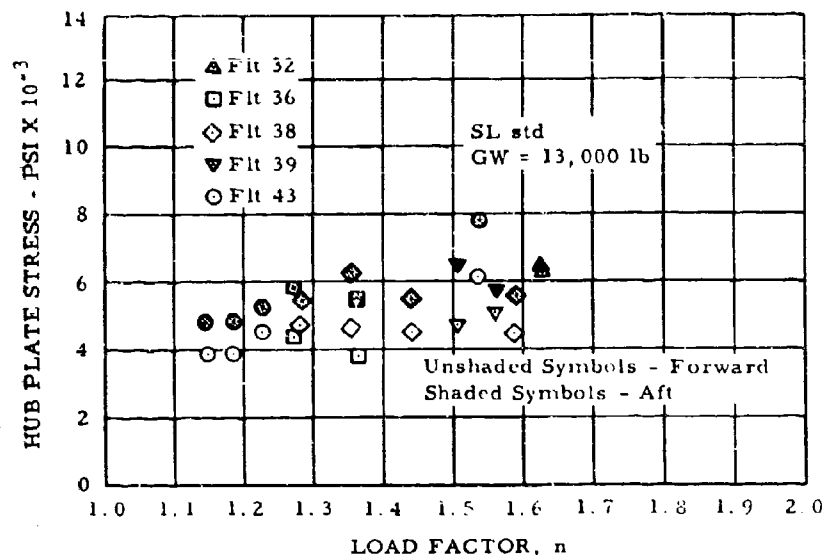


Figure 12. Peak Cyclic Hub Plate Stress Versus Load Factor.

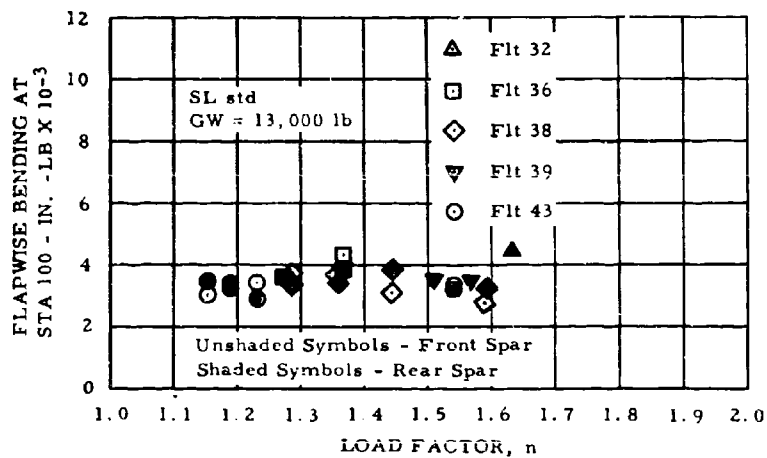


Figure 13. Peak Cyclic Flapwise Bending Moment at Station 100 Versus Load Factor.

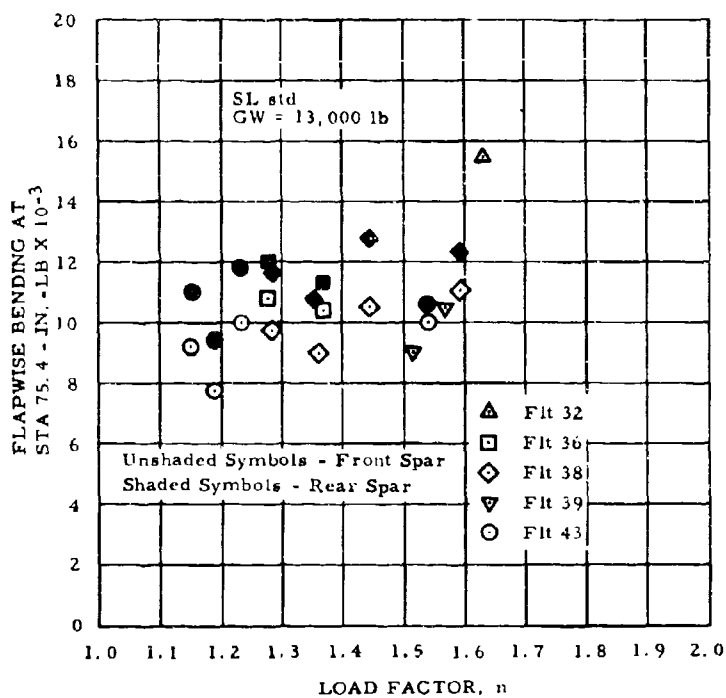


Figure 14. Peak Cyclic Flapwise Bending Moment at Station 75.4 Versus Load Factor.

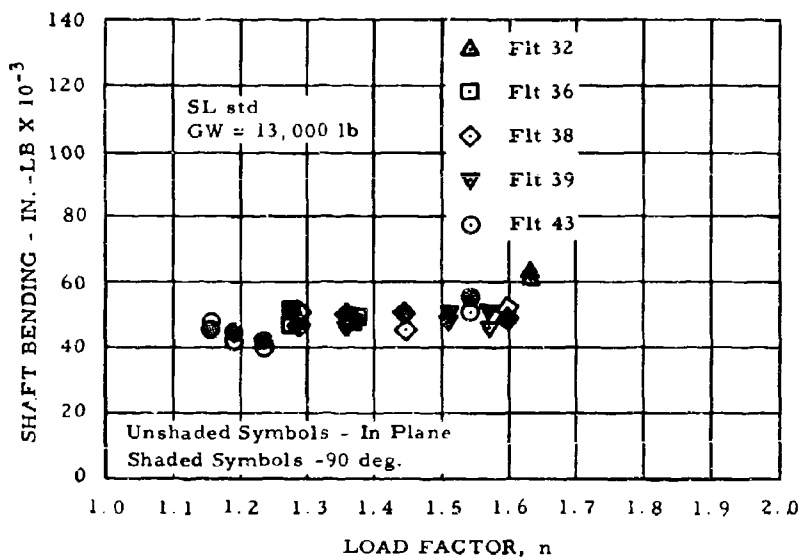


Figure 15. Peak Cyclic Shaft Bending Moment Versus Load Factor.

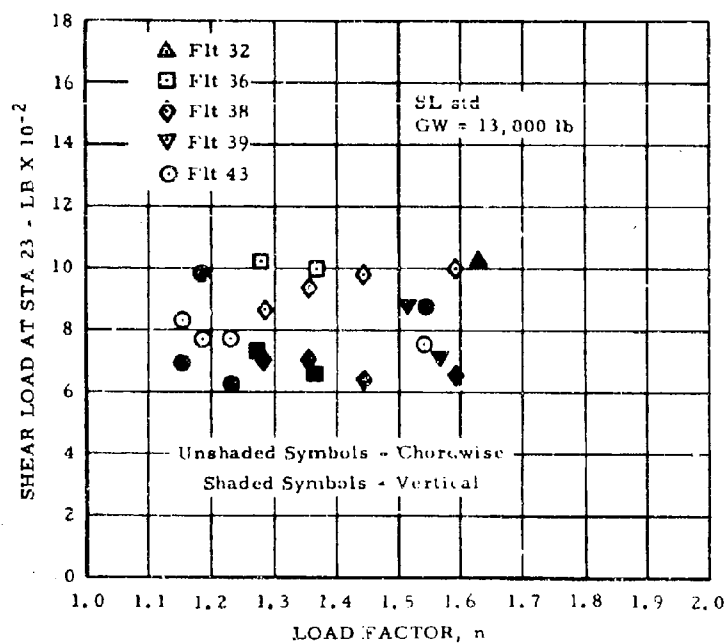


Figure 16. Peak Cyclic Shear Load at Station 23 Versus Load Factor.

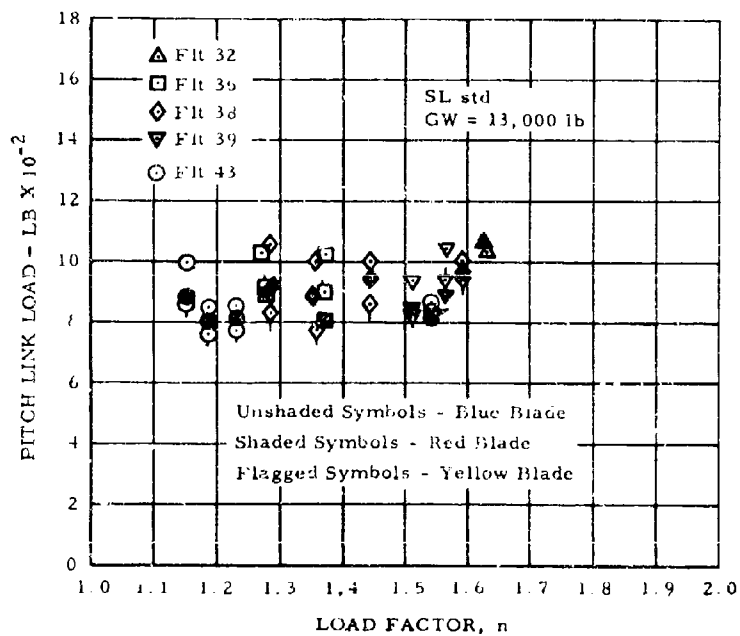


Figure 17. Peak Cyclic Pitch Link Load Versus Load Factor.

Rotor blade cyclic chordwise bending moments (spar axial load) were very closely monitored during the test program. Table II is a tabulation of actual cycle counts of cyclic spar axial loads greater than 7,000 pounds for all flights from flight 28 to the end of the program. Figures 18 through 21 present cyclic spar axial load spectra for four flights sampled during this program. These flights are considered to be representative of all flights flown at Edwards AFB during this program. A combination of data presented in Table II and Figures 18 through 21 was used to evaluate fatigue damage to the main rotor blades on a flight-by-flight basis.

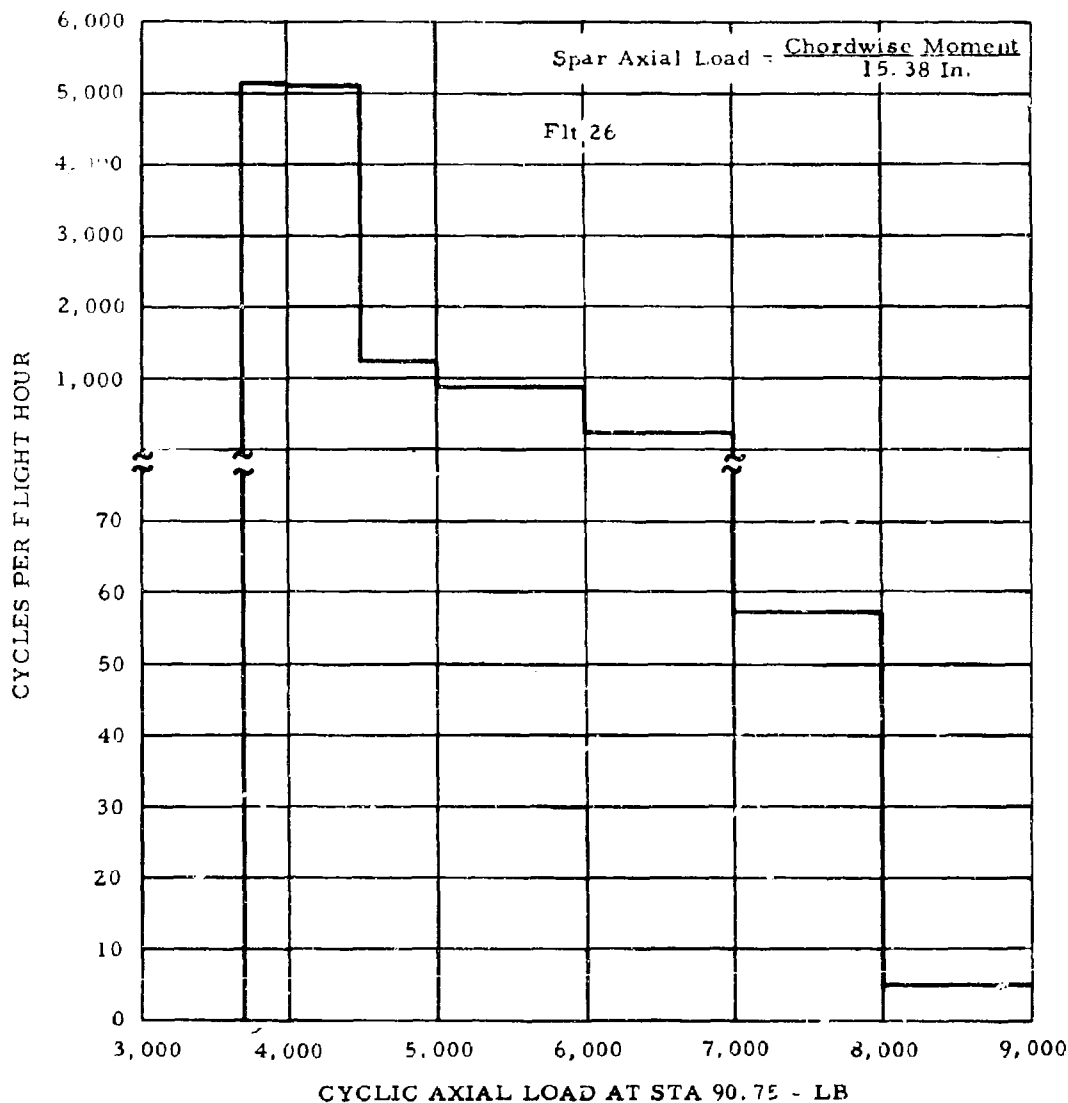


Figure 18. Blade Spar Cyclic Axial Load Spectrum, Flight 26.

TABLE II
NUMBER OF CYCLES OF BLADE SPAR AXIAL LOAD
GREATER THAN ±7,000 POUNDS

Flight Number	Time (hr)	±7,000 to ±7,500 lb		±7,500 to ±8,000 lb		±8,000 to ±8,500 lb		±8,500 to ±9,000 lb		±9,000 to ±9,500 lb		±9,500 to ±10,000 lb		±10,000 to ±10,500 lb		±10,500 to ±11,000 lb		±11,000 to ±11,500 lb		±11,500 to ±12,000 lb		±12,000 to ±12,500 lb		±12,500 to ±13,000 lb		±13,000 to ±13,500 lb		±13,500 to ±14,000 lb		±14,000 to ±14,500 lb	
		Axial Load	Axial Load	Axial Load	Axial Load	Axial Load	Axial Load	Axial Load	Axial Load	Axial Load	Axial Load	Axial Load	Axial Load	Axial Load	Axial Load	Axial Load	Axial Load	Axial Load	Axial Load	Axial Load	Axial Load	Axial Load	Axial Load	Axial Load	Axial Load	Axial Load	Axial Load	Axial Load	Axial Load	Axial Load	
28	0.27	9	2																												
29	1.17	11	10	1																											
30	1.38	2	1							2																					
31	1.00	21	5	1																											
32	1.27	17	2	1	1																										
33*	0.80	4	4	4	3	1	3	1	4	1	4	1	2	2	1	2	1	1													
34	0.10	11																													
35	1.42	36	13	2	2																										
36	1.18	22	9	2	1																										
37	0.65	56	8	4	1																										
38	1.37	7																													
39	0.75	13	5																												
40	0.42	12	5	2	1																										
41	0.45	2	2																												
42	0.88	8	7	2																											
43**	1.38	13	3	4	3	5	3	5	3	3	3	3	3	3	3	3	3	1	1												
44	1.12	21	9	3	2	1	1	1	1																						
Totals	15.61	255	85	26	16	9	8	9	5	9	8	4	5	5	1	1	1	1	1												

High loads on Flight 33 due to lateral stick pulse.

High loads on Flight 43 occurred during recovery from a vertical climb.

*High loads on Flight 33 due to lateral stick pulse.

**High loads on Flight 43 occurred during recovery from a vertical climb.

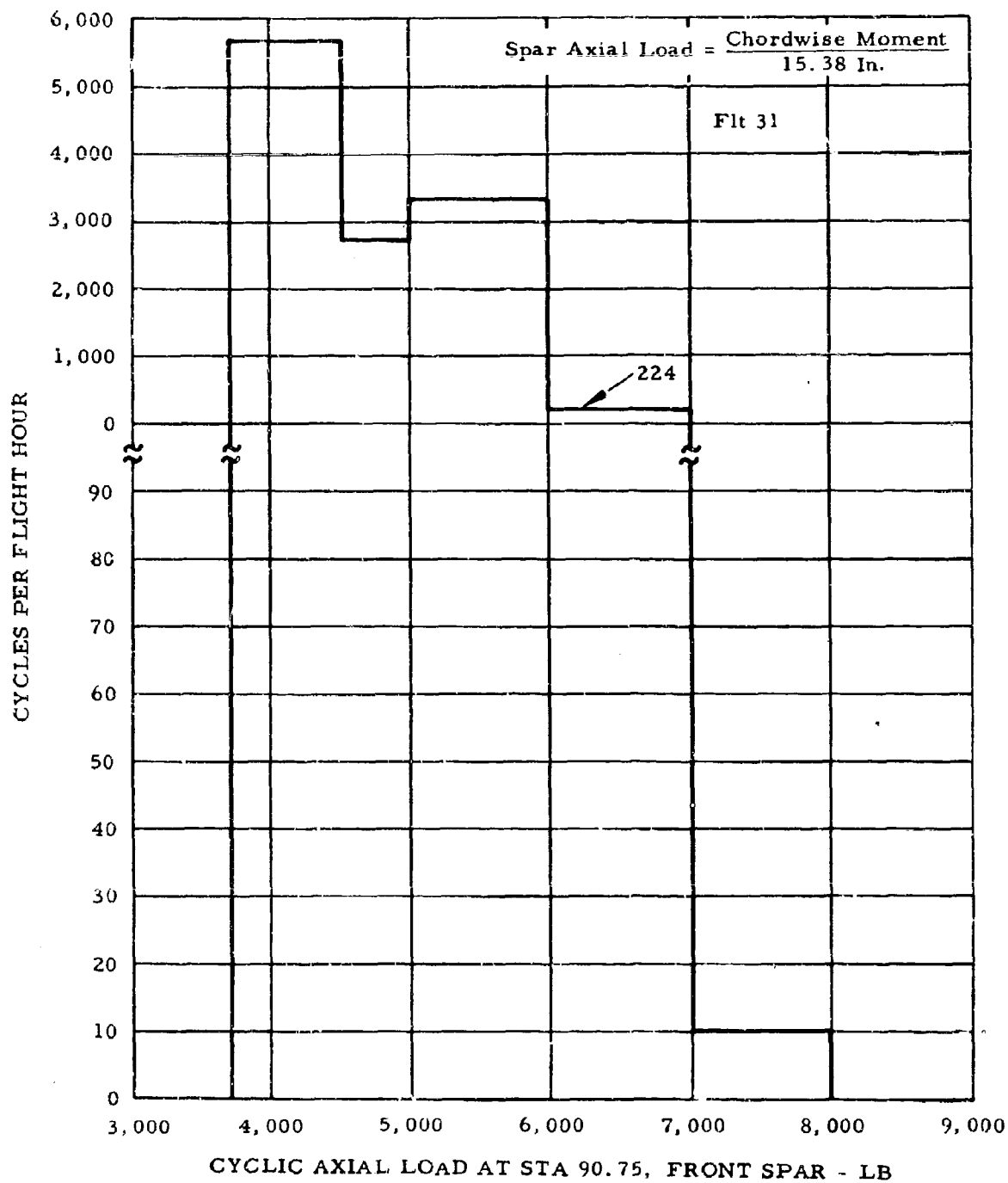


Figure 19. Blade Spar Axial Load Spectrum, Flight 31.

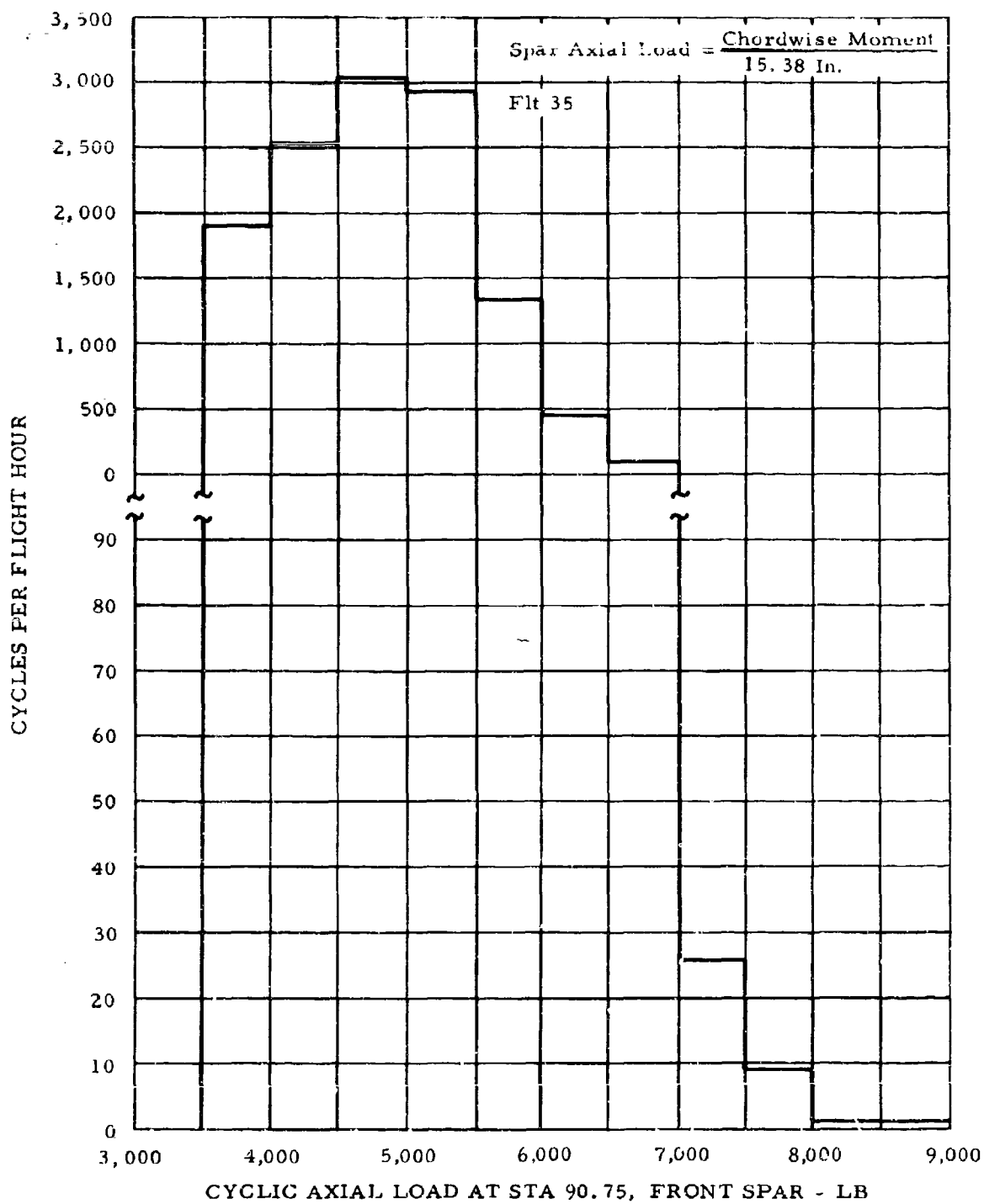


Figure 20. Blade Spar Cyclic Axial Load Spectrum, Flight 35.

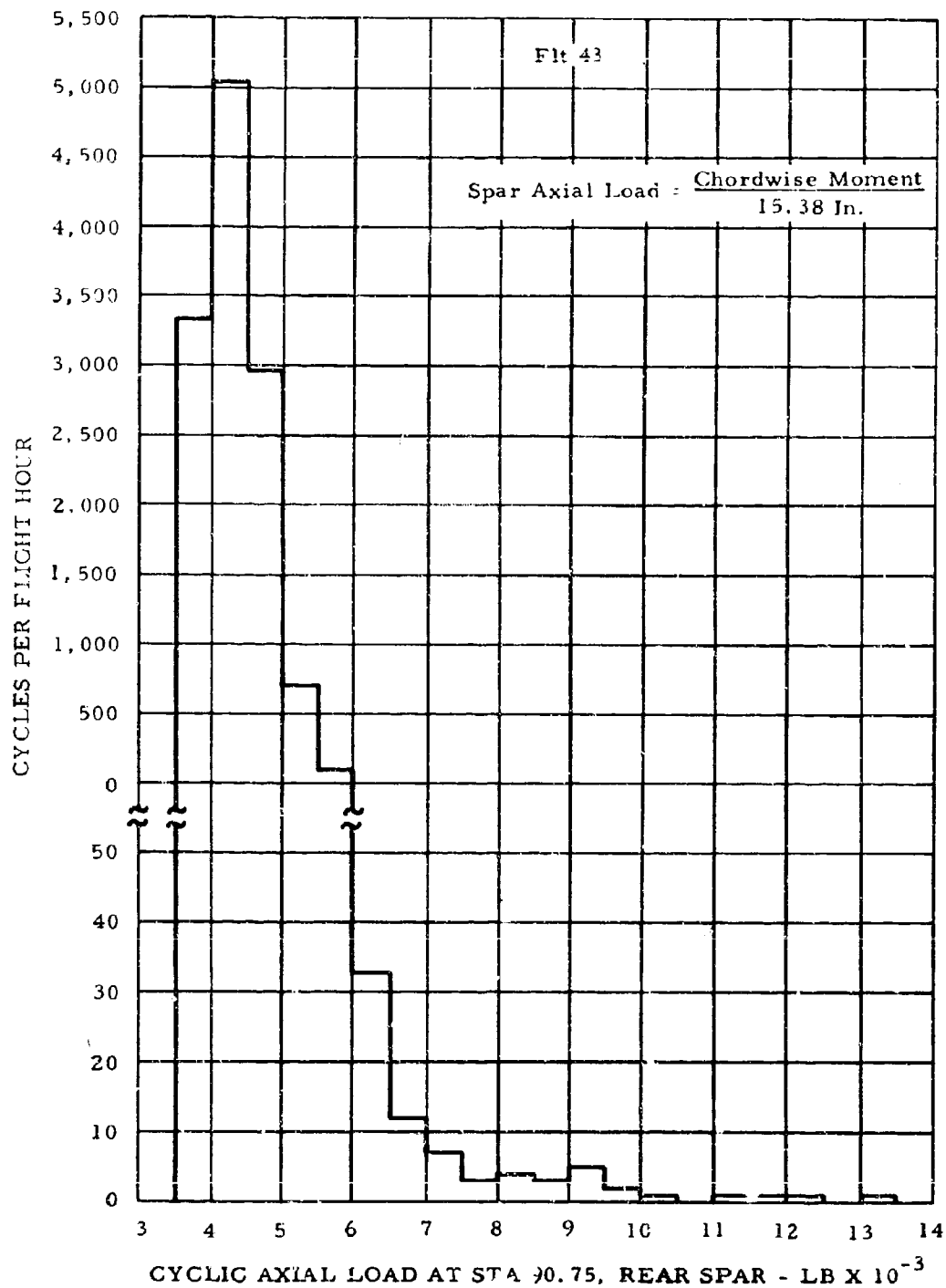


Figure 21. Blade Spar Cyclic Axial Load Spectrum, Flight 43.

Figure 22 shows the amplitude of peak cyclic chordwise blade bending moments along the span of the blade during level flight at 120-knot TAS.

The variation of cyclic flapwise blade bending moments along the span of the blade is shown on Figure 23 for level flight at 120 knots. Approximately 7,650 in. -lb of the peak of 15,400 in. -lb that occurred near blade station 65 is due to the coupling of chordwise fatigue loads.

For a number of stabilized level flight conditions, blue-blade pitch link load was measured at the points corresponding to blue-blade azimuth positions of 90 degrees (advancing blade) and 270 degrees (retreating blade).

Figure 24 presents these measured pitch link loads versus tip Mach number. Also shown on Figure 24 are pitch link loads for the same points with the load due to strap windup subtracted out, leaving essentially the load due to aerodynamic forces. The increase in pitch link load due to the aerodynamic loads at the extremes of M_T obtained is small compared with the load due to strap windup, indicating that the NACA 0018 airfoil used is free of significant moment divergence up to $M_T = 0.82$ on the advancing tip and up to 11.46-degree angle of attack at $M_T = 0.45$ to 0.50 on the retreating tip.

Structural and Operating Temperatures

1. Rotor Temperatures

Temperatures of the rotor and associated components were recorded on a Brown recorder. Inputs from thermocouples were located in various parts of the blades and were channeled to three switching boxes, then to a hot reference junction box, through the rotor slip ring, finally terminating at the Brown recorder.

Data from the Brown recorder were read and analyzed and produced operating temperatures of the following rotor components and systems: (1) blade tip gas, (2) front and rear spars, (3) flexures, (4) ribs, (5) spar cooling air, (6) outer skins, (7) gas duct walls, (8) rotor shaft, (9) tip transducer housing, (10) blade root cooling air, (11) rotor spoke assembly, (12) ball joint inner surface, (13) upper and lower bearings, and (14) inboard articulate duct seals.

Figure 25 shows the location of the thermocouples along the rotor and its accompanying tabulation summarizes the maximum temperatures recorded during the flight test program (flights 23 through 44) together with the estimated limit temperatures associated with that section of the

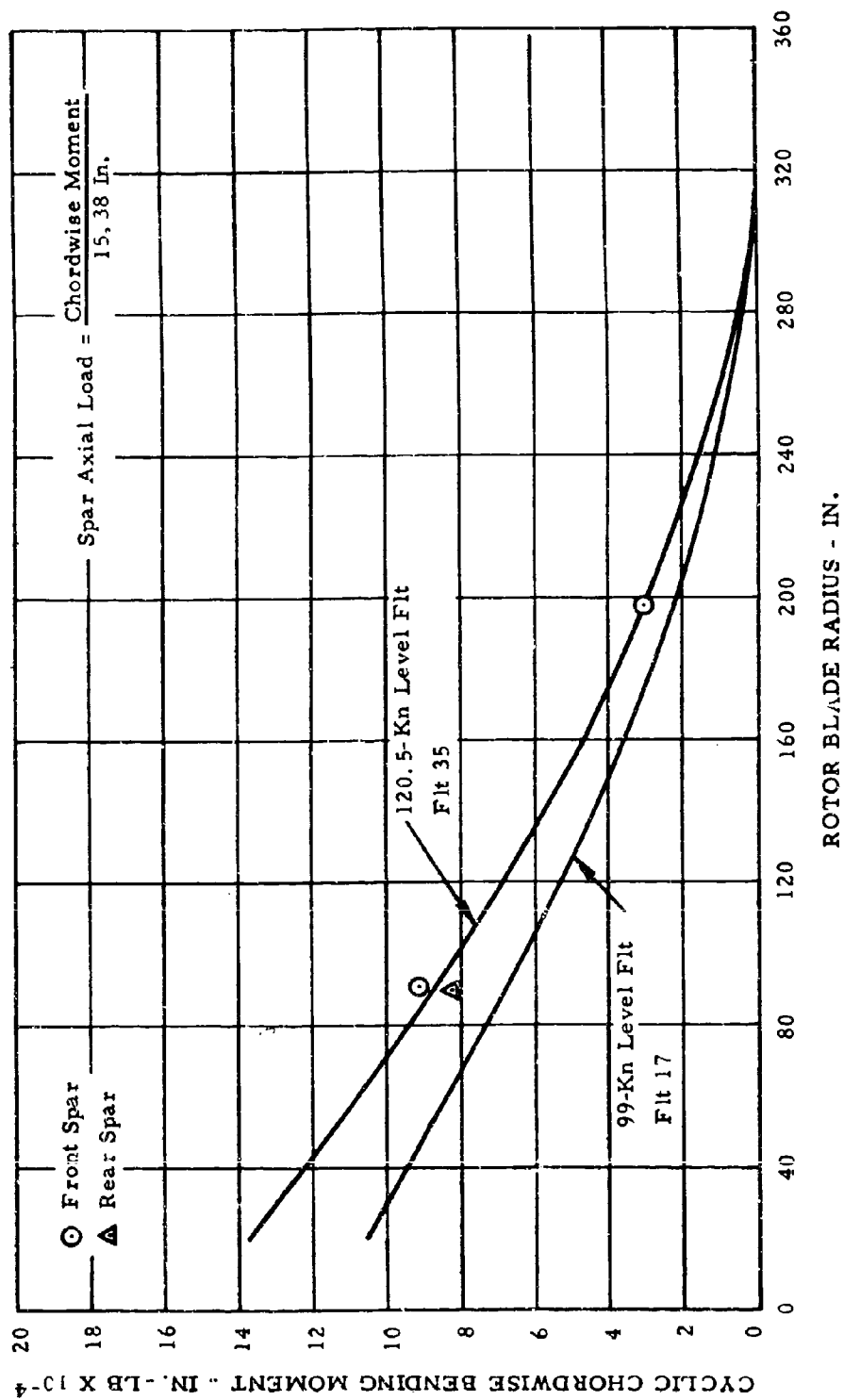


Figure 22. Cyclic Chordwise Bending Moment Versus Blade Radius.

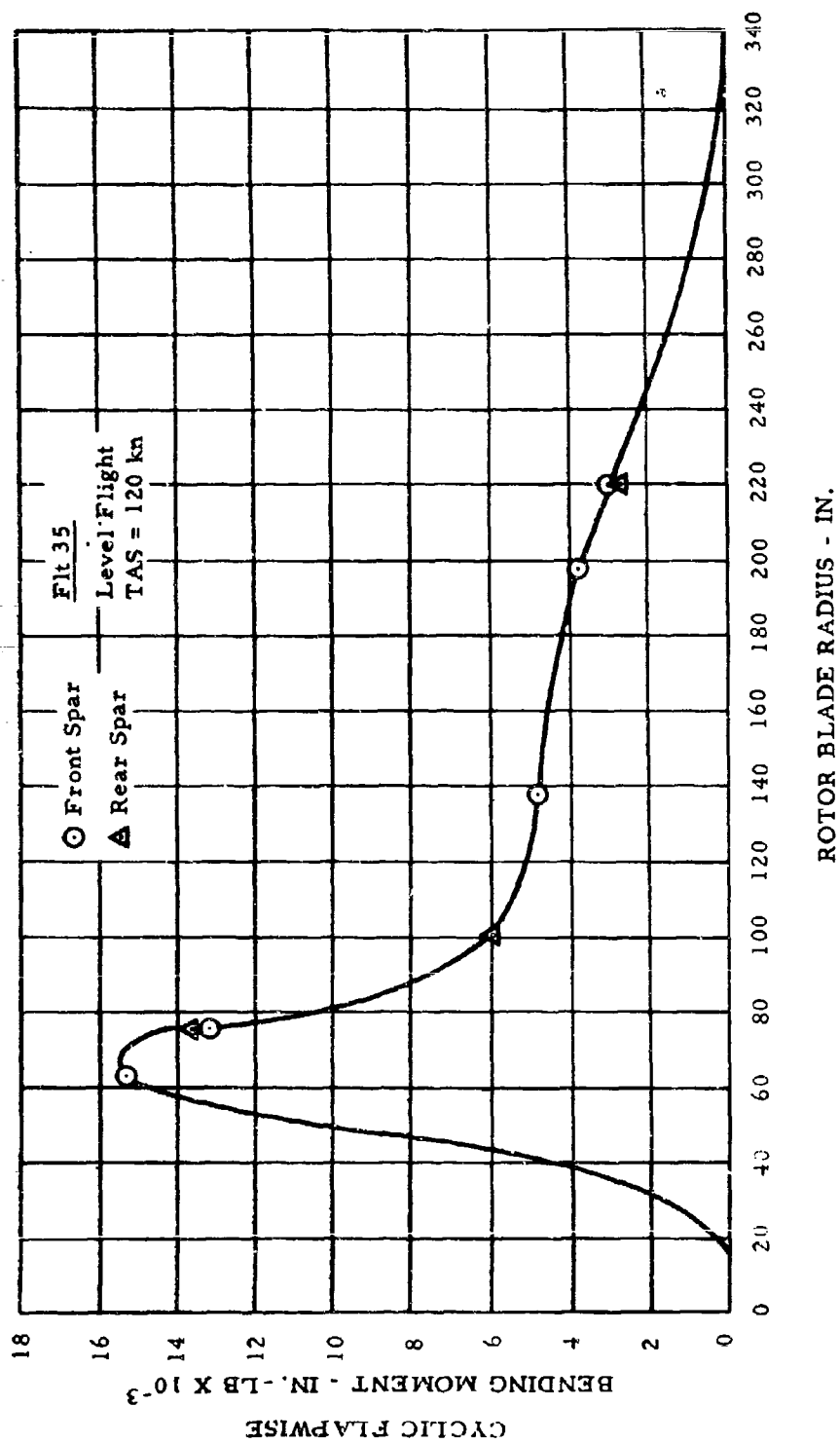


Figure 23. Cyclic Flapwise Bending Moment Versus Blade Radius.

rotor. Structural temperatures of the Hot Cycle propulsion system, including the blade spars, skins, ribs, flexures, ducts, hub, bearings, and shaft, were at or below the estimated operating temperatures and in most cases considerably below the design temperatures for the maximum power condition.

2. Powerplant and Airframe Temperatures

Temperatures of the powerplant and airframe components were recorded in a manner similar to that for the rotor temperatures, except that no hot reference junction box was used inasmuch as a slip ring was not needed. Operating temperatures of the following powerplant and airframe

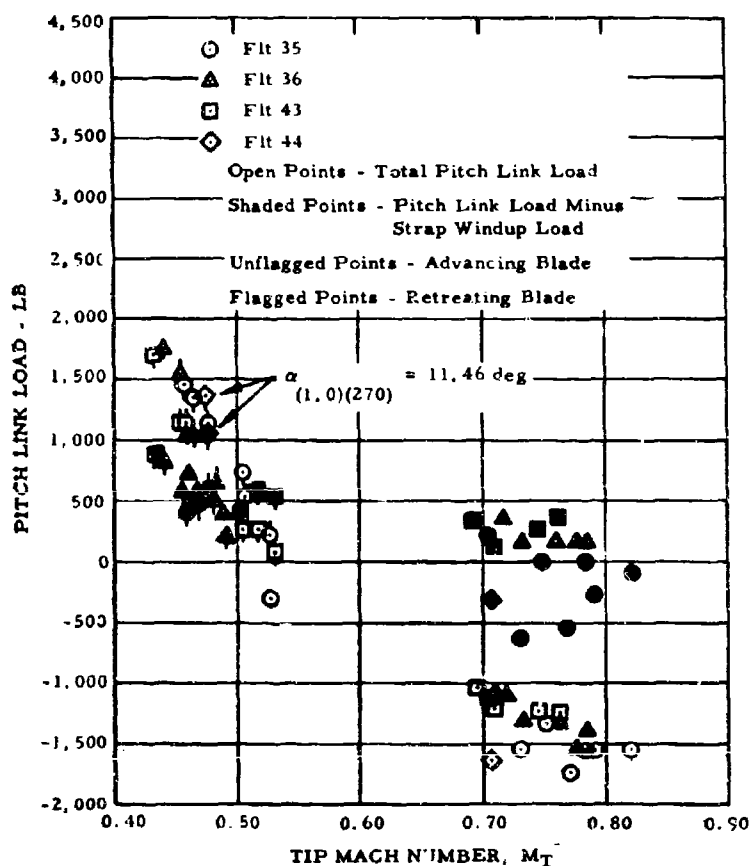


Figure 24. Pitch Link Load Versus Tip Mach Number - Blue Blade.

components were read and analyzed from the Brown recorder: (1) engine and engine accessories, (2) engine and diverter-valve bay, (3) lateral pylons and nacelles, (4) radial and thrust rotor support bearing housings, (5) aft fuselage and yaw-control valve compartment, (6) yaw-control valve supply duct and Y-duct blankets, (7) yaw-control valve supply duct and Y-duct bays, and (8) yaw-control valve outlets.

Figure 26 shows the location of the thermocouples throughout the powerplant and airframe of the XV-9A. The tabulation included in this figure summarizes the maximum temperatures recorded during the flight test program together with the estimated limit temperature associated with that section of the airframe and powerplant.

On flights 26 and 27, the engine-mounted electrical generator temperatures exceeded limits. Inspection of the generators disclosed no evidence of temperature damage. To correct this potential problem, additional cooling was provided for both the generator and the engine bay by adding a generator ram air scoop and by adding nacelle cowling louvers. The rework dropped temperatures to well below the estimated limit temperature.

Engine fuel was used as the cooling medium for the hydraulic system oil. The estimated maximum fuel temperature of 150 degrees F was exceeded on six occasions for very short durations; however, the temperature was below the 175-degree-F maximum allowed by the engine manufacturer's specification.

Performance

The 20-hour follow-on flight test program achieved a much wider flight envelope than that obtained in the initial 15-hour flight test program. Maximum speed of 120 knots and altitudes in excess of 10,000 feet were reached, as well as high rates of climb and single-engine rotor flight. The performance results were consistent with the earlier whirl test and 15-hour flight test programs. Data reduction techniques and graphical presentations of results are generally consistent with those of Reference 1; therefore, only those items that represent changes are treated in detail in the following paragraphs.

1. Rotor Power Available

For the Hot Cycle propulsion system, analysis of rotor power available serves two purposes. First, it is used for the establishment of maximum power available for use in establishing hover ceiling, maximum rate of

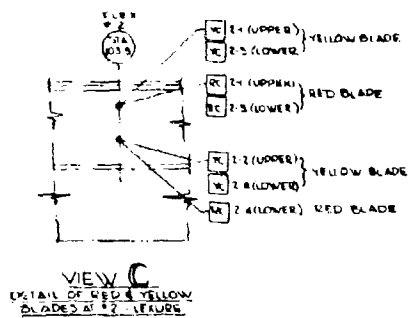
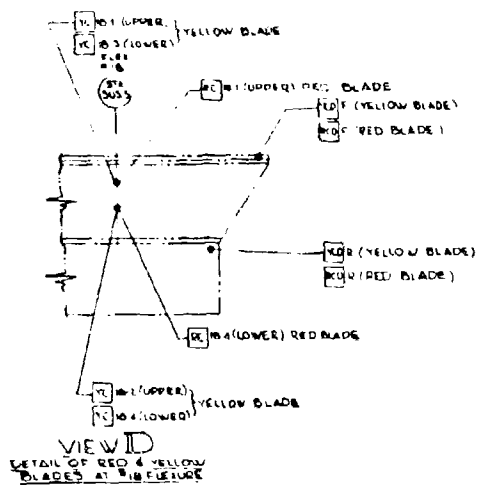
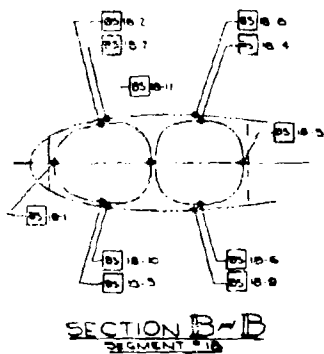


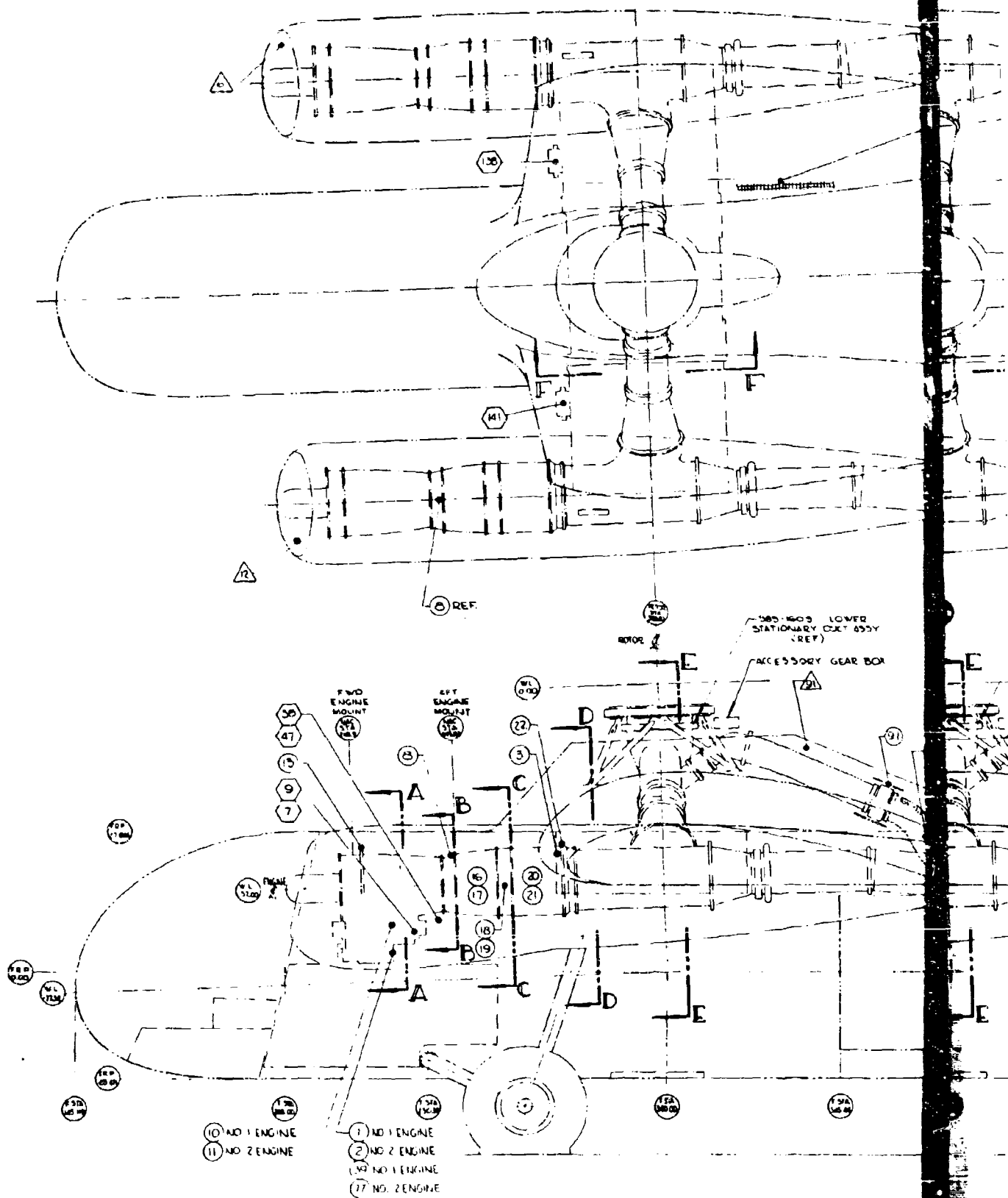
Figure 25. Maximum Rotor Operating Temperatures.

ITEM NO. DESCRIPTION	LOCATION	MAX TEMP RECORDED	STATION TEMP
CC1.1	STATION 105.5 FLEXURE #2-UPPER-FORWARD		600°
BC1.1	105.5 FLEXURE #2-UPPER-AFT	412°	
BC1.2	105.5 FLEXURE #2-LOWER-FORWARD	418°	
BC1.3	105.5 FLEXURE #2-LOWER-AFT	535°	
BC1.4	105.5 FLEXURE #2-UPPER-FWD	174°	
BC1.5	105.5 FLEXURE #2-UPPER-AFT	413°	
BC1.6	105.5 FLEXURE #2-LOWER-FWD	615°	
BC1.7	105.5 FLEXURE #2-LOWER-AFT	677°	
BC1.8	105.5 FLEXURE #2-UPPER-FWD		
BC1.9	105.5 FLEXURE #2-UPPER-AFT	450°	
BC1.10	105.5 FLEXURE #2-LOWER-AFT	440°	
BC1.11	105.5 FLEXURE #2-UPPER-FWD	583°	
BC1.12	105.5 FLEXURE #2-UPPER-AFT	595°	
BC1.13	105.5 FLEXURE #2-LOWER-FWD	575°	
BC1.14	105.5 FLEXURE #2-LOWER-AFT		
BC1.15	105.5 FLEXURE #2-UPPER-FWD	540°	
BC1.16	105.5 FLEXURE #2-UPPER-AFT	517°	
BC1.17	105.5 FLEXURE #2-LOWER-FWD	305°	
BC1.18	105.5 FLEXURE #2-LOWER-AFT	515°	
BC1.19	105.5 FLEXURE #2-UPPER-FWD	547°	
BC1.20	105.5 FLEXURE #2-UPPER-AFT	500°	
BC1.21	105.5 FLEXURE #2-LOWER-FWD	368°	
BC1.22	105.5 FLEXURE #2-LOWER-AFT	512°	
BC1.23	105.5 FLEXURE #2-UPPER-FWD	541°	
BC1.24	105.5 FLEXURE #2-UPPER-AFT	275°	
BC1.25	105.5 FLEXURE #2-LOWER-FWD	515°	
BC1.26	105.5 FLEXURE #2-LOWER-AFT	467°	
BC1.27	105.5 FLEXURE #2-UPPER-FWD	445°	
BC1.28	105.5 FLEXURE #2-UPPER-AFT	455°	
BC1.29	105.5 FLEXURE #2-LOWER-FWD	475°	600°
BC1.30	105.5 FLEXURE #2-LOWER-AFT	100°	1000°
BC1.31	105.5 FLEXURE #2-UPPER-FWD	100°	1000°
BC1.32	105.5 FLEXURE #2-UPPER-AFT	736°	1000°
BC1.33	105.5 FLEXURE #2-LOWER-FWD	671°	1000°
BC1.34	105.5 FLEXURE #2-LOWER-AFT	750°	600°
BC1.35	105.5 FLEXURE #2-UPPER-FWD	250°	600°
BC1.36	105.5 FLEXURE #2-UPPER-AFT	730°	600°
BC1.37	105.5 FLEXURE #2-LOWER-FWD	290°	600°
BC1.38	105.5 FLEXURE #2-LOWER-AFT	1030°	1150°
BC1.39	105.5 FLEXURE #2-UPPER-FWD	1150°	
BC1.40	105.5 FLEXURE #2-UPPER-AFT	1150°	
BC1.41	105.5 FLEXURE #2-LOWER-FWD	911°	950°
BC1.42	105.5 FLEXURE #2-LOWER-AFT	1012°	950°
BC1.43	105.5 FLEXURE #2-UPPER-FWD	1000°	950°
BC1.44	105.5 FLEXURE #2-UPPER-AFT	1035°	1150°
BC1.45	105.5 FLEXURE #2-LOWER-FWD	990°	1150°
BC1.46	105.5 FLEXURE #2-LOWER-AFT	280°	600°
BC1.47	105.5 FLEXURE #2-UPPER-FWD	740°	600°
BC1.48	105.5 FLEXURE #2-UPPER-AFT	597°	600°
BC1.49	105.5 FLEXURE #2-LOWER-FWD	240°	600°
BC1.50	105.5 FLEXURE #2-LOWER-AFT	955°	1150°
BC1.51	105.5 FLEXURE #2-UPPER-FWD	265°	250°
BC1.52	105.5 FLEXURE #2-UPPER-AFT	255°	250°
BC1.53	105.5 FLEXURE #2-LOWER-FWD	240°	800°
BC1.54	105.5 FLEXURE #2-LOWER-AFT	255°	500°
BC1.55	105.5 FLEXURE #2-UPPER-FWD	250°	150°
BC1.56	105.5 FLEXURE #2-UPPER-AFT	235°	250°
BC1.57	105.5 FLEXURE #2-LOWER-FWD	1140°	1150°
BC1.58	105.5 FLEXURE #2-LOWER-AFT	1145°	1150°

ITEM NO. DESCRIPTION	LOCATION	MAX TEMP RECORDED	STATION TEMP
BC1.59	STATION 105.5 FLEXURE #2-UPPER-FWD		600°
BC1.60	STATION 105.5 FLEXURE #2-UPPER-AFT		600°
BC1.61	STATION 105.5 FLEXURE #2-LOWER-FWD	563°	600°
BC1.62	STATION 105.5 FLEXURE #2-LOWER-AFT	550°	600°
BC1.63	STATION 105.5 FLEXURE #2-UPPER-FWD	490°	600°
BC1.64	STATION 105.5 FLEXURE #2-UPPER-AFT	380°	600°
BC1.65	STATION 105.5 FLEXURE #2-LOWER-FWD	250°	250°
BC1.66	STATION 105.5 FLEXURE #2-LOWER-AFT	280°	250°
BC1.67	STATION 105.5 FLEXURE #2-UPPER-FWD	235°	250°
BC1.68	STATION 105.5 FLEXURE #2-UPPER-AFT	215°	250°
BC1.69	STATION 105.5 FLEXURE #2-LOWER-FWD	551°	600°
BC1.70	STATION 105.5 FLEXURE #2-LOWER-AFT	505°	
BC1.71	STATION 105.5 FLEXURE #2-UPPER-FWD	350°	
BC1.72	STATION 105.5 FLEXURE #2-UPPER-AFT	475°	
BC1.73	STATION 105.5 FLEXURE #2-LOWER-FWD	440°	
BC1.74	STATION 105.5 FLEXURE #2-LOWER-AFT	400°	
BC1.75	STATION 105.5 FLEXURE #2-UPPER-FWD	395°	
BC1.76	STATION 105.5 FLEXURE #2-UPPER-AFT	430°	600°

2. THE ROTATING COUPLES CALLED OUT ON THIS DRAWING ARE FOR ROTATING THE SHAFTS. SEE 385 901 FOR STATIONARY.
 1. IN NOTES WITHIN COUPLE LOCATION THE LETTER INSIDE LETTERS IS BLADE B (BLUE) R (RED) Y (YELLOW)
 NOTE:

C



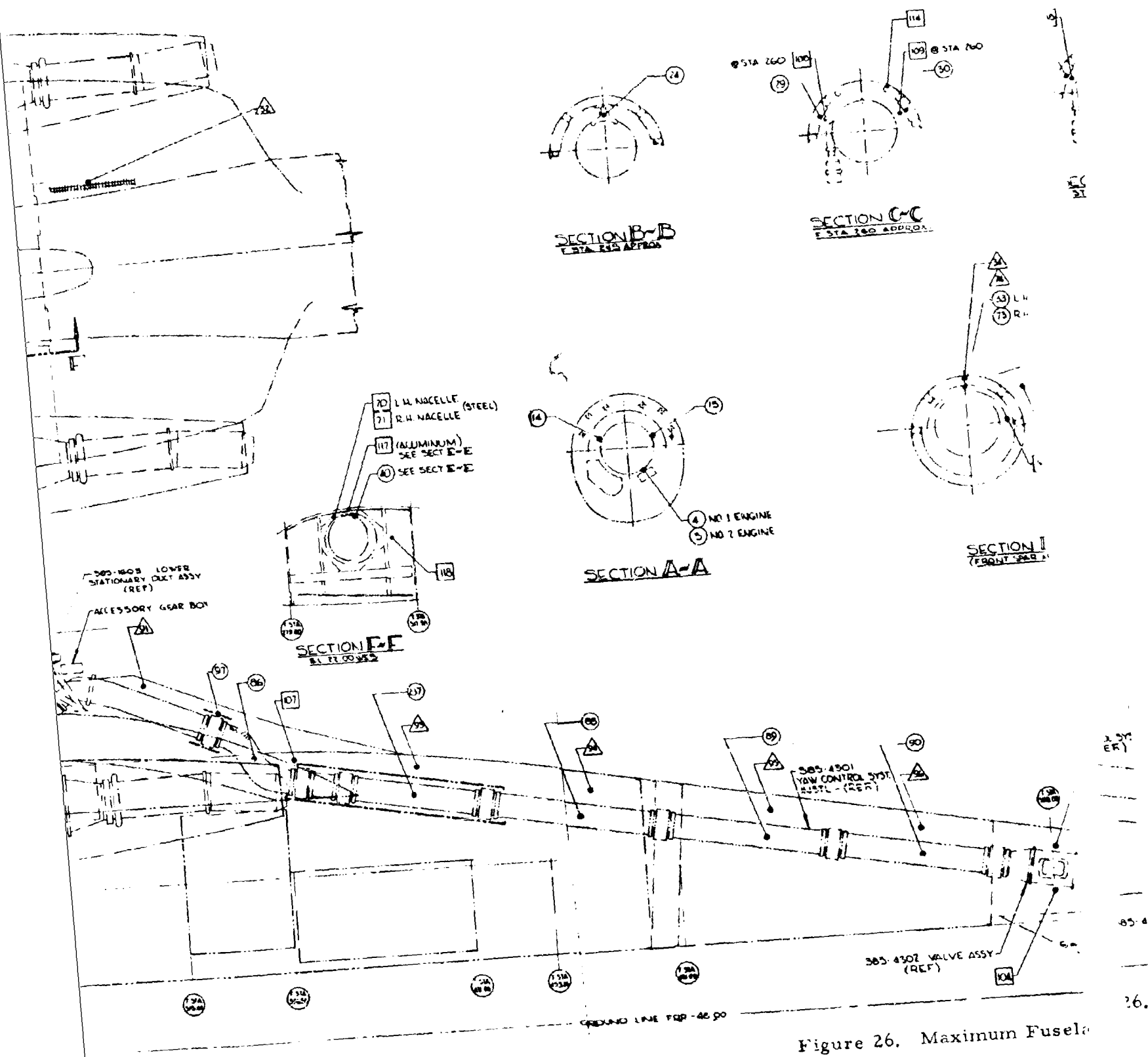
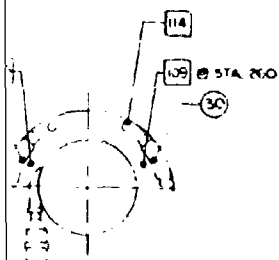
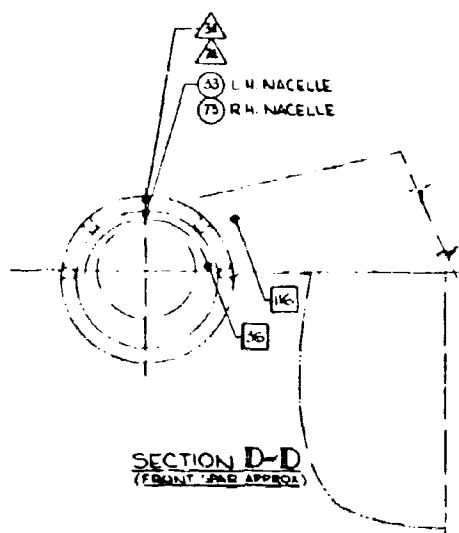


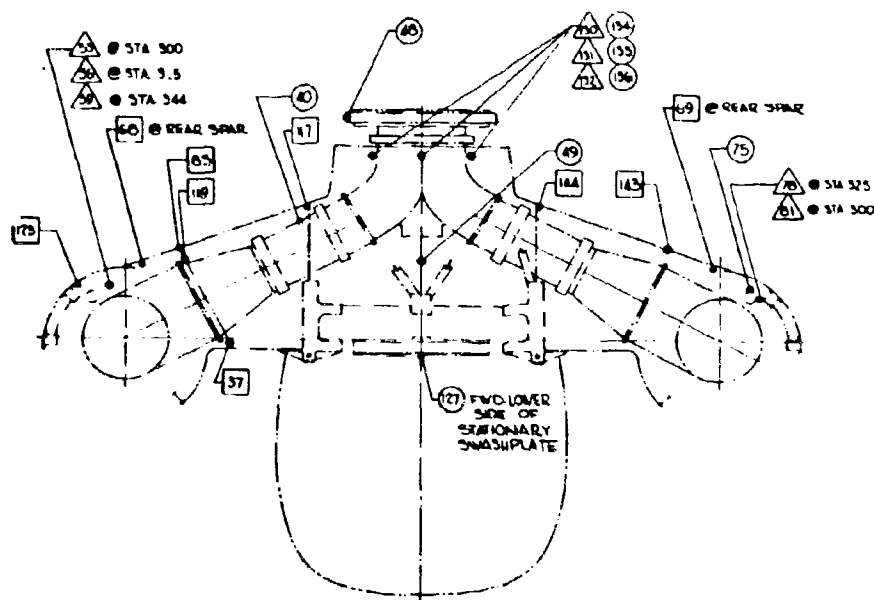
Figure 26. Maximum Fuselage



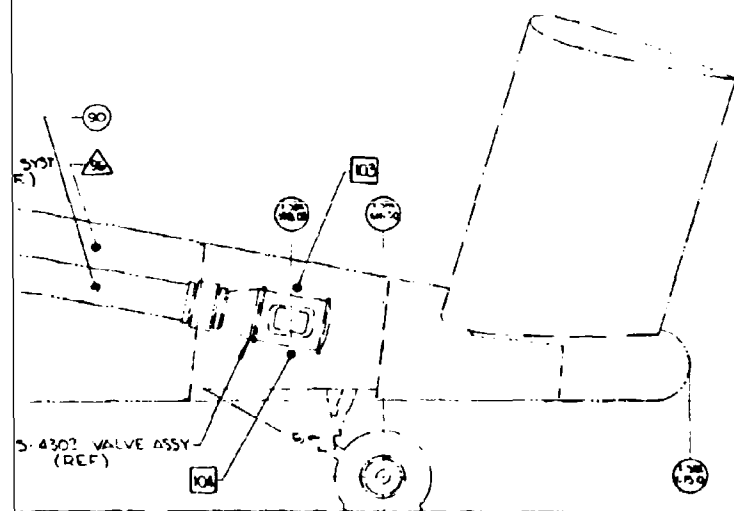
SECTION C-C
STA 260 APPROX



SECTION D-D
(FRONT FWD APPROX)



SECTION E-E
STA 300 APPROX



- 6 ESTIMATED & RECORDED TEMP IN FAHRENHEIT.
 5 THE NUMBER WITHIN THE GEOMETRIC FORMS (1,2,3,4) BELOW INDICATE THE THERMOCOUPLE NO. AS NOTED IN TABLE ABOVE TITLE BLOCK.
 4 Δ INDICATES AN "AIR" THERMOCOUPLE.
 3 \square INDICATES A "STRUCTURE" THERMOCOUPLE.
 2 \circ INDICATES A "CASE" THERMOCOUPLE.
 1 \bullet INDICATES A "FLUID" THERMOCOUPLE.
 NOTE:

MP IN FAH
 METRIC FI
 E THERMO
 TIVE TITLE
 COUPLE.
 THERMOU
 THERMOU
 THERMOU
 THERMOU

6. Maximum Fuselage Operating Temperatures.

ITEM NO.	TYPE	LOCATION	MAX. TEMP. (°F)	MIN. TEMP. (°F)
1	CASE	GENERATOR CASE - NO. 1 ENGINE (FWD)	208°	210°
2	CASE	GENERATOR CASE - NO. 2 ENGINE (FWD)	199°	210°
3	CASE	EXHAUST FRAME - NO. 1 ENGINE	227°	1100°
4	CASE	IGNITION BOX - NO. 1 ENGINE	218°	220°
5	CASE	IGNITION BOX - NO. 2 ENGINE	234°	230°
6	AIR	1. NO. 2 ENGINE (REF. TC 130)	104°	AMB
7	FLUID	ENGINE OIL IN - NO. 1 ENGINE (REF. TC 147)	205°	225°
8	CASE	FUEL NOZZLE INLET - NO. 1 ENGINE	214°	220°
9	FLUID	ENGINE OIL IN - NO. 1 ENGINE	212°	225°
10	CASE	ENGINE OIL PUMP - NO. 1 ENGINE	219°	200°
11	CASE	ENGINE OIL PUMP - NO. 2 ENGINE	210°	200°
12	AIR	T ₂ NO. 1 ENGINE	91°	AMB
13	CASE	FRONT FRAME - NO. 1 ENGINE	150°	200°
14	CASE	ENGINE COMPRESSOR - NO. 1 ENGINE	242°	200°
15	CASE	ENGINE COMPRESSOR - NO. 1 ENGINE	242°	200°
16	CASE	ENGINE COMBUSTOR - NO. 1 ENGINE	244°	250°
17	CASE	ENGINE COMBUSTOR - NO. 1 ENGINE	228°	280°
18	CASE	ENGINE TURBINE - NO. 1 ENGINE	1020°	1150°
19	CASE	ENGINE TURBINE - NO. 1 ENGINE	1112°	1180°
20	CASE	ENGINE EXHAUST FRAME - NO. 1 ENGINE	1084°	1100°
21	CASE	ENGINE EXHAUST FRAME - NO. 1 ENGINE	1001°	1100°
22	CASE	ENGINE EXHAUST ADAPTOR CLAMP - NO. 1 ENGINE	630°	880°
23				
24	CASE	AFT ENGINE MOUNT BRACE	448°	200°
25				
26				
27				
28				
29	CASE	INSULATION BLANKET TUNNEL AREA - NAC STA 260 (APPROX)	352°	400°
30	CASE	INSULATION BLANKET TUNNEL AREA - NAC STA 260 (APPROX)	316°	400°
31				
32				
33	CASE	INSULATION BLANKET CROSSOVER SHROUD - LH NACELLE	411°	400°
34	AIR	CROSSOVER SHROUD - LH NACELLE	234°	280°
35				
36	STRUCT	CROSSOVER SHROUD - INNER SURFACE - RH NACELLE	262°	280°
37	STRUCT	CANTED RIB - LH NACELLE - LOWER	385°	400°
38	FLUID	FUEL IN - NO. 1 ENGINE	183°	191°
39	CASE	GENERATOR CASE - NO. 1 ENGINE (AFT)	183°	220°
40	CASE	INSULATION BLANKET - TRANSITION DUCT	336°	400°
41				
42				
43				
44				
45				
46				
47	FLUID	FUEL IN - NO. 2 ENGINE	160°	181°
48	CASE	ROTOR - UPPER BEARING (REF. TC 148)	189°	210°
49	CASE	ROTOR - LOWER BEARING (REF. TC 148)	171°	210°
50				
51				
52	AIR	FINNED TUBING - ROTOR OIL (REF. TC 158)	100°	AMB
53	AIR	LH NACELLE - STA. 300 (APPROX) TOP	347°	260°
54				
55				
56	AIR	LH NACELLE - STA. 325 (APPROX) TOP	343°	400°
57				
58				
59	AIR	LH NACELLE - STA. 346 (APPROX) TOP	349°	450°
60				
61				
62				
63				
64				
65				
66				
67				
68	STRUCT	LH NACELLE - SPARE CAP - UPPER REAR	208°	200°
69	STRUCT	RH NACELLE - SPARE CAP - UPPER REAR	232°	200°
70	STRUCT	LH NACELLE - BL 22 FRAME - TOP FLANGE	244°	280°
71	STRUCT	RH NACELLE - BL 22 FRAME - TOP FLANGE	218°	280°
72				
73	CASE	RH NACELLE - CROSSOVER SHROUD INSULATION BLANKET	406°	400°
74	AIR	RH NACELLE - CROSSOVER SHROUD	347°	280°
75	CASE	RH NACELLE - D. ENTER VALVE ACTUATOR	223°	275°

ITEM NO.	TYPE	LOCATION	MAX. TEMP. (°F)	MIN. TEMP. (°F)
76				
77	CASE	GENERATOR CASE - NO. 2 ENGINE (AFT)	205°	210°
78	AIR	RH NACELLE - STA 325 (APPROX) TOP	441°	400°
79				
80				
81	AIR	RH NACELLE - STA 300 (APPROX) TOP	341°	270°
82				
83	STRUCT	LH NACELLE - STA 300 (APPROX) UPPER SKIN CANTED RIB	215°	230°
84				
85				
86	CASE	INSULATION BLANKET - 385-4325 DUCT	417°	450°
87	CASE	INSULATION BLANKET - 385-4322-1 DUCT	421°	450°
88	CASE	INSULATION BLANKET - 385-4322-1 DUCT	392°	430°
89	CASE	INSULATION BLANKET - 385-4322-3 DUCT	387°	480°
90	CASE	INSULATION BLANKET - 385-4322-1 DUCT	252°	430°
91	AIR	AFT FUSELAGE	111°	200°
92				
93	AIR	AFT FUSELAGE	181°	200°
94	AIR	AFT FUSELAGE	95°	200°
95	AIR	AFT FUSELAGE	180°	200°
96	AIR	AFT FUSELAGE	117°	200°
97	CASE	YAW DUCT BELLOW'S SHIELD	345°	200°
98				
99				
100				
101				
102				
103	STRUCT	FUSELAGE SKIN - YAW VALVE	113°	230°
104	STRUCT	LONGERON - YAW VALVE	104°	230°
105				
106				
107	STRUCT	FUSELAGE FRAME @ STA 376.50	199°	250°
108	STRUCT	LH NACELLE - TUNNEL - STA 260 (APPROX) LEFT SIDE	631°	700°
109	STRUCT	LH NACELLE - TUNNEL - STA 260 (APPROX) RIGHT SIDE	532°	700°
110				
111				
112				
113				
114	STRUCT	LH NACELLE - ENGINE MT TRUSS - NAC STA 260 (APPROX)	446°	600°
115				
116	STRUCT	LH NACELLE - FRONT SPAR - ALUMINUM WEB	226°	250°
117	STRUCT	LH NACELLE - UPPER SKIN - BL 22.00 @ STA 300 (APPROX)	210°	250°
118	STRUCT	LH NACELLE - BL 22.00 SHEAR PANEL	179°	230°
119	STRUCT	LH NACELLE - CANT RIB CAP @ STA 300 (APPROX)	284°	250°
120				
121				
122				
123	STRUCT	LH NACELLE - SKIN @ STA 300 (APPROX) 45° FROM Z	244°	400°
124				
125				
126				
127	CASE	STATIONARY DISK/PLATE BEARING	115°	175°
128				
129				
130	AIR	"Y" DUCT BAY	190°	280°
131	AIR	"Y" DUCT BAY	130°	250°
132	AIR	"Y" DUCT BAY	189°	250°
133				
134	CASE	"Y" DUCT INSULATING BLANKET	418°	450°
135	CASE	"Y" DUCT INSULATING BLANKET	290°	450°
136	CASE	"Y" DUCT INSULATING BLANKET	—	450°
137				
138	FLUID	RH NACELLE - HYDRAULIC OIL INLET - FUEL/OIL COOLER	189°	275°
139				
140				
141	FLUID	LH NACELLE - HYDRAULIC OIL INLET - FUEL/OIL COOLER	183°	275°
142				
143	STRUCT	RH NACELLE - UPPER SKIN - CANT RIB - STA 300 (APPROX)	207°	280°
144	STRUCT	RH NACELLE - UPPER SKIN - BL 22 @ STA 300 (APPROX)	199°	250°
145				

climb, and so forth. Second, because no torquemeter is available, as is the case in a shaft-driven helicopter, analysis of rotor power available must be made to establish the power required by the Hot Cycle helicopter.

For the analysis of rotor power available, one of the fundamental parameters is nozzle area. The engine maps (Figures 27 through 35) indicate that the total rotor system exit area is close to the 52.55-square-inch exit area per engine for which the engines were calibrated and at which they operate most efficiently.

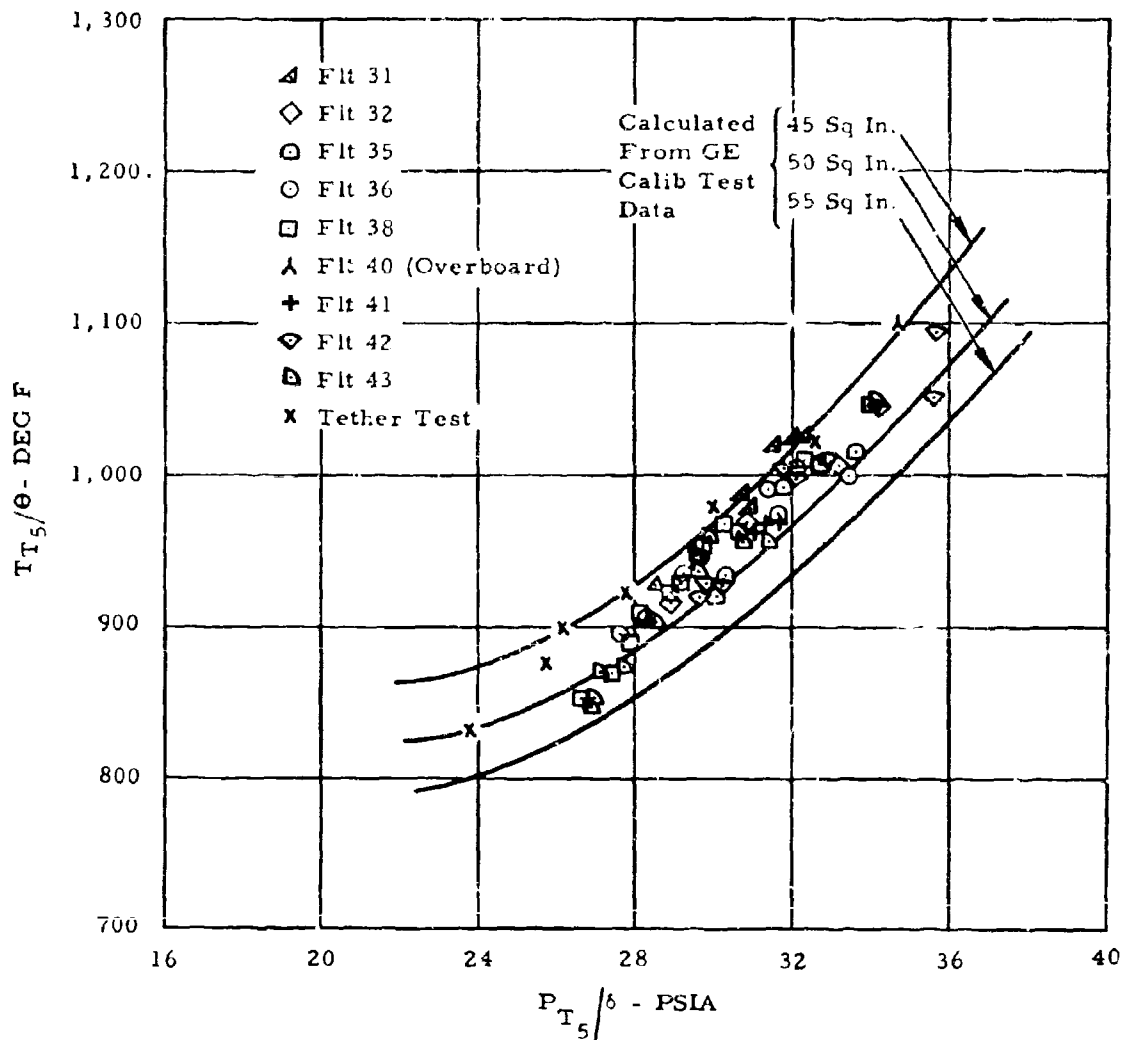


Figure 27. Temperature Versus Pressure, Engine S/N 027.

Figures 27, 28, and 29, in addition to defining nozzle area, can be used to detect any engine deterioration in the form of increased temperature at a given pressure. No such trend was visible in this program. Figures 30, 31, and 32 are used to calculate engine mass flow. Figures 33, 34, and 35 are used to set the topping limit on the engines for maximum power.

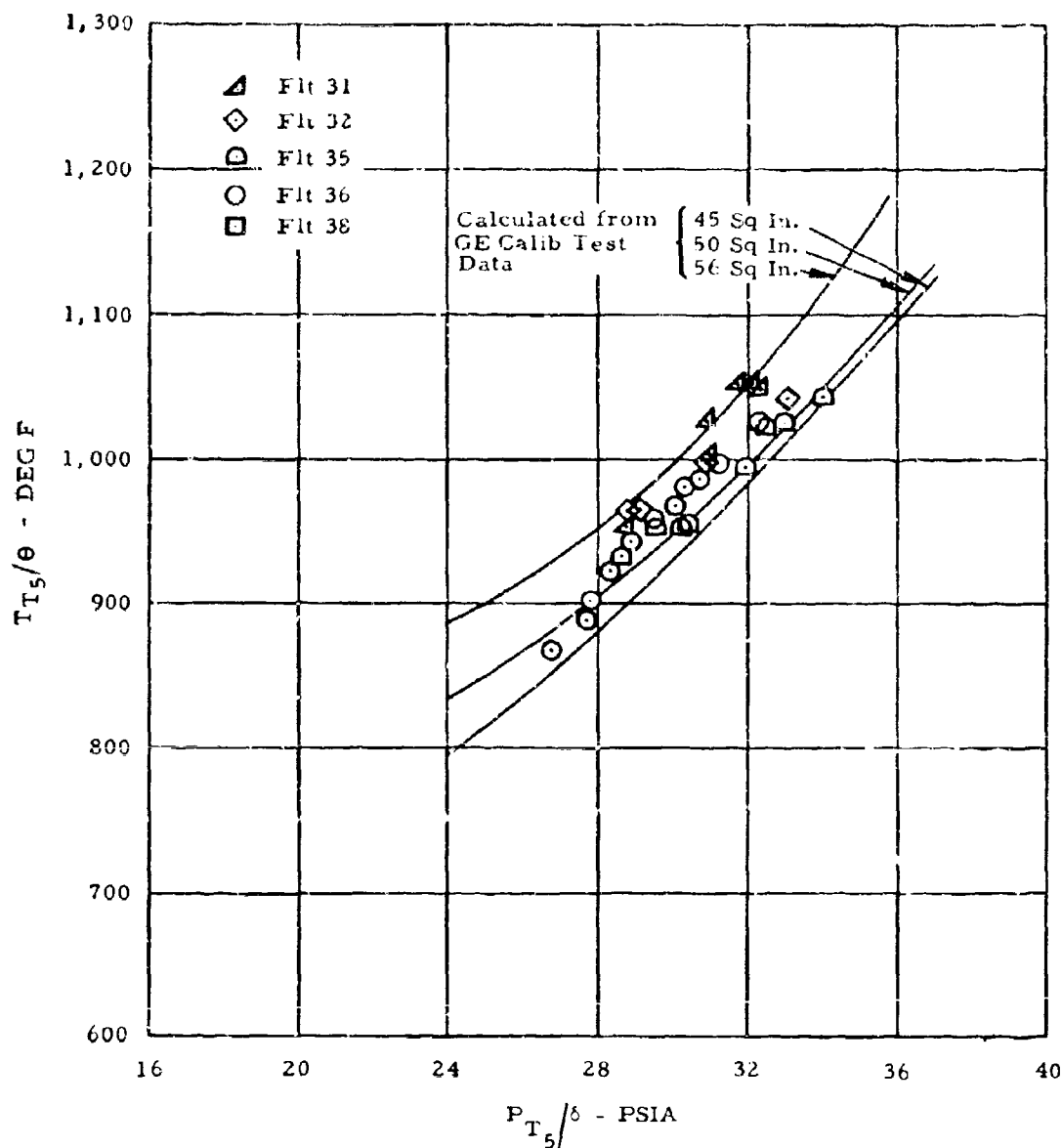


Figure 28. Temperature Versus Pressure, Engine S/N 026.

Engine quality as defined by the T_5 versus P_5 relationship is summarized in Figure 36, where results from the present tests are seen to be consistent with those from earlier flight and whirl testing.

2. Rotor Tip Total Pressures

The rotor tip total pressure was measured with total pressure pickups located at the outboard end of the blade duct. These measured values

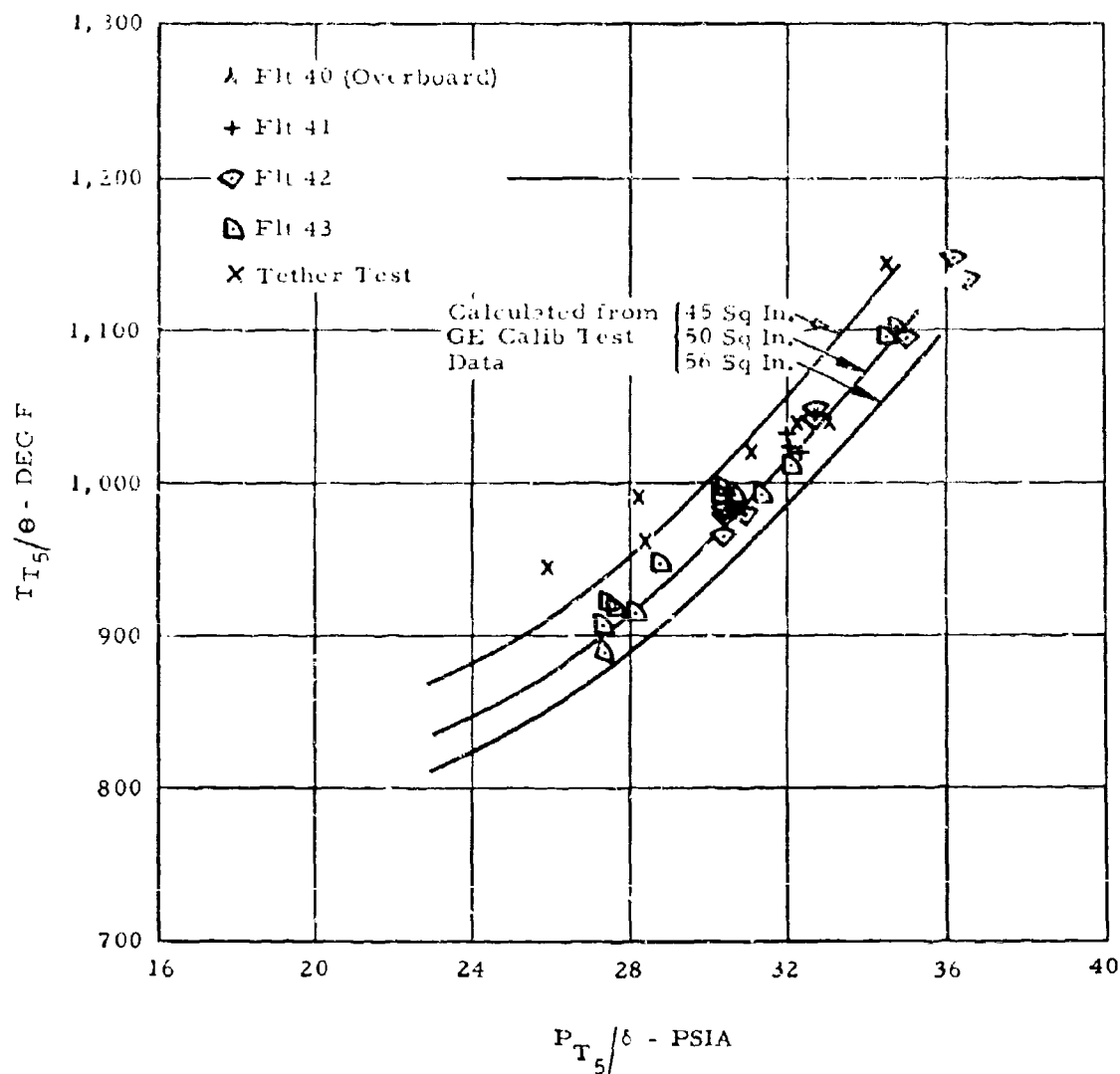


Figure 29. Temperature Versus Pressure, Engine S/N 101.

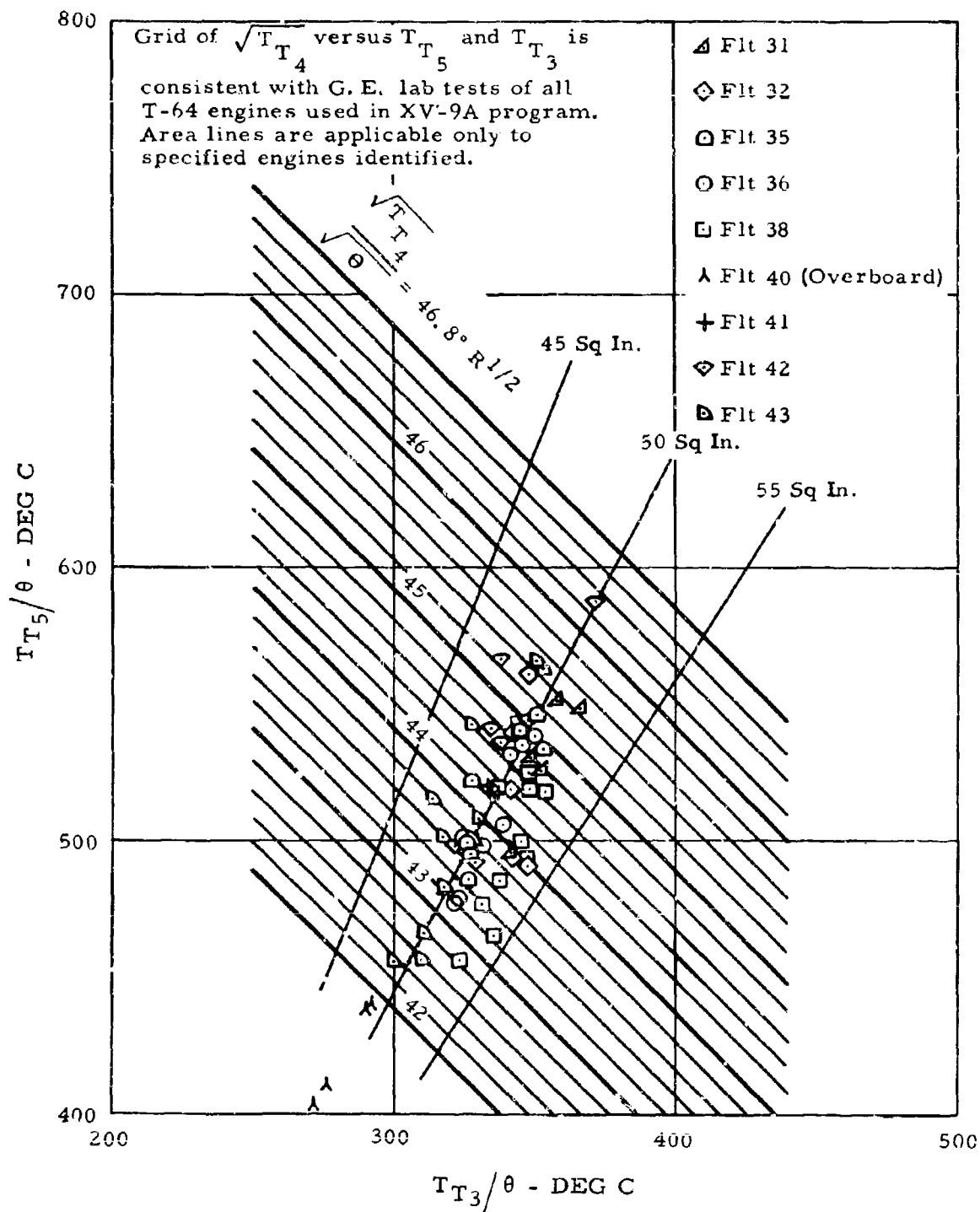


Figure 30. Engine Temperature Relationship, Engine S/N 027.

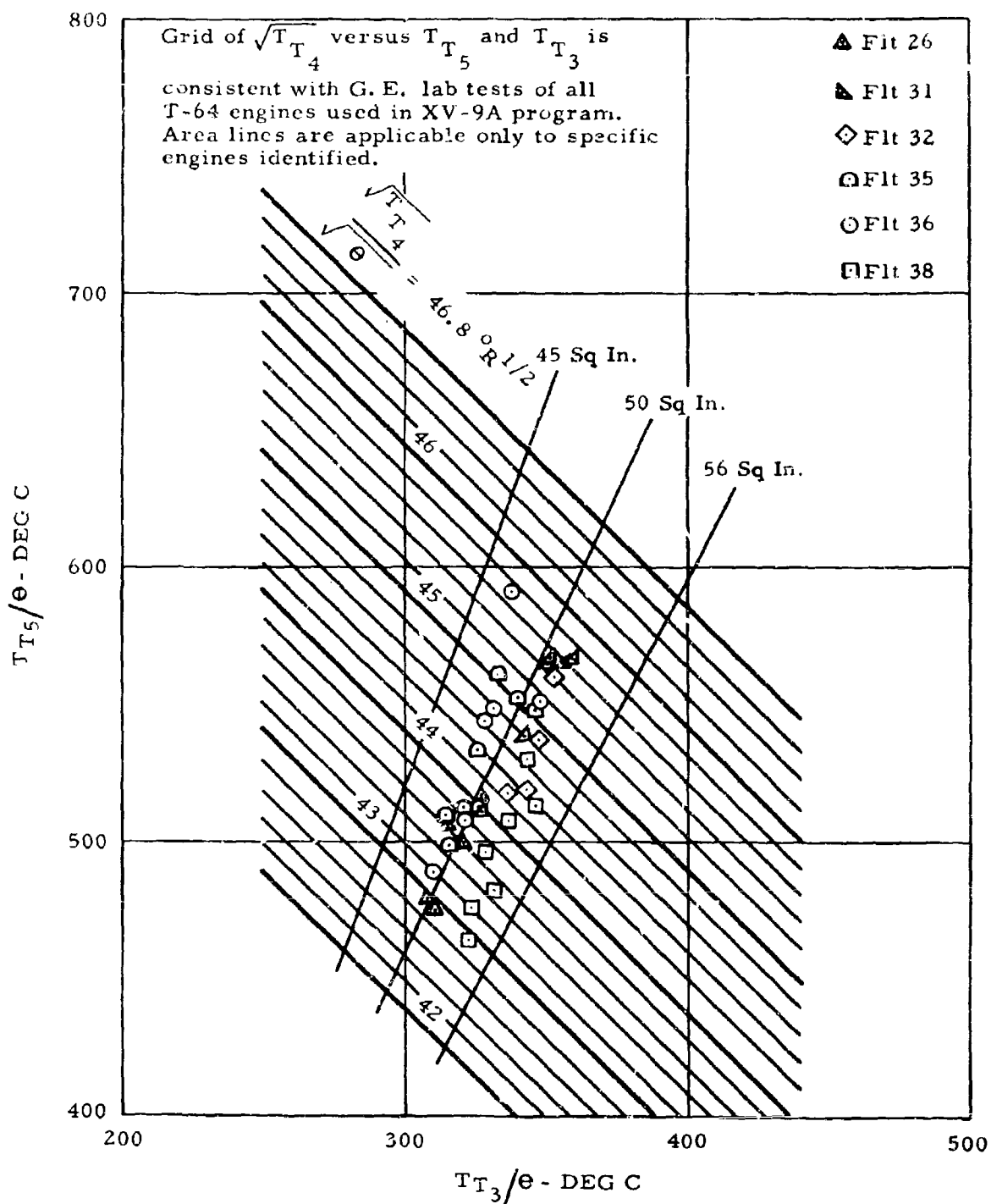


Figure 31. Engine Temperature Relationship, Engine S/N 026.

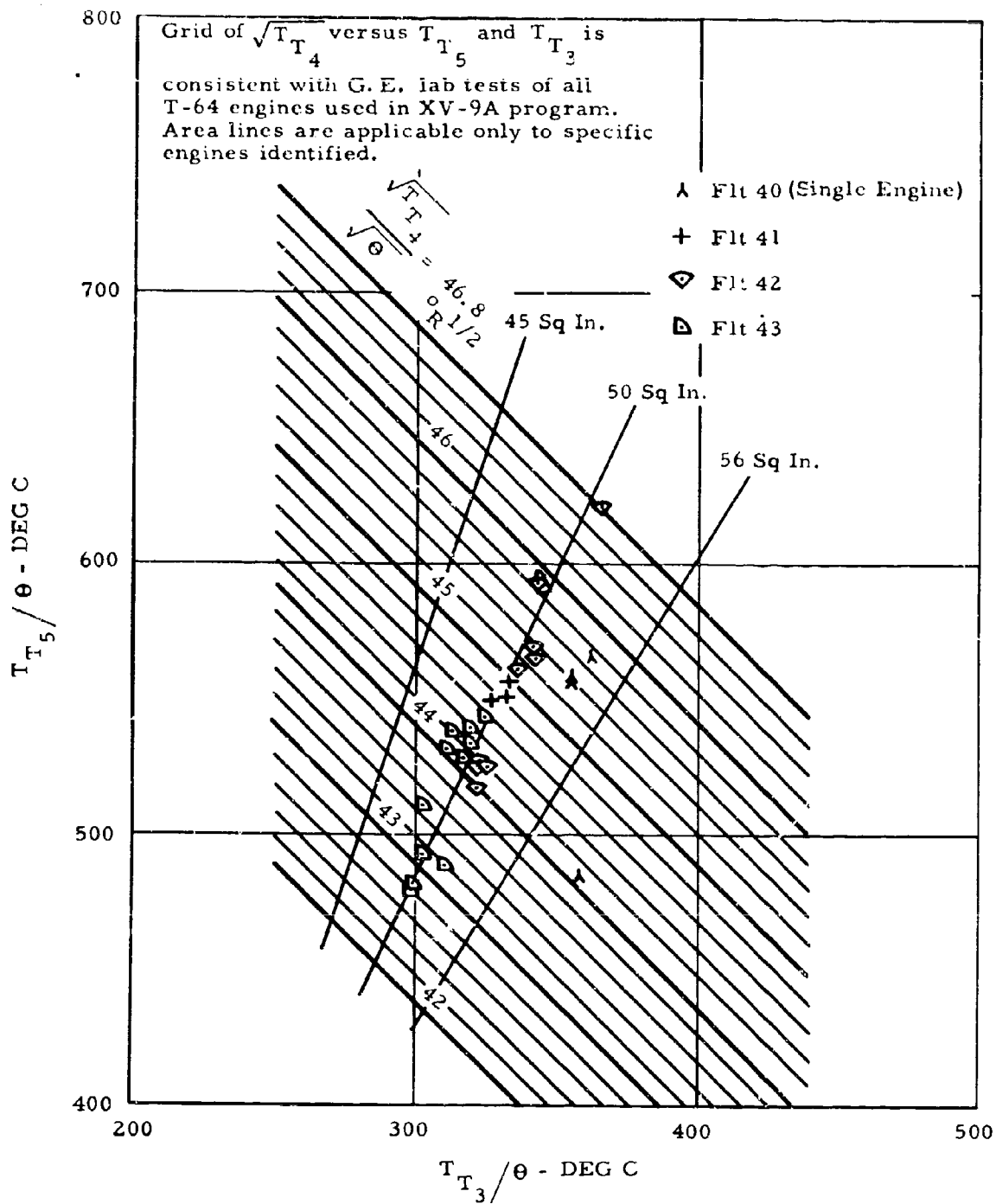


Figure 32. Engine Temperature Relationship, Engine S/N 101.

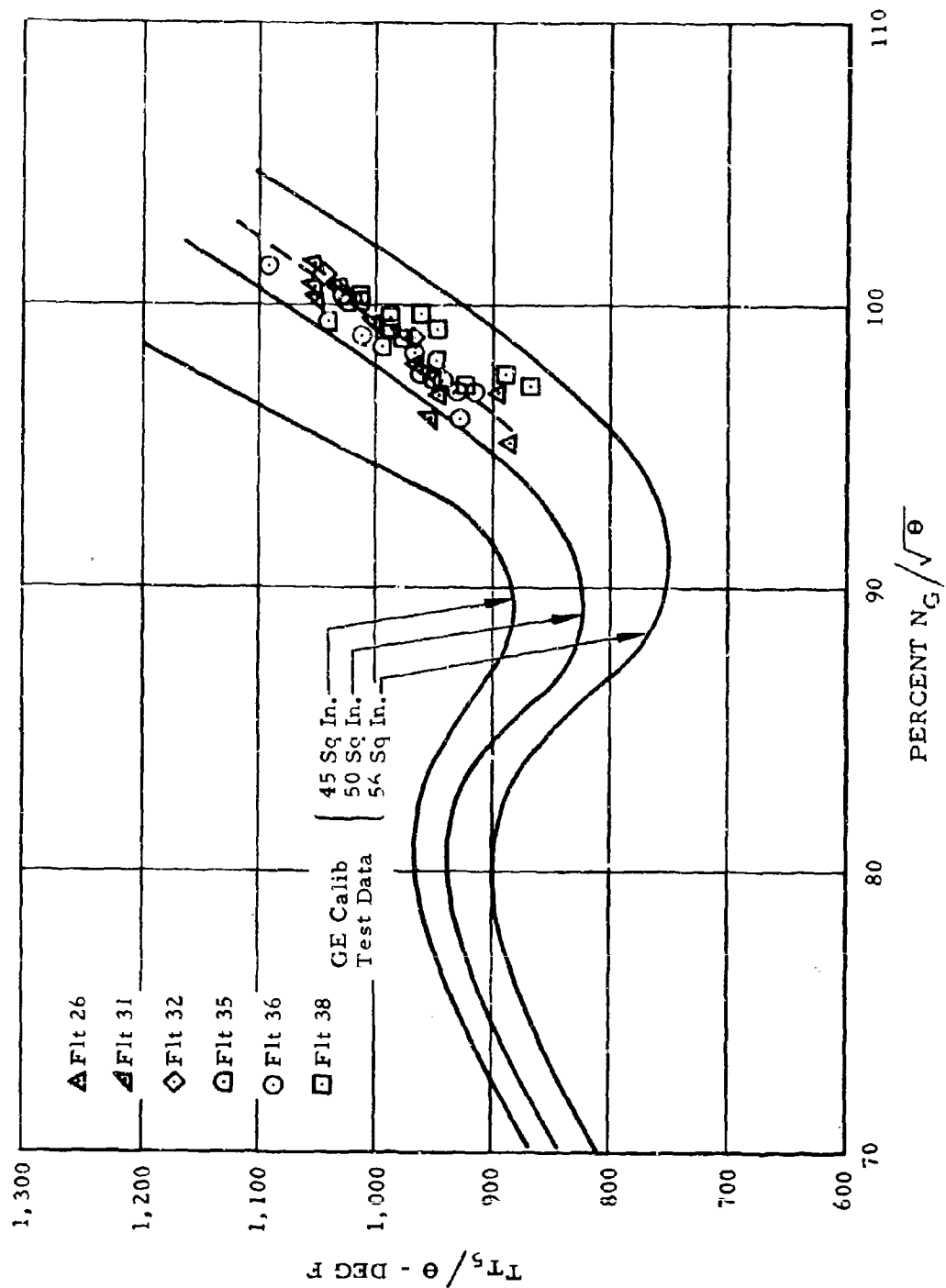


Figure 33. T_{T5}/θ Versus Percent $N_G/\sqrt{\theta}$, Engine S/N 026.

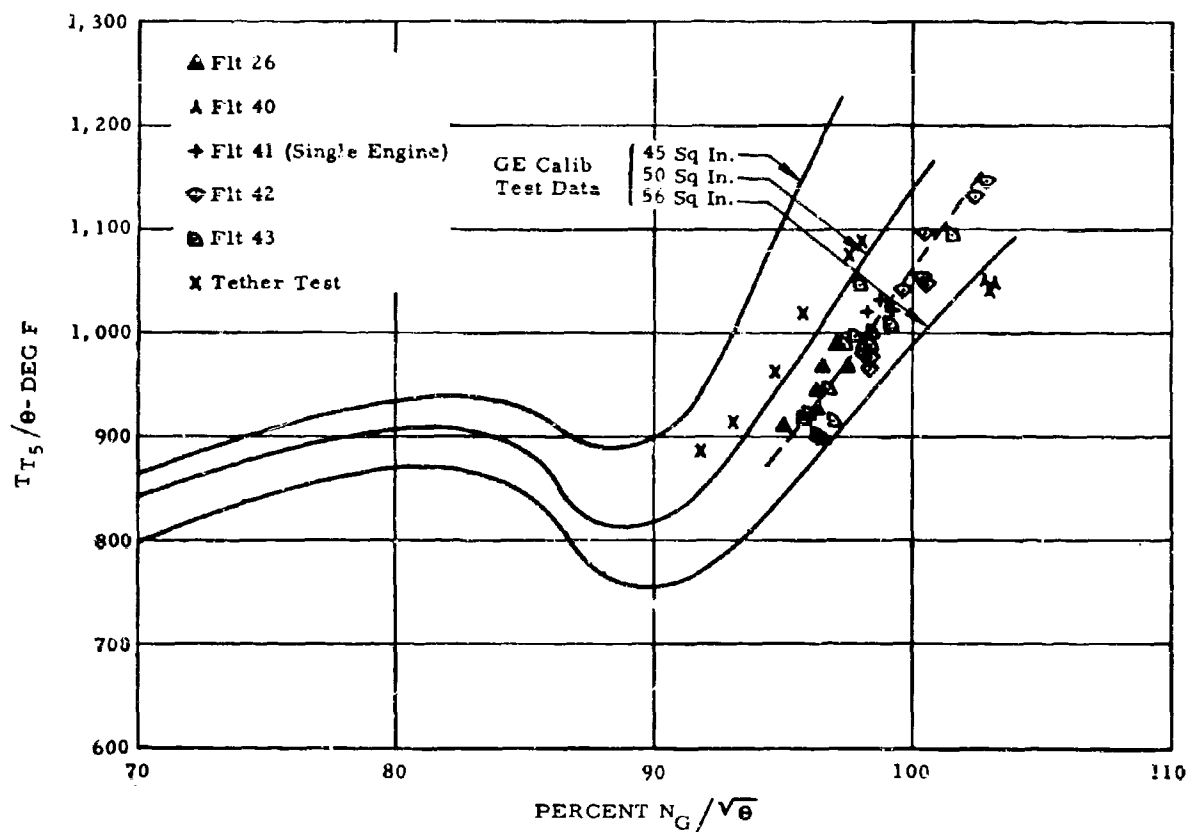


Figure 34. T_{T5}/θ Versus Percent $N_G/\sqrt{\theta}$, Engine S/N 101.

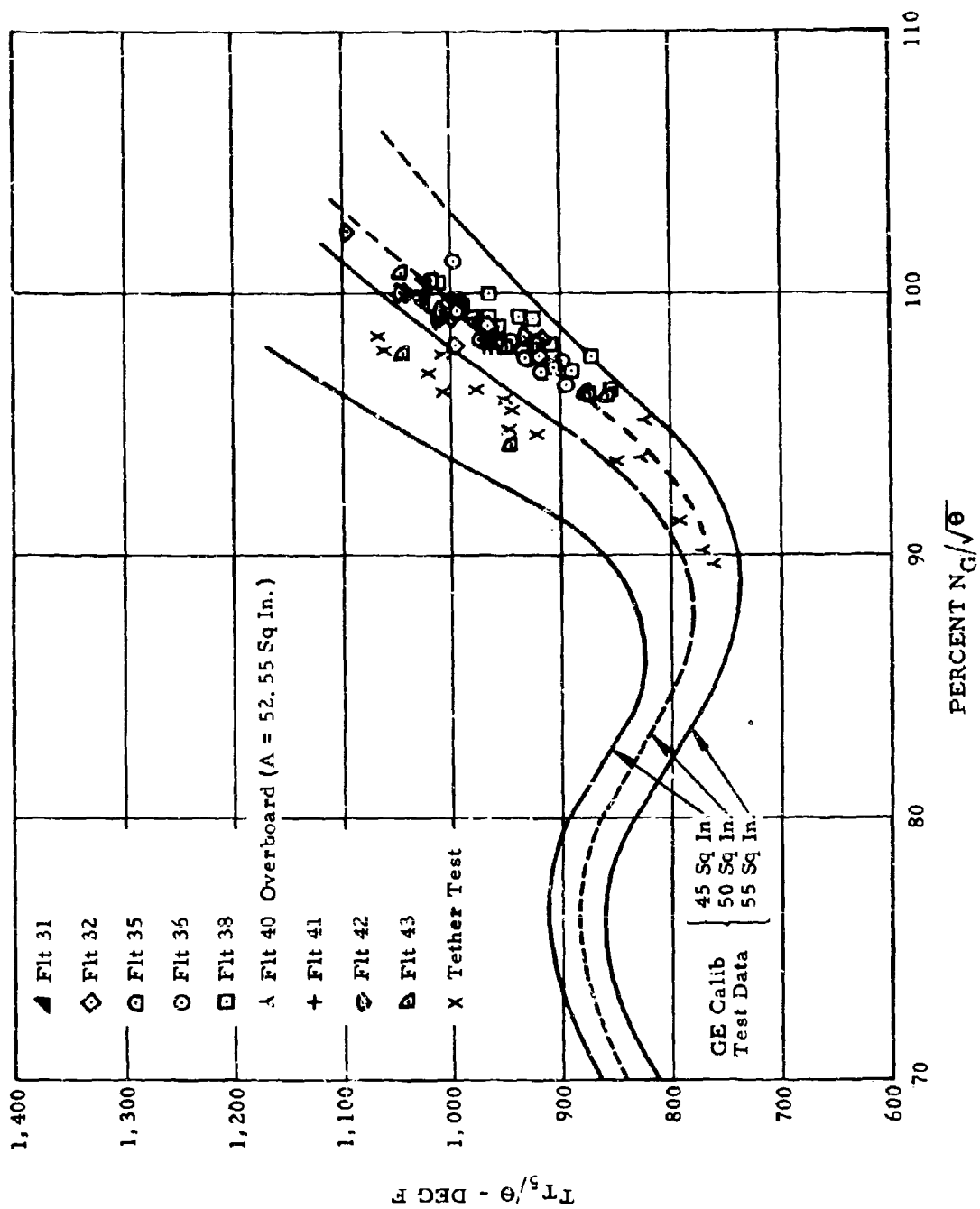


Figure 35. T_5/θ Versus Percent $N_G/\sqrt{\theta}$, Engine S/N 027.

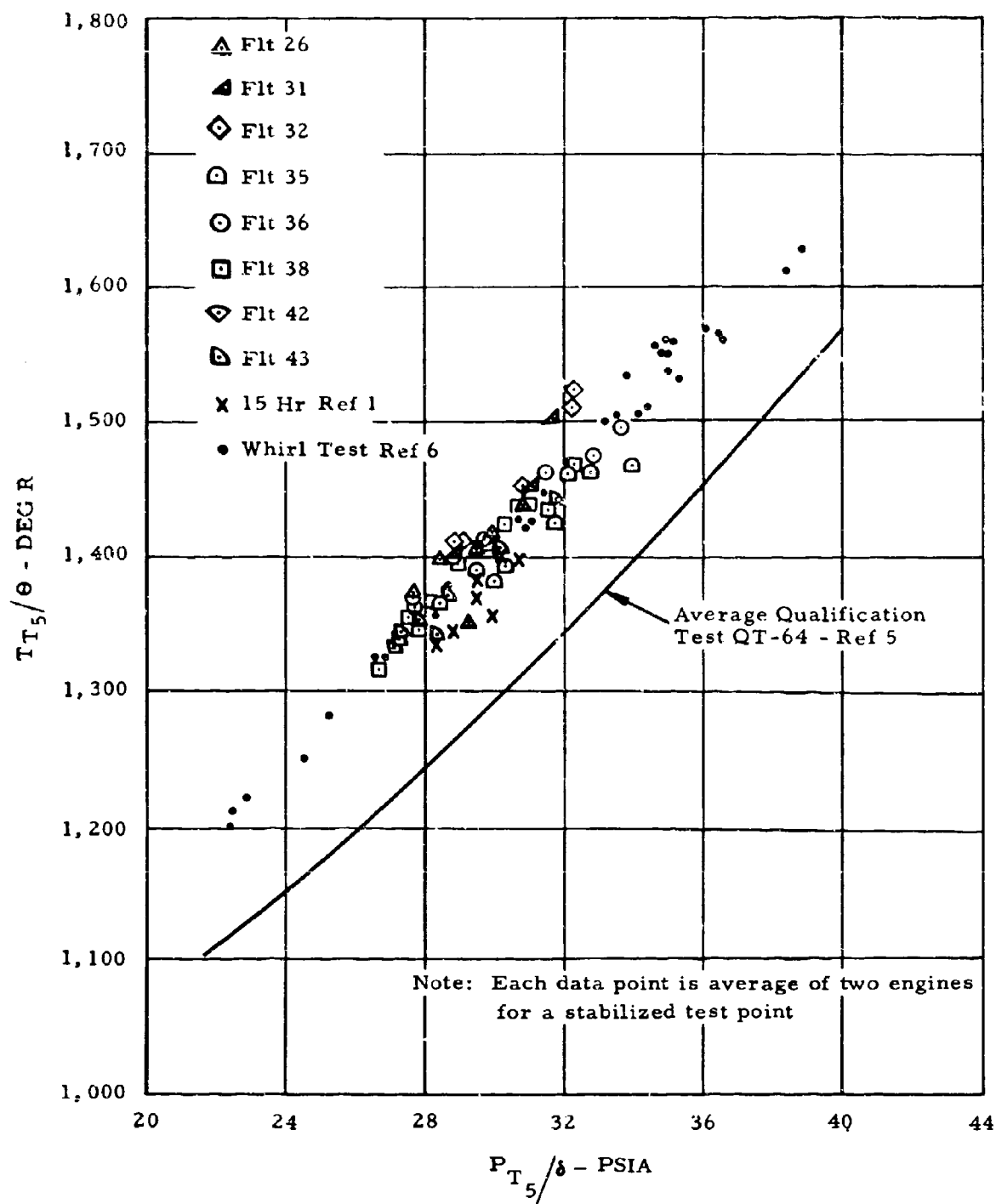


Figure 36. Engine Discharge Temperature Versus Pressure.

were used, in conjunction with measured engine condition data, to establish rotor power. An alternate method of obtaining tip total pressure is to use the results of the tether test as presented in Figure 88 of this report. This latter procedure eliminates one possible source of instrumentation inaccuracies.

3. Rotor Specific Fuel Consumption

Figure 37 presents specific fuel consumption versus referred horsepower (which is defined as $RHP/\delta\sqrt{\theta}$) for each flight condition. The rotor power available for each data point was computed using the method discussed in Reference 1. The fuel flow was obtained from the photopanel, and the SFC was computed by dividing the fuel flow by the rotor power available. Then the referred horsepower was obtained by dividing the rotor power available by the ambient pressure ratio (δ) and the square root of the ambient temperature ratio (θ). A mean line was drawn through the data for use in reducing to standard conditions.

The process of data correction from YT-64 to QT-64 engine performance, presented in Figure 38, includes corrections for leakage of flight test diverter valves and the T_5/θ difference (YT-64 to QT-64) of Figure 36 and for the air-fuel ratio deviation of Figure 39 (due to compressor bleed). This procedure, described in detail in Appendix IV of this report, is consistent with the methods used in Appendix IV of Reference 1.

Figure 38 presents a comparison of the actual fuel flow data (from Figure 39) with the specific fuel consumption corrected in the manner shown in Appendix IX of this report (the predicted effect of cleanup and use of QT-64 engines), and also with the originally estimated specific fuel consumption used in Reference 7. It should be noted that the corrected curve can be even further improved, in that the XV-9A tip cascade velocity coefficient appears to be susceptible to the improvements described in the Rotor System Tether Tests section of this report.

4. Speed-Power in Level Flight

Figures 40 and 41 present flight test data reduced to standard ambient conditions and to a gross weight of 14,500 pounds and 100-percent rotor speed. The data obtained at lower altitudes ($\approx 3,500$ ft) were reduced to 3,500-foot standard day and are shown in Figure 40. The data obtained at higher altitudes ($\approx 6,000$ ft) were reduced to 6,000-foot standard day and are shown in Figure 41.

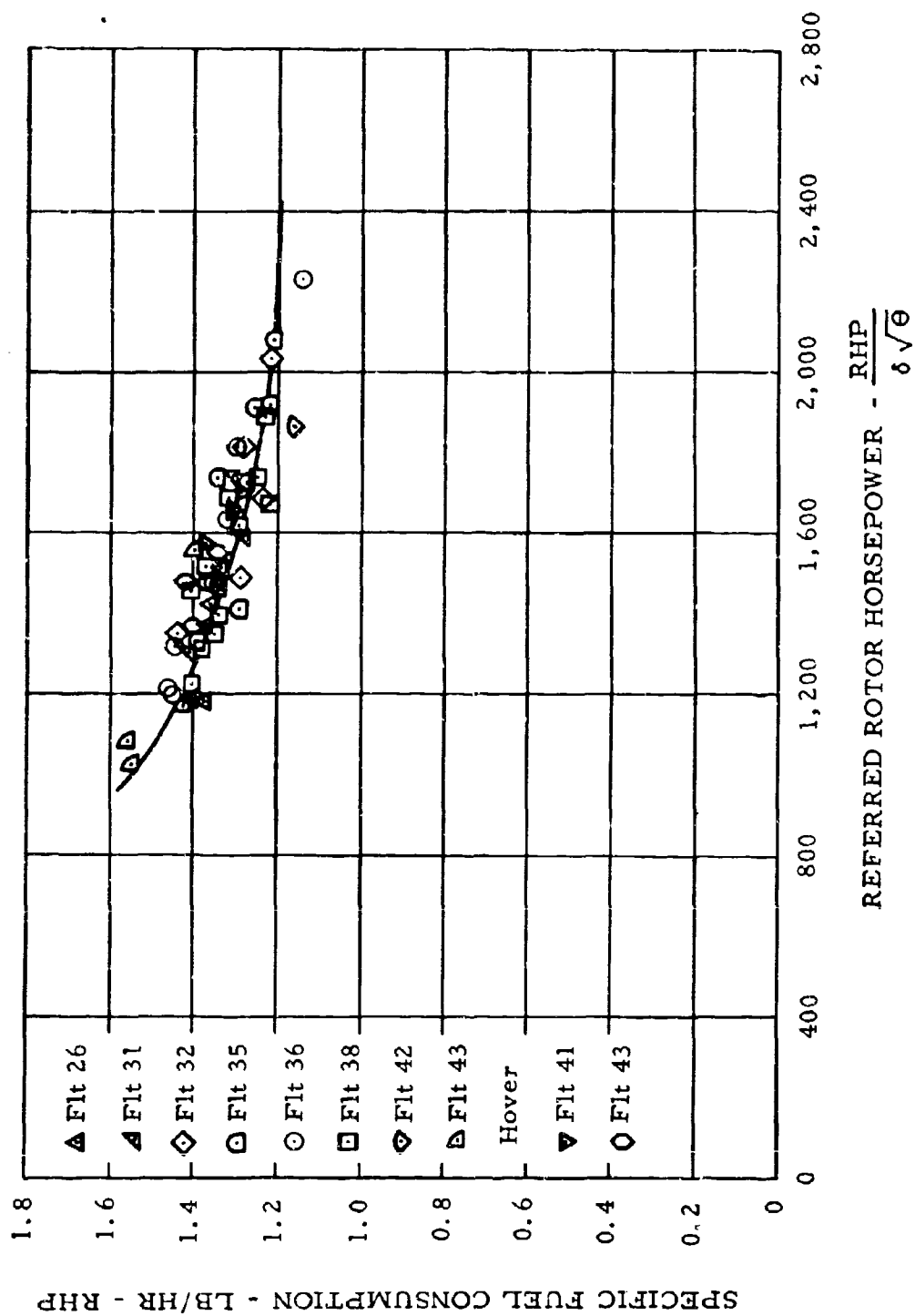


Figure 37. Observed Specific Fuel Consumption.

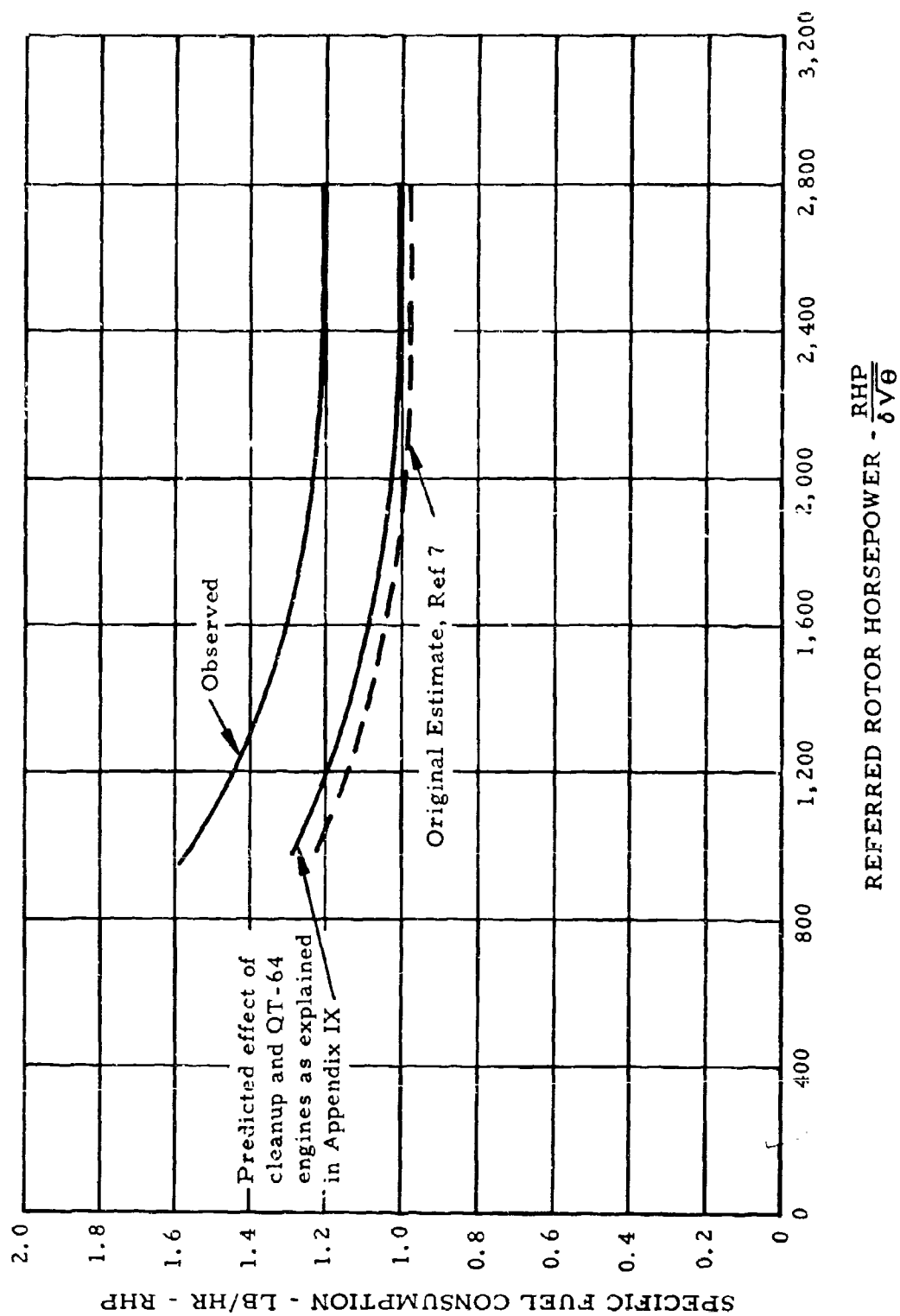


Figure 38. Comparison of Specific Fuel Consumption Versus Referred Rotor Horsepower.

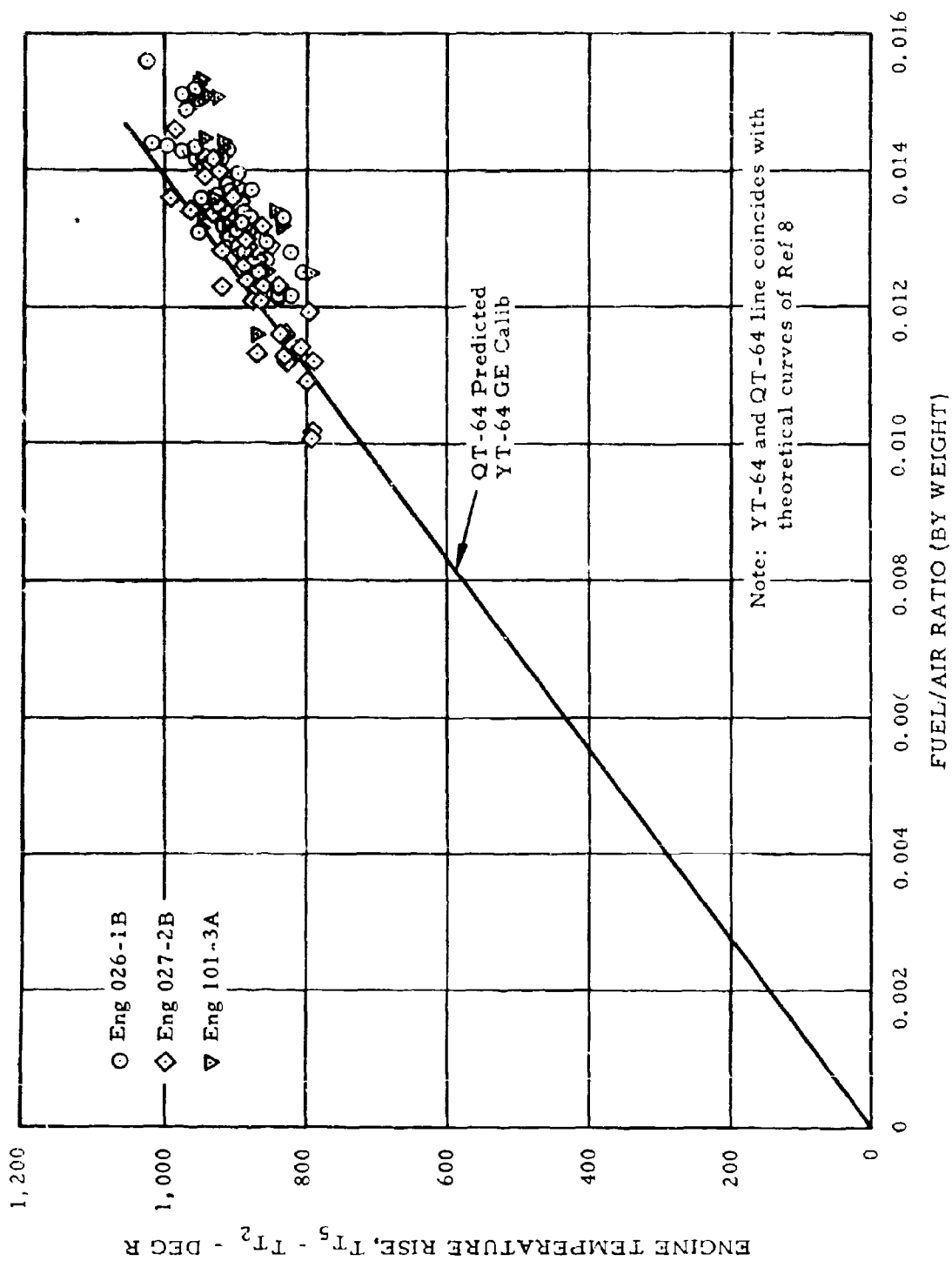


Figure 39. Temperature Rise Versus Fuel Air Ratio.

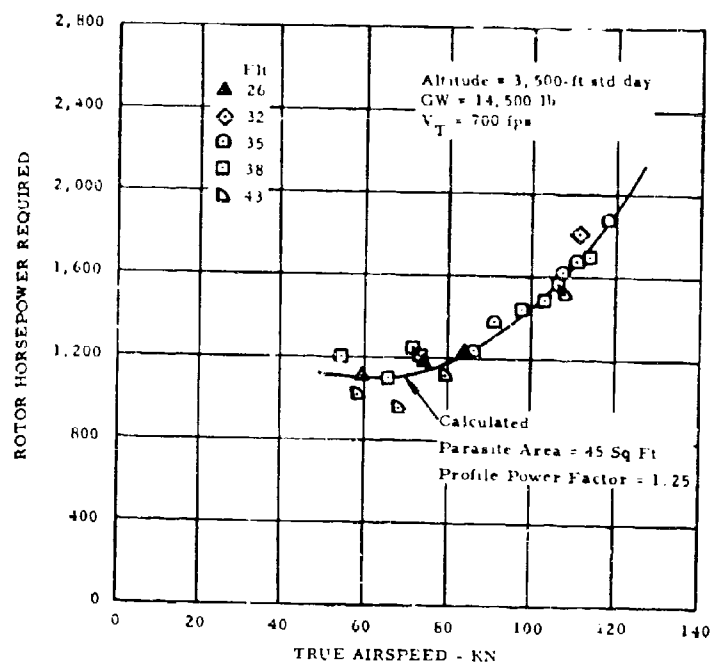


Figure 40. Level Flight Horsepower Required Versus True Airspeed, 3,500-Foot Altitude, Standard Day.

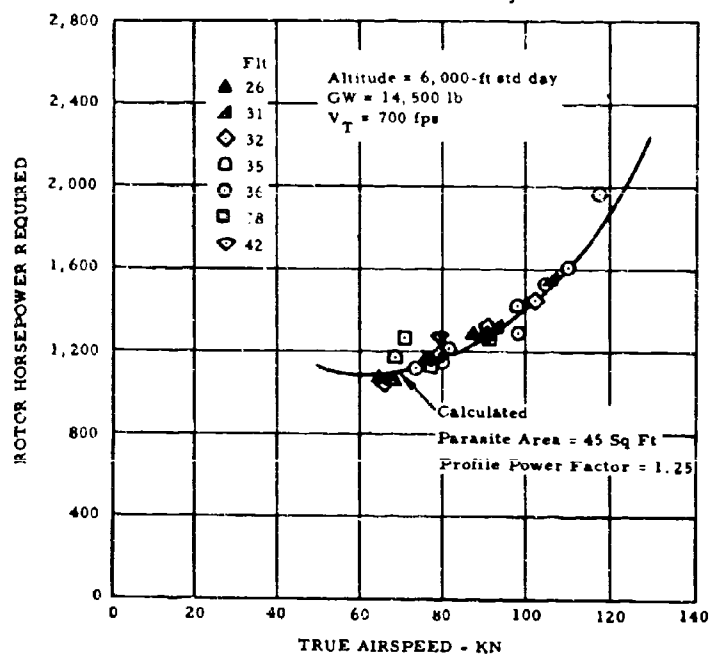


Figure 41. Level Flight Horsepower Required Versus True Airspeed, 6,000-Foot Altitude, Standard Day.

The rotor power available was computed from engine and rotor blade tip conditions, using the method discussed in Reference 1 and verified in Appendix IX. An allowance of 100 horsepower was made for blade-spar cooling, and 4 horsepower was allowed for engine-driven accessories. This allowance varies with density ratio and was subtracted from the computed rotor power available to give rotor power required for the individual flight.

The gross weight for each run was computed from the takeoff weight less the fuel burned up to the time of the run. The ambient conditions during each run were obtained from photopanel readings.

A comparison of experimental data with a series of theoretical curves established that the XV-9A parasite area was 45 square feet. These theoretical curves were calculated assuming a profile power factor (PPF) of 1.25, which was deduced from the hovering data presented later in this report.

Figure 42 presents a curve of rotor power required, including cooling and accessory losses, as a function of airspeed for sea level standard day, test weight, and 100-percent rotor speed. This curve was calculated using the above derived 45-square-foot parasite area and PPF of 1.25. A

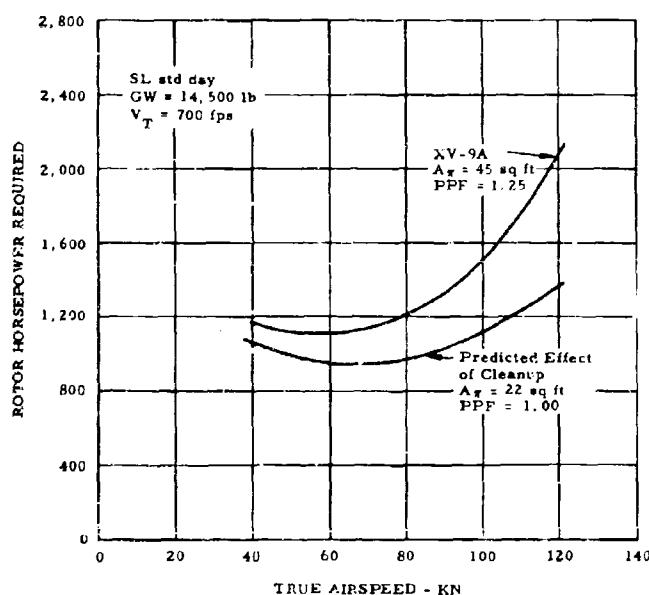


Figure 42. Level Flight Horsepower Required Versus True Airspeed, Sea Level, Standard Day.

second curve is shown in the figure to represent a "cleaned-up" ship. This curve assumes a parasite area of 22 square feet and a PPF of 1.00.

5. Fuel Flow Versus True Airspeed

Figures 43 and 44 present fuel flow data versus airspeed measured during the program. The data were corrected to the standard altitudes shown by the following procedure. The referred horsepower as a function of airspeed was calculated using the mean power curves of Figures 40 and 41. Using the mean line of Figure 37, the mean fuel flow lines of Figures 43 and 44 were obtained. The flight test data points were then corrected to standard ambient conditions by applying the percent deviation of fuel flow of the individual data points from the mean curve of Figure 38 to the mean lines of Figures 43 and 44.

Figure 45 presents fuel flow for the computed sea level performance on Figure 42, which was deduced in the same manner as explained above. The curve labeled "YT-64 engine, $A_{\pi} = 45$ sq ft and $PPF = 1.25$ " represents the performance of the XV-9A aircraft at sea level. The lower curve represents the predicted effect of a drag "cleanup" and the use of

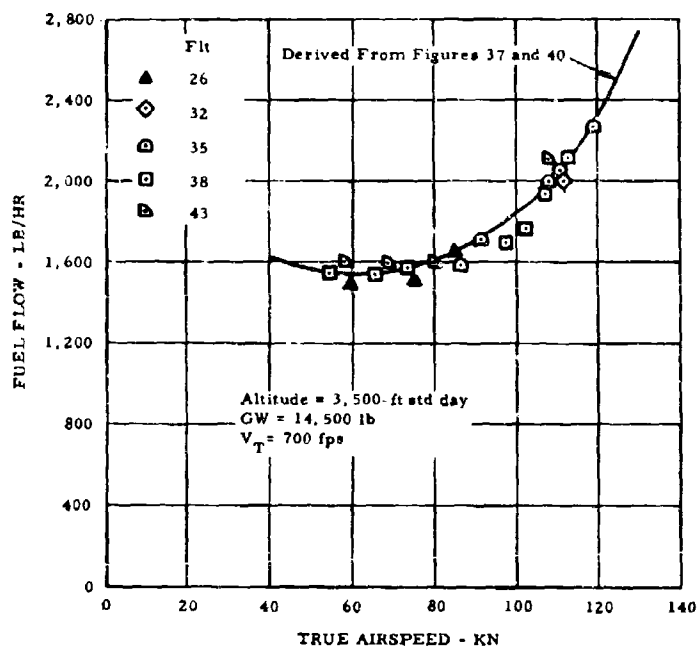


Figure 43. Fuel Flow Versus True Airspeed, 3,500-Foot Altitude, Standard Day.

fuel flow data for the QT-64 engine (rather than the YT-64 engine) as presented in Figure 38.

6. Maximum Airspeed and Airspeed Calibration

The maximum speed of the XV-9A was limited by collective pitch rather than power. Therefore, the correction of the flight test data to values of gross weight and altitude was done by plotting maximum speed versus C_T/σ .

Figure 46 presents true airspeed as a function of C_T/σ as limited by maximum collective pitch ($\theta_{0.75} = 9.8^\circ$). Test data for two high-speed flights are plotted along with the theoretical curve. The theoretical curve was computed for 103-percent rotor speed and used the parasite area deduced from the speed-power computations.

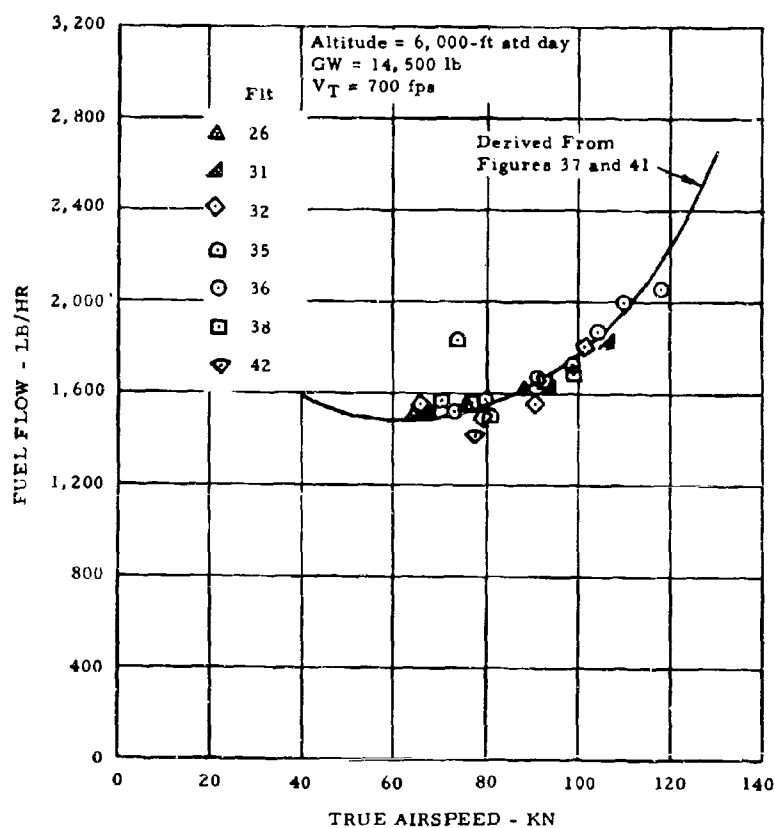


Figure 44. Fuel Flow Versus True Airspeed, 6,000-Foot Altitude, Standard Day.

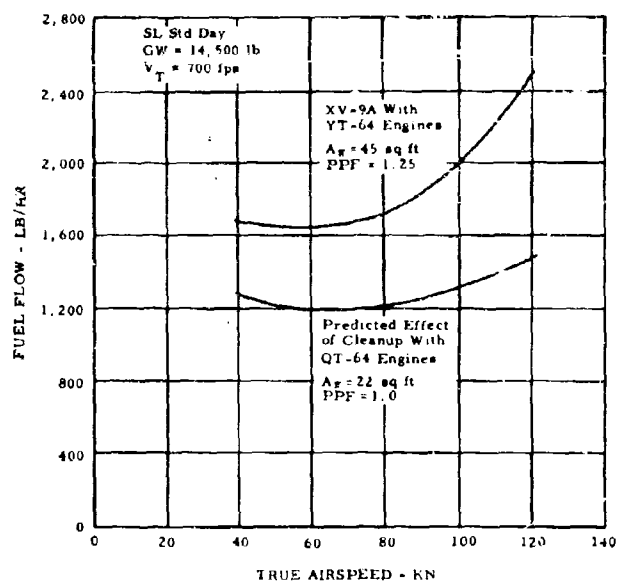


Figure 45. Fuel Flow Versus True Airspeed, Sea Level, Standard Day.

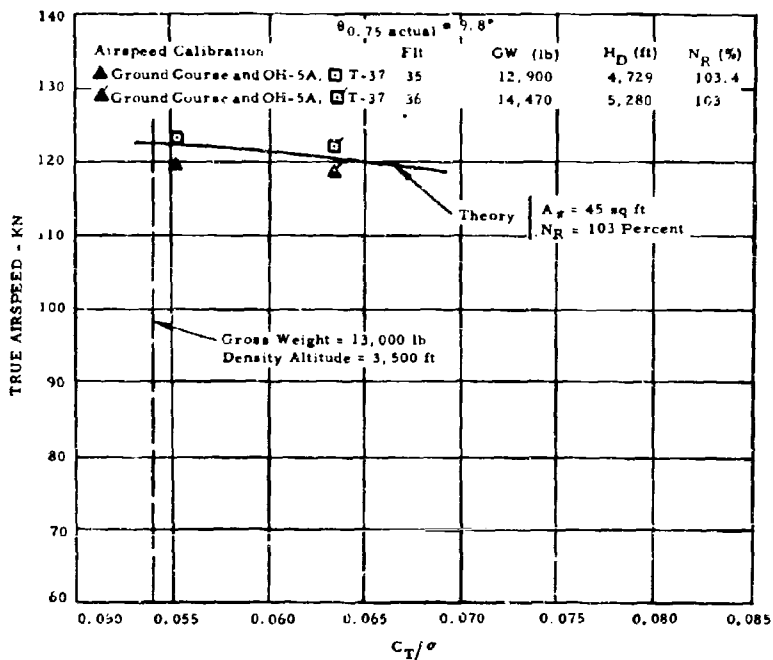


Figure 46. Maximum Airspeed for Full-Up Collective Pitch.

Figure 47 presents the airspeed calibration obtained by three different methods. Data points from flights 10 and 14 were obtained in ground-course speed runs during the initial 15-hour flight test program described in Reference 1. Further points were obtained during the follow-on flight test program using OH-5A and T-37 pacer aircraft. The values obtained from the OH-5A pacer aircraft fair in with the ground-course values, while the T-37 pacer aircraft points indicate a higher calibrated airspeed. Because of this variation, the maximum speed points were plotted on Figure 46 using both airspeed calibrations.

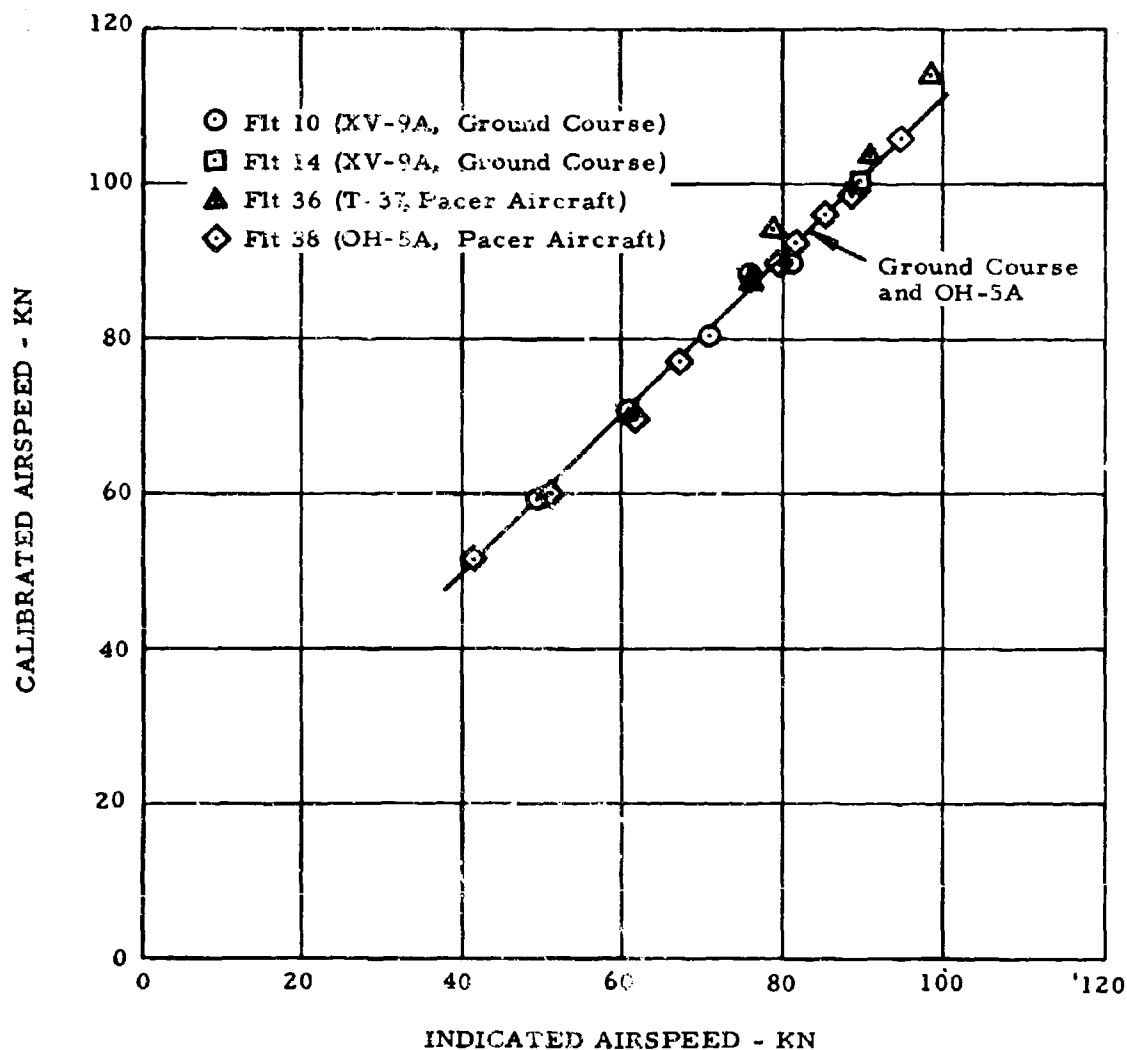


Figure 47. Airspeed Calibration - Photopanel.

7. Rate of Climb

Figure 48 presents the maximum rate of climb as a function of altitude for the XV-9A flight tests corrected to standard conditions. As the XV-9A was limited by maximum collective pitch, the test climb points were conducted at reduced power settings. Thus, curves are included on the figure to show the maximum rates of climb for normal and military power assuming no collective pitch restriction.

The test points were reduced to standard conditions in the following manner:

- a. For each test density altitude, the tape line rate of climb at test true airspeed was obtained from the test day rate of climb by the equation

$$R/C_{\text{tapeline}} = R/C_{\text{measured}} \times \frac{T_{\text{test}}^{\text{OR}}}{T_{\text{std}}^{\text{OR}}}.$$

- b. From the thermodynamic parameters, the rotor power available was computed using the method described in Reference 1. By subtracting out the cooling and accessory losses, the rotor power required is obtained.
- c. Since the rotor power required, the test weight, the ambient conditions, and the profile power factor deduced from hovering data were known, the parasite area was theoretically computed by using the methods of Reference 9. The parasite area during climb generally differs from the level flight parasite area because of the difference in fuselage angle of attack.
- d. The parasite area deduced for each test point was used to calculate the rate of climb for standard-day conditions at the test density altitude on the basis of the methods discussed in Reference 9. The results are plotted in Figure 48. The lowest rate-of-climb curve in Figure 48 represents the XV-9A as being limited by a maximum collective pitch of 9.8 degrees.

The curves of climb at normal power and at military power in Figure 48 are computed in the same manner, assuming no collective pitch limit.

Figure 48 indicates that the XV-9A has a 570-fpm rate of climb at 10,000-foot standard-day conditions. With the collective pitch limit removed, the rate of climb at 10,000 feet would be 1,300 feet per minute.

8. Rate of Descent at Idle Power

Figure 49 presents autorotational rate of descent of approximately 2,200 feet per minute at idle power corrected to standard day at 3,700-foot density altitude and at 13,000-pound gross weight. The method used to reduce the test data to standard conditions is the same as that described above for the rate-of-climb curve. The second curve on Figure 49 presents the predicted rate of descent for a cleaned-up XV-9A with a parasite area of 22 square feet and a profile power factor of 1.0. The predicted minimum autorotational rate of descent would be approximately 1,740 feet per minute.

9. Hover Performance

a. Hover Power Required

Figure 50 presents a plot of the calculated rotor thrust coefficient (C_T) in ground effect ($Z/D = 0.49$) for blade profile power factors of 1.0 and 1.25. Also shown are the reduced hover test points taken in ground effect ($Z/D = 0.49$). As can be seen, there is excellent agreement between the calculated curve for a blade $PPF = 1.25$ and the test data points. This indicates that hover power required in ground effect for the XV-9A can be accurately predicted by theory using a blade profile power factor of 1.25. The 25-percent increase in blade profile power of the XV-9A blade over that of a blade of normal construction is attributed primarily to the surface irregularities at the leading edge segment joints of the present blade. It is anticipated that future Hot Cycle blade designs will eliminate the leading edge segment joint roughness and thus reduce the blade profile power factor to 1.0.

Figure 51 presents similar calculated plots of C_T versus C_Q curves for PPF of 1.0 and 1.25 out of ground effect. The single stabilized hover test point obtained out of ground effect is shown to agree well with the calculated curves.

Figures 52 and 53 present calculated curves of gross weight versus rotor horsepower required for standard-day conditions at 3,500 feet. These curves were generated from the C_T versus C_Q curves of Figures 50 and 51. Also shown are the test points corrected to the same standard-day condition from the C_T versus C_Q test points of Figures 50 and 51.

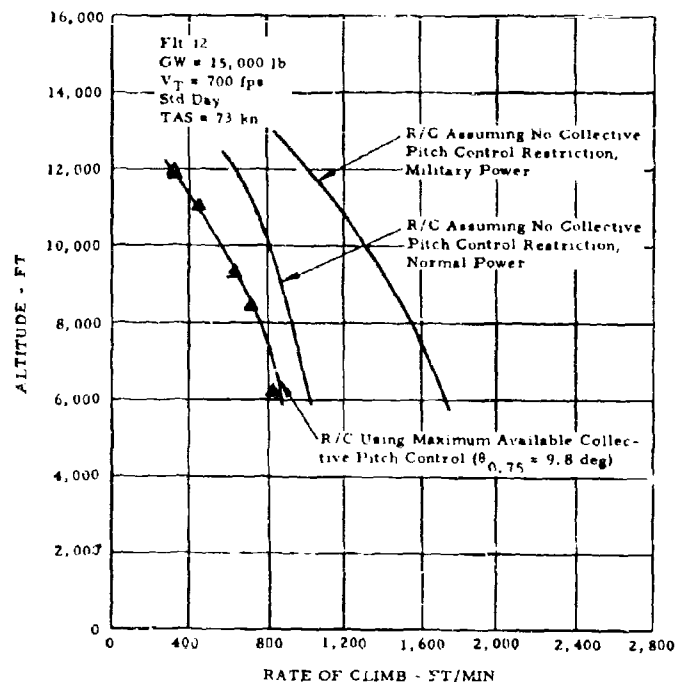


Figure 48. Rate of Climb.

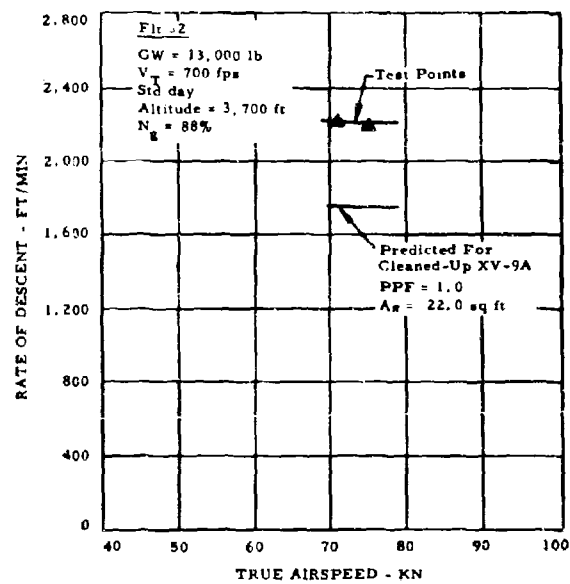


Figure 49. Autorotational Rate of Descent.

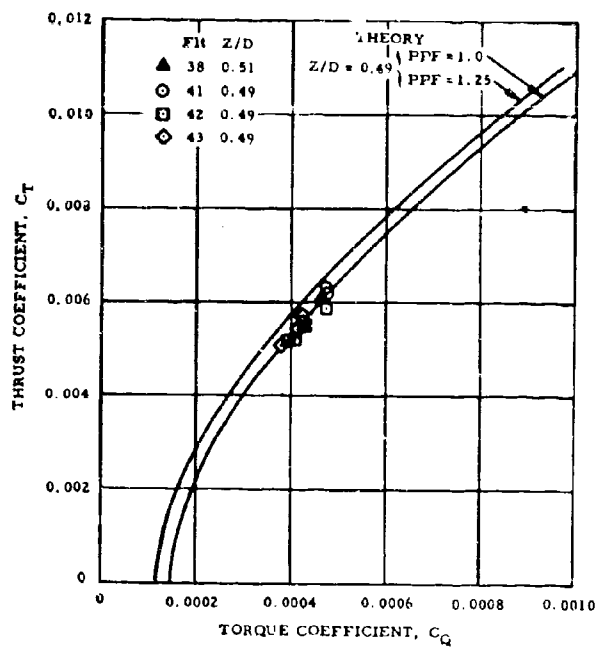


Figure 50. Thrust Coefficient Versus Torque Coefficient, Hover IGE.

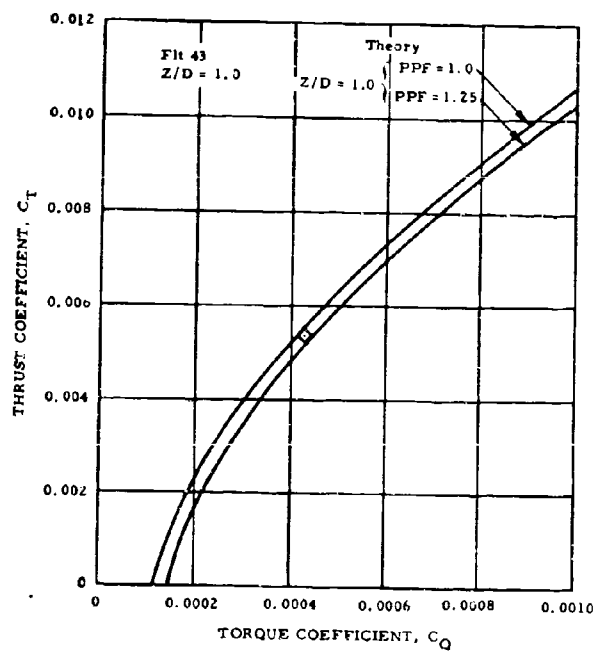


Figure 51. Thrust Coefficient Versus Torque Coefficient, Hover OGE.

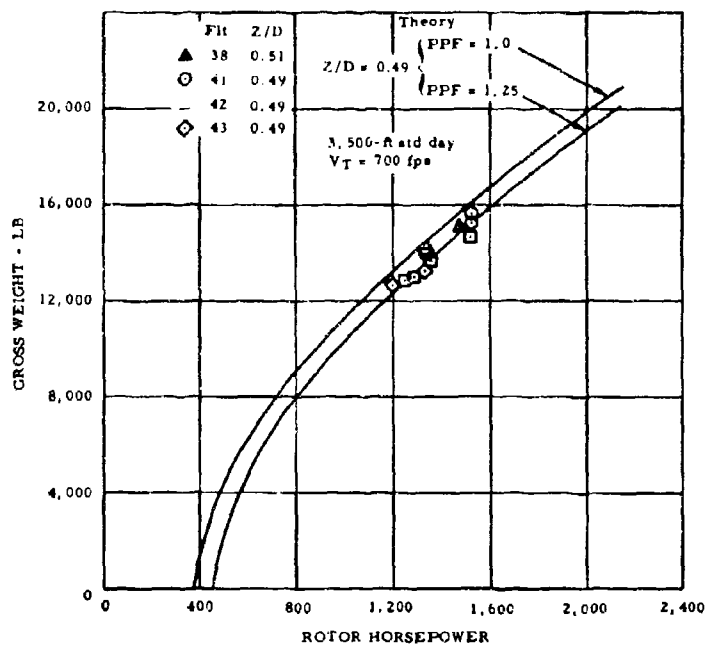


Figure 52. Gross Weight Versus Rotor Horsepower, Hover IGE.

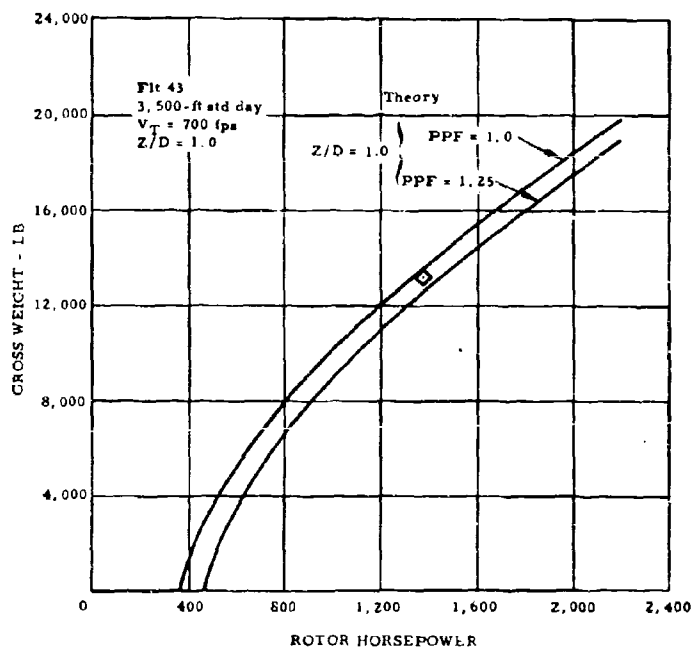


Figure 53. Gross Weight Versus Rotor Horsepower, Hover OGE.

b. Hover Power Available

Figure 54 presents the calculated referred rotor horsepower available ($RHP/\delta\sqrt{\theta}$) versus engine discharge temperature based on deduced component performance values (solid line). Also shown are the test points of calculated referred rotor horsepower versus measured referred turbine discharge temperatures obtained during the 20-hour flight test program. It can be seen that the calculated curve is in excellent agreement with the test data and can be considered as a mean curve through the mass of test points. This mean curve was used to determine the rotor horsepower available for the XV-9A. The maximum rotor horsepower available used to determine the hover and climb performance with the YT-64 engines (standard XV-9A configuration) was calculated by assuming that the engines were operating at their maximum temperature limit ($T_4 = 1,732$ degrees R) without exceeding the engine overspeed limit ($N_g = 103.2$ percent). The inlet air temperature rise was assumed to be 4 degrees C above the ambient temperature, based on hover flight test results.

Also shown on Figure 54 (as a dashed line) is the predicted referred rotor horsepower available versus referred turbine discharge temperatures for the QT-64 engines. In calculating the maximum rotor horsepower available for the QT-64 engines, the engines are again assumed to be operating at their temperature limit without exceeding the engine overspeed limit through correct sizing of the nozzle areas. The inlet air temperature rise for the QT-64 engines was assumed to be 1 degree C above ambient temperature, based on a nacelle design with improved internal cooling resulting in a lower inlet temperature rise.

c. Hover Ceiling

Figure 55 presents the hover ceiling in ground effect and Figure 56 presents the hover ceiling out of ground effect for the XV-9A. Also presented are predictions for a cleaned-up XV-9A. These curves were generated from the data presented in Figures 50, 51, and 54. The results are presented in Tables III and IV. Hover ceilings for the XV-9A are presented for both power and collective pitch control limitations.

10. Single-Engine Flight

Figure 57 presents a plot of altitude and velocity as a function of time during single-engine flight with one engine overboard. It can be seen that there was a slight rate of descent and decrease in airspeed during the

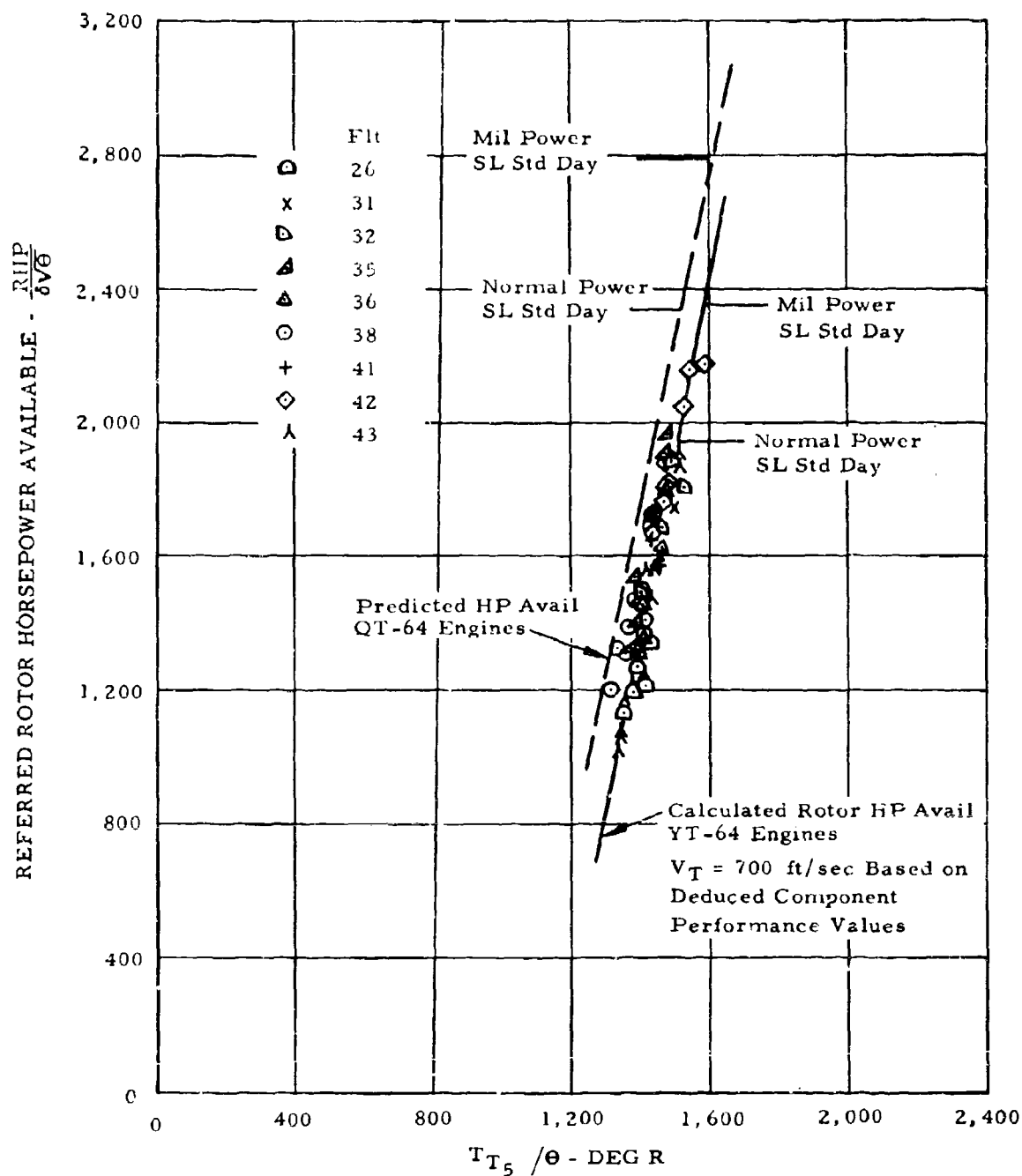


Figure 54. Referred Rotor Horsepower Available Versus Turbine Discharge Temperature.

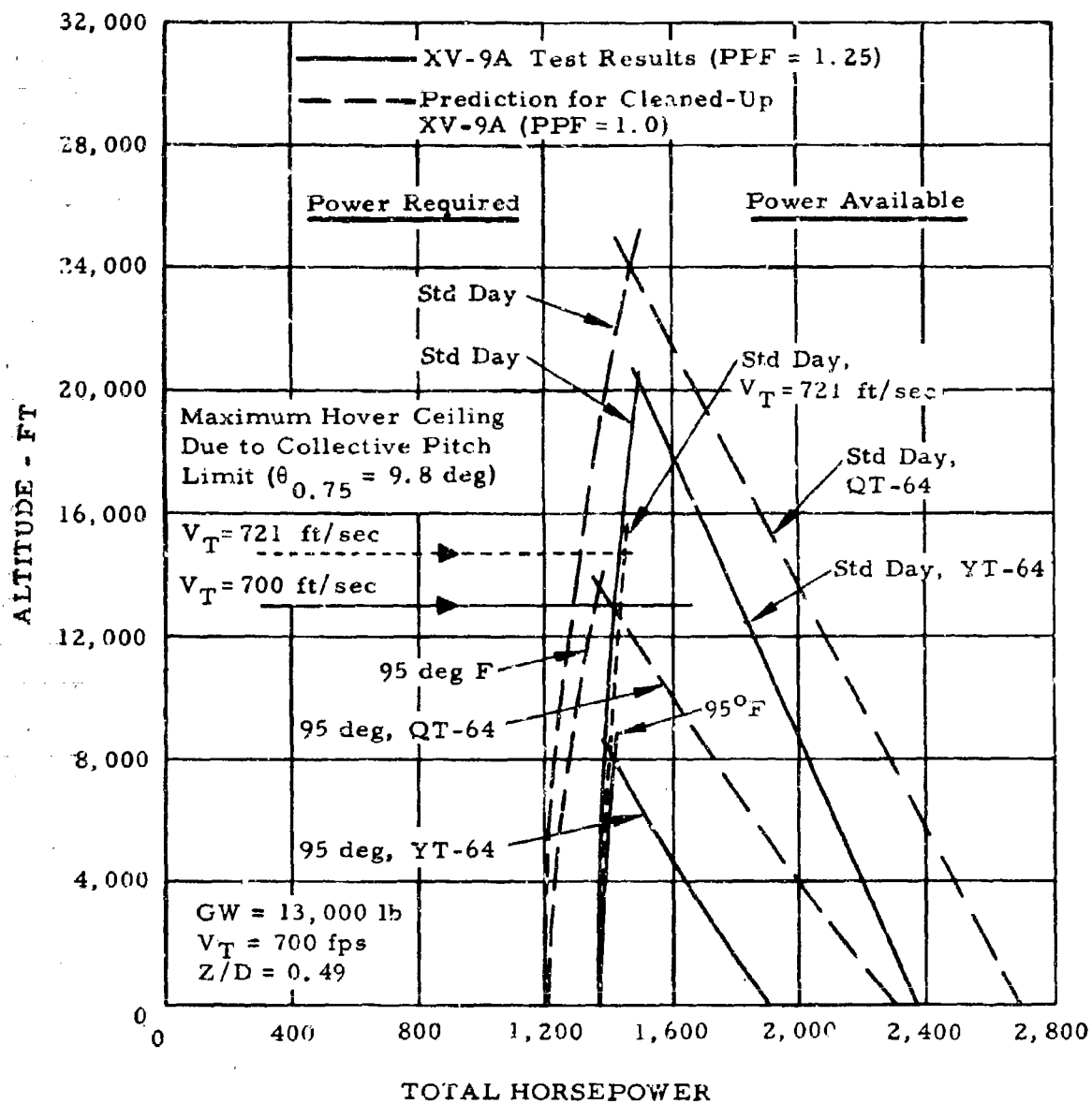


Figure 55. Hover Performance, IGE.

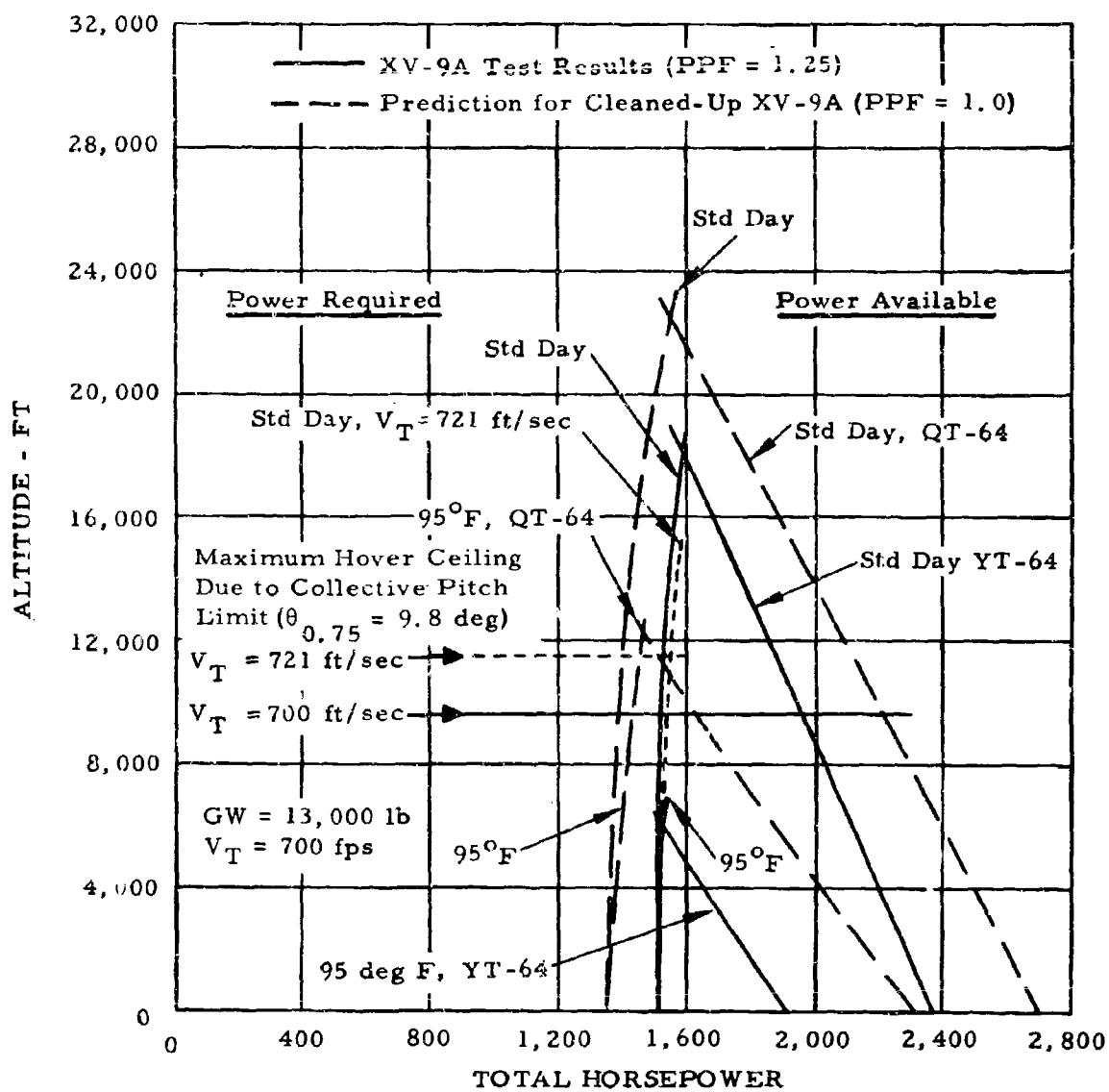


Figure 56. Hover Performance, OGE.

TABLE III
HOVER CEILING, IGE

Configuration	Standard Day		95°F Day	
	Power Limit	Collective Pitch Limit ($\theta_{0.75} = 9.8^\circ$)	Power Limit	Collective Pitch Limit ($\theta_{0.75} = 9.8^\circ$)
<u>XV-9A (YT-64 Engine)</u>				
PPF = 1.25 Cooling hp losses = $100 p/\rho_o$ Accessory hp = 4 $\Delta T_{inlet} = 4^\circ C$	20,000 ft	*12,950 ft	8,000 ft	
<u>Prediction for cleaned-up XV-9A (QT-64 Engine)</u>				
PPF = 1.0 Cooling hp losses = $50 p/\rho_o$ Accessory hp = 4 $\Delta T_{inlet} = 1^\circ C$	24,000 ft	-	13,700 ft	-
GW = 13,000 lb $V_T = 700$ ft/sec Z/D = 0.49				
*Hover ceiling can be increased to 14,700 feet by increasing the rotor speed to 103 percent.				

TABLE IV
HOVER CEILING, OGE

Configuration	Standard Day		95°F Day	
	Power Limit	Collective Pitch Limit	Power Limit	Collective Pitch Limit
<u>XV-9A (YT-64 Engine)</u>				
PPF = 1.25 Cooling hp losses = $100 p/\rho_o$ Accessory hp = 4 $\Delta T_{inlet} = 4^\circ C$	18,100 ft	*9,600 ft	6,000 ft	-
<u>Prediction for cleaned-up XV-9A (QT-64 Engine)</u>				
PPF = 1.0 Cooling hp losses = $50 p/\rho_o$ Accessory hp = 4 $\Delta T_{inlet} = 1^\circ C$	22,500 ft	-	12,200 ft	-
GW = 13,000 lb $V_T = 700$ ft/sec				
*Hover ceiling can be increased to 11,500 feet by increasing the rotor speed to 103 percent.				

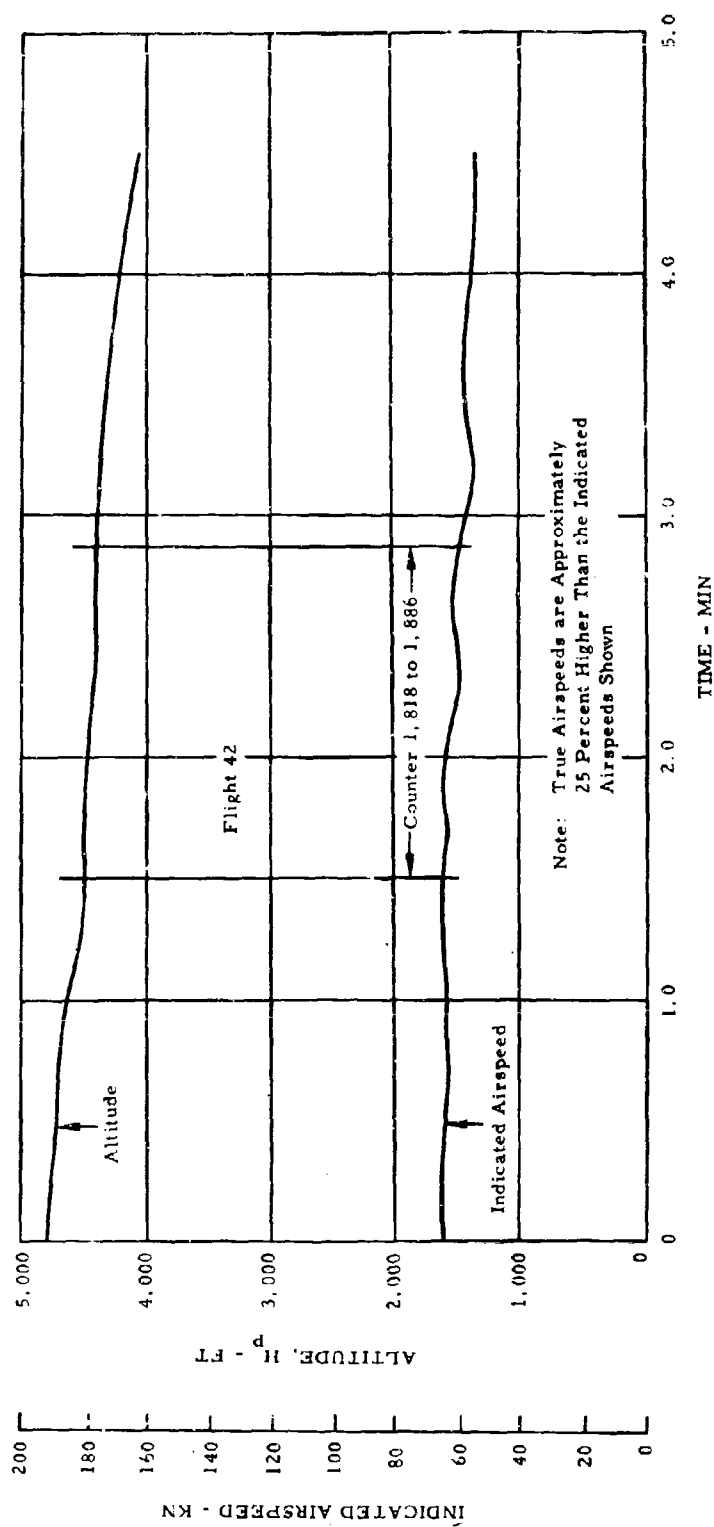


Figure 57. Single-Engine Flight.

single-engine operation. In reducing the flight test data to standard conditions, these were taken into account by converting the energy provided the system by the rate of descent and decrease in velocity to an effective forward thrust.

The ship was allowed to yaw approximately 30 degrees during the test. Thus, the data were reduced to standard conditions by computing the yawed parasite area, using the methods of Reference 9, from test weight and ambient conditions and from computed values of rotor power and overboard engine thrust obtained from the test thermodynamic parameters. Using the deduced parasite area, the rotor power required for yawed level flight with full thrust on the overboard engine was computed for standard conditions and weight. As shown in Figure 58, the rotor power required was 892 horsepower, while 1,080 rotor horsepower is available with one engine. Thus, single-engine flight can be easily made at the standard conditions. The reason the XV-9A did not actually achieve level flight is that the ambient temperature was 29 degrees F above standard (at 5,000-foot pressure altitude).

Figure 58 also presents a plot of rotor power required with zero yaw versus airspeed and with no jet thrust assistance. It can be seen that the rotor power required for single-engine flight at 30-degree yaw and with jet thrust assistance is less than the rotor power required for zero yaw with no assistance. Thus, the jet thrust assistance more than overcomes the increased drag due to the yawed condition.

11. Diverter Valve

Diverter valve leakage was measured twice: first, in connection with the initial 15-hour flight test program, and finally at the conclusion of the 20-hour follow-on flight test program. The effective leakage area was found to increase from 2.23 to 2.85 percent of total system mass flow. The leakage of both diverter valves was measured by placing an orifice flowmeter over one and then the other tailpipe, and running with both engines to the rotor. The diverter valve leakage, when combined with that for the rest of the ducting systems (see Leakage Test Results, Table XI), yields a loss of approximately 3 percent of the total system mass flow, which agrees closely with the value used in previous reports on the XV-9A.

Flying Qualities

The stability and control evaluation of the XV-9A has been determined by the method outlined in Reference 2, and the results are presented herein.

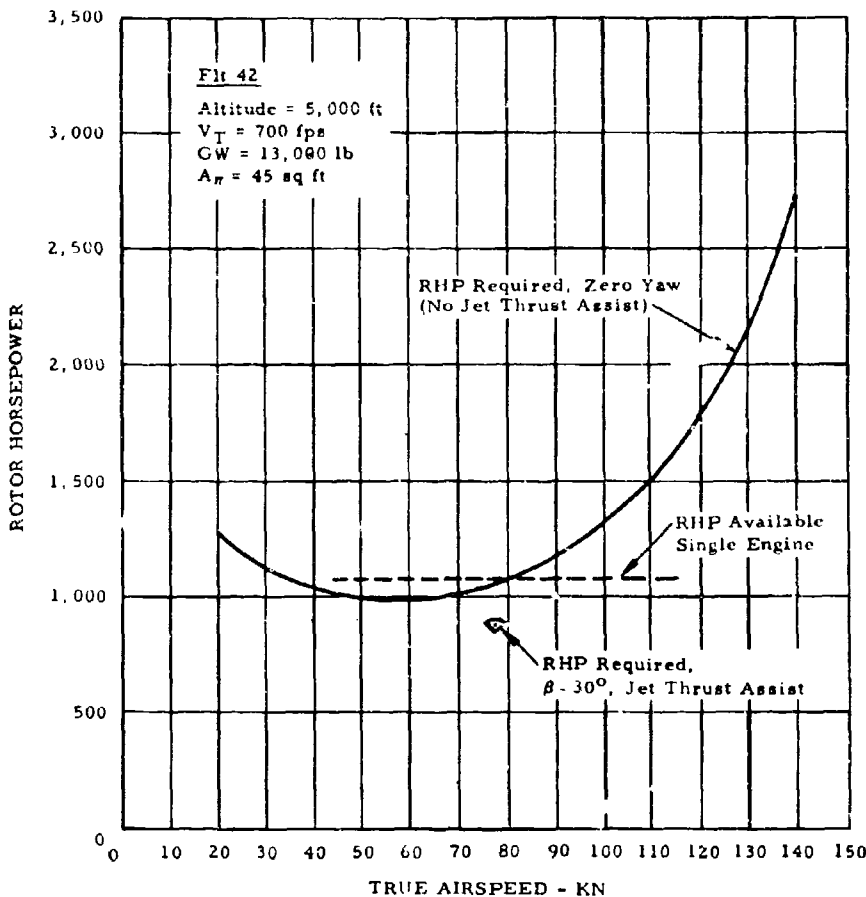


Figure 58. Rotor Horsepower Versus Airspeed - Single-Engine Flight.

In general, the flying qualities of the XV-9A were found to be marginally adequate for this type of research aircraft where an existing rotor system (whirl test rotor) is combined into a flight article with minimum modification to the basic rotor system.

1. Hover

a. Controllability

The control power during hover was determined by measuring the maximum angular acceleration resulting from step-type control displacements from trim about each axis. The results are presented in Figures 59, 60, and 61. The control powers (which are the ratios of accelerations measured from Figures 59, 60, and 61 to the

Flt 33

Hover at 27-ft wheel height

GW = 14,180 lb

CG = sta 296.4

Rotor RPM = 243

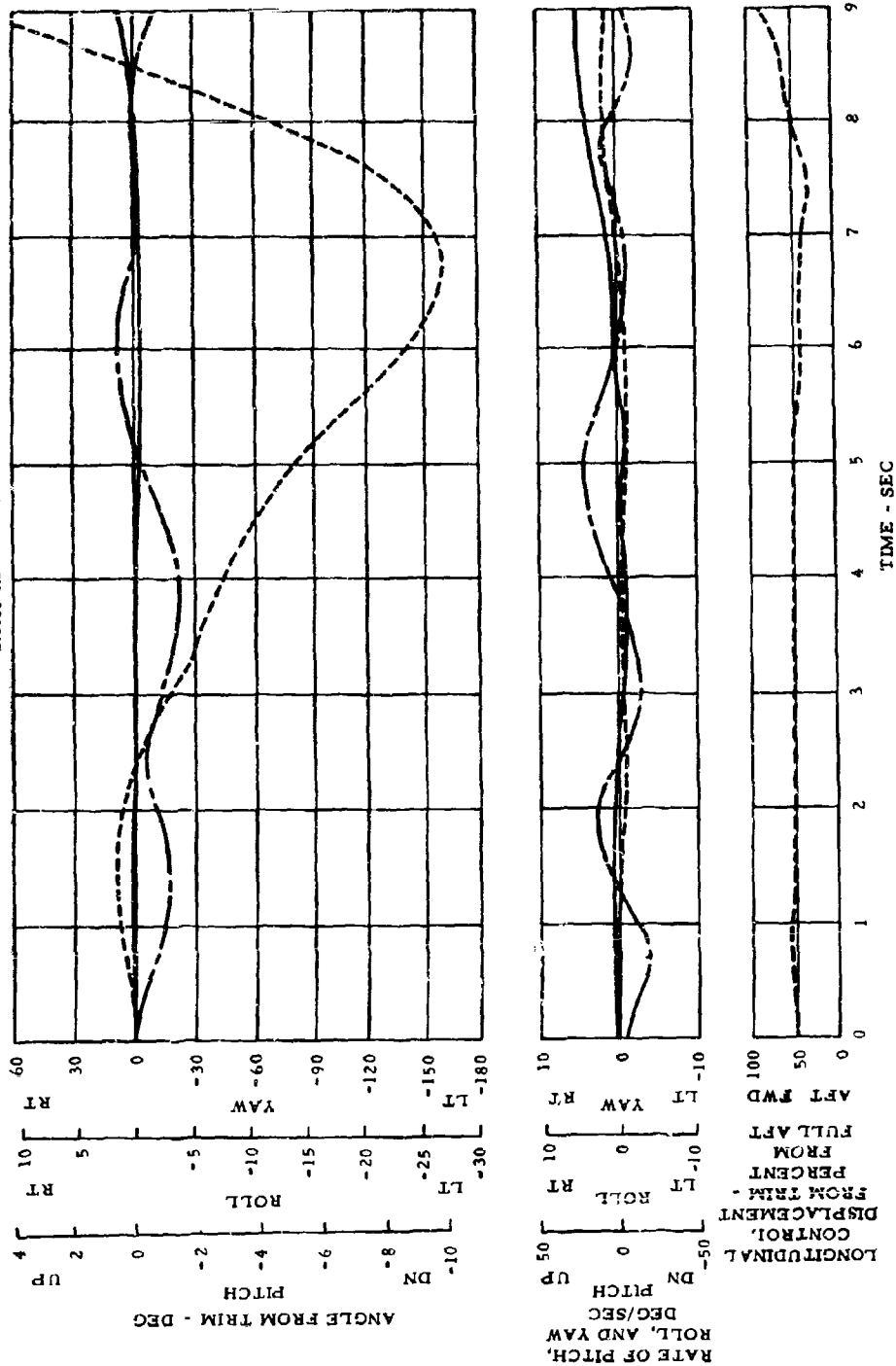


Figure 59. Aircraft Response to a Forward Longitudinal Step Input in Hover.

Flt 33

Hover at 27-ft wheel height
 GW = 13,900 lb
 CG = sta 297.6
 Rotor RPM = 243

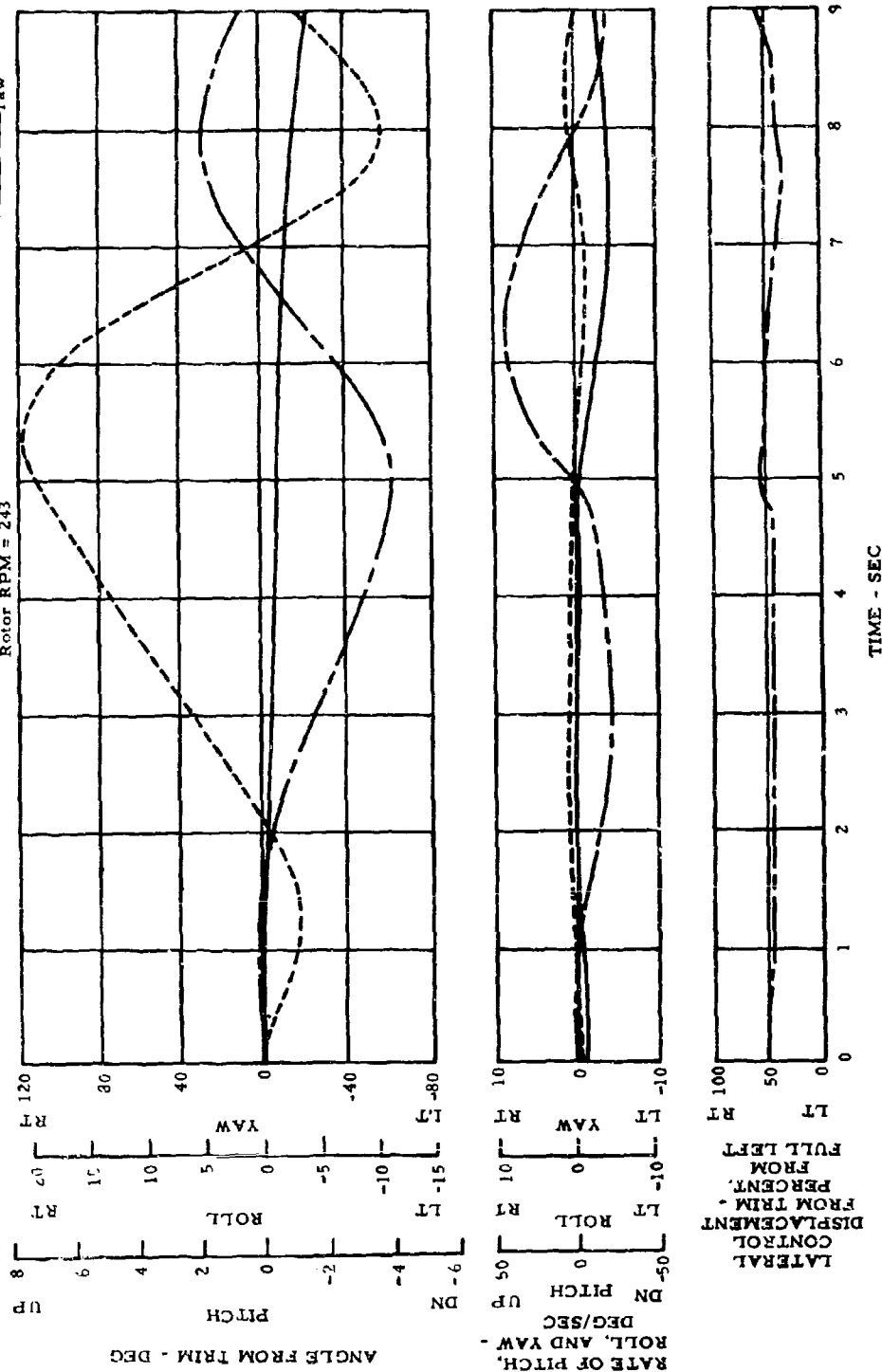


Figure 60. Aircraft Response to a Left Lateral Input in Hover.

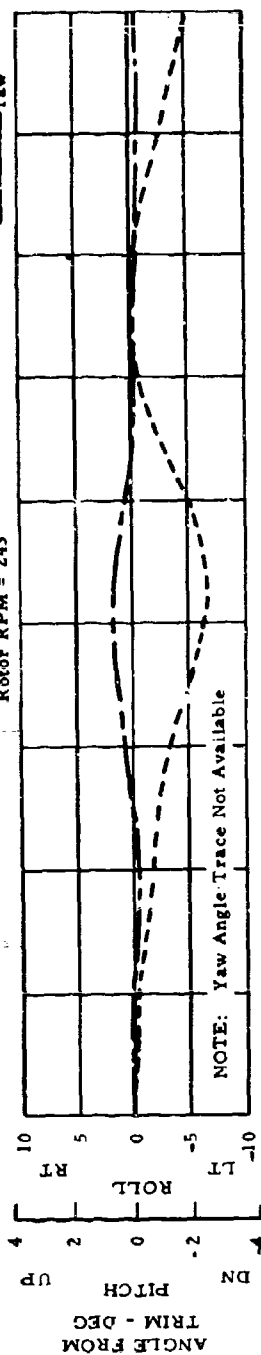
Flt 41

Hover at 27-ft wheel height

GW = 13,920 lb

CG = sta 297.5

Rotor RPM = 243



NOTE: Yaw Angle Trace Not Available

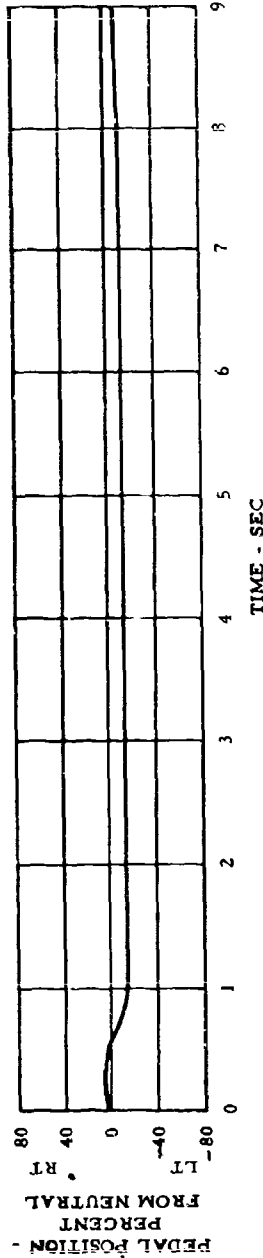
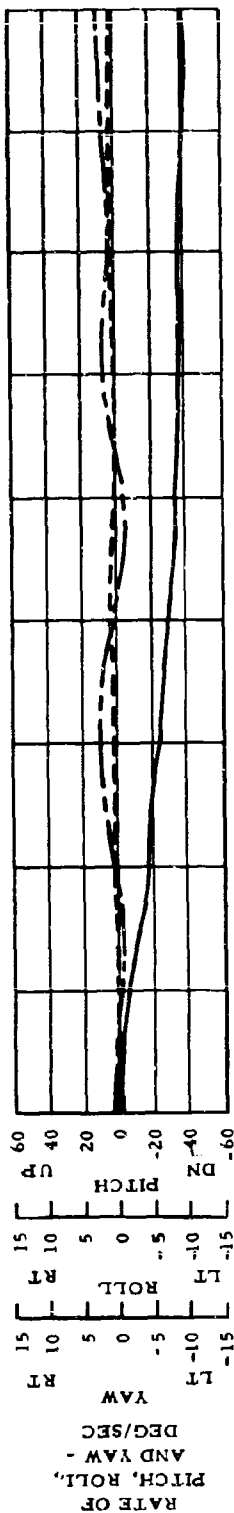


Figure 61. Aircraft Response to a Left Pedal Step Input in Hover.

control displacements from trim, given on the same figures) are presented in Table V and are compared with the theoretically calculated control powers. Also shown, for comparison purposes, are the minimum values of control power required by MIL-H-8501A for the test conditions.

TABLE V
CONTROL POWER

Axis	Gross Weight (lb)	Control Power (deg/sec ² /in.)		
		Measured	Theory	MIL-H-8501A
Pitch	14,180	4.5	4.7	4.1
Roll	13,920	10.0	10.8	9.0
Yaw	13,900	5.0	4.7	9.0

The comparison of measurement and theory shows good agreement, indicating that theory can be used to predict accurately the helicopter hover control power in pitch, roll, and yaw. Control powers about the pitch and roll axes are considered to be adequate based on MIL-H-8501A minimum requirements. However, the pilot's comments indicate that an increase would be desirable.

The yaw control jet system provides approximately one-half the directional control power required by MIL-H-8501A. Experience has indicated that the yaw requirement of MIL-H-8501A is too stringent for aircraft not incorporating large tail rotors because there is less source of yaw disturbance in gusty air. An increase in yaw control using the existing yaw control jet system could be realized at the expense of reduced performance capability. A more desirable approach from the standpoint of yaw thrust/rotor power ratio would be the use of a yaw fan or tail rotor that would also provide damping in yaw.

The effect of the present yaw control system on engine operation is shown in Figure 62. With full pedal step input, the increase in nozzle exit area, as seen by the engines, increases the engine speed to the topping speed limit. It is possible that at higher altitudes or lower temperatures the use of sustained full pedal displacement will overspeed the engines. Conversely, to prevent engine overspeeding, a compromise must be made in engine topping setting or the topping setting must be made a function of pedal position.

Flt 28

Hover at 27-ft wheel height
 GW = 15,100 lb
 CG = sta 297.5
 Rotor RPM = 243

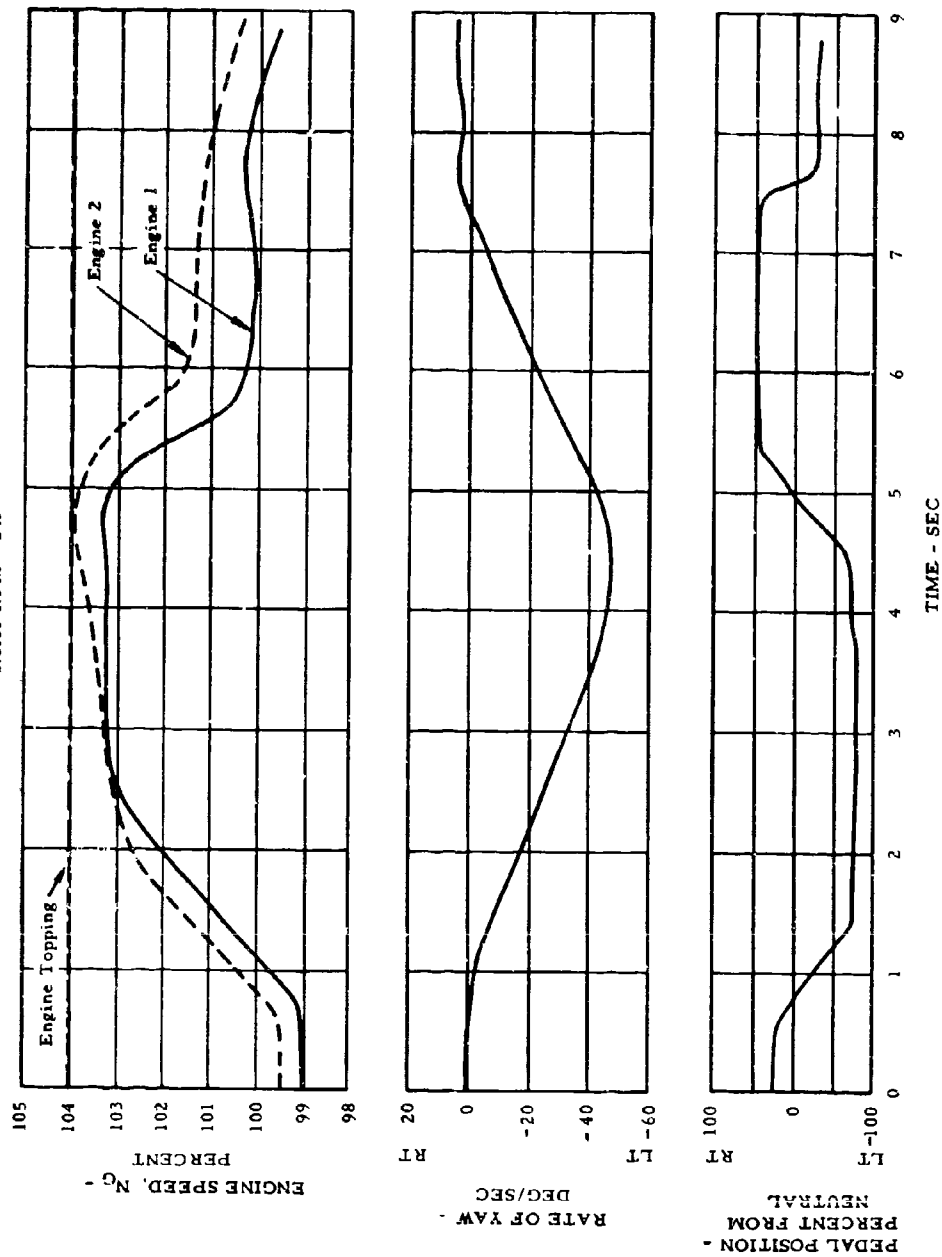


Figure 62. Aircraft Response to a Right Pedal Step Input in Hover.

b. Response to Pulse Inputs

Figures 63 and 64 present the response of the XV-9A to pulse-type inputs in pitch and roll. As can be seen, the motion in pitch following a forward pulse is a slow divergent pitch oscillation coupled with a shorter period rolling motion. A lateral pulse results in a similar coupled motion.

2. Sideward Flight and Rearward Flight

Figures 65 and 66 show the control positions versus speed up to 10-knot left and right sideward flight and up to 10-knot rearward flight.

3. Level Flight

a. Control Positions

Longitudinal, collective, and pedal positions during trimmed level flight were recorded as a function of airspeed at the forward (station 294), mid (station 298), and aft (station 301) center-of-gravity positions. For test conditions where fuel management could not always maintain the proper center-of-gravity positions, the data are corrected to the typical test center-of-gravity position. The results are presented in Figure 67. At the forward and mid center-of-gravity positions, there is adequate longitudinal control margin to fly at speeds in excess of 120 knots. However, as can be seen, there is inadequate available collective pitch at these airspeeds to produce the desired rotor lift. The trim pedal positions shown are for two different riggings of rudder surfaces at neutral pedal. Throughout most of the test program, the rudder surfaces were rigged 7 degrees to the right with neutral pedals and with closed yaw valve. This rigging resulted in essentially neutral pedal and, hence, in minimum yaw valve opening during cruise flight. For descent flight tests, which are discussed below, the rudder surfaces were rerigged to be neutral with neutral pedals. This rigging results in increased yaw valve opening during cruise flight.

b. Speed Stability

Longitudinal speed stability was obtained by recording the stick positions at constant power (fixed collective) settings and increasing and decreasing the airspeeds 20 knots from trim. The results are presented in Figure 68 for trim speeds of 70 to 95 knots. The stick position gradients vary from neutrally stable for decrease in speeds from trim to slightly unstable for increasing speeds from

FIG. 33

Hover at 27-ft wheel height

GW = 14,300 lb

CG = sta 296.5

Rotor RPM = 243

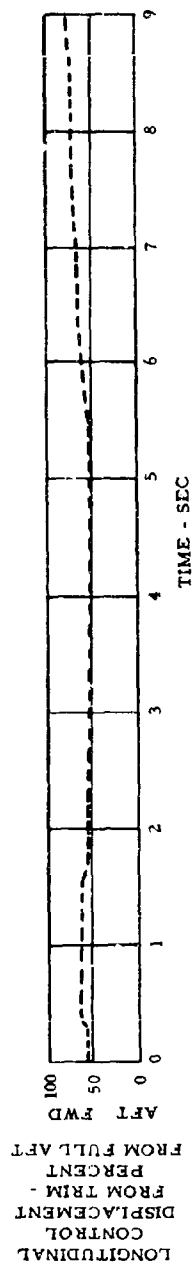
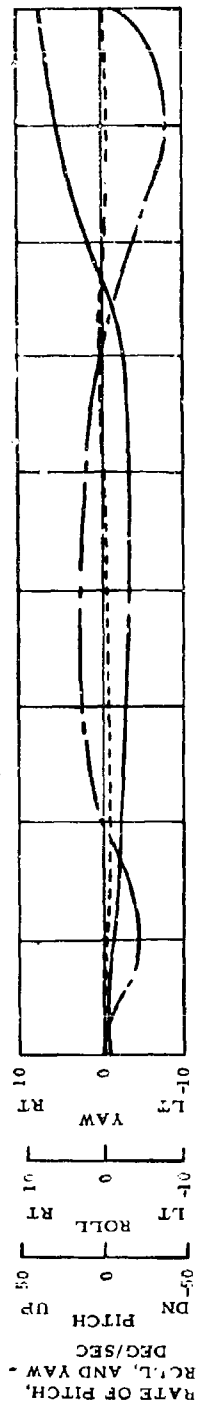
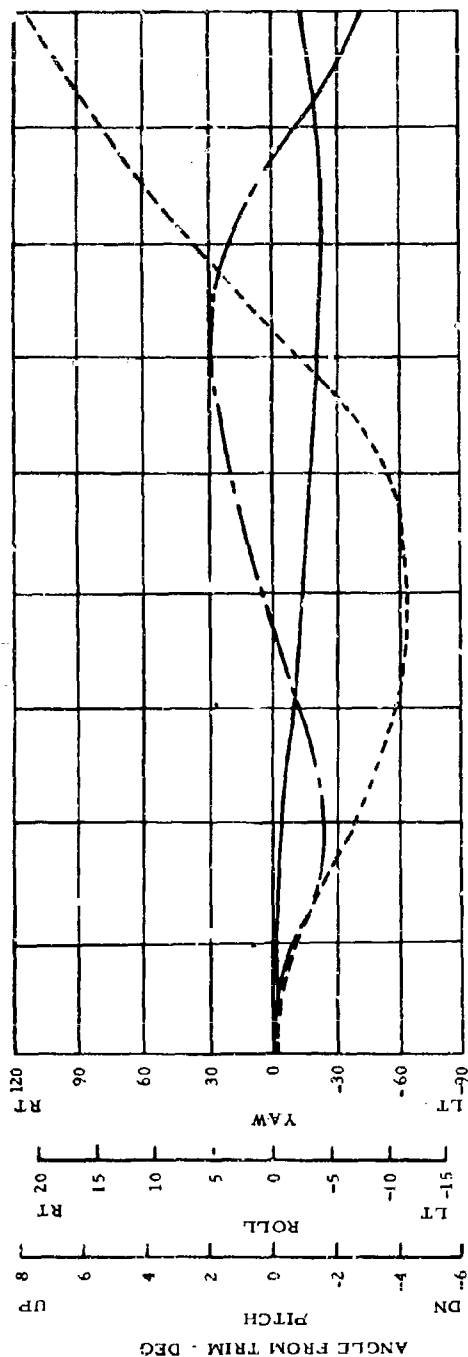


Figure 63. Aircraft Response to a Forward Longitudinal Pulse Input in Hover.

FIG. 33

Hover at 27-ft wheel height
 CW = 14,030 lb
 CG = sta 297
 Rotor RPM = 243

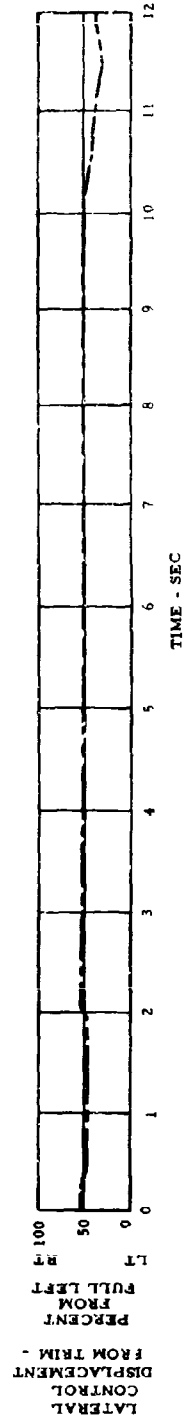
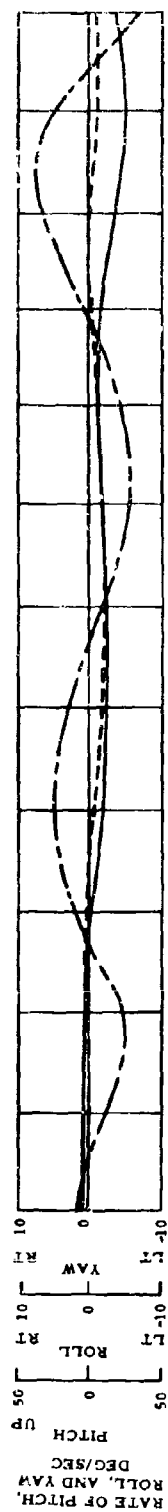
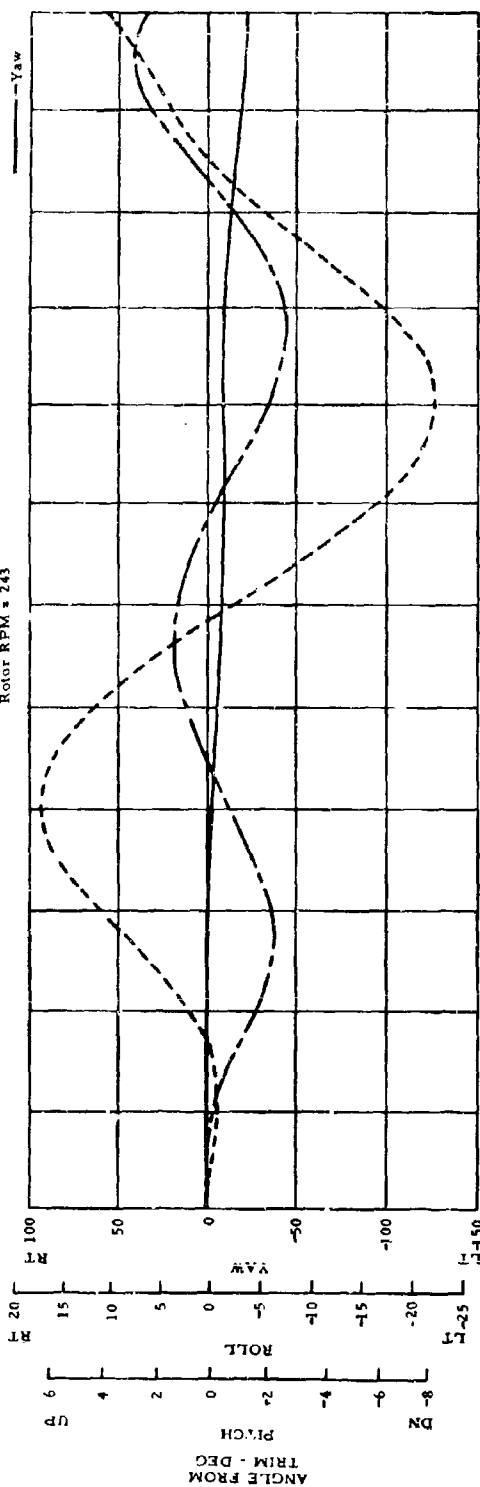


Figure 64. Aircraft Response to a Left Lateral Pulse Input in Hover.

Flt 39

GW = 13,400 lb

CG = Sta 298

$N_R = 103\%$

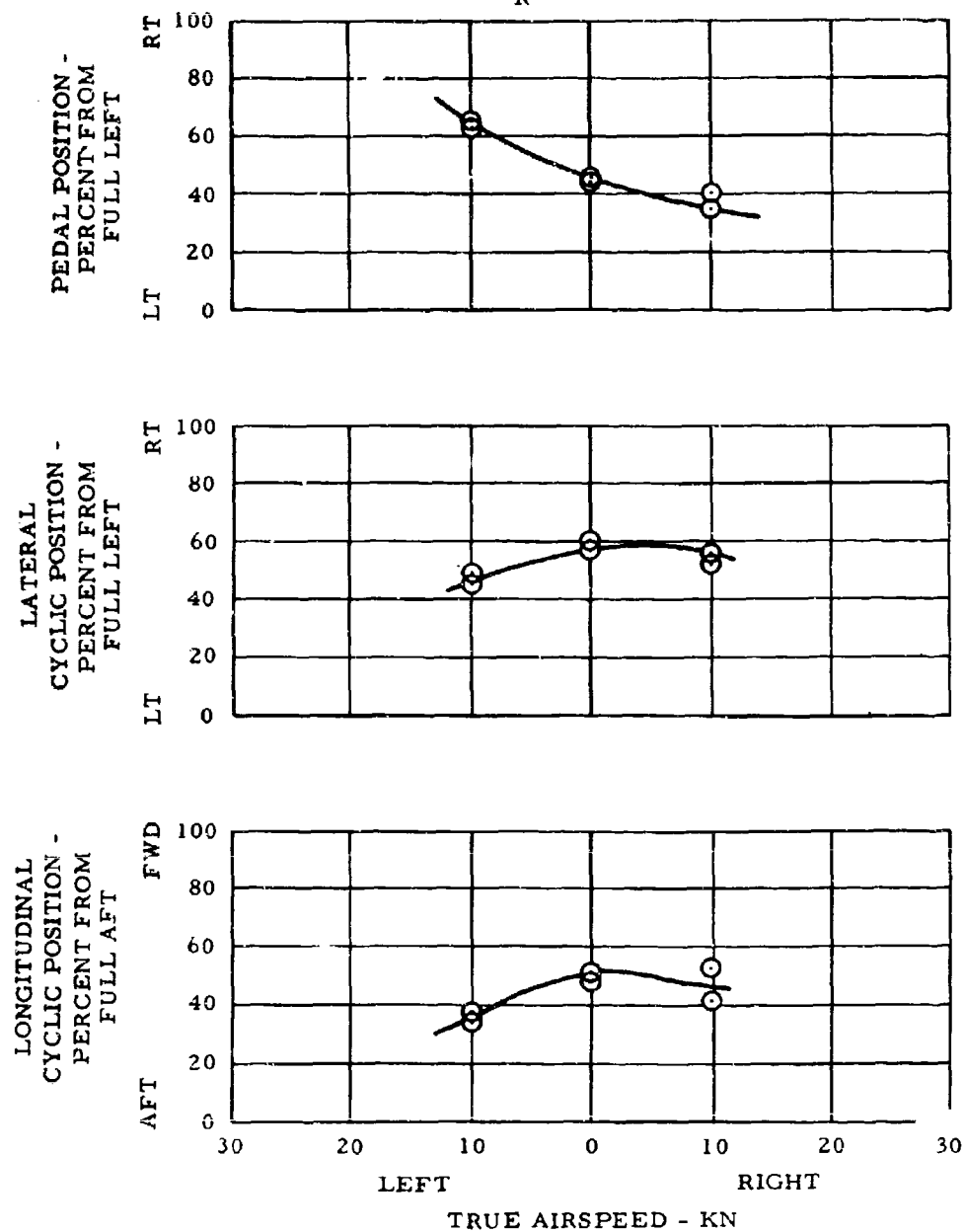


Figure 65. Control Positions in Sideward Flight.

trim. Improvement in speed stability could be obtained by increasing the nose-down incidence of the stabilizer. However, this would be at the expense of reduced forward stick margins at high speeds.

c. Static Lateral Directional Stability

Static directional stability and effective dihedral in level flight were investigated by recording the pedal positions and lateral stick positions required to maintain various magnitudes of sideslip angles at constant airspeeds. Results are presented in Figure 69. The XV-9A effective dihedral is approximately neutrally stable for sideslips to the left and unstable for sideslips to the right.

Figure 69 also shows that the aircraft is marginally stable directionally for sideslip to the right and unstable for sideslip to the left.

A preliminary investigation of the measured stabilizer loads was made in an effort to explain the reasons for the lack of directional stability. From steady level-flight sideslip tests, the stabilizer loads and sideslip angles were measured to determine the rate of change of stabilizer load with sideslip angles. With these measured parameters, the tail efficiency in forward flight was calculated as follows:

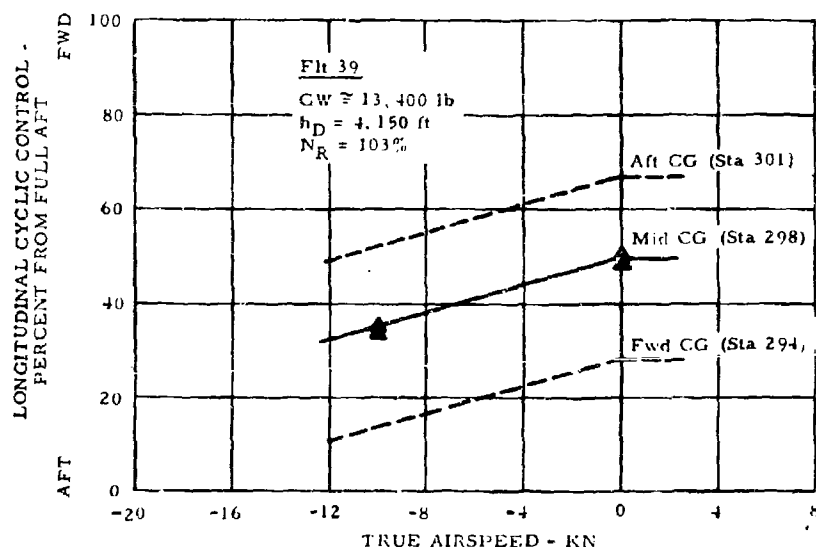


Figure 66. Rearward Flight Longitudinal Cyclic Control Position Versus Speed.

Flt	N _R	H	CG _{corr}	GW	Density Alt	Rudder Rigging
▲ 30	100%	2.5 deg	Sta 298	14,590 lb	4,000 ft	Rudder Surfaces 7 Deg Rt with Neut Pedals
● 38	101%	2.5 deg	Sta 294	14,375 lb	4,345 ft	Rudder Surfaces Neut with Neut Pedals
□ 39	102%	2.5 deg	Sta 301	13,930 lb	55,000 ft	Rudder Surfaces Neut with Neut Pedals

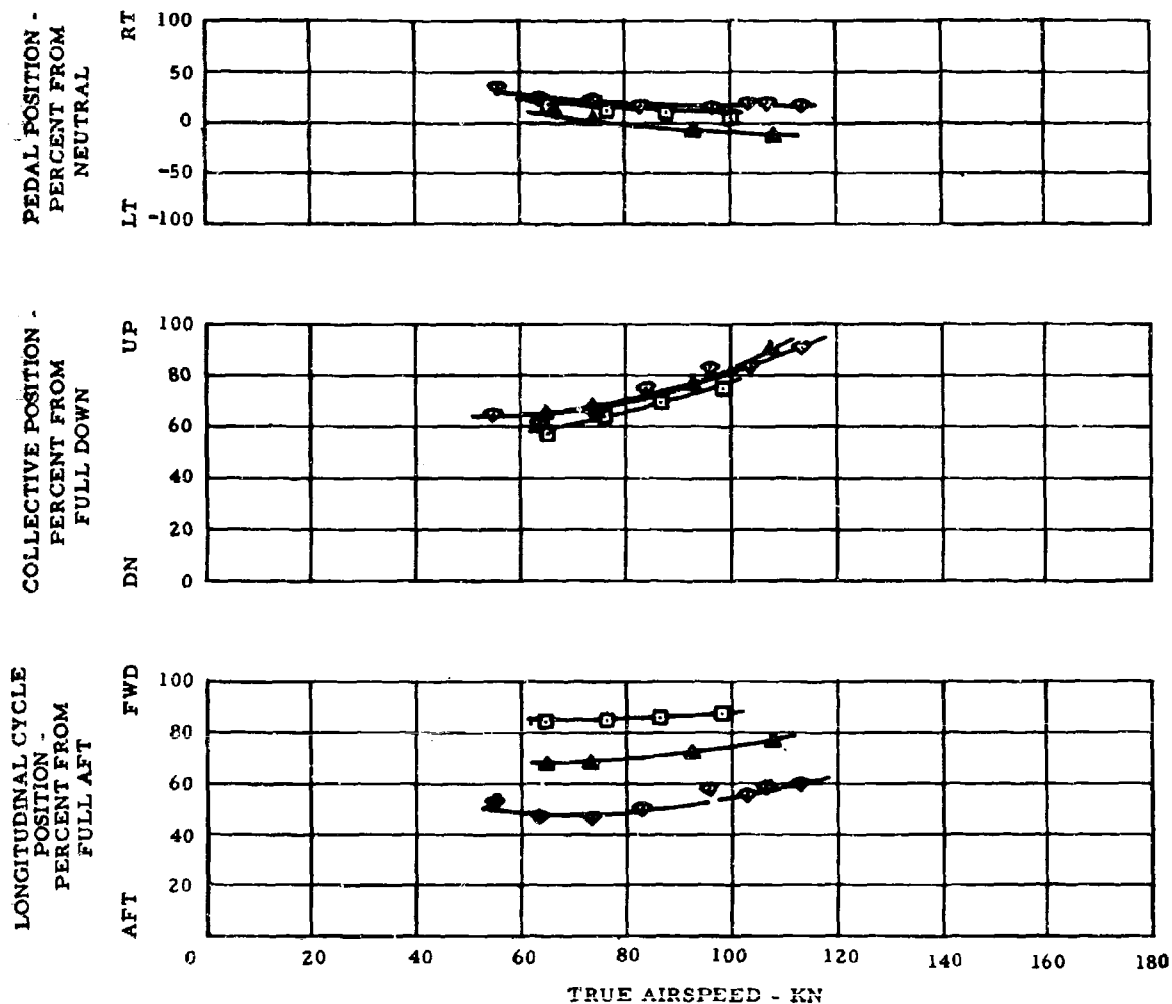


Figure 67. Level Flight Control Position Versus Airspeed.

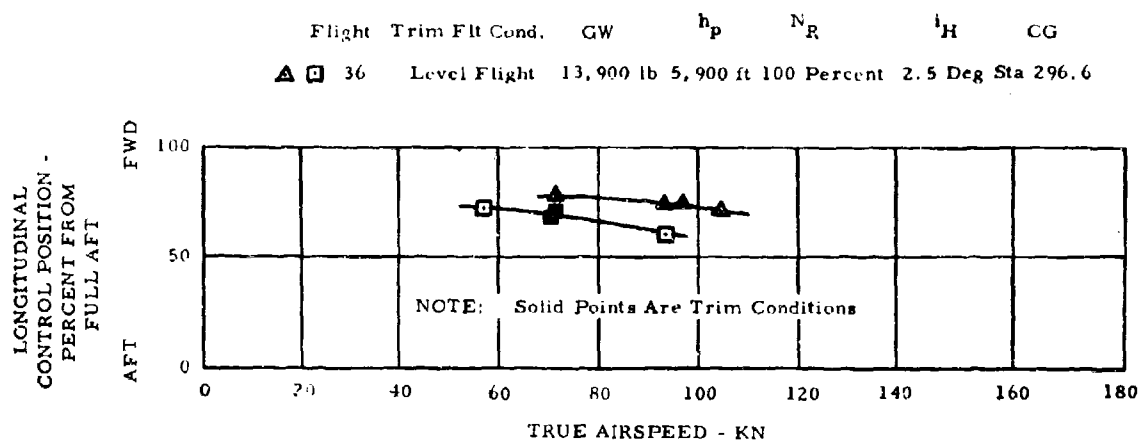


Figure 68. Speed Stability.

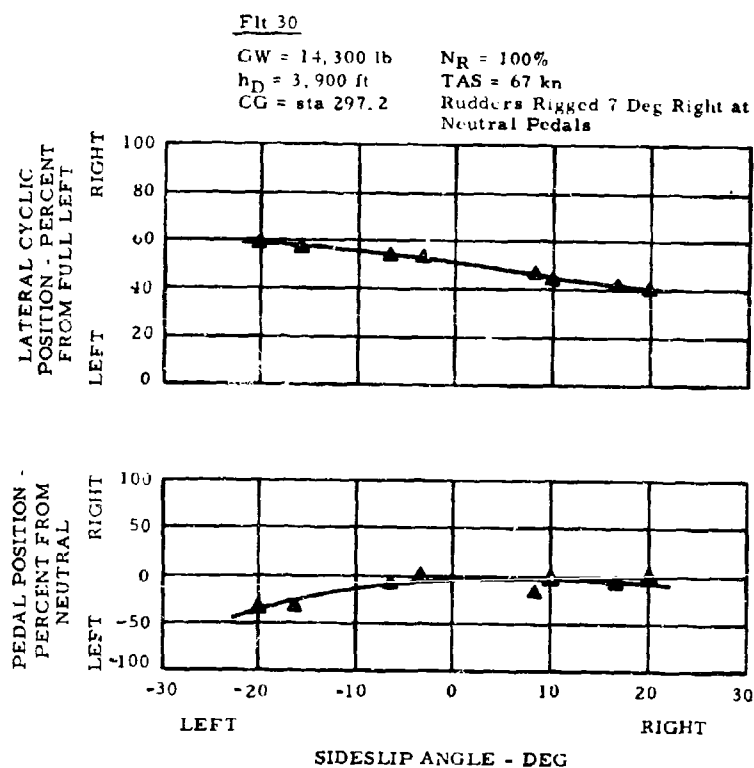


Figure 69. Static Directional Stability in Level Flight.

According to V-tail theory of Reference 10, the rate of change of the stabilizer side force with sideslip angles can be written:

$$\frac{\partial Y_t}{\partial \beta} = C_{L\beta N} K q \eta_t \left(1 + \frac{\partial \sigma}{\partial \beta}\right) S_t \sin^2 \Gamma$$

where:

$$\eta_t \left(1 + \frac{\partial \sigma}{\partial \beta}\right) = \text{tail efficiency factor}$$

$$C_{L\beta N} = \text{tail lift curve slope}$$

$$\Gamma = \text{V-tail dihedral angle}$$

$$K = \text{V-tail lift curve slope correction factor from page 3, Reference 10.}$$

With the above equation and the measured increments in stabilizer loads (normal to the surface) and sideslip angles from flight, the tail efficiency factor can be calculated as follows:

$$\eta_t \left(1 + \frac{\partial \sigma}{\partial \beta}\right) = \frac{\Delta Y_t / \Delta \beta}{C_{L\beta N} K q S_t \sin^2 \Gamma}$$

where:

$$\Delta Y_t = (\Delta Y)_{\text{measured}} \times \sin \Gamma$$

As an example case, from flight 26, during steady level-flight sideslips, TAS = 84.7 knots, $h_D = 3,830$ feet, the stabilizer loads and sideslip angles were measured as follows:

Record number 2017

$$\beta = +0.5 \text{ degree}$$

$$\text{rh stabilizer load} = 55.0 \text{ pounds}$$

Record number 2024

$$\beta = +6.96 \text{ degrees}$$

$$\text{rh stabilizer load} = 110.0 \text{ pounds.}$$

Thus:

$$\Delta \beta = 6.96 - 0.50 = 6.46 \text{ degrees}$$

$$\Delta Y_{\text{measured}} = 110.0 - 55.0 = 55 \text{ pounds, or}$$

$$\Delta Y_{\text{measured}} / \Delta \beta = 8.51 \text{ pounds/degree}$$

From the V-tail geometry

$$S_{\text{total}} = 54 \text{ square feet}$$

$$\text{taper ratio, } \lambda = 1.0$$

$$AR_{\text{geometry}} = 4.35$$

$$K = 0.714 \text{ (page 3, Reference 10)}$$

$$C_{L_{\beta N}} = 0.061 \text{ per degree}$$

$$\Gamma = 45 \text{ degrees.}$$

Stabilizer efficiency factor for the XV-9A in forward flight is calculated to be

$$\eta_t \left(1 + \frac{\partial \sigma}{\partial \beta} \right) = \frac{8.51}{(0.061)(0.714)(21.6) \left(\frac{54}{2} \right) \sin \Gamma}$$
$$= 0.475.$$

The above results indicated that the V-tail was less than 50 percent effective. The primary reason for this low effectiveness of the stabilizer can readily be seen when one examines the tuft photo of Figure 70, taken during flight at approximately 80-knot CAS. The stabilizer is operating in the region of low dynamic pressure created by the large flow separation at the rotor hub-pylon junction. A drag cleanup in the area of the rotor hub and pylon would undoubtedly improve the directional stability by a significant amount.

d. Damping in Roll

In this section, a theoretical calculation of damping in roll of the XV-9A free-floating hub rotor system is presented and is compared with the measured damping in roll. Only rotor damping in roll is presented here, because the measurements of damping in pitch are complicated by the damping contribution of the horizontal stabilizer and angle-of-attack stability effects. Rotor damping in pitch is essentially equal to rotor damping in roll. The theoretical method presented in Reference 11, modified to include the blade strap-windup effects presented in Reference 12, is used to calculate the damping in roll. Using equations (9) and (10) of Reference 11, modified to include blade strap windup effects, the damping in roll, L_p , can be calculated from the following equations.

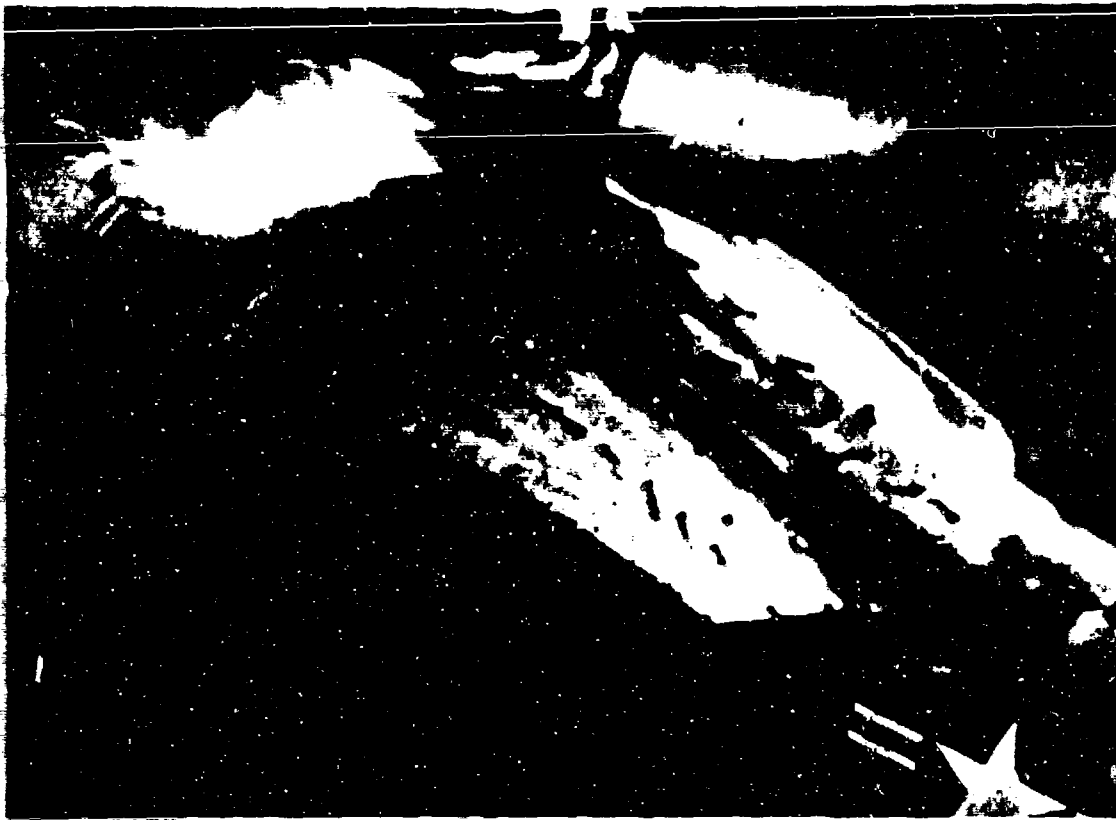


Figure 70. Tuft Behavior in Cruise Flight.

$$(L_p)_{\text{theory}} = Th_R \frac{\Delta b}{p} \left[1 + 1.5 \frac{\Delta b_1}{\Delta b'} \frac{cf}{T} \frac{S_1 S_2}{h_R l} \right]$$

where:

$$\frac{\Delta b'}{p} = -\frac{27}{\gamma \Omega} \left[1.0 - 0.29 \frac{\theta^{3/4}}{C_T \sigma} \right]$$

$$\frac{\Delta b'}{\Delta b_1} = \frac{3}{2} \left[1.0 - 0.29 \frac{\theta^{3/4}}{C_T \sigma} \right]$$

For the XV-9A rotor characteristics:

Gross weight	= 14,020 lb
Ω	= 25.44 rad/sec
γ	= 5.68

$$\begin{aligned}
 o &= 0.091 \\
 h_R &= 4.4 \text{ ft} \\
 \text{Centrifugal force} &= 130,766 \text{ lb/blade} \\
 \frac{S_1 S_2}{l} &= \frac{(0.488)(0.884)}{4.6} = 0.0937 \\
 \theta_{3/4 \text{ measured}} &= 6 \text{ deg} = 0.105 \text{ radian} \\
 \rho &= 0.0021 \text{ slug/cu ft}
 \end{aligned}$$

$$\frac{C_T}{\sigma} = \frac{14,020}{(0.0021)(2,375)(700)^2(0.091)} = 0.0632$$

$$\frac{\Delta b'_p}{p} = - \frac{27}{(5.68)(25.44)} \left[1.0 - 0.29 \left(\frac{0.105}{0.0632} \right) \right] = - 0.0965$$

$$\frac{\Delta b'_1}{\Delta b_1} = 1.5 \left[1.0 - 0.29 \left(\frac{0.105}{0.0632} \right) \right] = 0.778$$

Solving for the rotor damping in roll, L_p ,

$$\begin{aligned}
 (L_p)_{\text{theory}} &= - (14,020)(4.4)(0.0965) \left[1 + 1.5 \left(\frac{1}{0.778} \right) \left(\frac{130,766}{14,020} \right) \left(\frac{0.0937}{4.4} \right) \right] \\
 &= - 8,250 \text{ ft-lb/rad/sec.}
 \end{aligned}$$

A flight test measurement of damping in roll in forward flight was obtained from the recorded time history of a lateral cyclic step input shown in Figure 71. Inasmuch as the rolling moment due to the displacement of the lateral cyclic control from trim is balanced out by the damping in roll at the time of maximum rolling velocity (and, hence, zero angular acceleration), the measured damping in roll can be determined as follows:

$$(L_p)_{\text{measured}} = - Th_R \frac{(\Delta A_1)_{\text{measured}}}{(P_{\text{max}})_{\text{measured}}}$$

$$\text{Gross weight} = 14,020 \text{ lb}$$

$$h_R = 4.4 \text{ ft}$$

$$\text{Measured lateral cyclic control displacement} = 7.5 \text{ percent of total travel}$$

$$\text{Total lateral cyclic pitch displacement} = 14 \text{ deg}$$

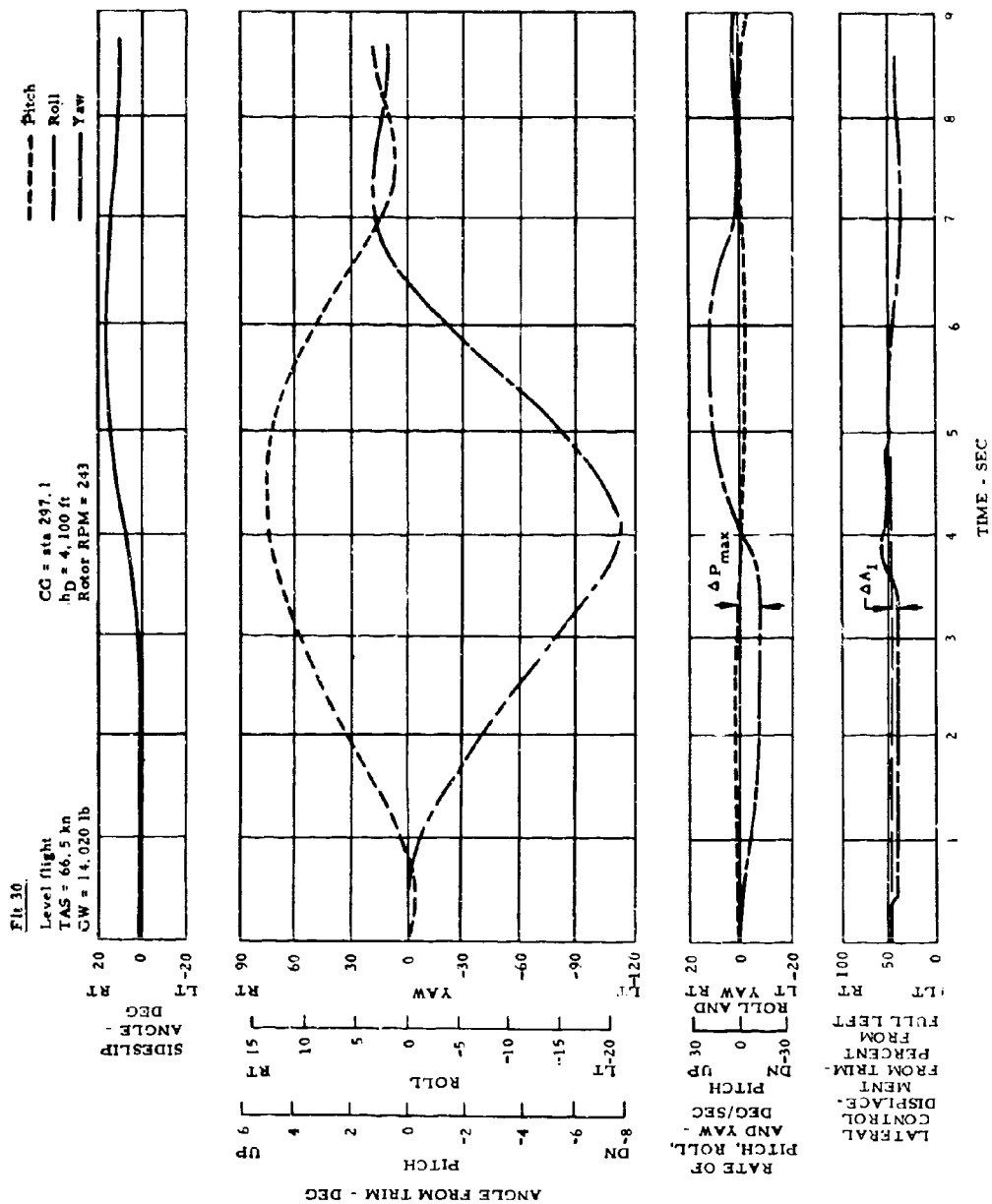


Figure 71. Aircraft Response to a Left Lateral Step Input in Level Flight.

$$(\Delta A_1)_{\text{measured}} = (7.5 \text{ percent}) \times (14) = 1.05 \text{ deg}$$

$$(P_{\text{max}})_{\text{measured}} = 8 \text{ deg/sec}$$

$$\begin{aligned} (L_p)_{\text{measured}} &= - (14,020)(4.4) \left(\frac{1.05}{8} \right) \\ &= - 8,110 \text{ ft-lb/rad/sec} \end{aligned}$$

The excellent agreement between theory and measured roll damping indicates that the theoretical method of calculating rotor damping can be used to predict accurately the rotor damping of the free-floating hub rotor system.

e. Dynamic Stability

Figures 72, 73, and 74 show the helicopter motion following longitudinal, lateral, and directional control pulse inputs at approximately 80-knot TAS. As can be seen from Figure 72, the longitudinal dynamic characteristics of the XV-9A following a pull and return control displacement meet the MIL-H-8501A requirements that the aircraft's normal acceleration shall not deviate from 1.0 g by 0.25 g within 10 seconds from the start of the disturbance. The actual helicopter motion about the pitch, roll, and yaw axes following a control pulse input is a slow, divergent, oscillating motion. As discussed previously, substantial improvement in forward flight stability, both static and dynamic, could be realized by minimizing the large flow separation at the rotor hub-pylon junction and, hence, by improving the effectiveness of the stabilizers.

4. Climb

a. Longitudinal Static Stability

Figure 75 presents the measured longitudinal cyclic and collective control positions versus airspeed in climb. Results show that the slope of the stick position versus speed is slightly unstable. A nose-down change in stabilizer incidence would provide improved speed stability. As can be seen, there is adequate margin of longitudinal cyclic control. Some increase in collective control travel would be desirable.

b. Lateral Directional Stability

The directional stability and effective dihedral in climb were obtained by first trimming the helicopter at the desired climb speed

FIG 72

Level Flight
 GW = 13,870 lb
 CG = Sta 297.4
 $\bar{h}_D = 8.500$ ft
 Rotor RPM = 243

----- Pitch
 ----- Roll
 ----- Yaw

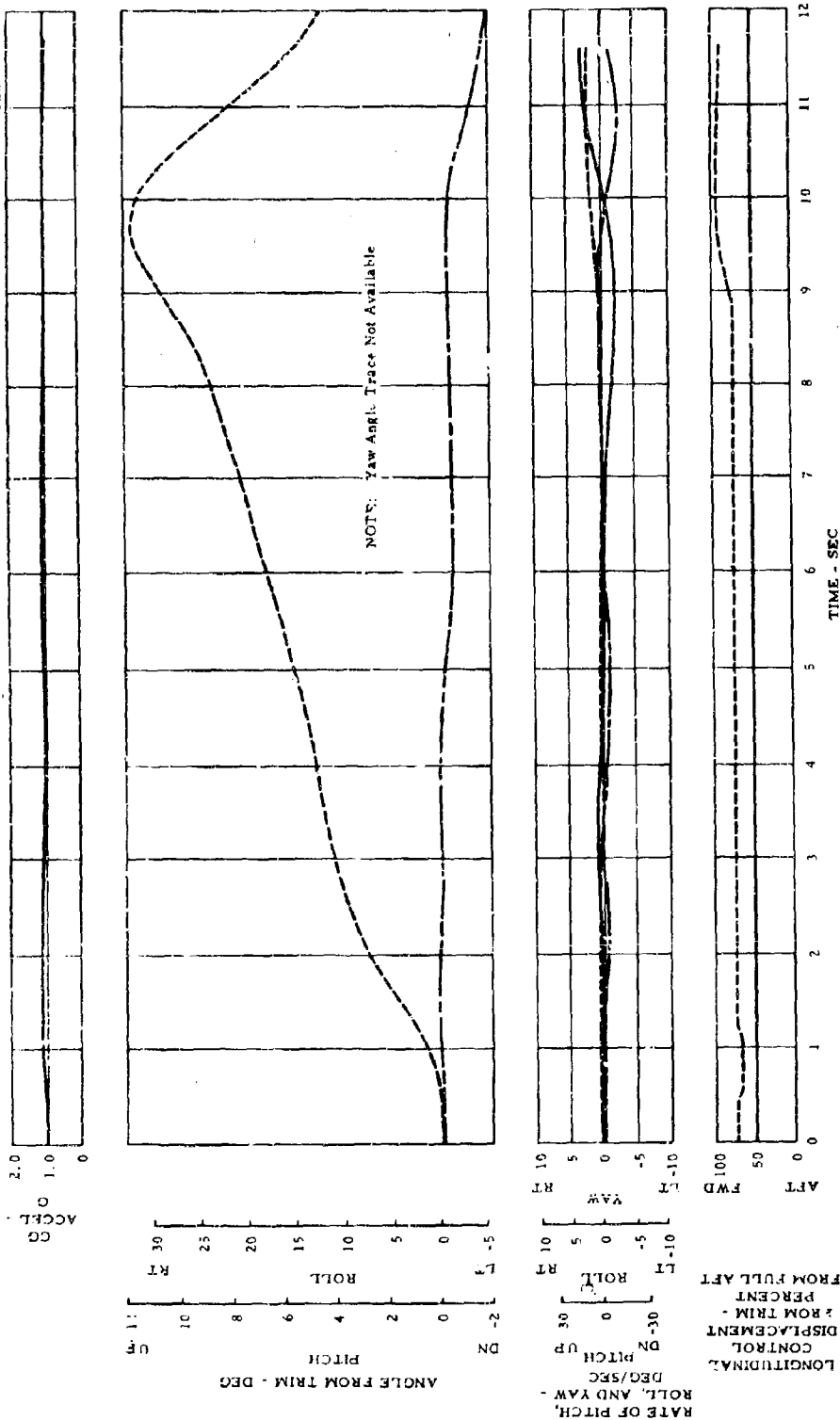


Figure 72. Aircraft Response to an Aft Longitudinal Pulse Input in Level Flight.

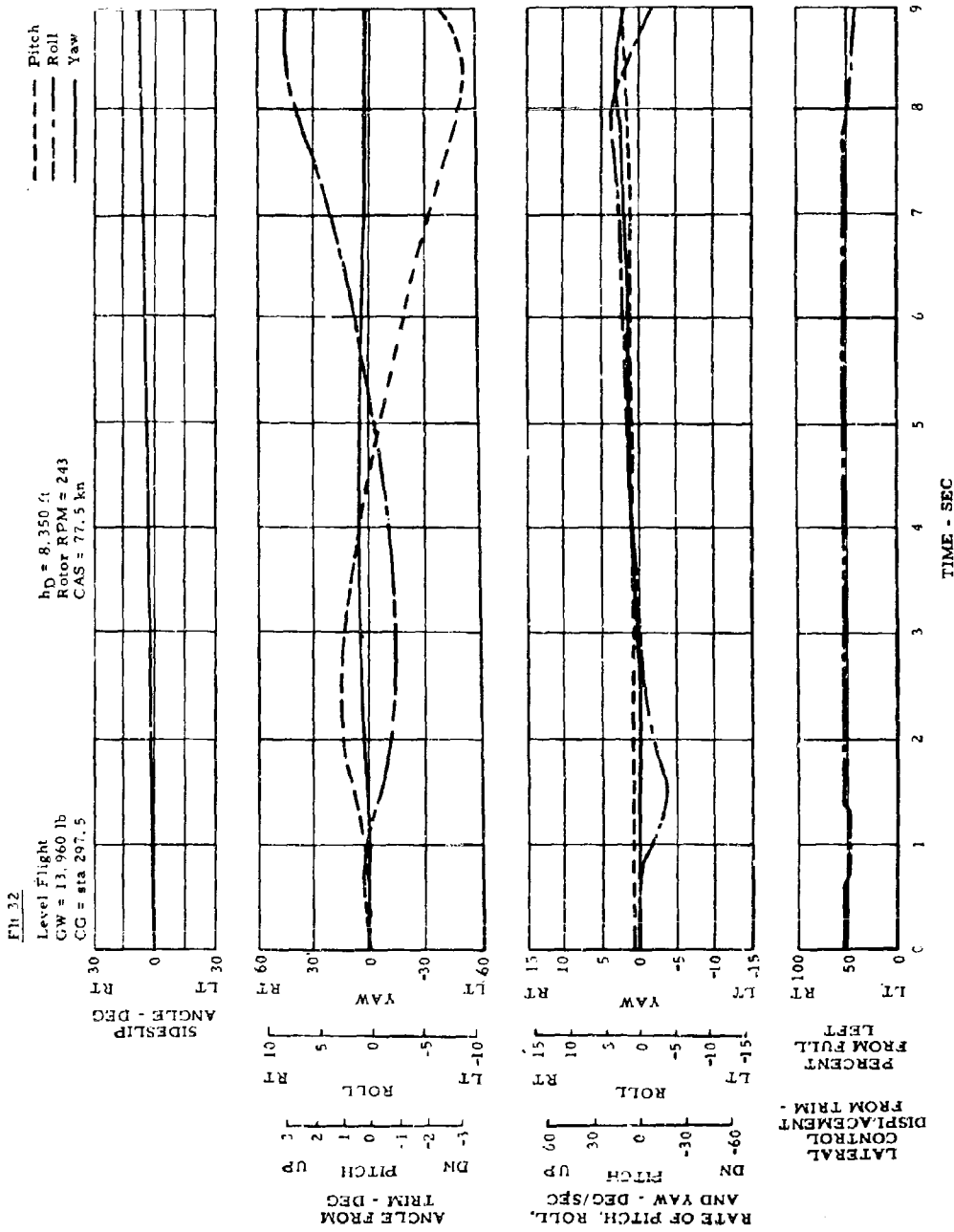


Figure 73. Aircraft Response to a Left Lateral Pulse Input in Level Flight.

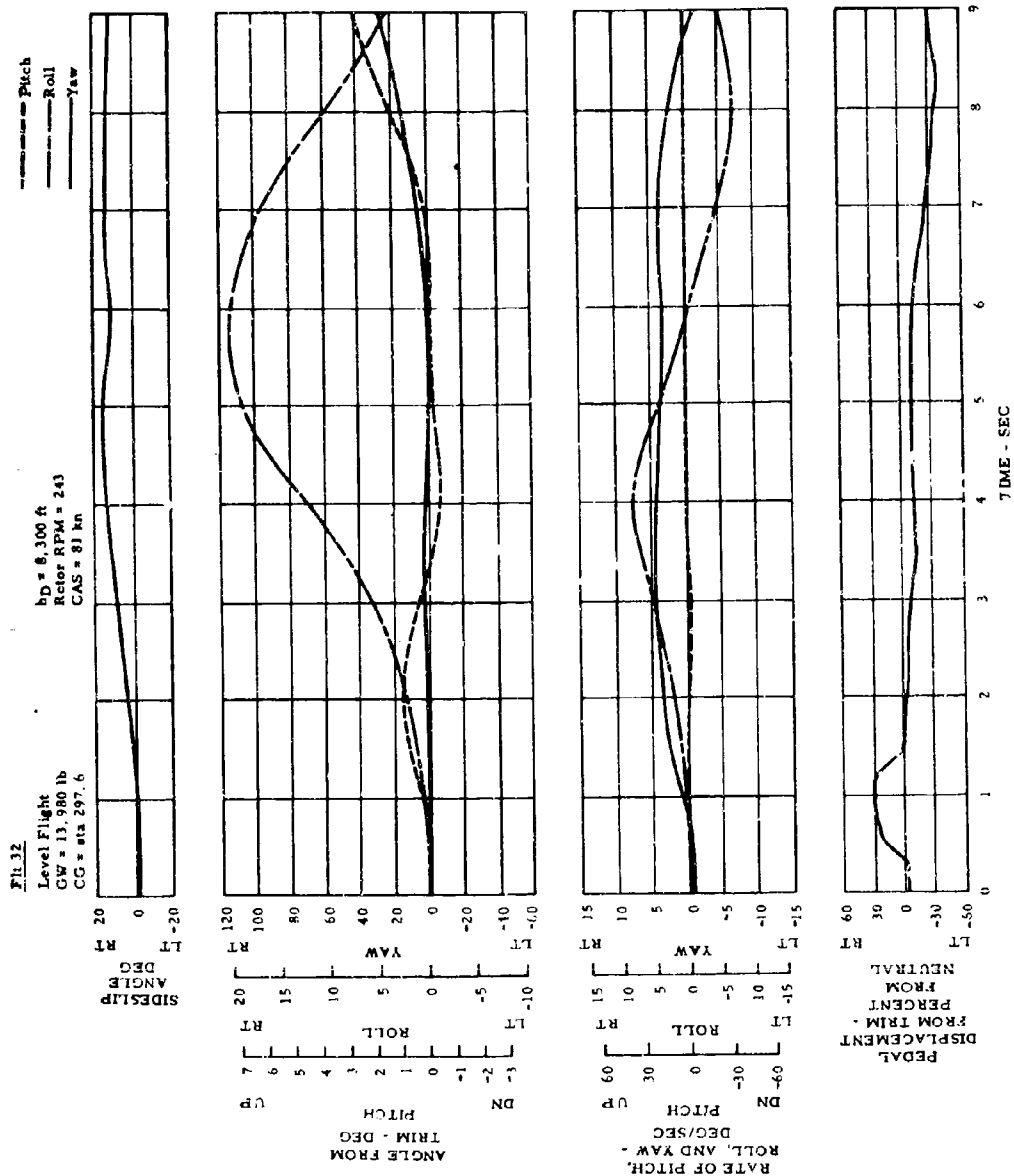


Figure 74. Aircraft Response to a Right Pedal Pulse Input in Level Flight.

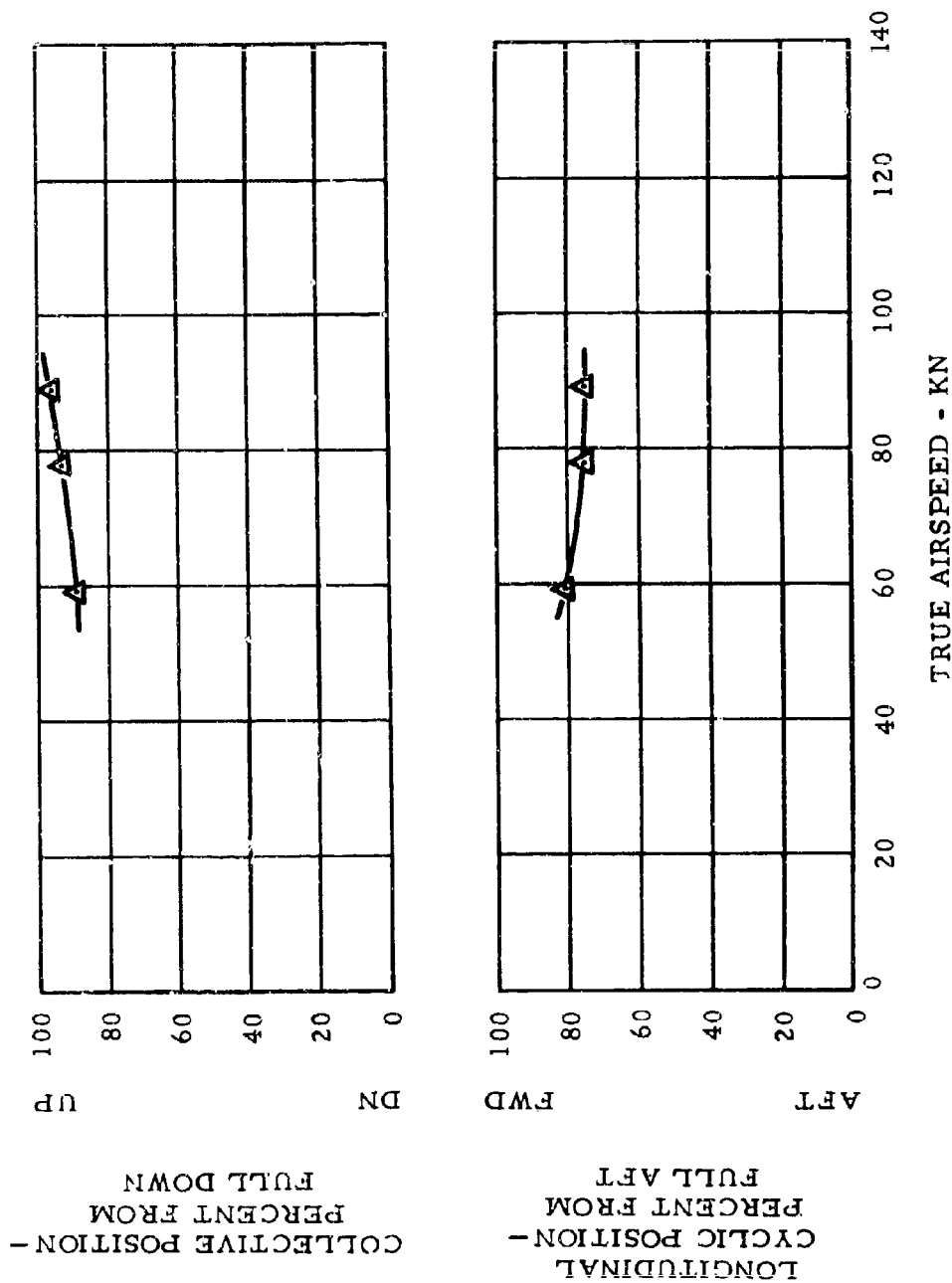


Figure 75. Control Position Versus Airspeed in Climb.

and then yawing the aircraft slowly in one direction and then in the other. The pedal positions, lateral stick positions, and sideslip angles were then read at the points of zero yaw angular acceleration (the helicopter is approximately trimmed in yaw at these points). The results are presented in Figure 76. Data show that the aircraft is marginally stable directionally for the limited right sideslip angles tested. For left sideslip angles, some directional instability appears to occur.

The effective dihedral is slightly unstable. A drag cleanup as discussed previously would improve the climb lateral directional stability.

5. Descent

a. Longitudinal Static Stability

Only qualitative evaluation of the longitudinal static stability in descent is discussed here, since the aircraft was flown at only what was considered to be the best descent airspeed (60-knot CAS).

In steady descents, the measured longitudinal cyclic stick position was approximately 54 to 57 percent from full aft. The aircraft static longitudinal stability in descent was qualitatively observed by the pilot to be unstable. A nose-down change in stabilizer incidence would improve the static longitudinal stability.

b. Lateral Directional Stability

The static directional stability and effective dihedral in descent were obtained by a method similar to that used in determining the lateral stability in climb. The results are presented in Figure 77 for two preset rudder surface positions. For flight 35, the rudder surfaces were rigged 7 degrees to the right with neutral pedals. As stated previously, this rigging, which was used throughout most of the flight test program, resulted in minimum yaw valve opening (best performance) during cruise flight. However, in descent this rudder rigging resulted in excessive left pedal. For flight 38, the rudder surfaces were rerigged to be neutral at neutral pedal. This rigging reduced the left pedal requirement during descent from approximately 50 percent to 20 percent left pedal from neutral.

The static directional stability in descents for both rudder riggings is unstable for sideslip angles to the left and neutrally stable for

Flight N_R CG CW TAS h_p Flt Configuration
 Δ 36 100% Sta 298 14,920 lb 70 kn 3,370 ft Rudders Rigged 7 Deg
 Right at Neutral Pedals

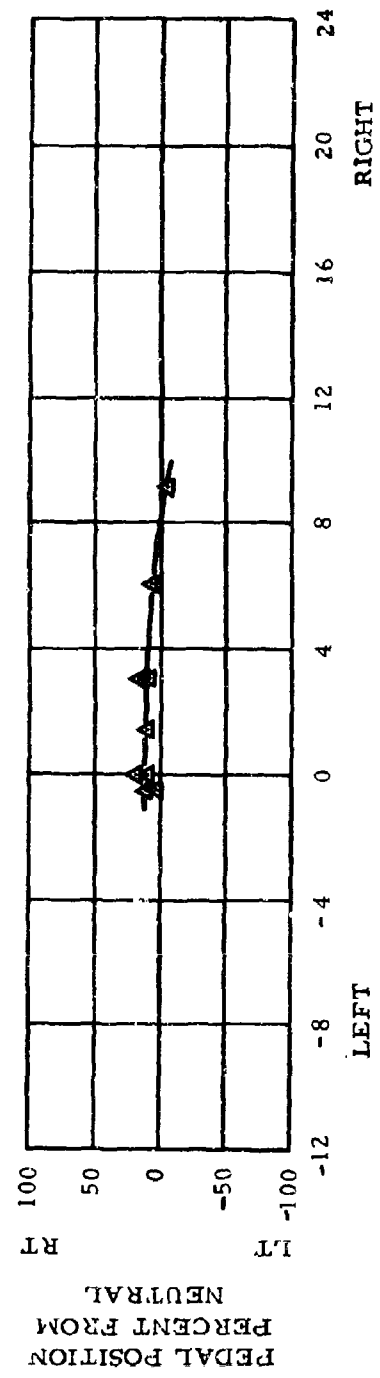
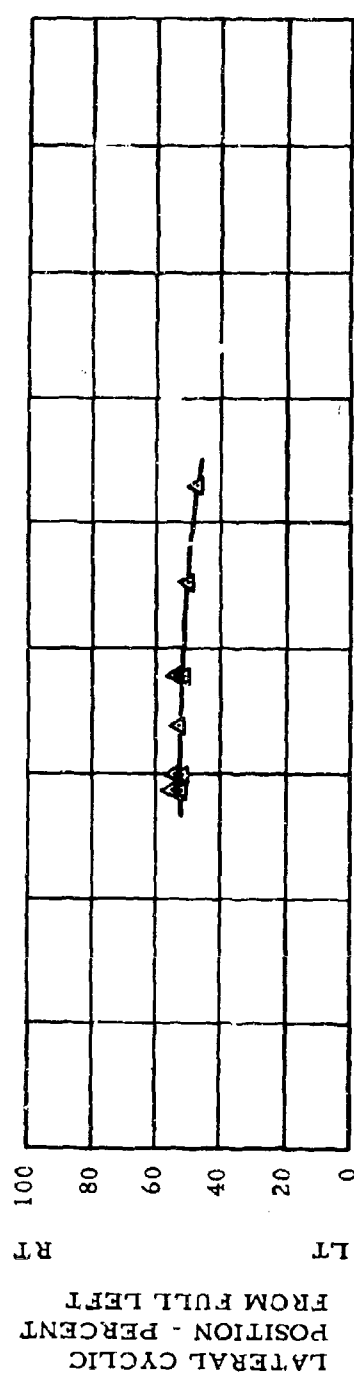
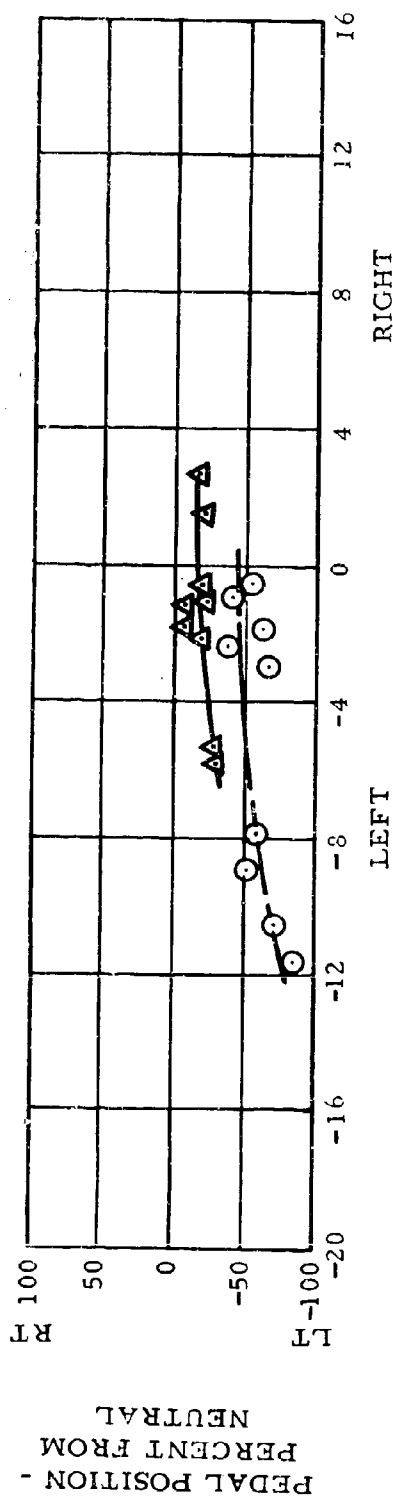
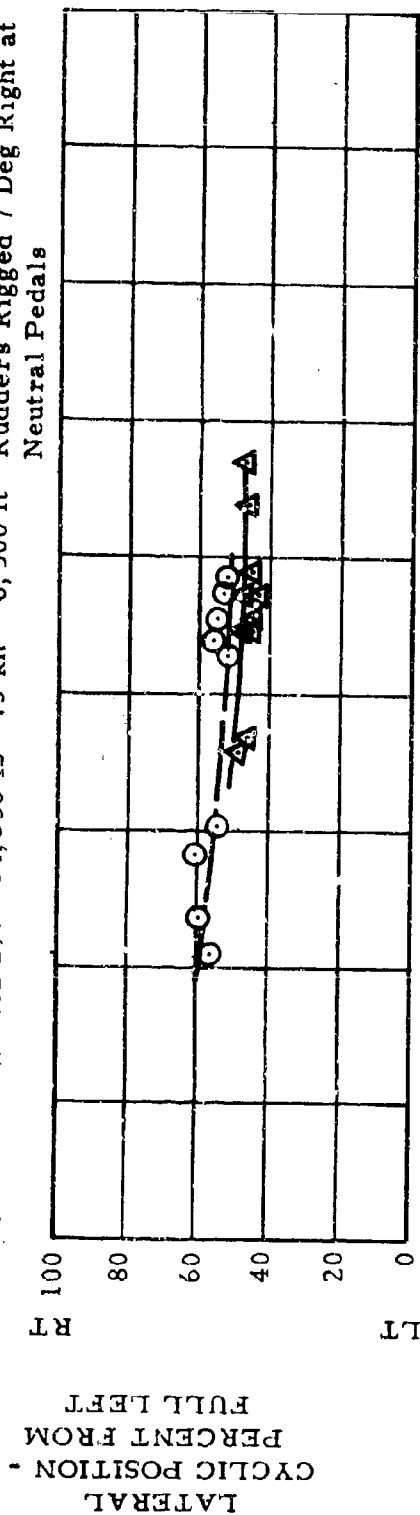


Figure 76. Static Directional Stability in Climb.

Flt	N _R	CG	GW	TAS	h _p	Flt Configuration
Δ 38	100%	Sta 295	13,130 lb	75 kn	7,920 ft	Rudders Neut When Pedals Neut
○ 35	100%	Sta 297	14,350 lb	73 kn	6,500 ft	Rudders Rigged 7 Deg Right at Neutral Pedals



SIDESLIP ANGLE - DEG

Figure 77. Static Directional Stability in Descent.

sideslip angles to the right. The effective dihedral is slightly unstable.

The required improvement in lateral stability, as discussed previously, could be obtained by reducing the large flow separation ahead of the tail area at the pylon-hub junction.

6. Vibration

Figure 78 presents vibratory acceleration at the center of gravity, and Figure 79 presents vibratory acceleration on the structure near the pilot's seat. For these stabilized level flight points, there is no increase in vertical or lateral vibratory acceleration at the center of gravity as airspeed increases. Cyclic lateral acceleration at the pilot's seat remains at the same level over the range of speeds flown. The cyclic vertical acceleration at the pilot's seat begins to rise at speeds above 100 knots.

Vibratory vertical accelerations at the center of gravity reached slightly higher levels during transition to forward flight and full-power climb (± 0.63 g), 20-degree banked turns at 80 knots (± 0.50 g), and flare maneuvers (0.65 g). Vibratory vertical accelerations at the pilot's seat were slightly higher for the same maneuvers also, reaching ± 0.40 g during transition and climb, ± 0.35 g during the 20-degree banked turns, and ± 0.50 g during flare maneuvers.

As noted in Reference 1, although the magnitude of the vibratory acceleration at the pilot's seat is higher than specified in MIL-H-8501A, vibrations measured on structure, as these were, tend to be higher than those felt by the pilot. Also, a fuselage resonance near 3 per rev (12 cps) of the rotor was noted during shake tests reported in Reference 1. The majority of the high vibratory accelerations noted in this program were at this frequency.

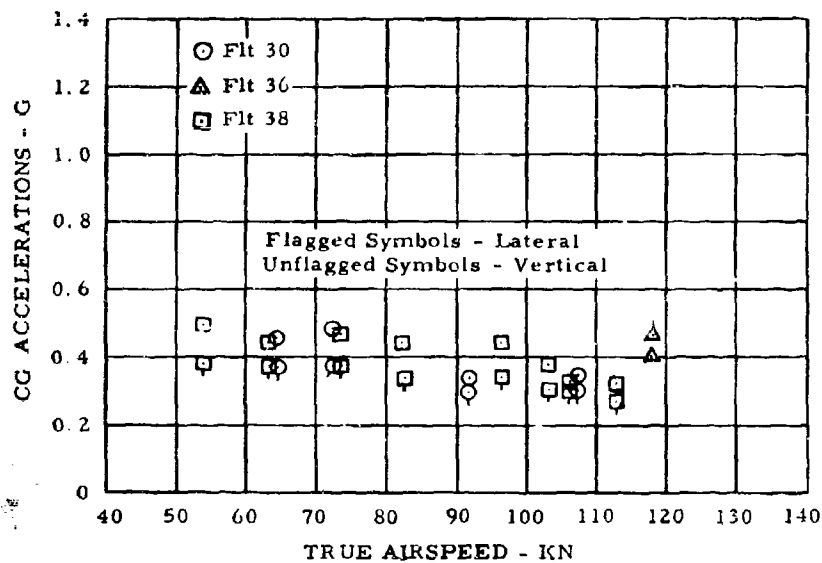


Figure 78. Typical Vibratory Accelerations at Center of Gravity Versus True Airspeed.

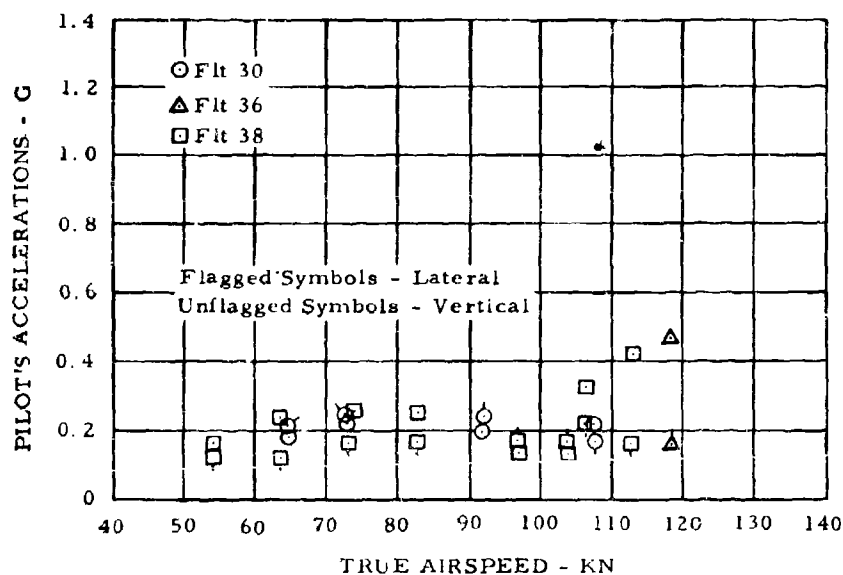


Figure 79. Typical Vibratory Accelerations at Pilot's Seat Versus True Airspeed.

ROTOR SYSTEM TETHER TESTS

INTRODUCTION

The rotor system tether tests were run to determine the performance of individual Hot Cycle rotor components, including blade tip-cascade nozzle velocity coefficient and flow coefficient and rotor-blade ducting pressure drop.

TEST SETUP

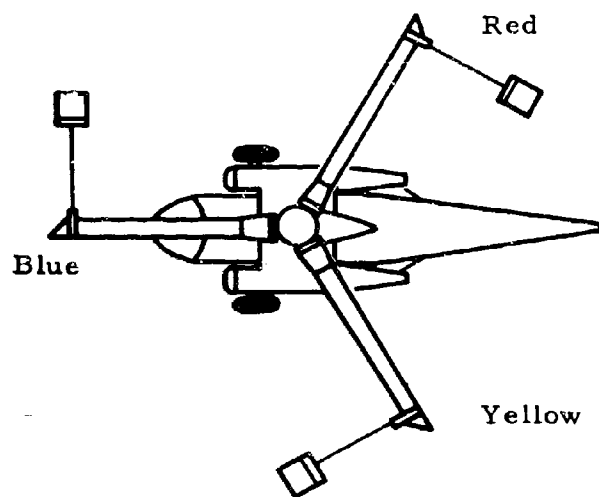
The test setup (Figures 80 and 81) was designed to measure the tip thrust as a function of engine power with the rotor held stationary. The rotor was restrained by a tether system consisting of one load-bearing strap around each blade (at blade station 308) attached to a load cell that was in turn anchored to a large forklift truck. The tip total pressure and temperature and static pressure drop along the rotor blade ducts were of major interest. The duct static pressure was measured at five stations along the blue blade by installing a pressure tap into the cavity formed where segments are connected by a flexure. The pressure leaks into this cavity through the lap joint between the blade ducts of the two segments. This cavity was normally sealed from the atmosphere, so it formed an ideal plenum chamber for obtaining an accurate average duct static pressure.

Duct centerline total pressure and total temperature at the tip nozzle entrance were measured by the probes used during the flight program.

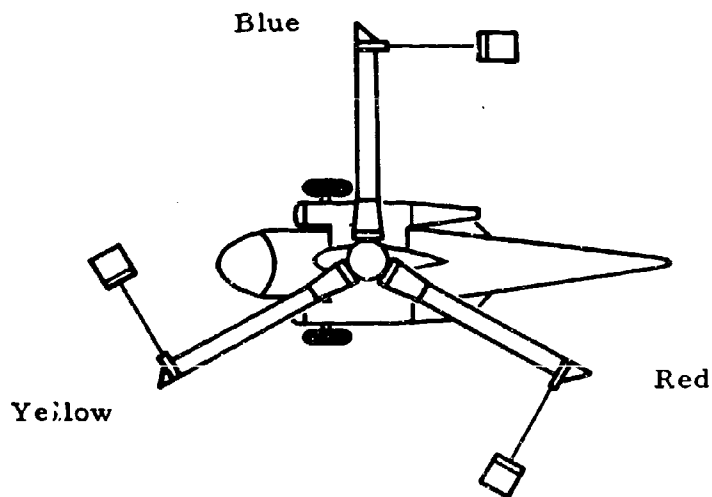
The yaw-control valve was sealed off to eliminate any loss of gas due to the built-in leakage that is present when the valve is in the closed position.

The rotor-blade leading and trailing-edge fairings, along with the nacelle cowlings, were removed to provide cooling for testing. A water sprinkling system was set up as a precaution in case overheat problems might be encountered during a test run. The fuselage and power module area were cooled by a large air blower that forced outside air up the center of the aircraft through the hatch in the fuselage just below the rotor.

During the test program, two blade-root configurations were used. The first system (runs 1, 4, and 5) was essentially a normal setup with the blades resting on their droop stops and the hub free to rotate. With this setup it was not possible to measure the individual blade thrust because a moment could be carried through the blade root to the hub and into the blade root of another blade.

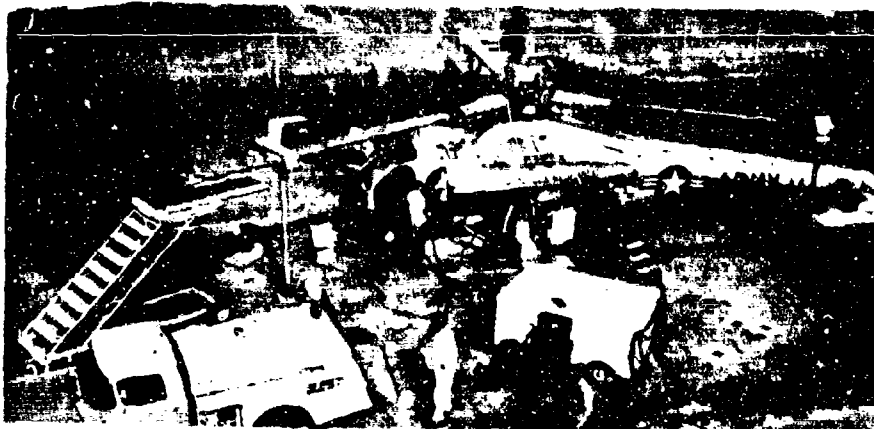


Runs 1, 2, and 3



Runs 4 and 5

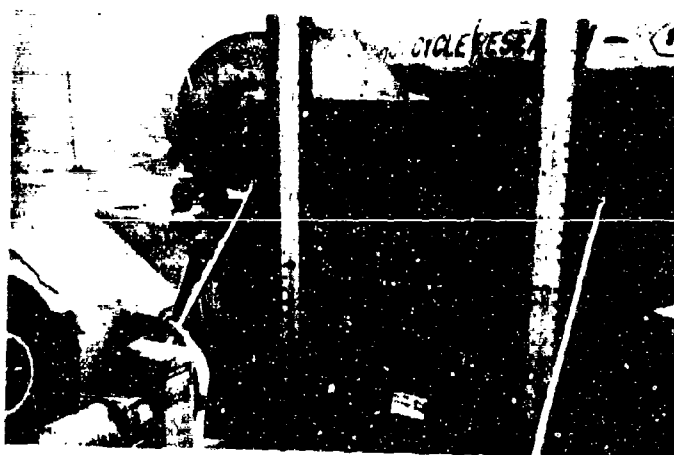
Figure 80. Tether Test Blade Orientation.



Overall Test Setup



Typical Tether Sling and Load Cell



Exterior Photo Panel Setup

Figure 81. Tether Test Setup.

The second system (runs 2 and 3) was devised to allow measurement of individual blade tip thrust. The droop stops were removed, allowing the entire weight of the blade root end to rest on the freely pivoting feathering ball. In this configuration, the blade could be orientated about the lead-lag axis so both retention straps were slack and unable to carry any load. With the straps unable to carry any load, the only moment that could be carried between the blade root and the hub was feathering ball friction about the lead-lag axis. The hub was locked to prevent rotation caused by the horizontal shear at the feathering ball that is the result of the tip restraint being located slightly inboard of the tip jet.

Diverter valve leakage was measured during the last two test points of run 5, so this information could be used in correcting gas flow to the rotor blades.

TEST PROCEDURE

The engines were started in the overboard position and then diverted to the rotor and accelerated to a predetermined power setting. Setting the power required approximately 1 minute; taking the data, another minute. These 2-minute runs were possible without overheating the propulsion system. After each test point, the gas flow was switched overboard for approximately 5 minutes to allow the rotor system to cool.

During each test point in a run, data were manually recorded from the outside photopanel in order that a running check could be kept on system performance. A summary of test runs is shown on Table VI.

TEST INSTRUMENTATION

The following equipment was used to record the parameters shown in Table VII:

- One photopanel installed in the aircraft for display of engine parameters

- One photopanel located outside the aircraft for display of rotor blade pressure data

- Three strain-gage indicators measuring blade tip-thrust load cell data

- One temperature indicator and switching unit for monitoring blade and propulsion system temperatures.

TABLE VI
ROTOR SYSTEM TETHER TEST SUMMARY

Date	Run Number	Engine 1 (S/N027-1A) Run (Hours)	Engine 2 (S/N101-3A) Run (Hours)
10-12-65	1	00:21	00:20
10-13-65	2	02:40	02:36
10-14-65	3	01:33	01:30
10-18-65	4	01:38	01:36
10-19-65	5	01:13	01:09
Cumulative Total		37:04	72:42

TABLE VII
ROTOR SYSTEM TETHER TEST INSTRUMENTATION PARAMETERS

Item	Number of Parameters	Visual	Photopanel	Brown Recorders
Tip thrust	3	Balance Box		
Tip gas temperature (blue blade only)	2 avg	Meter	Meter	Thermocouples
Tip gas total pressure	2/blade		Gage	
Blue-blade duct static pressure, stations 116, 166, 216, 266, and 310	5	Gage	Gage	
Turbine out temperature	2	Gage	Gage	
Turbine out pressure	2	Gage	Gage	
Compressor out pressure	2		Gage	
Compressor out temperature	2		Gage	
Engine rpm	2	Tachometer	Tachometer	
Engine inlet temperature	2	Thermometer		Thermocouples
Fuel flow	2	Turb Meter	Turb Meter	

TEST RESULTS

The results of the rotor system tether tests can be divided into two categories -- blade-tip cascade performance and duct pressure recovery. The test results are discussed under those headings. The test data are summarized in Tables VIII and IX.

Blade-Tip Cascade Performance

Aerodynamic performance of the blade-tip cascades can be studied most readily in terms of velocity coefficient, C_V , flow coefficient, C_W , and thrust coefficient, C_F , as presented in Figures 82, 83, and 84, respectively. In each of these figures, the axes are chosen for ease of plotting test results and a background of constant coefficient lines is provided. This technique makes it possible to plot data while the test is still in progress so that any ambiguities can be explored before the setup is changed.

Since the three nozzle coefficients are interrelated through the equation $C_F = C_V \times C_W$, once faired values are selected for two of the coefficients, the third value is fixed. The three values selected in Figures 82, 83, and 84 offer the best available simultaneous fairing of all three data sets. These values are as follows:

$$C_V = 0.94$$

$$C_W = 0.99$$

$$C_F = 0.93$$

The implications of these coefficients in terms of overall rotor system performance are discussed in a later paragraph of this section.

Duct Pressure Recovery

Measurement of duct average static pressures at five stations along the blue blade permits a direct evaluation of blade duct friction factor, as illustrated in Figure 85. Once again, a presentation is chosen for ease of data plotting, with the more complicated calculational procedures confined to the preparation of background grids. Based on direct measurements of duct area and cascade throat area, a duct Mach number of 0.39 is predicted at the rotor tip, and the background grid of Figure 85 is based on this value. The static pressure data confirm the duct Mach number of 0.39 and further indicate a friction coefficient, f , of 0.003 -- a value that is entirely consistent with the Reynolds number and smoothness of the XV-9A ducts. For $f = 0.003$ and $M = 0.39$, the duct total

TABLE VIII

[illegible]

TABLE IX

*In. He abe.

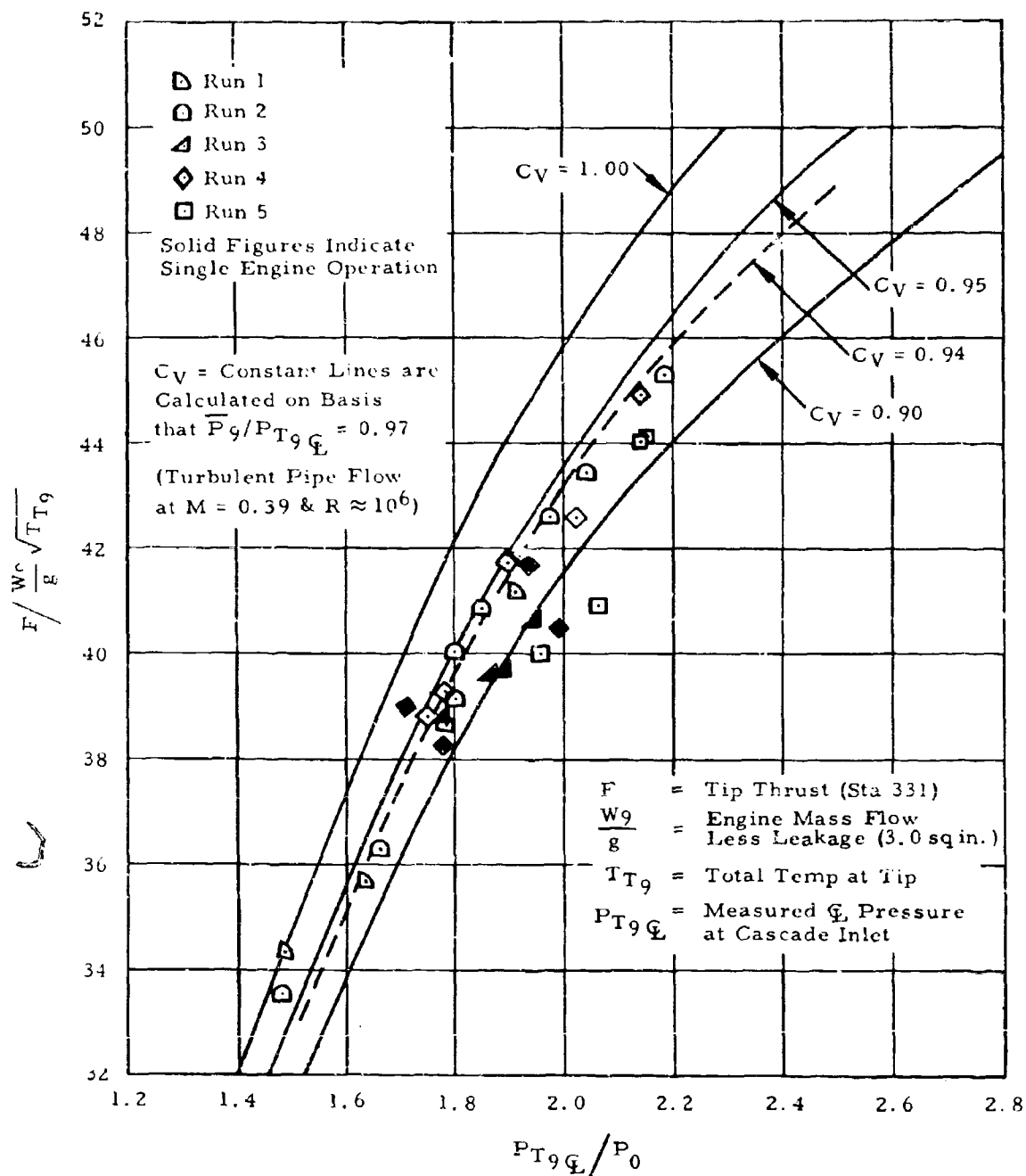


Figure 82. Tether Test Velocity Coefficient.

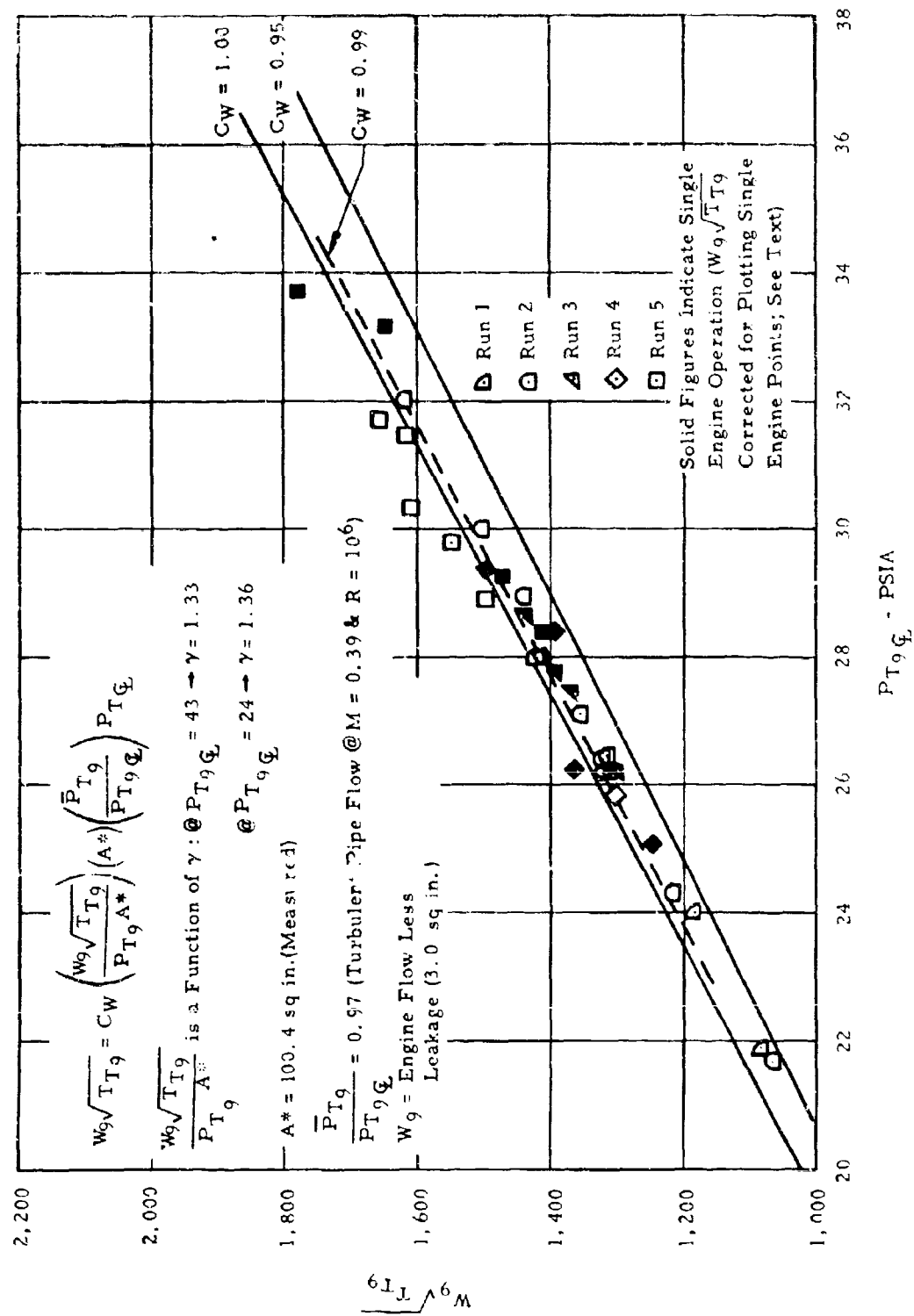


Figure 83. Tether Test Flow Coefficient.

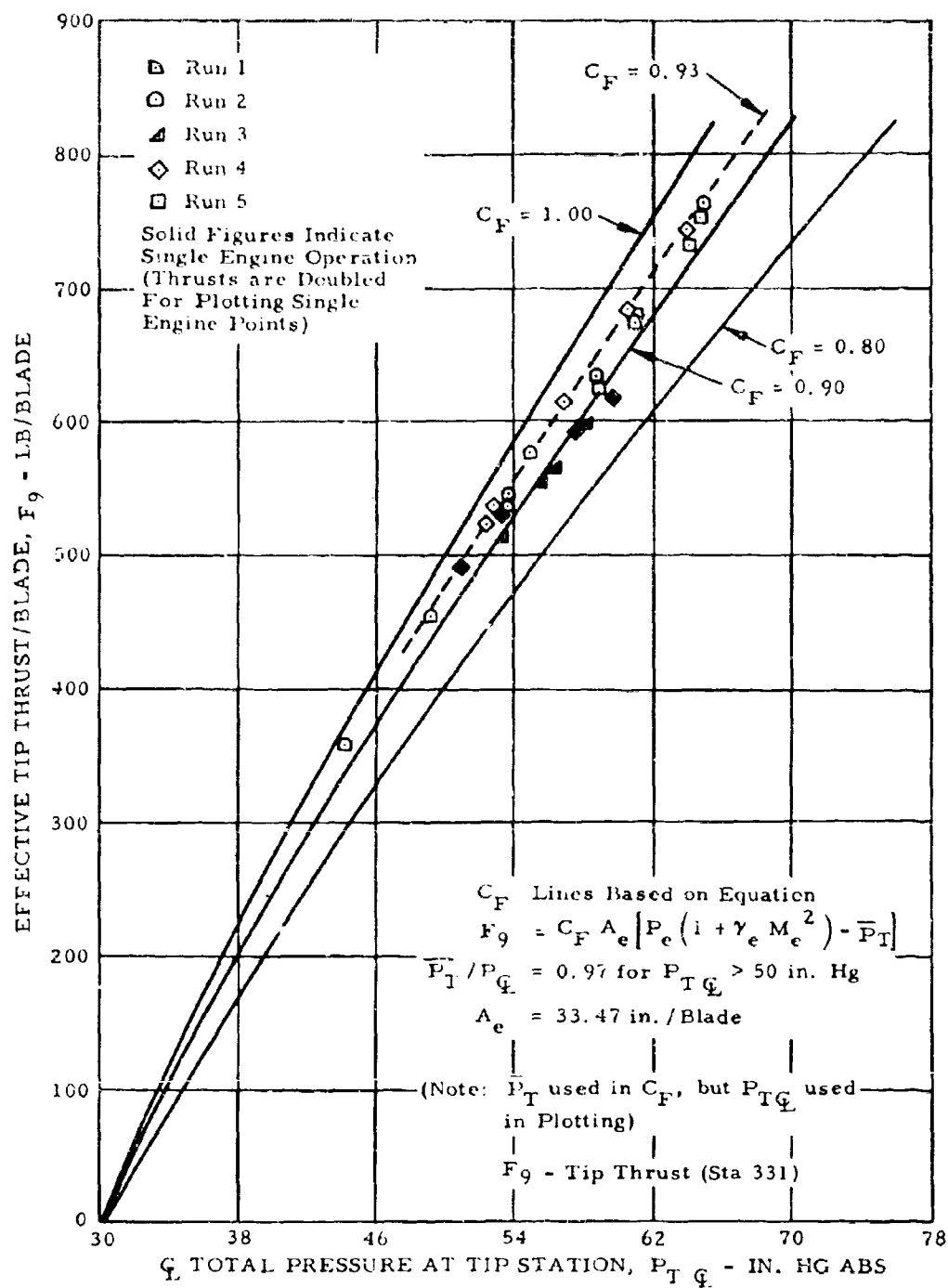


Figure 84. Tether Test Thrust Coefficient.

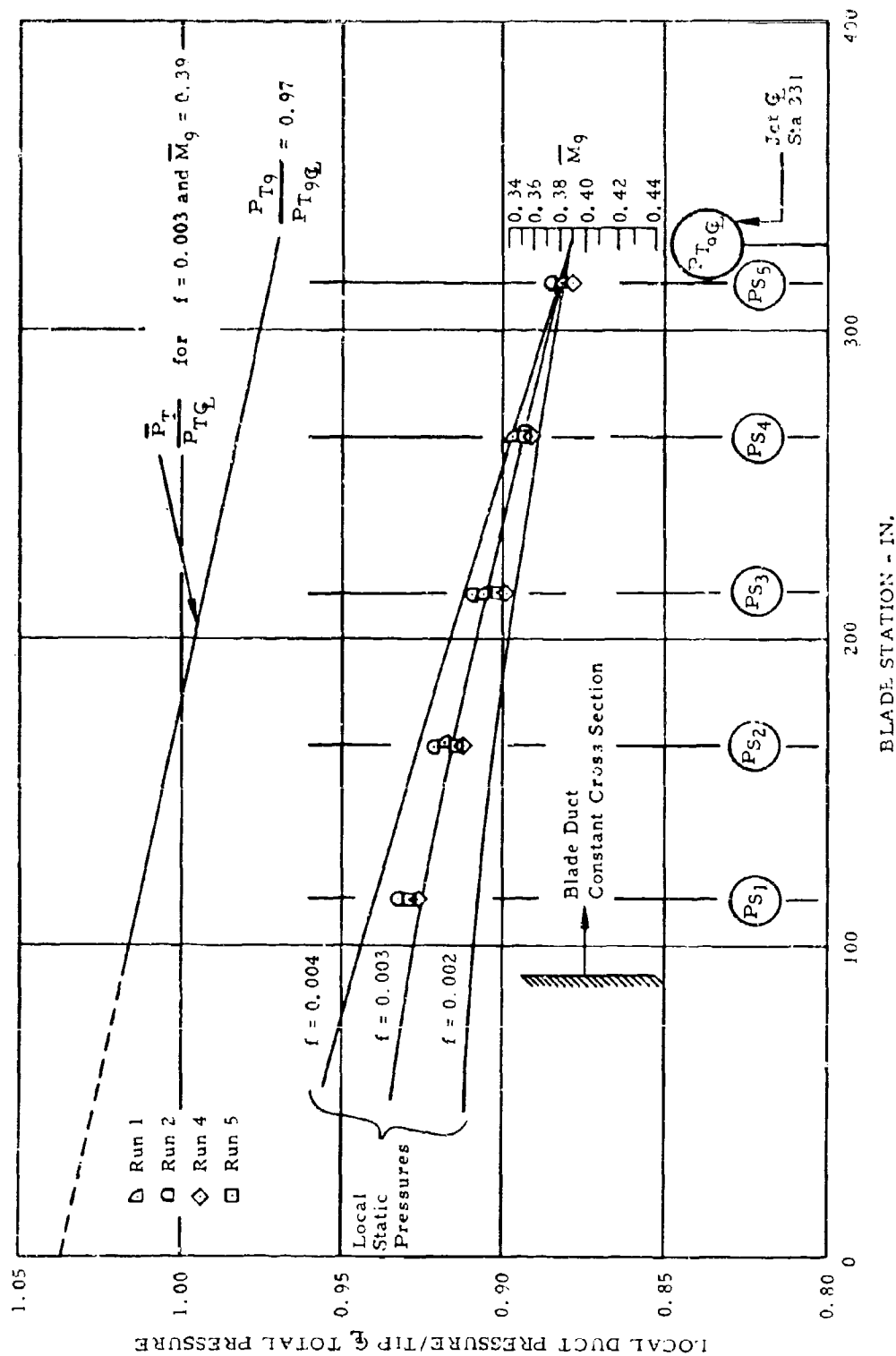


Figure 85. Tether Test Blade Duct Friction Factor Determination.

pressure gradient is included in Figure 85. Note that the static pressure gradient is steeper than the total pressure gradient; thus the measurement of static pressures represents the more sensitive technique for evaluating duct friction factor. Also, average static pressure is much easier to obtain than average total pressure, which would involve rake techniques.

An overall view of duct pressure recovery in the XV-9A is available in Figure 86. The solid line represents nonrotating recovery and is based on measurements as shown. Only the losses in the rotor segment from the hub to blade station 91 have not been measured directly, and the 1/2-percent loss (in addition to extrapolated duct friction loss) obtained by difference is an entirely reasonable value for this segment.

Duct pressure recovery under rotating operation is a function of the parameter $\%N_R / \sqrt{\theta_5}$. In Figure 86, a typical result ($\%N_R / \sqrt{\theta_5} = 62$) is shown. This curve has been calculated from a digital program based on stepwise summations of friction loss and centrifugal pumping along the blade duct.

In Figure 87, overall system pressure recovery is studied as a function of the parameter $\%N_R / \sqrt{\theta_5}$ over the full range from tether to normal helicopter flight. The most important finding from Figure 87 is that the large scatter band of flight test rotor tip pressure lies below the line based on tether test coefficients. Historically, since the whirl stand tests of 1962, the observed tip pressure recovery has been rising throughout the XV-9A test program (see Figure 88 of this report and Figure 28 of Reference 1 for examples). The only configuration changes that could have affected tip total pressure recovery are the minor changes in tip cascade effective flow area that accompanied the change to the flight test blade tip cascades after whirl testing and a subsequent small area reduction by installation of "mice" prior to the 20-hour follow-on flight test program. At most, these two changes could not have accounted for more than a 2-percent increase in tip total pressure recovery, whereas the observed increase has amounted to at least 4 percent. Centrifugal effects on the pressure transducers and the effects of rotating versus stationary resistance of the rotor slip rings represent two areas where complete calibration procedures have not been practical. Either of these items could lead to the difficulties that have been experienced. In any event, with a complete and consistent pressure recovery breakdown now available from tether tests, it is logical to obtain flight tip pressures from observed PT_5 and $\%N_R / \sqrt{\theta_5}$ through the use of Figure 87. Figure 88 presents the flight test data in greater detail. As is discussed in detail in a later paragraph, incorporation of these tether test coefficients has little effect on the previously reduced flight test results.

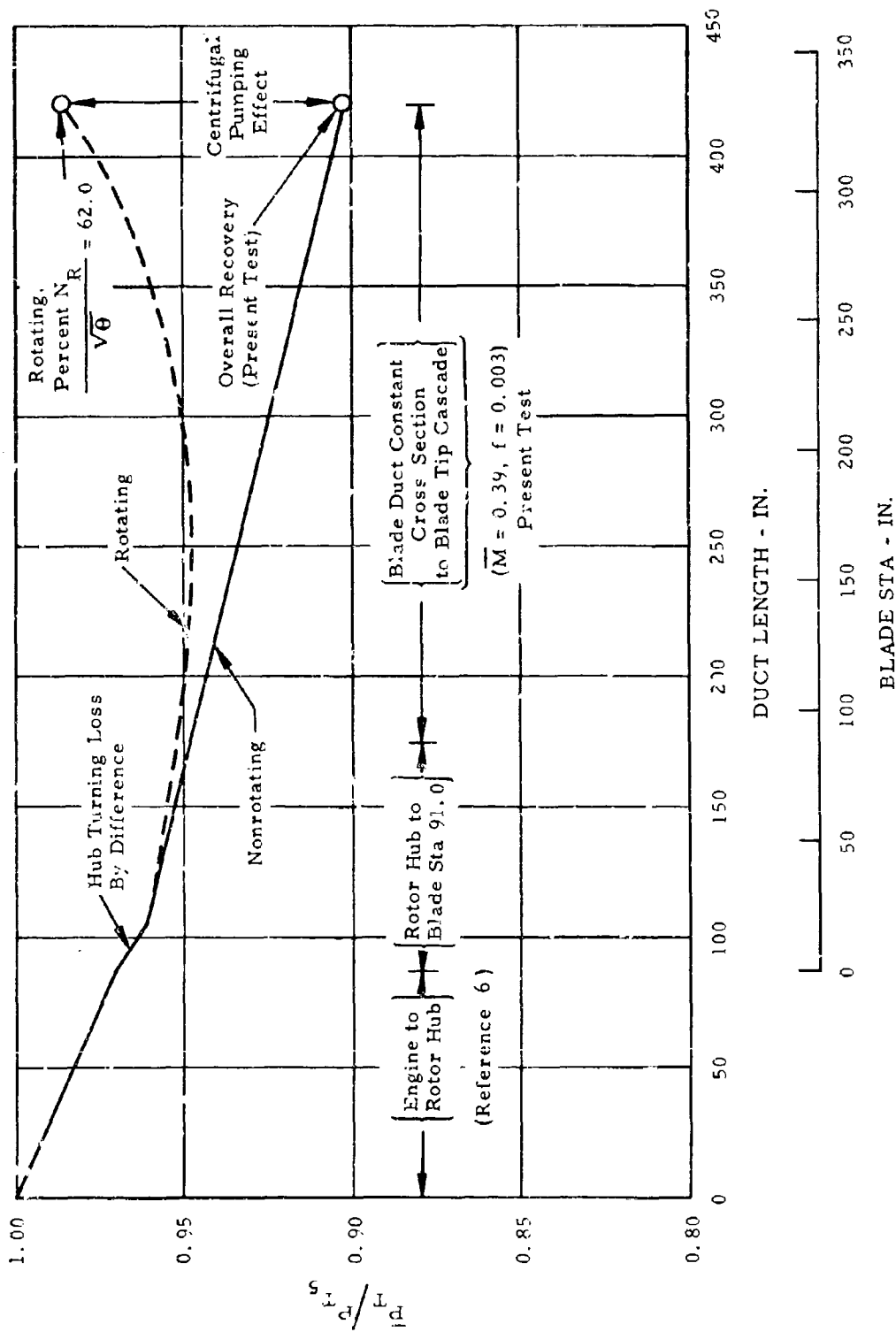


Figure 86. Duct System Pressure Variation.

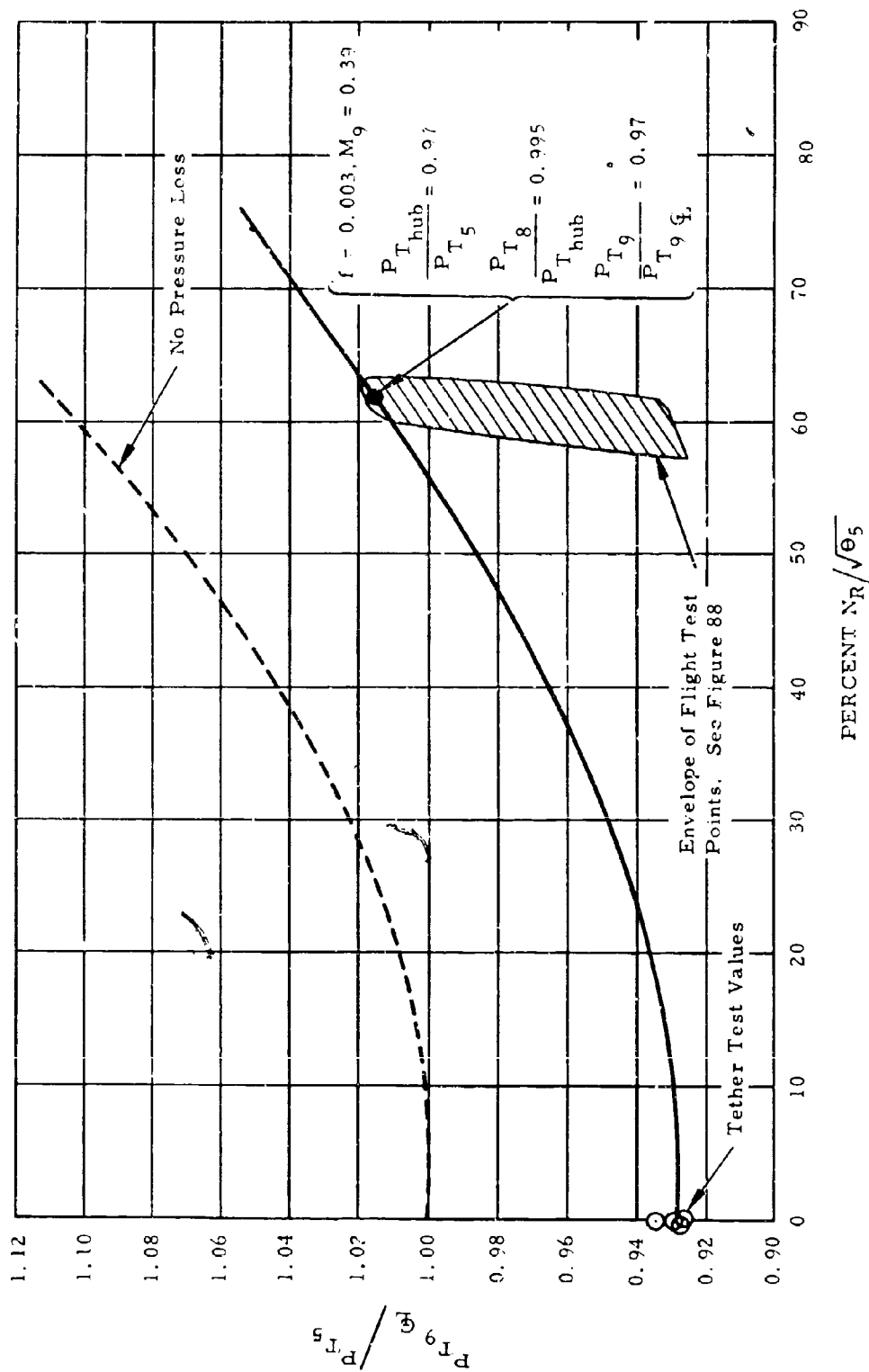


Figure 87. Rotor System Pressure Ratio Versus Rotor RPM - Flight and Tether Tests.

Blade Tip Cascade Area Measurement

At the conclusion of the tether tests, the blade tip cascades were removed and their minimum exit flow areas were measured. This measurement was performed with inside calipers, and care was taken to locate the minimum dimension at each point. During operation, the cascades are subject to a temperature approximately 1,000 degrees F higher than that prevailing during area measurement. For Rene 41, with a coefficient of linear expansion of 7.5×10^{-6} in./in./deg F, this temperature increase results in a 1.5-percent increase in area. The results of these measurements are summarized in Table X.

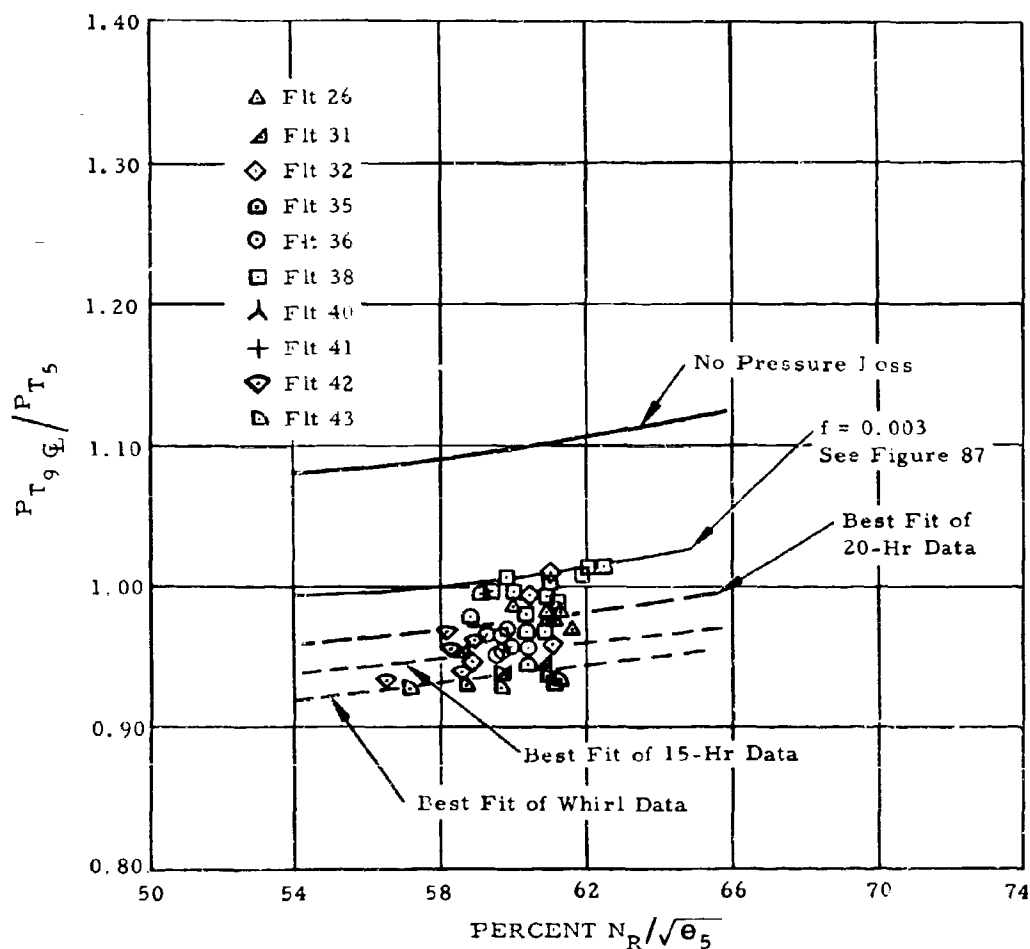


Figure 88. Rotor System Pressure Ratio Versus Rotor RPM - Flight Test.

TABLE X
BLADE TIP CASCADE AREAS

Cascade	Full Open Area		Closed Area		<u>Area Closed</u> <u>Area Open</u> (Hot)
	Cold (sq in.)	Hot (sq in.)	Cold (sq in.)	Hot (sq in.)	
Red blade	33.16	33.65	16.38	16.63	0.494
Yellow blade	32.68	33.17	16.37	16.61	0.501
Blue blade	33.09	33.59	15.93	16.17	0.481
Total	98.93	100.41	48.68	49.41	0.492

Single Engine Operation

A few tether test points were taken during single-engine operation and with the tip cascades at their minimum area (see Table X) settings. Results from these runs have been included on the appropriate graphs along with the normal two-engine data.

Cascade flow coefficient, C_w , for the single-engine configuration is studied in Figure 83. The single-engine mass flow points have been multiplied by the cascade open/closed area ratio of (1.0/0.492) for comparison with the twin-engine data. The flow coefficient of the cascades in their single-engine configuration appears to be entirely consistent with that of the open configuration. In fact, the flow coefficient correlation of Figure 83 must be considered excellent; and there is nothing to suggest that the cascades exhibit any unusual mass flow handling characteristics.

The thrust performance of the cascades at reduced area is studied in both Figure 82 and Figure 84. In each case, the reduced area data points appear to be scattered more below than above the full-open data. The single-engine points are too few to permit a convincing fairing to be drawn, but it appears possible that the single-engine velocity coefficient is as much as 2 percent lower than the 94-percent value indicated for normal operation. Any distortion of flow conditions in the cascade capable of producing a large reduction in velocity coefficient would most certainly result in an appreciable reduction in flow coefficient as well. The absence of changes in flow coefficient, Figure 83, thus encourages an optimistic interpretation of the more scattered velocity and thrust coefficient results.

Duct pressure recovery results from the single-engine runs are consistent with expectations but do not lend themselves to quantitative interpretation. Overall pressure recovery from engine to rotor tip is not representative of rotating operation, because of the tortuous flow path from one engine

duct to the three rotor ducts through the nonrotating transition section. Blade duct pressure drops are so small at the reduced flow rates accompanying single-engine operation that nothing is added to the duct friction factor by preparing a study similar to Figure 85 for this case.

APPLICATION OF TETHER TEST RESULTS TO ROTOR PERFORMANCE

The rotor system tether test program has been concerned with two technical areas -- blade-tip-cascade performance and duct system pressure recovery. In each area, the test results call for changes in factors entering into rotor power available calculations. Coincidentally, the effects are in opposite directions, so there is little net change.

The present tests yield a cascade velocity coefficient of $C_V = 0.94$, whereas $C_V = 0.955$ has been used to work up the flight test data. This factor is a direct multiplier on gross jet thrust and is leveraged by rotor pumping drag so that each 1-percent change in C_V results in approximately a 1-1/2-percent change in net rotor tip thrust or rotor horsepower available. Thus, the 1-1/2-percent apparent reduction in C_V leads to a 2-1/2-percent reduction in rotor power for a given tip total pressure.

Rotor power available calculations throughout the XV-9A flight test program have taken the measured tip pressures at face value. In Reference 1, the inconsistencies in these data were pointed out, but no meaningful correction could be made prior to the rotor system tether tests. As has been summarized in Figure 88, use of the tether test pressure recovery results in increases in apparent tip total pressure ranging from approximately 3 percent on the most recent flight test data to perhaps 6 percent on the 15-hour flight test data.

A 1-percent change in tip total pressure leads to only a 3/4-percent change in net rotor horsepower. Thus, the reevaluation of tip total pressure leads to an increase in rotor power of 2-1/4 percent for the most recent flight tests and perhaps a 4-1/2-percent increase during whirl stand tests.

The overall change in rotor power available resulting from the tether test coefficients then becomes zero for the latest flight tests and perhaps a 2-percent increase during the first phase flight tests.

The blade-tip-cascade velocity coefficient of 0.94 falls a few percentage points below what might be taken as state of the art. There is reason to believe that a modest development effort would result in an improvement

to at least 0.96, and possibly to 0.98. Even the lesser of these improvements would yield a 3-percent gain in rotor power with a directly corresponding reduction in sfc.

Confirmation of the duct friction factor of 0.003 as originally predicted for the XV-9A blade ducts and of the very modest pressure losses through the diverter valves, rotating seal, and hub ducting is a welcome result in terms of validating the predicted performance of the Hot Cycle propulsion system.

TEARDOWN INSPECTION

INTRODUCTION

The purpose of the teardown inspection was to determine the effects of 35 hours of flight operation and 50 hours of ground rotor operation on the XV-9A Hot Cycle Research Aircraft. Special emphasis was given to those parts unique to the Hot Cycle concept, especially the rotor and propulsion system.

The components subjected to the most detailed inspection were the rotor blade spars, the hot gas ducting and seals, the rotor hub structural components, and the rotor control system. The rotor blade spars, hot gas ducting, and hot gas seals were visually inspected. The rotor structural components and rotor controls were subject to additional inspection techniques; Magnaflux inspection was used on ferrous components and Zyglo inspection on nonferrous components.

The teardown inspection included a series of leakage tests to provide information on the change in leakage caused by 85 hours of rotor operation. This leakage information was also necessary for performance calculations.

ROTOR SYSTEM LEAKAGE TESTS

The first test was run on the rotor system downstream of the diverter valves and consisted of a leakage test of the Y-duct and triduct, rotating seal, articulating duct assemblies, and rotor blades. The blade-tip cascades were removed, and the blades were sealed at the tip by expanding plugs. The yaw duct was disconnected at the Y-duct, and the ports were capped. The transition ducts were removed and the Y-duct was capped off at this point with plates that were ported for the air hose from the flowmeter. The airflow for the leakage tests was supplied by two gasoline-driven air compressors; these compressors were nominally rated at 105 standard cubic foot per minute (scfm) each. Airflow was measured by a rotometer. A brief check of this instrumentation and data reduction procedure was performed by flow-testing a known orifice area. The rotometer was then calibrated to measure standard cubic feet of air at 14.7 psia and 70 degrees F, so it was necessary to correct the readings for pressure and temperature. The correction was:

$$\text{scfm} = \text{cfm}_{\text{meter}} \sqrt{\left(\frac{P_{\text{meter in. Hg abs}}}{29.92 \text{ in. Hg abs}} \right)} \times \left(\frac{530}{T_{\text{meter } ^\circ\text{R}}} \right)$$

The leakage data were measured in cubic feet per minute, then converted to pounds per second, then into an effective area in square inches (see Table XI).

The rotor system was disassembled, and leakage checks were made on the individual rotor blades, not including the articulating duct assemblies. The Y-duct and triduct assembly was checked as an assembly, and most of the leakage of this assembly was attributed to the rotating seal. The yaw duct and yaw-control valve system were checked in two configurations, one with the outlets plugged to determine the duct leakage and the other with the outlets open and the valve in neutral position. With the outlets plugged, the leakage was too small to measure with the test setup. With the outlets open and with the valve in neutral position, the built-in leakage area of the valve was determined to be 0.58 square inch.

TABLE XI
PROPULSION SYSTEM LEAKAGE MEASUREMENT IN
SQUARE INCHES

Component	Before Whirl Test (March 1964)	After Whirl Test (June 1964)	Before Flight Test (July 1964)	After Flight Test (Nov 1965)
Blue blade	0	0	0.0120	0.0517
Red blade	0.0064	0.0318	0.0119	0.0142
Yellow blade	0.0016	0.0338	0.0119	0.0415
Rotor hub	0	0	0.00764	0.00735
Inboard articulate duct seals	-	-		-
Outboard articulate duct seals	-	0.080		-
Total rotor system	0.132	0.193		0.392
Diverter valve 1			1.03	1.61
Diverter valve 2			1.28	1.36
Total diverter valves			2.31	2.97
Total power system*				3.36 (3.2%)

*Does not include yaw control valve.

INSPECTION PROCEDURE

The general procedure adhered to during inspection included removal of components and identification according to their location on the aircraft, such as a part of engine S/N 027-1A, or engine S/N 101-3A or blue, red, or yellow blade. When the part was removed, it was first visually

inspected without cleaning, because traces of oil or soot, peeled paint, or stains can be very useful clues to the service environment of a particular component. If a part showed only normal or expected signs of wear and it was an accessory such as generator, fuel shutoff valve, instrument, or similar vendor-supplied item, the inspection was completed by this first visual inspection, provided the part had been working satisfactorily up to the time of the teardown. The engines were subject to a more thorough inspection, but they were not disassembled.

Critical parts of the Hot Cycle propulsion system were subject to additional inspection beyond the first visual check.

Propulsion System and Hot-Gas System

1. Engines

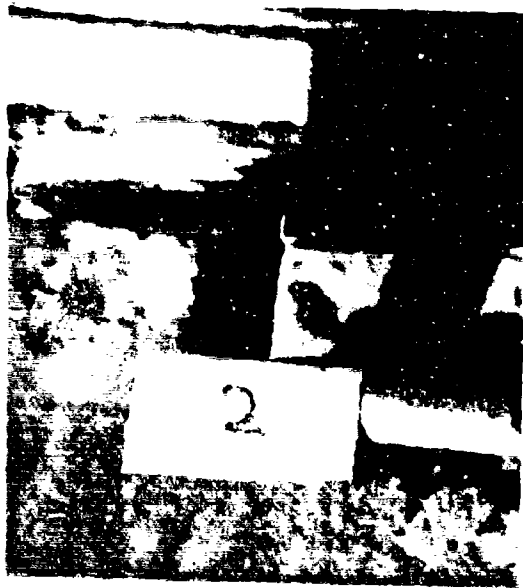
Both engines were removed from the aircraft and were stripped of all accessories that were not part of the actual engine. The engines were given an external inspection, after which MIL-L-7808 oil was sprayed into the compressor inlets. The fuel controls were plugged, leaving JP-4 as a preservative inside the units. Removal of the oil screen on engine S/N 027-1A to check for contamination was necessitated by the ingesting of a 1-foot-square piece of cloth at the conclusion of tether testing. No contamination was found on the screen. Examination of the forward guide vanes showed some of the vanes to be slightly bent, and the vane system was difficult to move. Engine S/N 101-3A appeared to be completely normal. The engine accessory drive, the drive shaft on the N₁ governor, the engine tachometer shaft, and the splined shafts on the hydraulic pump and generator all showed signs of fretting corrosion on each engine, as shown in Figure 89.

2. Engine-Diverter-Valve Seals

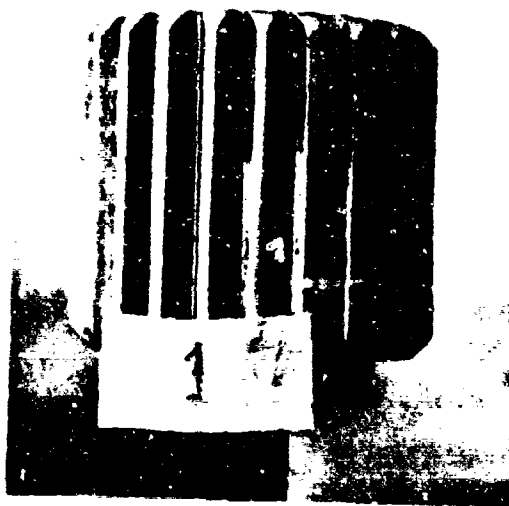
Seals from both assemblies showed negligible wear and the lip segments were still springy. There were indications of slight leakage between the segments, as evidenced by soot tracks on the sealing surface of the duct wall.

3. Diverter Valves

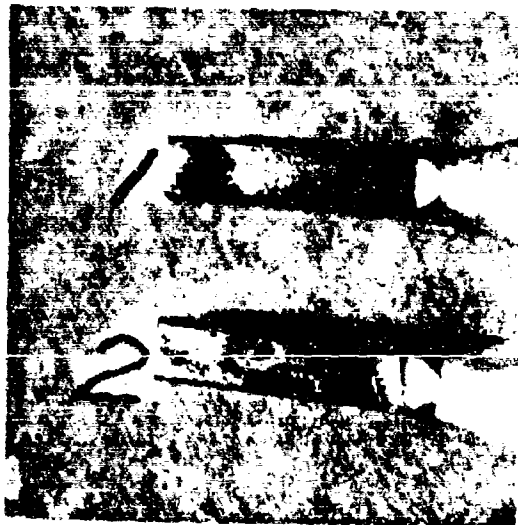
The diverter valves had been inspected at 5-hour intervals during the flight test program. Small cracks were discovered during the last periodic inspection and were repaired at that time. The teardown inspection did not reveal any new cracks, but there were still large gaps in the seals that were undoubtedly the main cause of valve leakage.



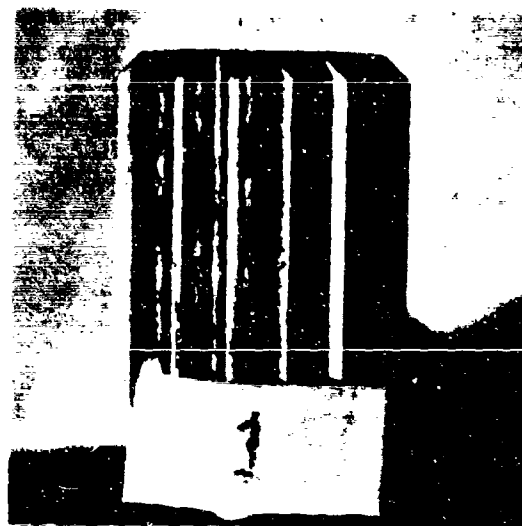
Tachometer



Generator



N_f Governor



Hydraulic Pump

Typical Parts With Fretting Corrosion

Figure 89. Engine Accessory Drive Couplings.

4. Transition Ducts

Both transition ducts were in excellent condition, the only sign of use being slight soot deposits. No cracks were found and there was no distortion.

5. Tail Pipes

Both tail pipes were in excellent condition. There were no cracks or distortion.

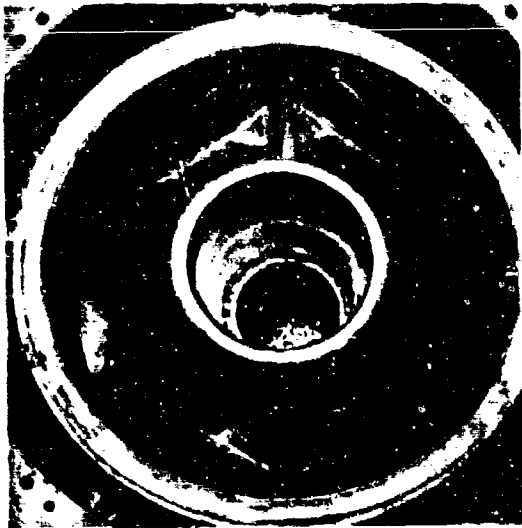
6. Y-Duct and Triduct

The insulation was stripped from the Y-duct and triduct so that the parts could be visually inspected for cracks. No cracks were found.

7. Hub Duct Rotating Seal Assembly

The hub duct seal assembly consists of an inner and an outer carbon seal. The inner seal is approximately 7 inches in diameter and the outer seal is approximately 17 inches in diameter. The inner seal is a one-piece carbon ring that rides on a flame-plated ring or flat washer-type of surface. This seal is free to move in a vertical direction and is spring-loaded vertically to load the carbon face against the flame-plated surface. The wear on the inner seal was very smooth and even around the circumference, as shown in Figure 90. The wear rate was difficult to establish because the carbon ring was within the drawing dimensional tolerance. There were slight indications of carbon transfer from the seal into the pores of the flame-plated ring.

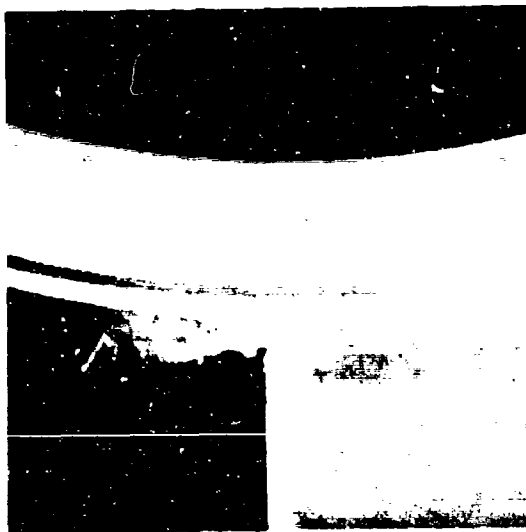
The outer seal is made from circular carbon segments that ride on a flame-plated section of the triduct wall. These segments are free to move in and out radially and are spring-loaded inward against the flame-plated surface. The segmented type of seal allowed the hot gas to attack more free edges than the one-piece inner seal, so edge decomposition and leakage were more of a problem on the outer seal. There were traces of soot on the seal holder, which showed that leakage was occurring between the butted ends of the carbon segments. There were also some chipped or eroded edges on some of the carbon segments, as shown in Figure 91. The overall condition of the carbon was good, and the flame-plated surface showed little carbon transfer. The wear rate was difficult to establish, because the segments were within the drawing dimensional tolerance.



Installation Carbon Ring (Light Circle in Center of Picture)



Closeup of Carbon Ring (Dark Narrow Band)

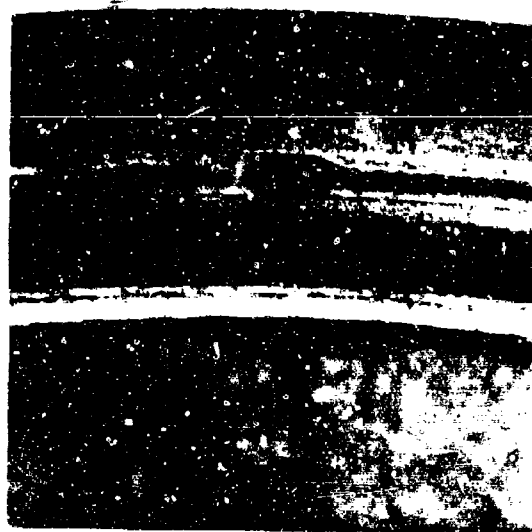
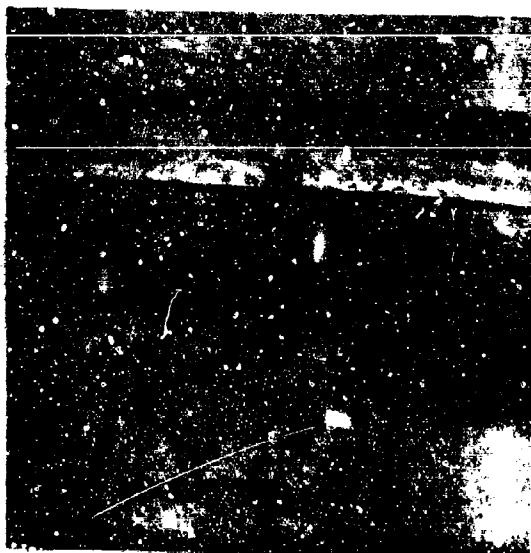


Rubbing Ring Tungsten Carbide Flame Plating



Closeup of Rubbing Ring

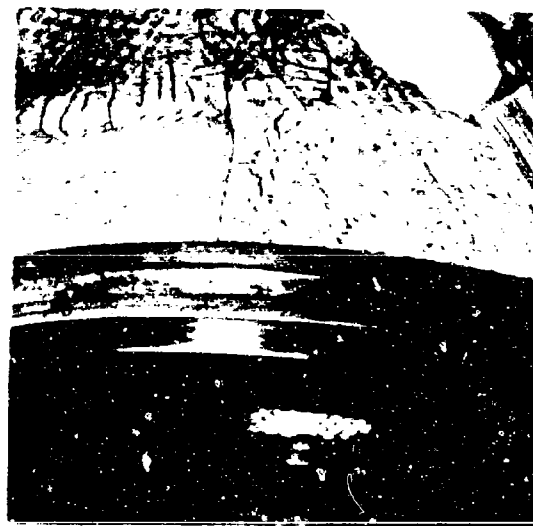
Figure 90. Rotating Seal, Inner.



Typical Unbroken Carbon Segments



Typical Broken Carbon Segment



Rubbing Ring Tungsten
Carbide Flame Plating

Figure 91. Rotating Seal, Outer.

Rotor System Structure and Components

1. Rotor Blade Spars

The removal torque was recorded for each blade-segment-to-spar bolt, and each bolt was placed in a numbered bag for identification. In order to assist in locating any gas leaks, the spars were then visually inspected for traces of soot and discoloration before they were cleaned. Traces of soot were found on the yellow blade spars at station 203.5. All instrumentation wiring and strain gaging were removed, and the spars were cleaned with solvent. No cracks were found by microscopic examination in and around the bolt holes, using a 40-power binocular type of scope.

There were some delaminations of the bonding used to bond the spar assembly together as well as to bond the solid root fittings to the spar. These delaminations had progressed only slightly during the test program, and their progress was noted at each periodic inspection during testing. The delamination of the bonding was not a problem, because generally it was confined to the point at which a single lamination was dropped off.

The blade-segment-to-spar bolts showed evidence of fretting and had circumferential scratches from being inserted through the hard stainless steel spars, as shown in Figure 92.

2. Blade Retention Straps

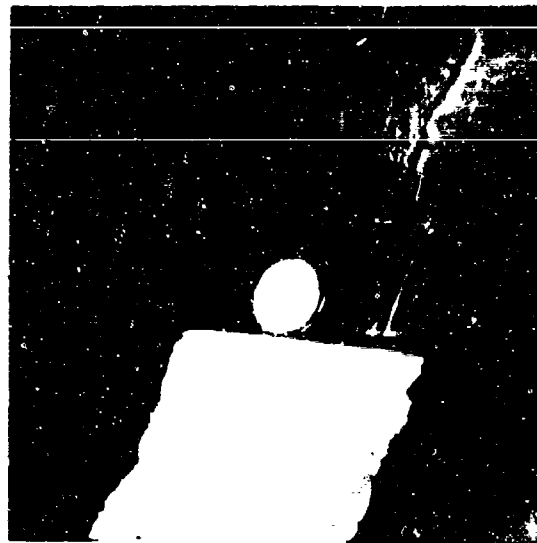
The retention straps were inspected with a 40-power microscope and were determined to be in very good condition. No cracks were found and the bolt holes were generally very smooth and free from fretting. One bolt hole had a chipped strap lamination approximately halfway inside the hole, as shown in Figure 93. This hole was the inboard hole on the outboard end of the red blade forward strap. The cause of this chip was not determined, but it appeared to have been done during assembly or disassembly. The surface finish of one strap (at the root-end forward blue-blade strap) showed roll or clamp-up marks, as can be seen in Figure 93. Examination of typical retention bolts (see Figure 93) showed the bolts to be in good condition.

3. Rotor Hub and Gimbal Assembly

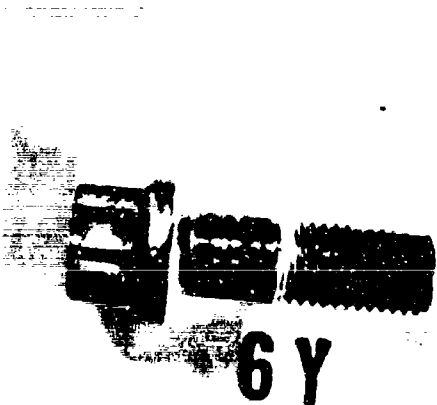
The gimbal assembly was removed from the hub, and the bearings were visually inspected and were determined to be in excellent condition. The gimbal support structure and the hub area around the retention-strap bolt holes were magnetically inspected and no cracks were found.



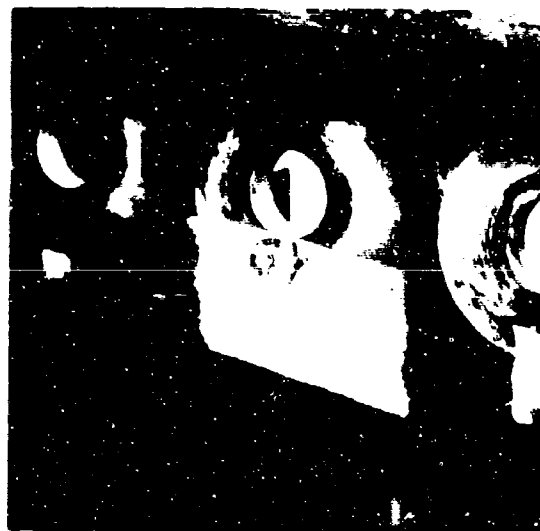
Typical Fretting Spar to Segment
Attach Bolts



Typical Holes in Spars

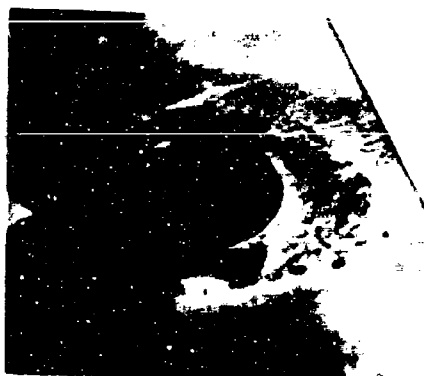


Typical Fretting Spar Attach
Bolts in Area of Root Fittings

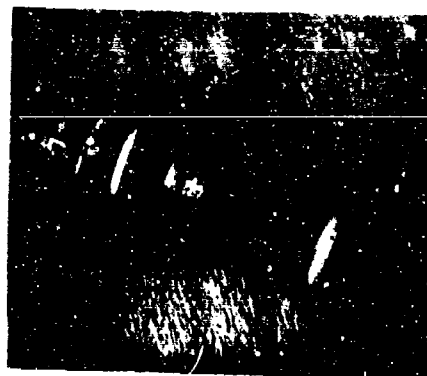


Typical Holes in Root Fittings

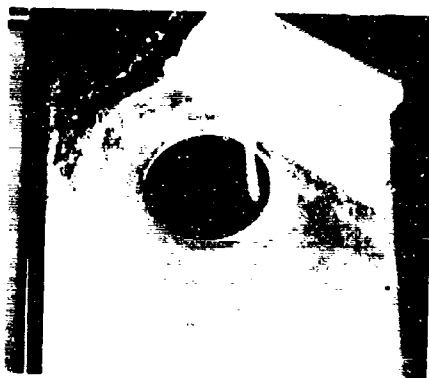
Figure 92. Spar to Segment Bolts.



Hole With Chipped Lamination



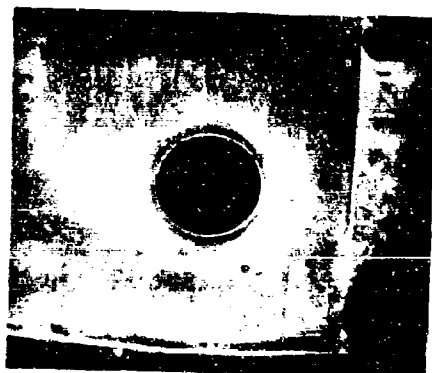
Bolt From Hole With Chipped Lamination - Note Scratch



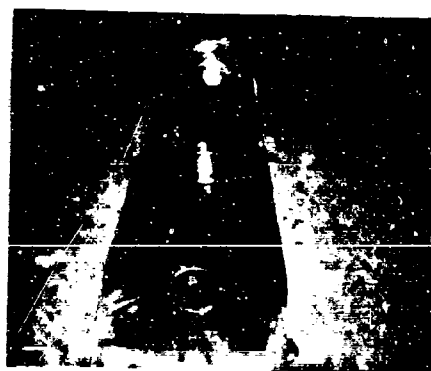
Typical Hole, Excellent Condition



Bolt From Hole in Excellent Condition



Roll or Clamp-Up Marks on One Strap End Only



Typical Surface Finish

Figure 93. Blade Retention Straps and Bolts.

4. Feathering Ball

Each feathering ball and bearing assembly was inspected visually and all were found to be in good condition. The Teflon cloth on the ring had been worn through to approximately 50 percent of its original thickness in some areas, but the average wear was approximately 15 percent. The chrome-plated aluminum feathering balls were in very good condition, with no cracking or peeling of the chrome and very little apparent wear.

5. Rotor Shaft

The rotor shaft has a large nut on each end that held the rotor assembly together and transferred all the thrust loads. The removal breakaway torque on these nuts was 6,400 foot-pounds for the lower nut and 4,780 foot-pounds for the upper nut. The installation torque was 5,400 foot-pounds nominal for both nuts.

The paint on the shaft had peeled and cracked on approximately 10 percent of the surface, but the paint had not been burned away. The splines on the shaft and the mating parts were in very good condition and there was no evidence of fretting.

The shaft was magnetically inspected and no cracks were found.

6. Spoke Assembly

The spoke was magnetically inspected and no cracks were found.

7. Rotor Radial and Thrust Bearings

The radial bearing and the thrust bearings were disassembled and the rollers and races visually inspected. All three bearings were in excellent condition, with no signs of brinelling, overheat, galling, or oil starvation. The oil seals were in good condition, but the silicone seals had retained their softness and sealing resiliency better than the neoprene seals.

8. Articulating Duct Assemblies

The articulating duct assembly for each blade consists of a gimble ball joint attached to the rotating triduct. The other end of the ball joint is attached to a circular duct that leads into a slip joint at blade station 42.5. The ball joint is sealed by carbon segments riding on a locally flame-plated area of the ball. The slip joint is composed of a segmented-leaf-type seal that rides on a flame-plated portion of the inboard circular duct.

section. The outboard end of the seal assembly clamps directly to a bifurcated section that divides the gas flow into the blade forward and aft ducts at station 60.5.

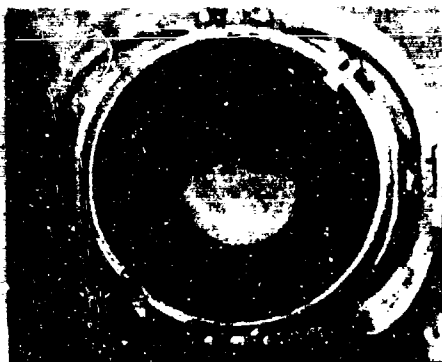
The tungsten carbide flame-plated surfaces of the ball joints were in excellent condition, and the carbon segments were in good condition except for some slight scoring, as shown in Figure 94. The inner wall of the root section of the articulating duct assembly in the area of the ball joint was distorted from a circular shape to a hexagon on all three parts, as shown in Figure 94. At the corners of this hexagon shape, there were short cracks in the spanwise direction, these cracks being most predominant in the red blade assembly. The hot gas was in direct contact with the duct wall at the sections where the cracks occurred. Neither the external wall nor the ball showed signs of distress. The distortion pattern of the inner wall with cracks at the corners could well have been the result of buckling caused by thermal stresses in the hot wall.

9. Rotor Blade Ducting

In the constant-section portion of the blade, hot gas ducting is made up of segments that slide together. The lap joint thus formed at each segment is not gas-tight without secondary sealing. This sealing is accomplished at the flexure couplings that tie the blade segments together at the exterior skin of the blade. The construction in this area forms a cavity about each lap joint that is then filled with self-curing silicone rubber compound to seal up any cracks and seams that would allow hot gas to escape.

External inspection of the rotor blades has provided clues to any leakage of the duct joints by traces of soot that appeared on the spars and blade skins. The blades were inspected continuously during the test program for traces of soot, which would indicate leakage.

Before the return flight to Culver City from Edwards Air Force Base, the first and only major repair to the rotor was performed. A bolt at the tip of the rear spar on the blue blade had failed. The failure was caused by the bolt being overheated, leading to stress alloying, and was the result of a gas leak at the closing rib of the tip segment just ahead of the cascade nozzle. Since the repair of this leak necessitated replacing the tip segment with a new part, the segment was removed at the first flexure inboard of the tip. Examination of the duct lap joints and the flexure area revealed that the silicone compound surrounding the lap joints had been broken down into a granular substance from the heat and gas erosion. The sealant was in good shape approximately one-half an inch from the lap



Deformed Duct Wall Inside Ball
Joint (Circular to Hexagon Shape)
Typical All Three Blades



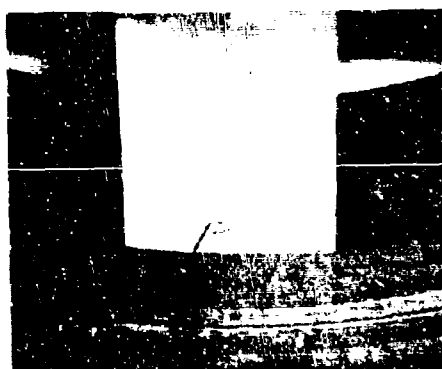
Typical Crack in Duct
Wall Inside Ball Joint



Red Blade Segment Seal
Typical Wear on Segmented Leaf Sliding Seals and Flame-Plated
Duct Walls



Red Blade Duct Wall



Typical Carbon Segment Seals - Note Slight Score Marks



Figure 94. Articulating Duct, Hub to Blade.

joint, because the silicone compound that had been partially destroyed by the hot gas was still providing insulation for the remainder of the material. The unaffected material still sealed the closing ribs and the external skin seams from leakage; in fact, the old compound had to be dug out of the cavity so the tip segment could be reset in new material.

Teardown inspection of the yellow blade revealed soot marks on the spars between the ninth and tenth blade segments, station 203.5; therefore, the blade was taken apart at that flexure. The inspection of this flexure (see Figure 95) revealed that the suspected leak was a very small seam leak between the flexure and the exterior skin of the blade. The flexure itself was in good condition. The yellow blade was also separated at station 241 for investigation of a slight bulge in the duct wall, as shown on Figure 96. Inspection of this flexure showed it to be in good condition. The bulge in the duct wall was at the slip joint between segments. The cause could not be definitely determined, but damage during assembly was a possibility. The yellow blade was also separated at the first flexure, station 91, and the exterior skin was removed from the bottom of the blade in the transition section. No cracks were found in either the flexures or the skins.

10. Blade-Tip-Cascade Nozzles and Actuating Cylinders

The blade-tip cascades were removed and were visually inspected for cracks, erosion, and signs of overheat. They were found to be in excellent condition. The physical minimum exit area of each cascade was measured with inside calipers and scale for use in performance calculations. The results of these measurements were shown in Table X.

The pneumatic blade-tip closure-valve actuating cylinders were removed and were disassembled. Inspection revealed a chip out of one Teflon piston seal that could not be explained, and all the cylinders had small longitudinal scratches. The small scratches could be polished out easily. The remainder of the seals and the rods were in good condition.

Control System Components

1. Rotor Control Actuators

The three servo cylinders were disassembled and were found to be in excellent condition. The cylinders, pistons, and piston rods were smooth, with no pitting, galling, or abnormal wear. Most of the seals were in good condition with only normal wear. The seals inside the cylinders that separated the tandem power cylinders had been leaking slightly, but they appeared to have been nicked during installation, which



Soot Tracks, Which Show Suspected
Leak - Aft Spar



Flexure Eleven - Shown For
Comparison - No Soot Tracks



Flexure Ten Looking Outboard -
Small Seam Leak, Upper Left
Dark Area



Flexure Ten Looking Inboard

Figure 95. Flexure Ten, Yellow Blade, Station 203.5.



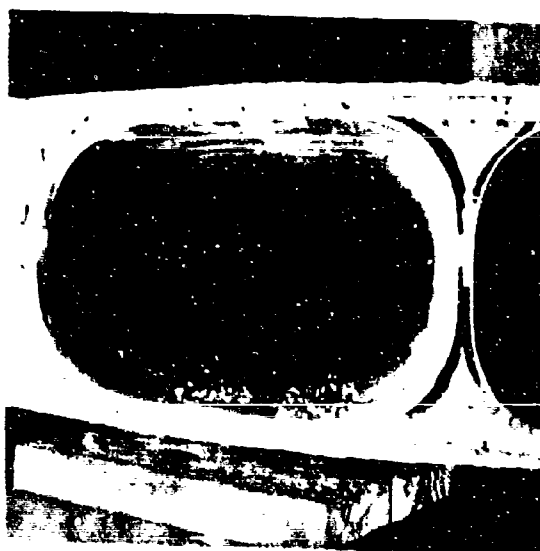
Bulge in Duct Wall, Forward Duct,
Flexure Thirteen, Station 241



Bulges in Duct Wall, Aft Duct,
Flexure Thirteen, Station 241



Flexure One, Station 91,
Looking Inboard



Typical Condition of Ducts, Station
203.5, Looking Outboard

Figure 96. Hot Gas Rotor Ducting, Yellow Blade.

had been a difficult process at best. The servo valves were also leaking slightly, as the O-rings had been shaved down to reduce breakout friction on the valves.

The piston for one-half of the tandem power system is attached to the piston rod by a pin (see Figure 97). Because the piston pin failed during the life-cycle test of the test servo actuator, the pins were changed in the flight actuators. The pin that failed was undersize and had a groove in the middle for the setscrew. The replacement pins were made to a slop-free push fit, and the groove was eliminated. The ends of the pins were also rounded to prevent scratching the cylinders if the pin shifted axially.

The replacement pins were in good condition except for slight marks where the pin and rod had relative motion caused by pin bending, as shown on Figure 97.

2. Swash Plate Assembly

The rotating and stationary swash plates were disassembled, Zyglol inspected, and found to be in excellent condition.

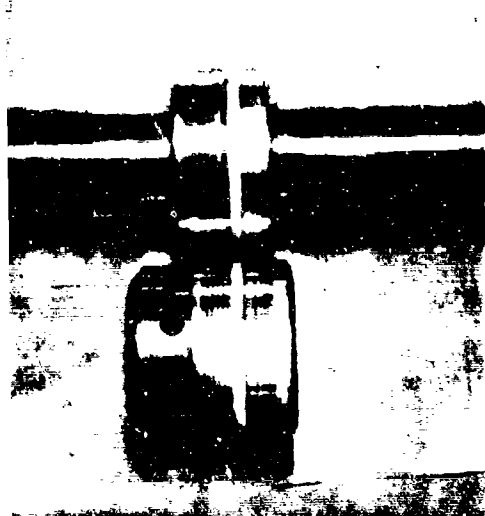
3 Blade Pitch Links and Control Rods

The pitch links and control rods were removed, cleaned, and magnetically inspected. The areas of concern were the material around the rod-end grease fittings and the last thread on the rod end near the head. Most rod-end cracks and failures, except for bearing failures, occur at these points. No cracks were found at the usual places in the pitch links or rod ends, but approximately 50 percent of the rod ends had cracks and chips around the retainer. These cracks were in the rod-end bodies where the metal was swaged over the retainers. Typical cracks can be seen in Figure 98. These cracks appear to have been caused by extreme angular motion of the rod ends. These extreme movements probably occurred during control check-out and calibration.

Approximately 25 percent of the jam nuts used on the rod ends were cracked longitudinally, probably from overtorque during assembly. The rod ends were in fair to good condition with respect to bearing looseness, radial free play, and smoothness of rotation.

4. Walking Beams

The upper and lower walking beams were magnetically inspected and no cracks were found. The tapered roller bearings used in the beams were in excellent condition, showing no visible wear, looseness, or brinelling.



Power Pistons and Rod



Piston Pins for All Cylinders -
Note Marks Near Ends

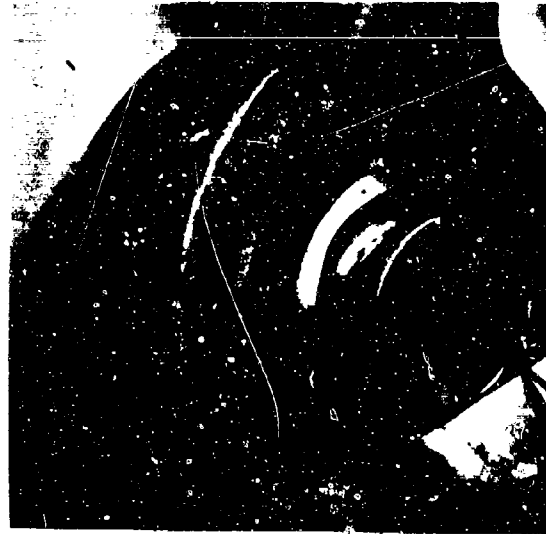
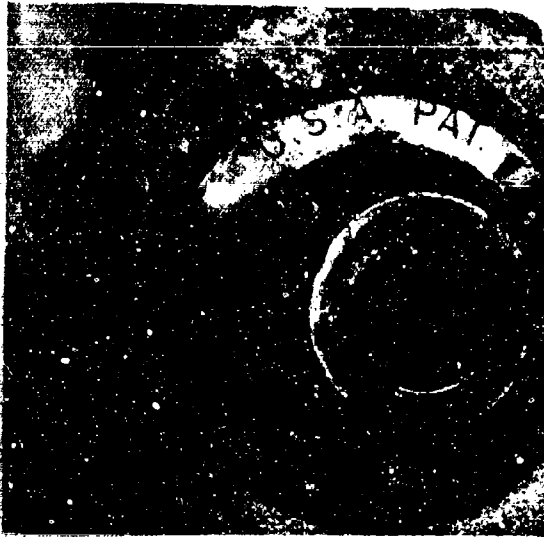


Extrusion Cylinder End Bearing,
Typical

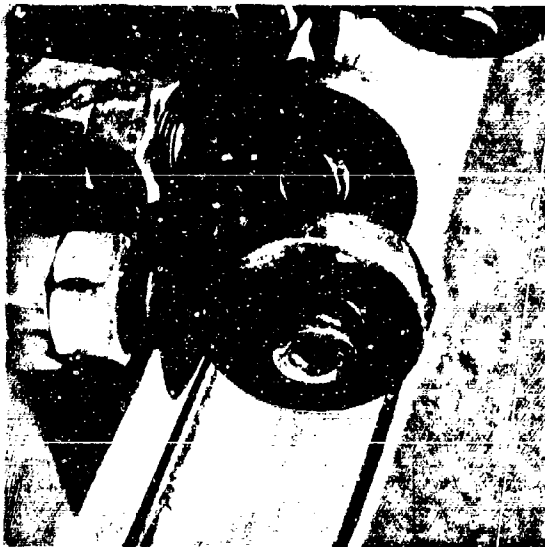


Rod External Lip Seal and Scraper,
Typical

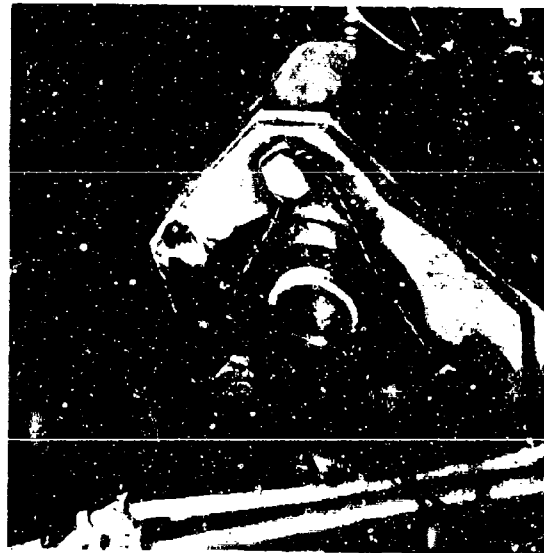
Figure 97. Servo Actuator Components.



Cracks and Chips in Swaged Area of Rod Ends Caused by
Extreme Control Displacement - Shafer P/N MR8AF



Typical Rod Ends as Removed



Seal Failure Trunnion Support
Bearing on Hub P/N 285-0511

Figure 98. Rod Ends and Self-Aligning Bearings.

5. Diverter Valve Actuators

The diverter valve actuators were removed and sent to the hydraulics laboratory for internal inspection. The inspection showed some small random scratches on the rods of both units, which could be polished out easily. The static seal at the removable end of one unit showed signs of overheat, and it had become hard and rough. All other seals appeared to be in good condition and the cylinder bores were smooth.

Structure

1. Power Module

The A-286 high-temperature stainless steel used in the power module was in excellent condition, there being no apparent cracks, distortion of shape, or signs of overheat. There were beginning signs of corrosion, since the aircraft had been exposed to the weather for more than one month during teardown inspection.

2. Fuselage and Empennage

The aluminum fuselage and empennage were in good condition, but the corrosion buildup on these unpainted surfaces had been quite rapid. A few minor rivets had popped loose in the pylon fairing, but no serious cracks or structural distress was found.

3. Engine Mounts and Rotor Support Structure

The tubular engine mounts and the tubular rotor support structure were all magnafluxed, and no cracks were found in these parts.

4. Landing Gear

The main and tail landing gear were visually inspected and found to be free of any cracks or structural distress. The wheels and tires were in good condition.

REFERENCES

- 1 Ground and Flight Tests, XV-9A Hot Cycle Research Aircraft Summary Report, Hughes Tool Company - Aircraft Division Report 65-13, USAAVLABS Technical Report 65-68, U. S. Army Aviation Materiel Laboratories, Fort Eustis, Virginia, March 1966.
- 2 Program Plan, 20-Hour Follow-On Flight Test, XV-9A Hot Cycle Research Aircraft, Hughes Tool Company - Aircraft Division Report 65-6, January 1965.
- 3 Aircraft Design, XV-9A Hot Cycle Research Aircraft Summary Report, Hughes Tool Company - Aircraft Division Report 64-11, USAAVLABS Technical Report 65-29, U. S. Army Aviation Materiel Laboratories, Fort Eustis, Virginia, August 1965.
- 4 Component Testing XV-9A Hot Cycle Research Aircraft Summary Report, Hughes Tool Company - Aircraft Division Report 64-26, USAAVLABS Technical Report 65-38, U. S. Army Aviation Materiel Laboratories, Fort Eustis, Virginia, November 1965.
- 5 T64 Gas Generator - QT Generalized Performance, Technical Memorandum TM-SE-625E-1570, General Electric Company, Lynn, Massachusetts, June 1962.
- 6 Engine and Whirl Tests, XV-9A Hot Cycle Research Aircraft Summary Report, Hughes Tool Company - Aircraft Division Report 64-23 (385-T-15), USATRECOM Technical Report 64-67, U. S. Army Transportation Research Command (changed to U. S. Army Aviation Materiel Laboratories), Fort Eustis, Virginia, February 1965.
- 7 Model Specification, XV-9A Hot Cycle Research Aircraft, Revision E, Hughes Tool Company - Aircraft Division Report 62-22, October 1963.
- 8 Mulready, R. C., The Ideal Temperature Rise Due to Constant Pressure Combustion of Hydrocarbon Fuels, Meteor Report UAC-9, United Aircraft Corporation, East Hartford, Connecticut, July 1947 (see also NACA TN 2357, 1951).
- 9 Performance Handbook, Hughes Tool Company - Aircraft Division Report XA-8016, 1965.

- 10 Purser, P. E. and Campbell, J. P., Experimental Verification of a Simplified Vee-Tail Theory and Analysis of Available Data on Complete Models with Vee-Tails, NACA TR 823, National Advisory Committee for Aeronautics, Washington, D. C., 1945.
- 11 Amer, K. B., Theory of Helicopter Damping in Pitch or Roll and a Comparison with Flight Measurements, NACA TN 2136, National Advisory Committee for Aeronautics, Washington, D. C., October 1950.
- 12 Hohenemser, K. H., and Perisho, C. H., Analyses of the Vertical Flight Dynamic Characteristics of the Lifting Rotor and Off-Set Coning Hinges, IAS Reprint No. 820, 26th Annual Meeting, Institute of Aerospace Sciences, New York, New York, January 27 - 30, 1958.
- 13 Sines, G., and Waisman, J. L., Metal Fatigue, McGraw Hill Publishing Inc., New York, New York, 1959.
- 14 Preliminary Design Study, Hot Cycle Research Aircraft Summary Report, Hughes Tool Company - Aircraft Division Report 62-31, USATRECOM Technical Report 62-102, U. S. Army Transportation Research Command (changed to U. S. Army Aviation Materiel Laboratories), Fort Eustis, Virginia, March 1963.

DISTRIBUTION

US Army Materiel Command	5
US Army Aviation Materiel Command	6
United States Army, Pacific	1
US Army Forces Southern Command	1
Chief of R&D, DA	2
Director of Defense Research and Engineering	1
US Army R&D Group (Europe)	2
US Army Aviation Materiel Laboratories	19
US Army Human Engineering Laboratories	1
US Army Ballistic Research Laboratories	2
Army Aeronautical Research Laboratory, Ames Research Center	1
Plastics Technical Evaluation Center	1
US Army Engineer Waterways Experiment Station	1
US Army Test and Evaluation Command	1
US Army Electronics Command	2
US Army Combat Developments Command, Fort Belvoir	2
US Army Combat Developments Command Transportation Agency	1
US Army Command and General Staff College	1
US Army Aviation School	1
US Army Tank-Automotive Center	2
US Army Aviation Test Board	2
US Army Aviation Test Activity, Edwards AFB	2
Air Force Flight Test Center, Edwards AFB	2
US Army Field Office, AFSC, Andrews AFB	1
Air Force Aero Propulsion Laboratory, Wright-Patterson AFB	1
Air Force Flight Dynamics Laboratory, Wright-Patterson AFB	1
Systems Engineering Group, Wright-Patterson AFB	4
Naval Air Systems Command, DN	18
Office of Naval Research	3
US Naval Research Laboratory	1
Naval Air Engineering Center, Philadelphia	1
Commandant of the Marine Corps	1
Marine Corps Liaison Officer, US Army Transportation School	1
Testing and Development Division, US Coast Guard	1
Lewis Research Center, NASA	1
NASA Scientific and Technical Information Facility	2
NAFEC Library (FAA)	2
US Army Aviation Human Research Unit	1
US Army Board for Aviation Accident Research	1
Bureau of Safety, Civil Aeronautics Board	2
US Naval Aviation Safety Center, Norfolk	1
Federal Aviation Agency, Washington, D. C.	2
Civil Aeromedical Institute, FAA	2
The Surgeon General	1
Bureau of Medicine and Surgery, DN	1
US Government Printing Office	1
Defense Documentation Center	20

APPENDIX I

DESCRIPTION OF TEST INSTRUMENTATION

The test instrumentation used for the 20-hour follow-on flight test program was basically identical with that used for the 15-hour program, with the exception of several modifications incorporated during the inspection and maintenance period prior to initiation of the follow-on flight program. A comprehensive description of the instrumentation installed and of the instrumentation procedures used has been presented in Appendix I of Reference 1. A listing of the installed equipment is presented in the following paragraphs. An instrumentation schematic is included as Figure 99.

DESCRIPTION OF TASKS ACCOMPLISHED DURING INSPECTION AND MAINTENANCE PERIOD

At the initiation of the 20-hour follow-on flight test program, the changes made to the instrumentation system to improve the capability and reliability were as follows:

1. Installed and calibrated new strain gages on the blade spars
2. Mounted the temperature recorders on shock mounts
3. Fabricated and installed temperature probes in the engine inlets
4. Replaced blade-to-hub thermocouple lead wire with wire having improved flexibility
5. Inspected, calibrated, and performed necessary repair of all recorders
6. Inspected and performed necessary repair of all wiring, plugs, and thermocouples
7. Increased sampling rate of the blade-tip-cascade gas temperature
8. Performed onboard calibration of most transducers, as well as laboratory calibrations
9. Improved screw attachments between hub-to-blade thermocouple wiring and thermocouple switch boxes
10. Inspected, cleaned, and oiled rotor slip ring

CALIBRATION PROCEDURE, ROTOR BLADE SPARS

Changing the blade-spar strain gages at the initiation of the program necessitated a complete laboratory calibration of the spars. The test fixture used for calibration supports the root end of the blade

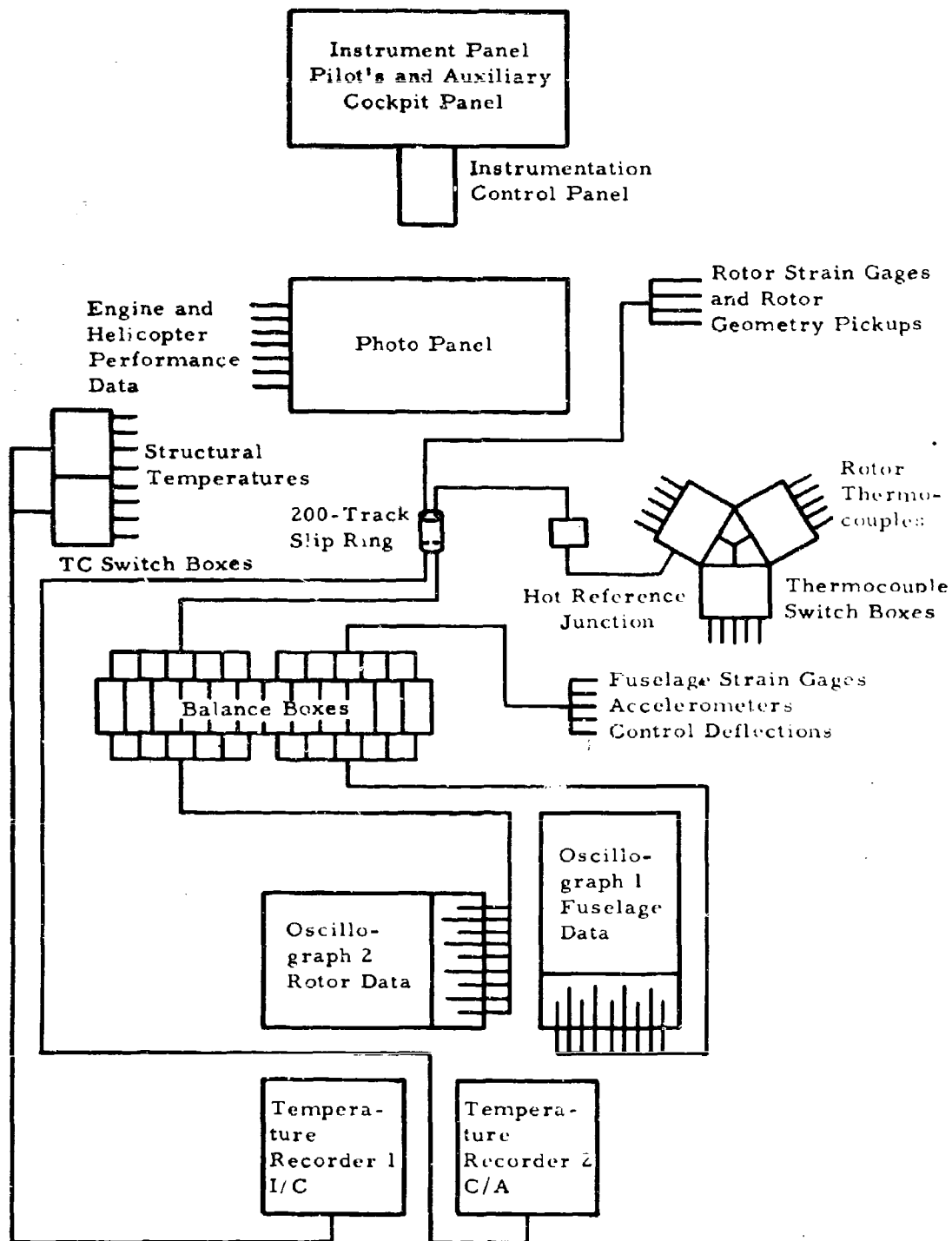


Figure 99. Instrumentation Schematic.

between a clamp around the feathering ball and a clamp around the blade at station 73.44, allowing the remainder of the blade to act as a cantilever beam. Loads were then applied at various blade stations to produce the desired flapwise or chordwise bending moments. The blade-skin torsion gages were also calibrated in this test fixture by applying a known couple to the blade tip and reacting the moment through the pitch arm.

RECORDING EQUIPMENT

1. Two 50-channel oscillographs, each having a 400-foot magazine
2. Two potentiometer-type 12-point thermocouple temperature recorders
3. One photopanel utilizing a 35-mm sequence camera with a 400-foot film magazine
4. One battery-powered communications tape recorder
5. Data correlation timing system
6. A 16-mm cockpit camera with a 400-foot film magazine

LIST OF INSTRUMENTATION MEASUREMENTS

Pilot's Panel, Direct-Reading Instruments

Airspeed indicator
Pressure altitude indicator
Rate of climb indicator
Attitude indicator, pitch and roll
Turn and bank indicator
Engine turbine speed indicator, each engine
Engine discharge pressure indicator, each engine
Engine exhaust gas temperature indicator, each engine
Engine fuel flow indicator, each engine
Engine oil pressure indicator, each engine
Engine oil temperature indicator, each engine
Fuel quantity indicator, dual reading, forward and aft tanks
Hydraulic pressure indicator, dual reading, both systems
Rotor tachometer
Rotor oil pressure indicator
Rotor oil temperature indicator
Tilt-stop indicator
Ammeter (2)
Voltmeter
Inverter frequency meter

Emergency rotor tachometer
Outside air temperature indicator
Compass

Auxiliary Cockpit Panel, Direct-Reading Instruments

Engine vibration amplitude indicator, each engine
Clock
Collective control position indicator
Longitudinal cyclic control position indicator
Lateral cyclic control position indicator
Rudder pedal position indicator
Pressure altitude indicator
Accelerometer, vertical
Engine discharge pressure indicator (sensitive), each engine
Data correlation counter
Oscillograph record counter
Film footage counter, photopanel

Photopanel (35-mm Sequence Camera), Flight Parameters and Engine Performance

Airspeed indicator
Pressure altitude indicator
Rotor tachometer
Collective-pitch position indicator
Engine turbine discharge pressure indicator, each engine
Engine turbine discharge temperature indicator, each engine
Engine compressor discharge pressure indicator, each engine
Engine compressor discharge temperature indicator, each engine
Engine turbine speed indicator, each engine
Engine fuel flow indicator, each engine
Engine inlet temperature indicator, each engine
Clock
Data correlation counter
Fuel counter, both engines
Outside air temperature indicator
Tip cascade position indicator

Oscillograph 1, 50-Channel, Performance, Stability and Control, and Structural Load Measurements

Rotor rpm and azimuth
Collective-pitch position

Compressor discharge pressure, each engine
 Turbine discharge pressure, each engine
 Power lever angle, each engine
 Compressor variable geometry position, each engine
 Engine rpm, each engine
 Engine mount acceleration, vertical, each engine
 Engine mount acceleration lateral, each engine
 Blade-tip gas pressure, three blades (forward and aft ducts)
 Angle of sideslip
 Yaw-control duct pressure
 Yaw-control outlet duct pressure
 Y-duct crossflow vane position
 Longitudinal, cyclic-control position
 Lateral cyclic-control position
 Rudder pedal position
 Rudder surface position
 Rate of pitch
 Rate of roll
 N₁ governor shaft rpm, each engine
 Diverter valve position, each valve
 Rate of yaw
 Pitch attitude
 Roll attitude
 Directional heading
 Vertical acceleration at center of gravity
 Lateral acceleration at center of gravity
 Control actuator position, right hand
 Control actuator position, left hand
 Control actuator position, vertical
 Fuselage-longeron axial strain, station 321, upper left hand
 Fuselage-longeron axial strain, station 321, lower left hand
 Fuselage-longeron axial strain, station 321, upper right hand
 Fuselage-longeron axial strain, station 321, lower right hand
 Stabilizer bending, left hand forward spar
 Stabilizer bending, left hand rear spar
 Stabilizer bending, right hand forward spar
 Stabilizer bending, right hand rear spar
 Data correlation

Oscillograph 2, 50-Channel, Rotor Geometry, Blade and Hub
Structural Load Measurements

Rotor rpm and azimuth
 Collective-pitch position

Strap windup, blue blade

Blade pitch angle

Blade flapping angle

Hub tilt angle

Flapwise bending, station 63, front and rear spar, blue blade

Flapwise bending, station 75.4, front and rear spar, blue blade

Flapwise bending, station 100, front and rear spar, blue blade

Flapwise bending, station 140, front and rear spar, blue blade

Flapwise bending, station 220, front and rear spar, blue blade

Flapwise bending, station 270, front and rear spar, blue blade

Chordwise bending, station 90.75, front and rear spar, blue blade

Chordwise bending, station 149.0, front and rear spar, blue blade

Chordwise shear, station 23, feathering ball, blue blade

Vertical shear, station 23, feathering ball, blue blade

Duct torsion, station 15, inboard articulate duct, yellow blade

Blade torsion, station 38, blue blade

Blade torsion, station 83, blue blade

Main shaft bending, WL-12.0 in plane of blue blade

Main shaft bending, WL-12.0, 90 degrees to blue blade

Hub gimbal lug bending

Hub plate strain, forward and aft

Pitch-arm-link load (3 blades)

Swashplate drag-link load

Acceleration, lateral, upper bearing support

Acceleration, longitudinal, upper bearing support

Acceleration, vertical, fuselage at horizontal stabilizer

Acceleration, lateral, fuselage at horizontal stabilizer

Acceleration, vertical, cockpit

Acceleration, lateral, cockpit

Longitudinal cyclic position

Lateral cyclic position

Longitudinal stick force

Lateral stick force

Cascade valve position

Landing gear oleo position, both oleos

Airspeed

Temperature Recorder 1 (Chromel-Alumel), Rotor Temperatures

Blade-tip gas temperature, blue blade

Front spar temperatures, blue blade

Rear spar temperatures, blue blade

Flexure temperatures, blue blade

Rib temperatures, blue blade

Spar cooling-air temperatures (3 blades)

Outer-skin temperatures, blue blade
Gas-duct wall temperatures, blue blade
Rotor shaft temperatures
Tip transducer housing temperature
Root cooling-air temperature
Spar temperatures, forward and aft
Rotor spoke temperatures
Ball-joint inner surface temperature
Lower bearing housing temperature
Inboard articulate duct-seal temperature

Temperature Recorder 2 (Iron-Constantan), Structural Temperatures

Engine and engine accessory temperatures
Engine and diverter valve bay temperatures
Lateral pylon temperatures
Radial and thrust bearing housing temperatures
Aft fuselage and yaw valve compartment temperatures
Yaw duct and Y-duct blanket temperatures
Y-duct bay temperatures
Yaw valve outlet temperatures

APPENDIX II ROTOR BLADE FATIGUE LIFE COMPUTATION

The S-N curve used in calculating XV-9A rotor blade life in Appendix III of Reference 3 was based on fatigue testing of a full-scale root-end specimen of the rotor blade at room temperature.

To substantiate this S-N curve, additional fatigue testing has been conducted on reduced-scale specimens simulating the blade spar, the blade segment and its bolt attachment to the spar. Testing was conducted at room temperature as well as at a simulated 300-degree-F temperature difference between the blade segment and the spar. This temperature differential duplicates the conditions in the actual rotor blade as measured during flight testing of the XV-9A.

Flight Test Data

(Temperatures on segment 1 as shown on Figure 15 of Reference 1.)

<u>Thermocouple</u>	<u>Temperature (deg F)</u>
BS 1-1 Forward duct at front spar, station 96	Typical 580
B 13 Front spar at station 91	Typical 125
BS 1-5 Rear duct	Typical 525
B 3C Rear spar at station 90	Typical 100

Since the difference in temperature between the duct and spar is on the order of 425 to 455 degrees F, it seems reasonable to assume that the spar-to-segment temperature differential is approximately 300 degrees F.

The method used to compare the fatigue data from the reduced-scale spar fatigue test specimens with the full-scale root-end fatigue test specimens was to plot the cyclic bearing stress in the bolt hole versus the number of load cycles to failure or to the end of the test.

The data from the specimens tested at room temperature are in good agreement with the data from the full-scale root-end fatigue test specimen. All the specimens are in the same failure range (Figure 100). Failure in all the specimens occurred in the bolt holes. These are the bolt holes required for attaching the blade spars to the blade segments.

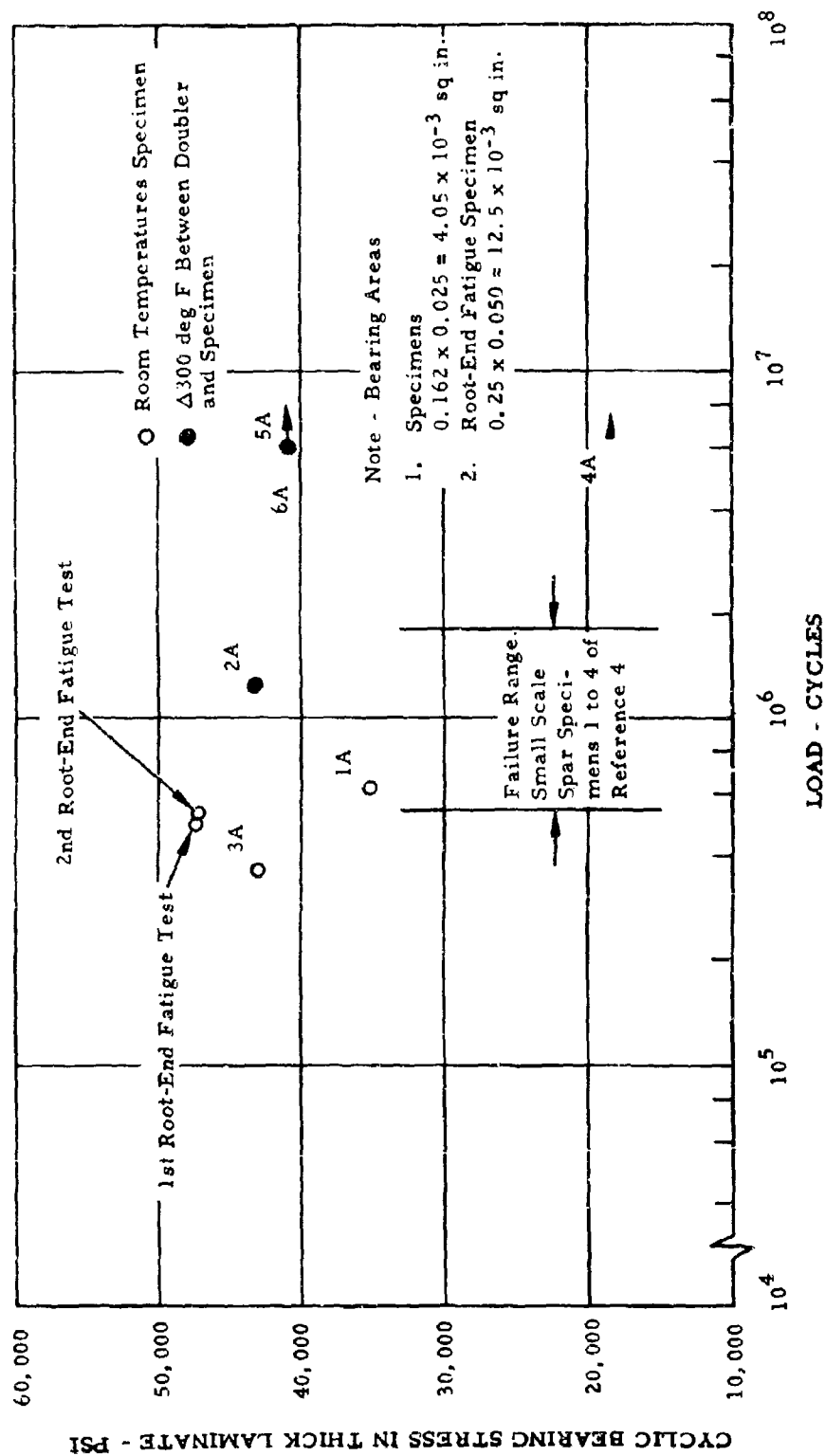


Figure 100. Cyclic Spar to Segment Bolt Bearing Stresses Versus Load Cycles.

Fatigue tests on reduced scale spar specimens tested at 300-degree-F differential temperature showed a considerable improvement in fatigue life (Figure 100). This improved life is attributed to the temperature differential strains in the blade segment causing the steady and cyclic bearing loads to be reduced for nominal bolt fit. Not only the reduction in steady and cyclic bolt load that results in lower stresses in the bolt hole but also the reduction in stress concentration factor K_t make for an improved loading condition at the bolt hole.

As illustrated in Figure 101, the ratio of cyclic bearing stress to cyclic tension stress at a loaded bolt hole has been shown to have a direct effect on the stress concentration factor K_t at the bolt hole (Reference 13, page 331, Figure 15.7).

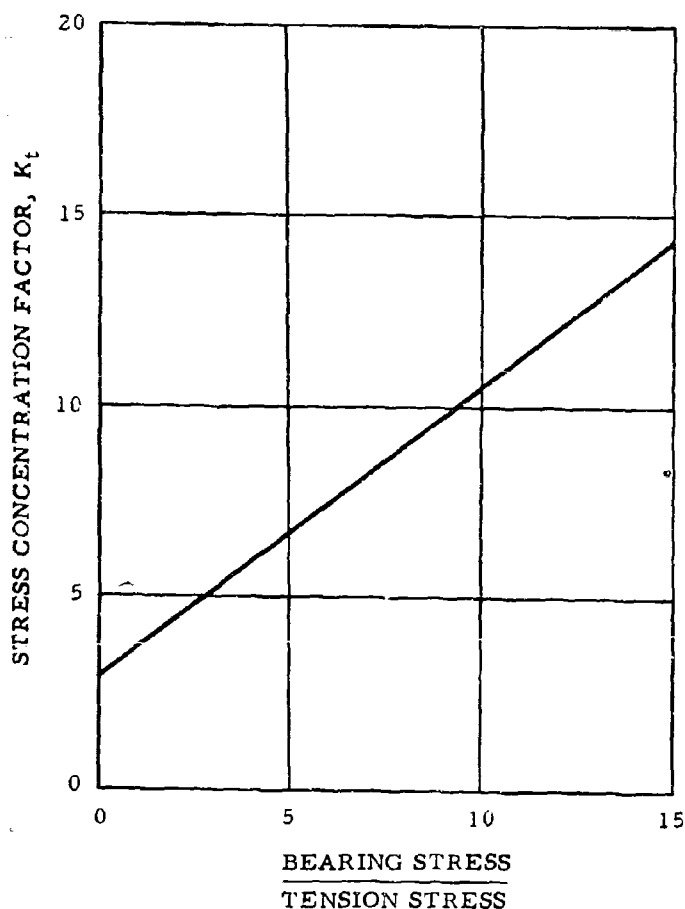


Figure 101. Bolt Hole Stress Concentration Factor.

From Figure 102, the calculated cyclic load carried by the spar-to-segment attaching bolts at room temperature is high and is not greatly affected by bolt fit until the bolt slop exceeds 0.010 inch. This range of load is representative of the bolt loads that the full-scale root-end fatigue test specimen experienced. This means that the full-scale test specimen experienced cyclic loads at the bolt hole 2 to 2-1/2 times greater than on the actual rotor blade for equal chordwise moments.

As a basis for comparing the data, the bolt bearing area is taken as the nominal bolt hole diameter (0.25 inch) times the 0.051-inch lamination. This is the thickest lamination in the spar and is next to the shear surface between the spar and blade segment. This is the lamination on which the bearing load tends to peak.

$$\text{Cyclic bearing stress} = \frac{593 \text{ lb}}{0.25 \text{ in.} \times 0.051 \text{ in.}} = 47,500 \text{ psi (Figure 103).}$$

The cyclic axial load in the spar from chordwise shear is 5,500 to 6,000 pounds, which gives a nominal cyclic tension stress of 6,000 psi.

The ratio of cyclic bearing stress to cyclic tension stress from the full-scale blade root-end fatigue test indicates that the K_t value is 8 to 9.

$$\frac{\text{Cyclic bearing stress}}{\text{Cyclic tension stress}} = \frac{47,500 \text{ psi}}{6,000 \text{ psi}} = 7.94$$

$$K_t = 9 \text{ (from curve)}$$

Applying this same stress ratio to the small-scale spar fatigue data and plotting this data on the S-N curve (Figure 104) show that an S-N curve with a greater endurance limit results when the temperatures are properly simulated. Figures 102 and 103 show that a reduction in steady bolt load resulting from differential temperature strains also causes a reduction in the cyclic bolt load. This is true for all bolt fits except tight fits. Since tight bolt fits, which are bolt fits of less than 0.002-inch bolt slop, are not typical of the actual XV-9A blade, this curve can be neglected. Inspection of the XV-9A spar bolt holes at the end of whirl tests and at the end of the 15-hour flight test program showed that the tolerances resulted in a tighter than a nominal bolt fit.

Using the cyclic load of 269 pounds from Figure 103 for a nominal bolt fit at the 300-degree-F differential temperature and dividing this by the bolt bearing area gives the following cyclic bearing stress.

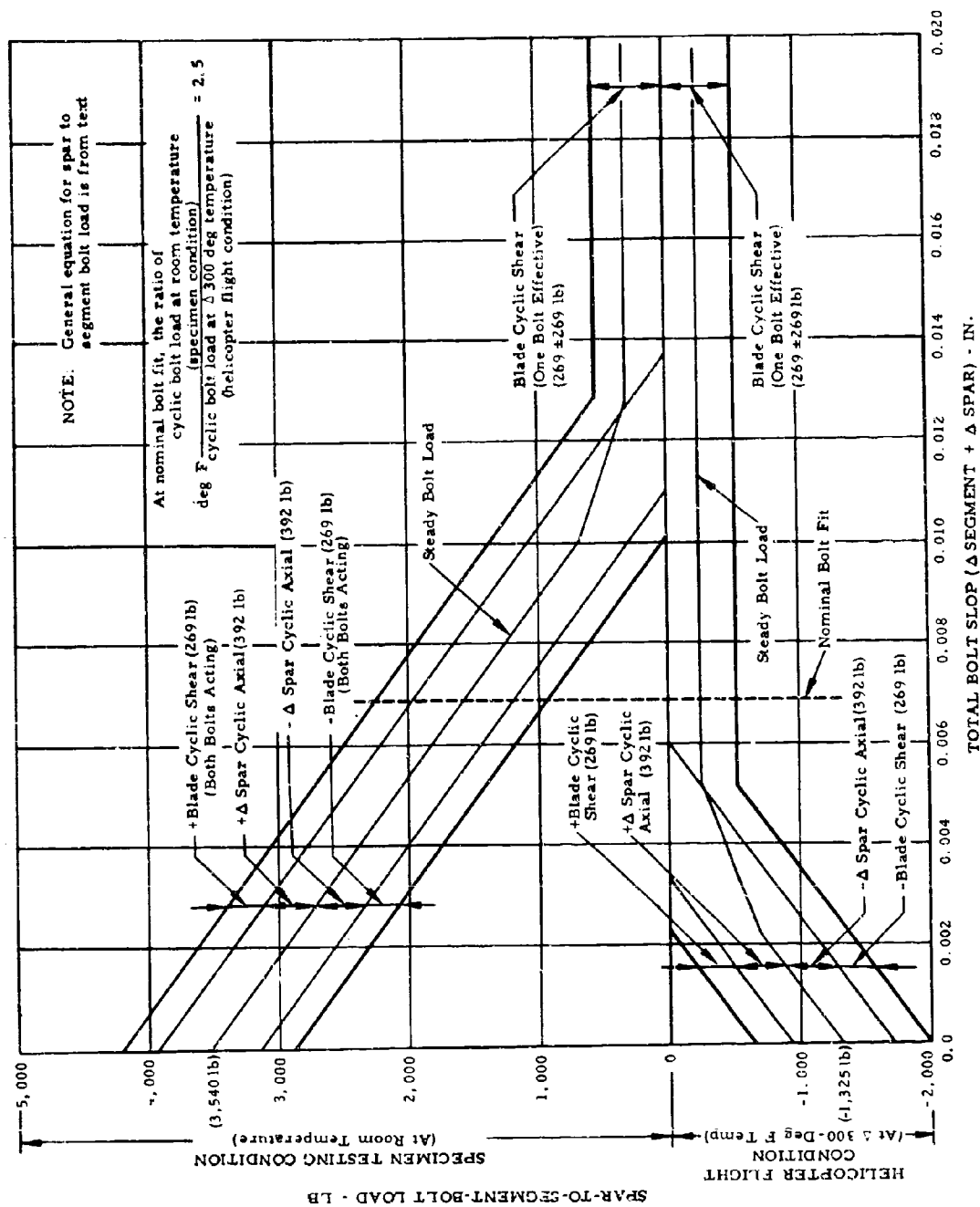


Figure 102. Spar-to-Segment-Bolt Load Versus Bolt Slop.

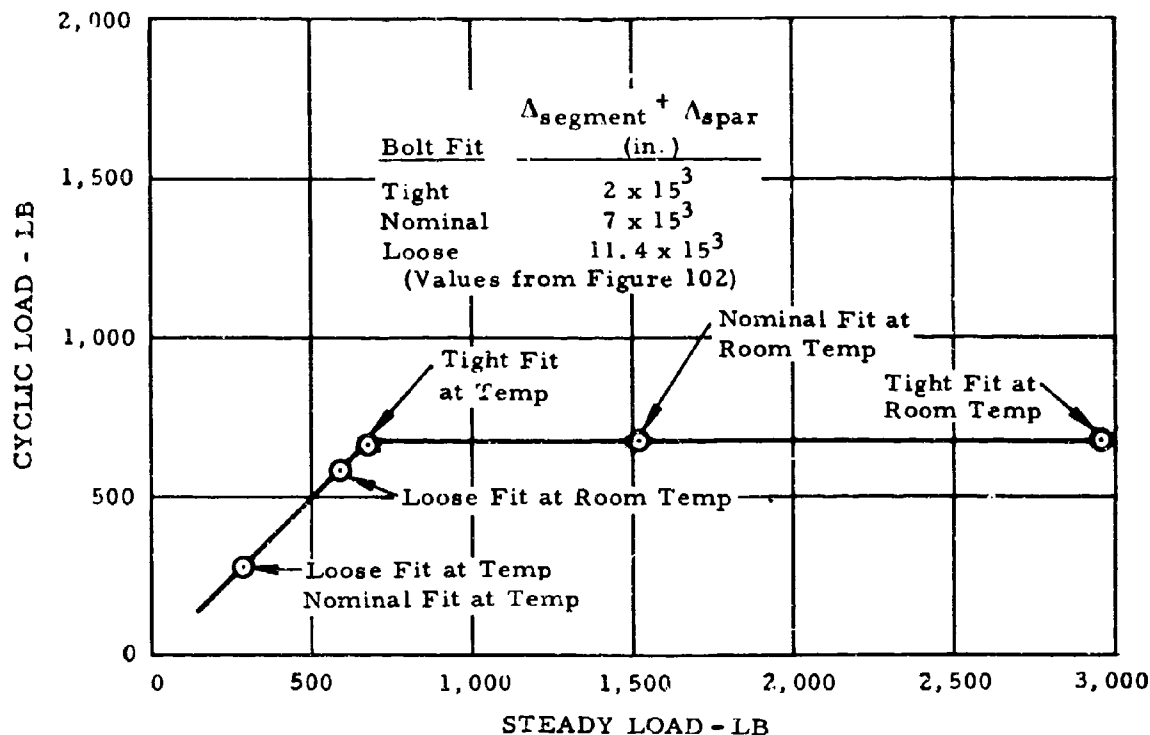


Figure 103. Bolt Loads - Spar to Segment Cyclic Load Versus Steady Load.

$$\text{Cyclic bearing stress} = \frac{269 \text{ lb}}{0.25 \text{ in.} \times 0.051 \text{ in.}} = 21,100 \text{ psi}$$

The value of K_t is calculated as follows:

$$\frac{\text{Cyclic bearing stress}}{\text{Cyclic tension stress}} = \frac{21,100 \text{ psi}}{6,000 \text{ psi}} = 3.52 \quad K_t = 5.5 \text{ (from curve)}$$

Applying this K_t value to the reduced scale spar specimens shows a further improvement in the S-N curve, as seen in Figure 104.

As seen in Figure 104, the S-N curve based on the full-scale blade root-end fatigue test specimen is too conservative to use in calculating blade life, because of the absence of temperature effects. A median curve is shown on Figure 104, which takes into account temperature effect. This S-N curve is also conservative to use in calculating blade life, as the

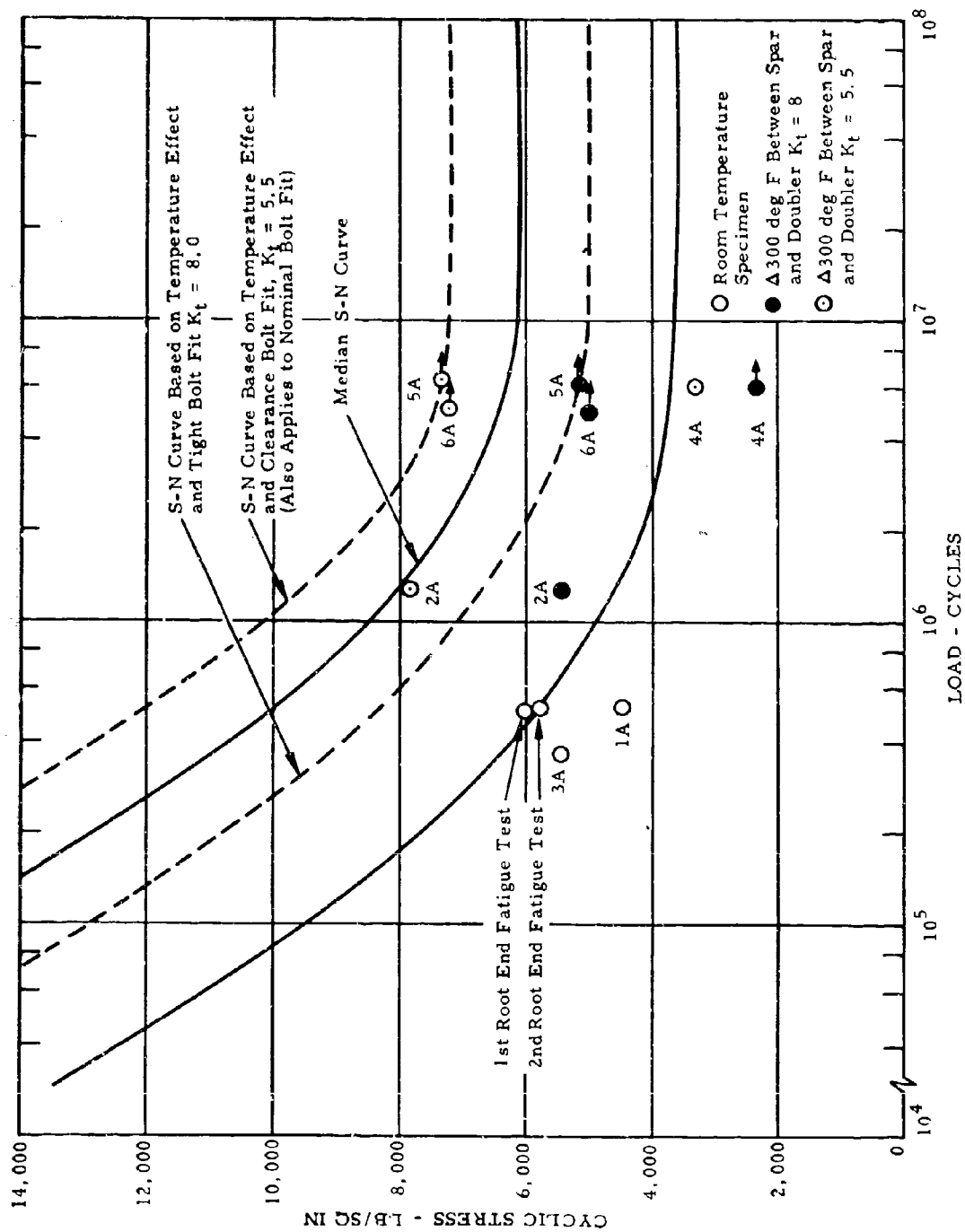


Figure 104. S-N Curve, Spars - Chordwise Bending Stress.

S-N curve for nominal bolt fit (which is the upper boundary of the range in Figure 104) should theoretically be used. This conclusion is justified by the inspection of the XV-9A spar, which showed that the hole sizes were toward the loose tolerance. The XV-9A blade life conservatively calculated, using the median S-N curve, shows a life of 1,590 hours (see Table XII). It is believed that this blade life is representative of the actual blade with its looser bolt tolerances and at the observed temperature conditions.

TABLE XII
ROTOR BLADE LIFE

Load Spectrum - Flight 35				
Cyclic Axial Load Sta 90.75 (lb)	Cyclic Axial Stress Sta 90.75 (lb/sq in.)	n Cycles Per 100 Hours	N Life Cycles From Median S-N Curve	n/N
5,500-6,000	5,790-6,310	135,000	6,000,000	0.0225
6,000-6,500	6,310-6,840	46,000	2,800,000	0.0164
6,500-7,000	6,840-7,370	10,000	1,900,000	0.0052
7,000-7,500	7,370-7,900	2,600	1,400,000	0.0019
7,500-8,000	7,900-8,410	900	1,050,000	0.0009
8,000-9,000	8,410-9,430	120	650,000	0.0002

$$\text{Service life} = \frac{100 \text{ hr} \times 0.75}{0.0471} = 1,590 \text{ hr}$$

This blade life is based on the median S-N curve shown on Figure 104.

ANALYSIS

General equation for spar-to-segment attachment bolt load:

$$\text{Bolt load} = \left[\Delta_{cf} - \left(\Delta_{\text{segment bolt slop}} + \Delta_{\text{spar bolt slop}} \right) - \Delta_{300^\circ F \text{ diff}} \right] \frac{AE}{L} +$$

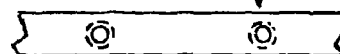
$$\left[\pm \Delta_{\text{spar cyclic axial}} \pm \left(\Delta_{\text{segment bolt slop}} + \Delta_{\text{spar bolt slop}} \right) \right] \frac{AE}{L} \pm \frac{\text{Chordwise Cyclic Blade Shear}}{2}$$

$$\frac{AE}{L} = \frac{29 \times 10^6 \times 0.062 \text{ sq in.}}{6.25} = 0.288 \times 10^6 \text{ lb per in.}$$

General equation for $\left(\begin{matrix} \Delta_{\text{segment}} \\ \text{bolt} \\ \text{slop} \end{matrix} + \begin{matrix} \Delta_{\text{spar}} \\ \text{bolt} \\ \text{slop} \end{matrix} \right) > \Delta_{300^\circ\text{F diff}} > \Delta_{\text{cf}} > \Delta_{\text{spar cyclic axial}}$

- a. Bolt load = [chordwise cyclic blade shear (269 ± 269 lb)]

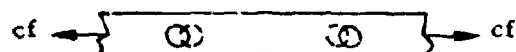
Inboard spar-to-segment bolt



a. Unloaded Spar

- b. Δ_{cf} = spar axial elongation due to centrifugal force = $\frac{60,000 \text{ psi}}{29 \times 10^6 \text{ psi}} \times$

$$6.75 \text{ in.} = 12.29 \times 10^{-3} \text{ in.}$$



b. Centrifugal Force Only; Room Temperature

- c. $\Delta_{300^\circ\text{F}}$ = segment elongation due to 300-deg F temperature differential between blade segment and spar = $300^\circ\text{F} \times 9 \times 10^6 \frac{\text{in.}}{\text{in.} \times \text{deg F}} \times$

$$6.25 \text{ in.} = 16.9 \times 10^{-3} \text{ in.}$$



c. $\Delta_{300^\circ\text{F}}$ Temperature Strain Has Overcome Bolt Slop and Centrifugal Force Strain (Net Temperature Strain)

- d. $\Delta_{\text{cyclic axial load}}$ = cyclic elongation of the spar due to cyclic chordwise blade bending

$$= \frac{6,000 \text{ lb}}{0.95 \text{ sq in.}} \times \frac{6.25 \text{ in.}}{29 \times 10^6}$$

$$= \pm 1.36 \times 10^{-3} \text{ in.}$$



d. Bolt Slop Has Relieved Bolt Centrifugal Force Strain and $\Delta_{300^\circ\text{F}}$ Strain (No Net Strain)

APPENDIX III
RESULTS OF SIMULATED HOT CYCLE SPAR TESTS WITH THERMAL
GRADIENTS BETWEEN SPAR AND DOUBLER

SUBJECT

This appendix presents the results of small-scale spar specimen fatigue tests conducted in the HTC-AD structures test laboratory during the months of June and July 1965.

PURPOSE

The purpose of the tests was to determine the effect of thermal gradients between the spar and simulated segments on the fatigue strength of a laminated specimen simulating the spar of the XV-9A research vehicle.

TEST SPECIMEN

Each of the six specimens was made up of 15 AM355 stainless steel laminations bonded together between laminations with HT 424. Lamination thicknesses were: first, 0.025 inch; second through fourteenth, 0.007 inch; and fifteenth, 0.009 inch. A doubler of 0.050 inch by 1.0 inch was bolted to one side of each specimen, simulating a segment attachment on an actual blade. See Figure 105.

Specimen details are shown in Figure 106.

TEST SETUP

The specimens were run in an axial tension fatigue machine of the below-resonance type operating at a speed of 30 cps.

When the specimens were run with heat applied, a quartz lamp heater was located on the doubler side of the specimen. Insulating and reflecting materials were located so that only the doubler was heated. Figures 107 through 110 show the hot and cold setups.

TEST PROCEDURE

The fit of the 0.163-inch-diameter pin to the holes in the specimen and doubler was an important criterion. Pin sizes, hole sizes, and hole spacing in specimen and doubler were all carefully measured to obtain the desired fits.

STRAIN GAGED DOUBLER

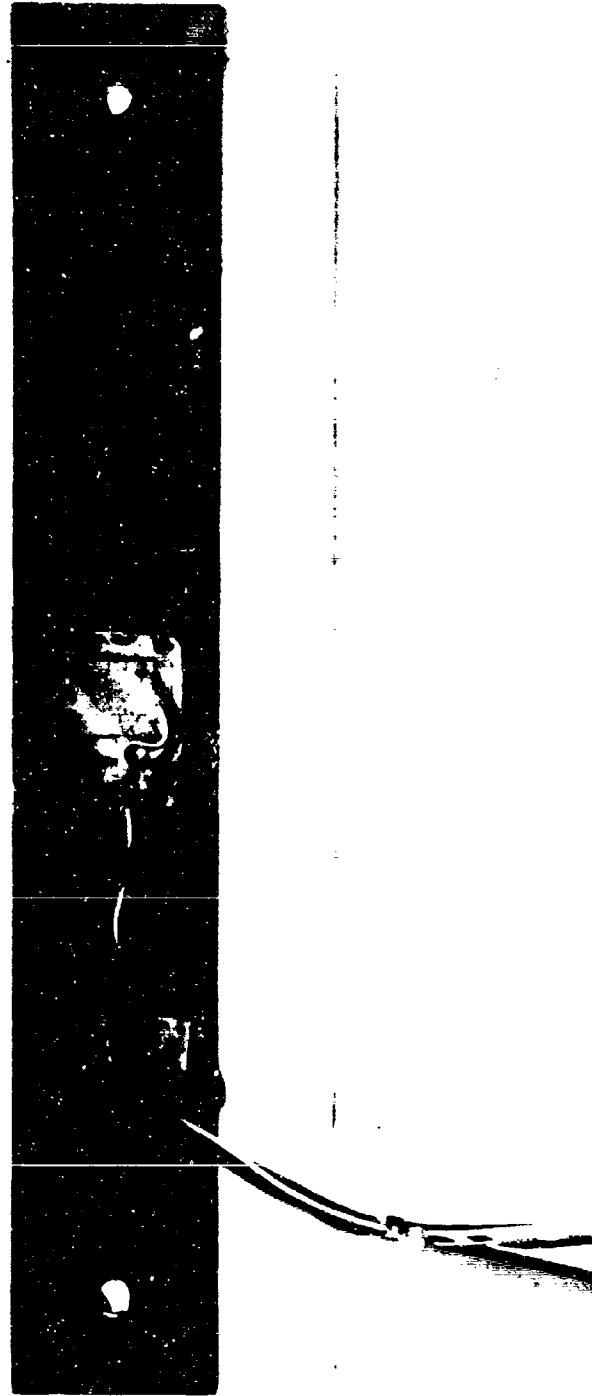


Figure 105. Typical Doubler in Milled Out Area and Thermocouples.

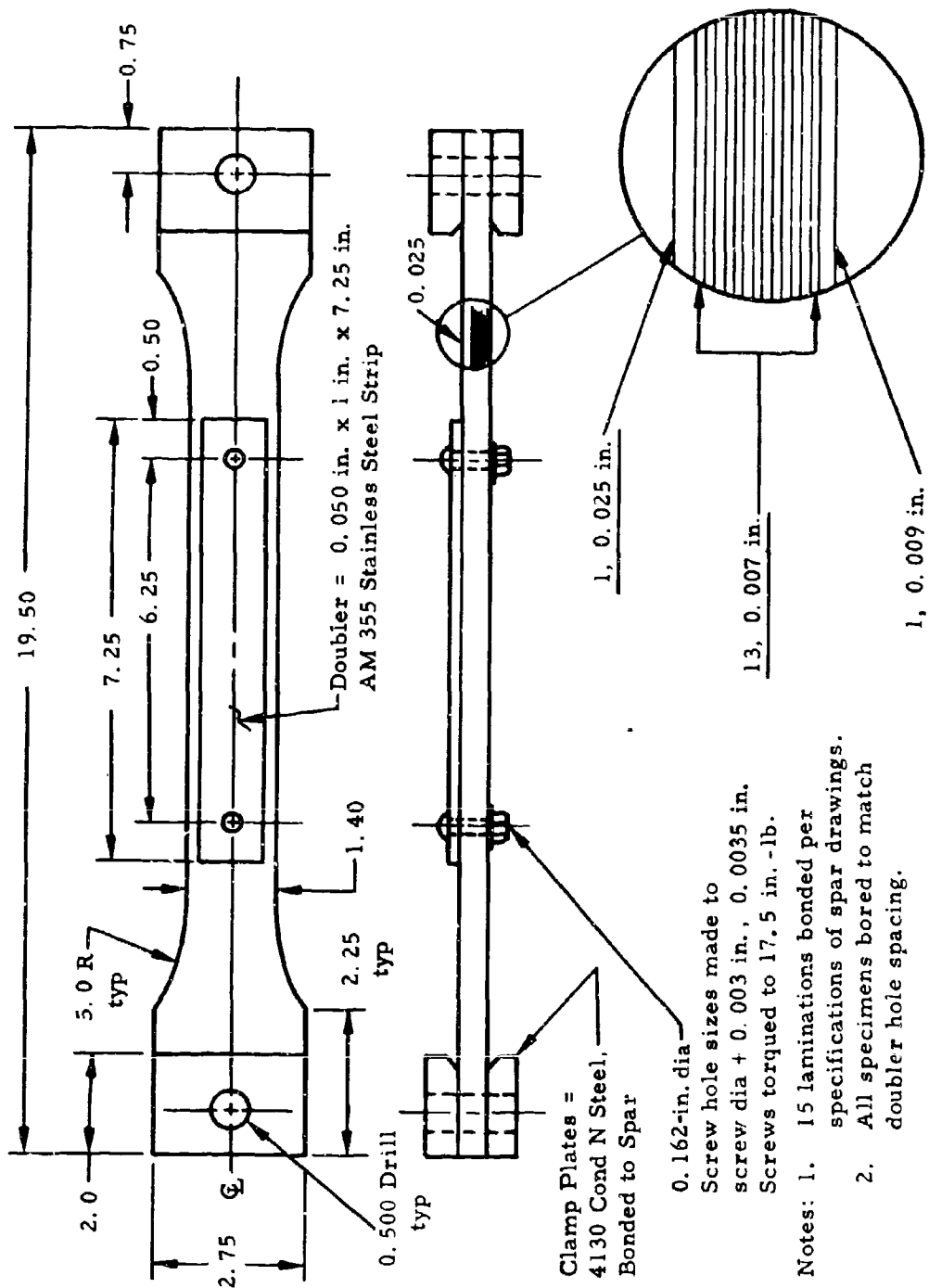


Figure 106. Fatigue Test Specimen.

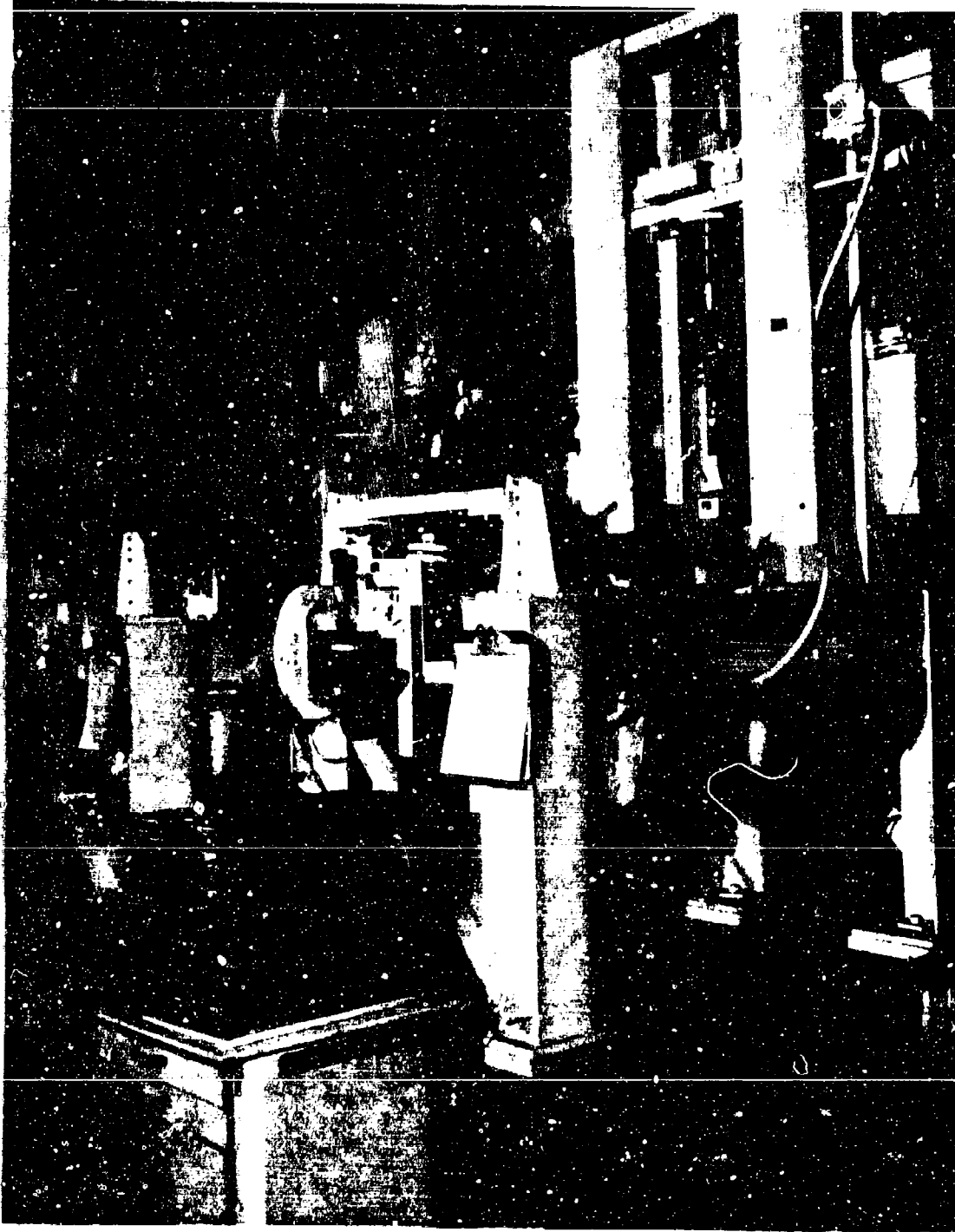


Figure 107. Overall View of Cold Specimen Setup (Room Temperature).

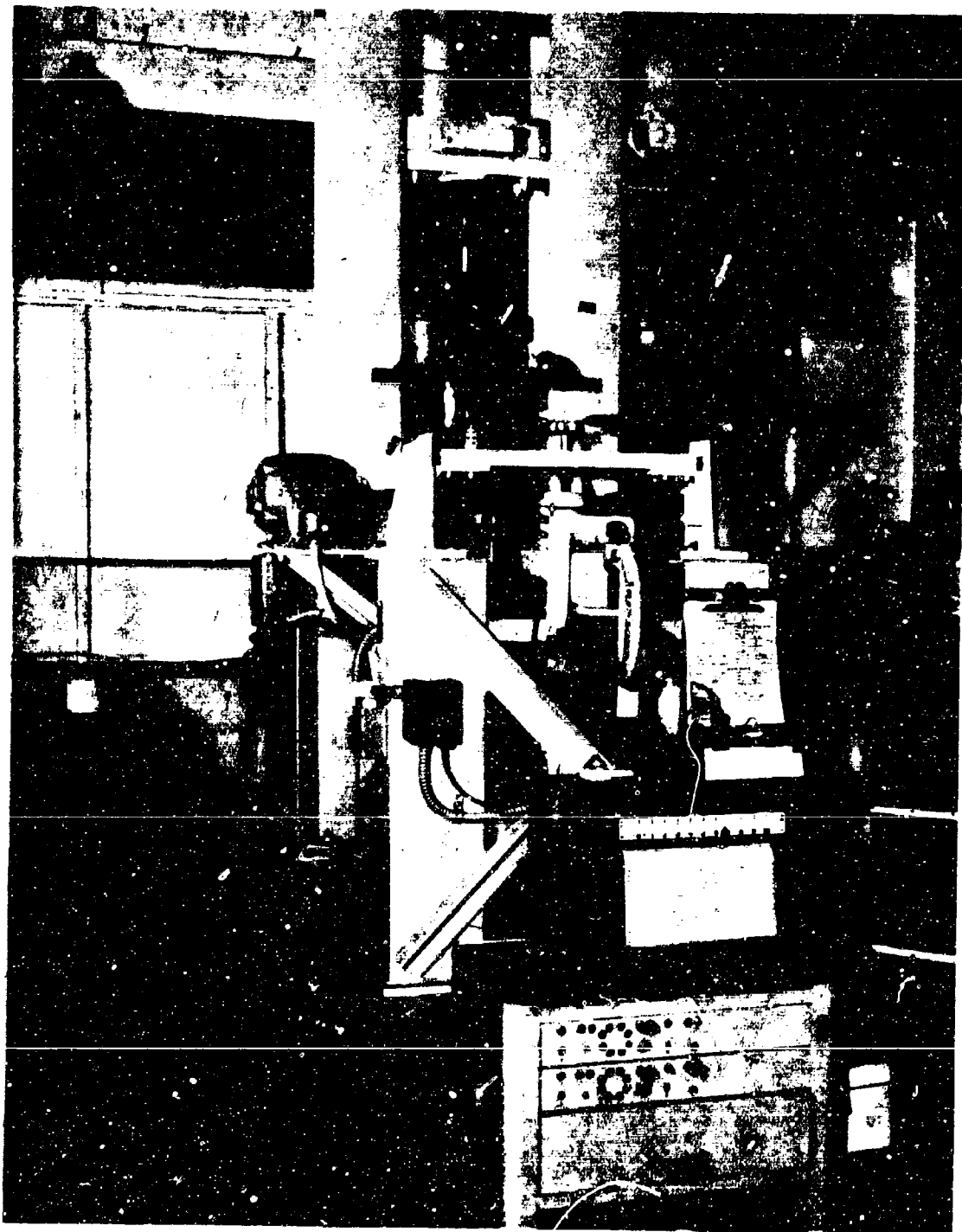


Figure 108. Overall View of Heated Specimen Setup.

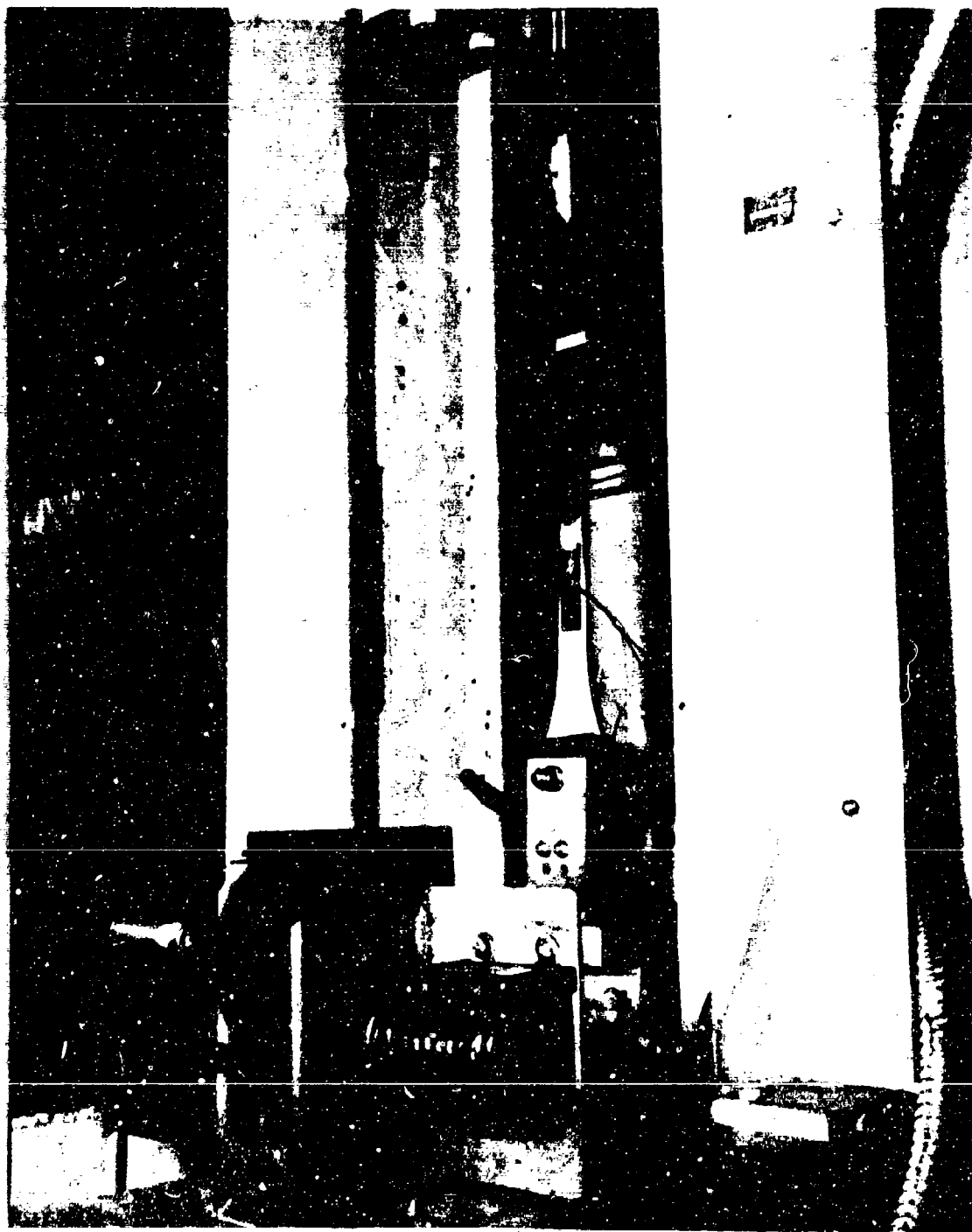


Figure 109. Closeup of Cold Specimen.



Figure 110. Closup of Heated Specimen.

After assembly of the doubler with the spar, the specimen was installed in the test machine and run at room temperature to obtain cold load distributions. The specimens were then heated to obtain a 300-degree-F temperature differential between the far side of the spar and the doubler and run at the same external loads as cold.

INSTRUMENTATION

The load applied to the entire specimen was monitored by a strain-gaged load cell that was in series with it.

The proportion of that load that went into the doubler was monitored by strain gages mounted on the doubler.

The temperature measurements were made with iron-constantan thermocouples monitored on a recording potentiometer.

TEST LOADS

The loads applied to the specimen, externally, were $11,000 \pm 1,500$ pounds. The amount of load that was induced into the doubler was influenced by many factors, the primary factors being temperature, hole diameter, center distances, and pin diameter.

The loads induced into the doubler were as follows:

Specimens at room temperature	Steady	545 to 1,037
	Cyclic	± 144 to ± 195
Specimens run at elevated temperatures	Steady	0 to 300
	Cyclic	± 74 to ± 175

TEST RESULTS

Table XIII indicates the loads, fits, conditions, and other pertinent data recorded during the tests. Figures 111, 112, and 113 illustrate the specimens after completion of testing.

TABLE XIII
FATIGUE TEST RESULTS

Specimen Number	Fit of Doubler to Spar	Temperature of Specimen During Test	Steady Load Recorded (lb)	Cyclic Load Recorded (lb)	Cycles Tested	
					To Failure	With No Failure
1	Nominal ^a	Ambient (70°F)	600	144	521,000	
2 } Same Specimen	Tight ^b	Ambient (70°F)	1,037	187		1,000
	Tight ^b	300°F Differential ^c (typical)	300 ^d	175	1,290,000	
3	Tight ^b	Ambient (70°F)	732	175	361,000	
4	Nominal	Ambient (70°F)	545	185		1,000
4	Nominal	300°F Differential	0	74		6,000,000
5	Tight	Ambient (70°F)	728	189		1,000
5	Tight	300°F Differential	0	166		6,000,000
6	Tight	Ambient (70°F)	783	195		1,000
6	Tight	300°F Differential	0	162		5,000,000

^aCenter distances same; hole sizes same

^bDoubler center distances 0.005 inch shorter than spar; holes same size.

^cMaximum temperature of doubler outer surface = 410°F.

^dMaximum temperature of spar opposite side = 110°F.

^eDoubler buckled, causing compression in doubler.

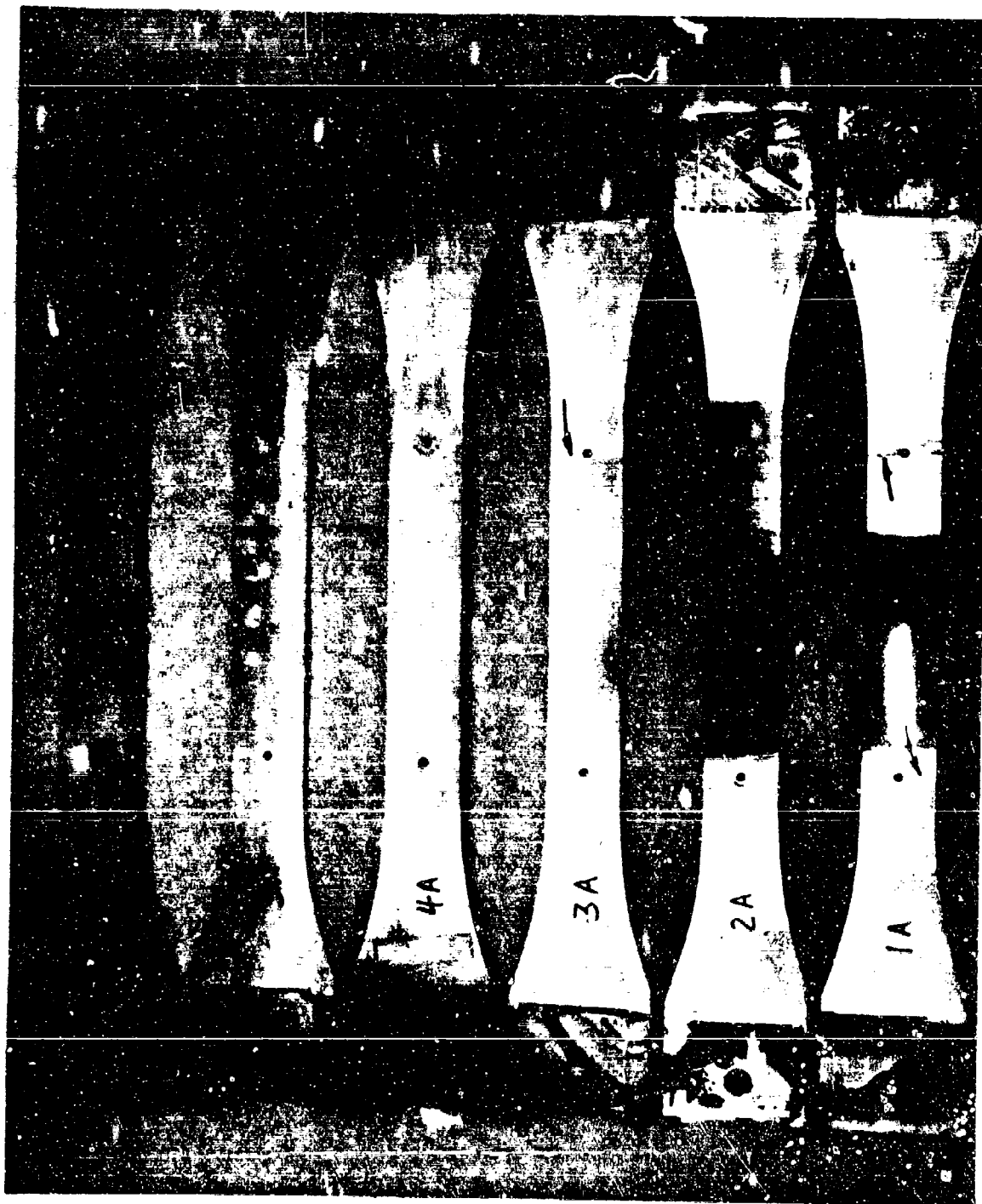


Figure 111. View of Side "A" of Specimens After Test Failures in 1 and 3.

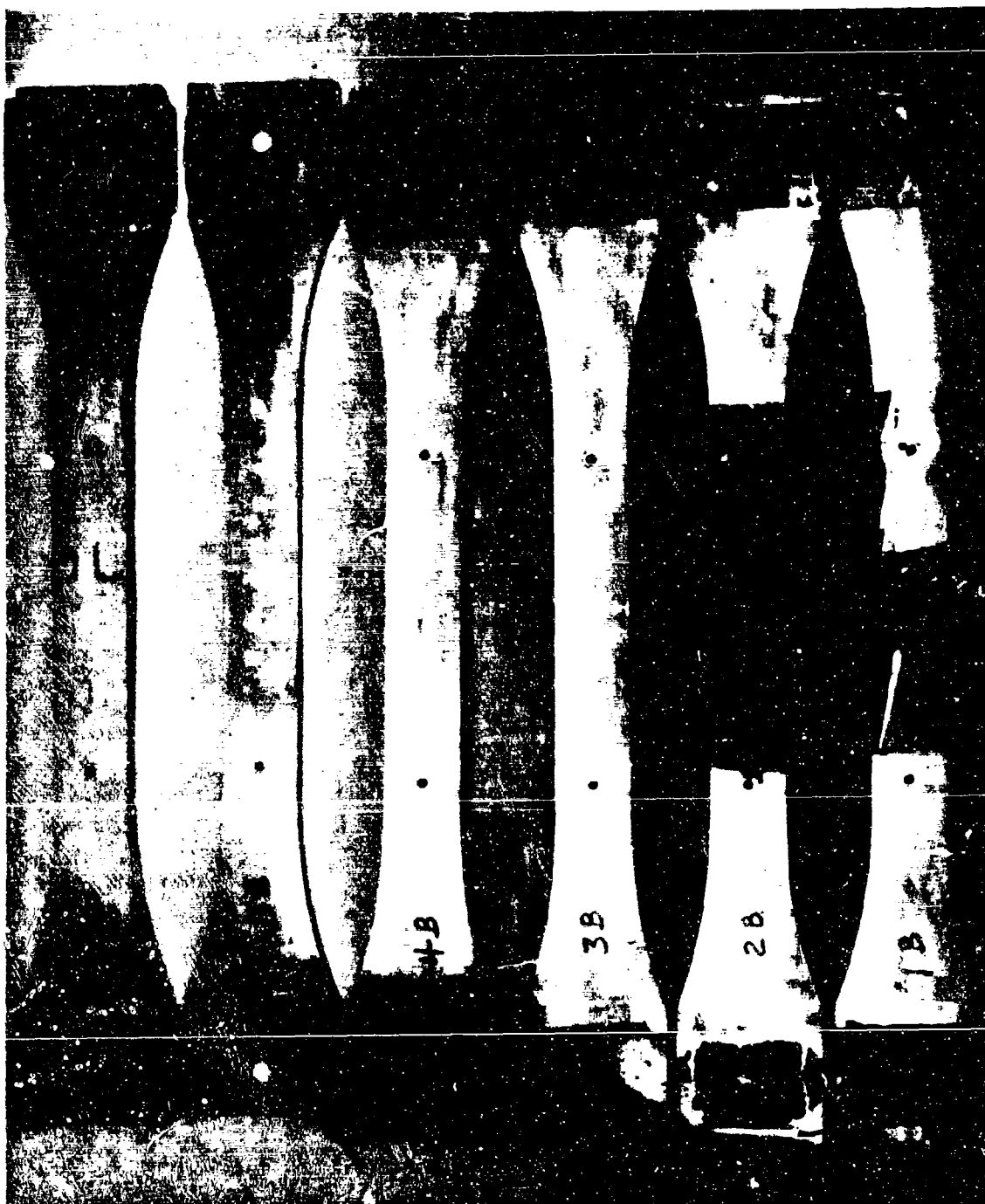


Figure 112. View of Side "B" of Specimens After Test Failure in Specimen 2.

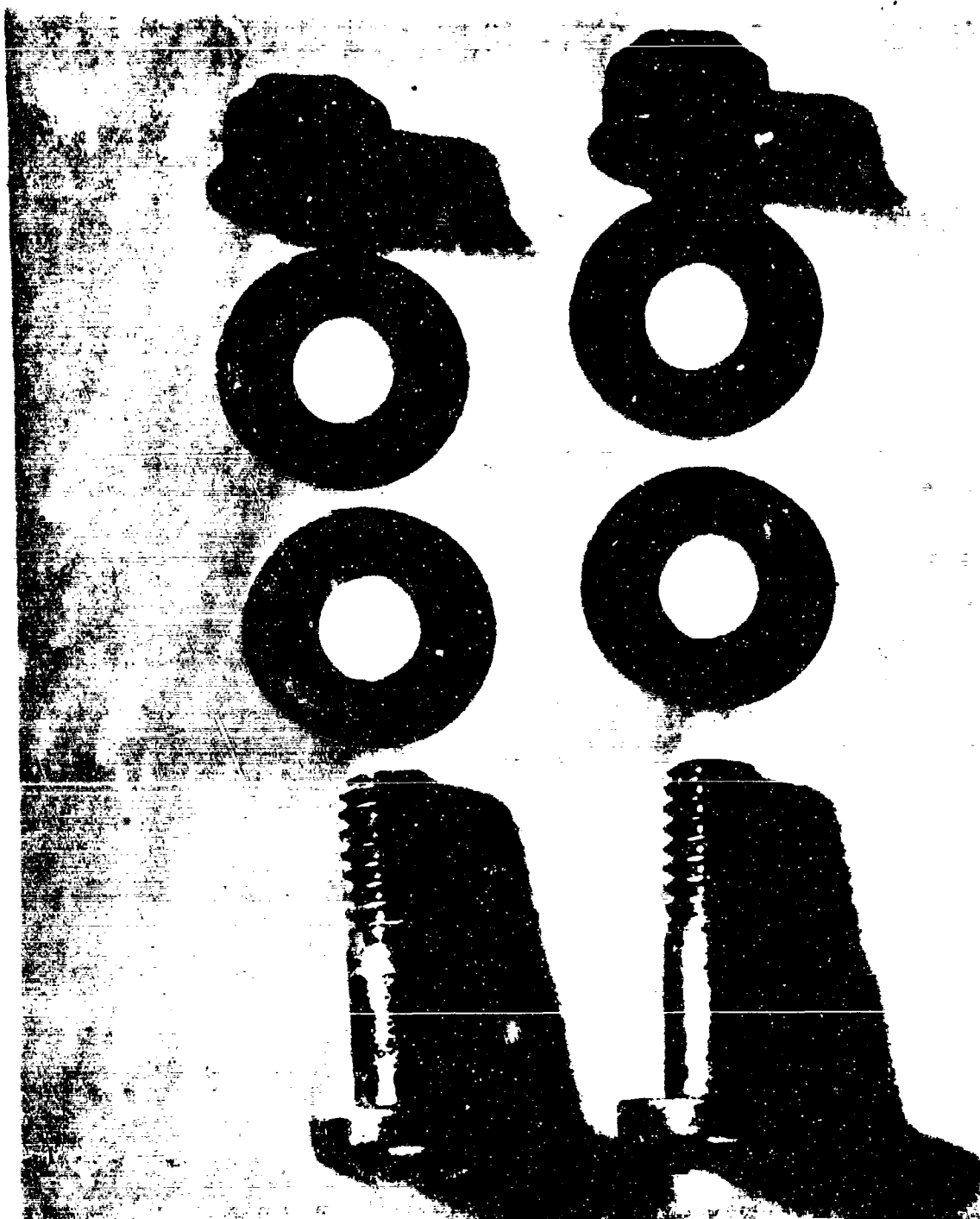


Figure 113. Typical Pins Removed From Doublers - Note Impressions From Spar Laminations.

CONCLUSIONS

High accuracy of the steady loads recorded in the doubler when heated was not possible because:

An increase in temperature changes the bridge balance position, since the interconnecting wires were not of matched resistance.

A temperature gradient existed between the two sides of the doubler, causing an arching effect and thus creating some bending strain that was recorded by the gages. The gages were located in a milled-out section close to the neutral axis. However, it is practically impossible to be absolutely insensitive to some bending.

From the results obtained, it can be concluded that the application of heat, which causes the reduction in steady stress in the doubler, will substantially increase the endurance limit of the specimens.

APPENDIX IV
DESCRIPTION OF TASKS ACCOMPLISHED DURING
INSPECTION AND MAINTENANCE PERIOD

Prior to the start of flight testing, a comprehensive inspection of the rotor system, propulsion system, fuselage, empennage, landing gear, electrical and hydraulic systems, flight controls, and test instrumentation was accomplished to assure flight safety and proper functioning during the flight test program. Minor modifications were incorporated to improve operation of the aircraft, systems, and test instrumentation. These changes were determined by the inspection activities and by analysis of test data and flight operating experience from the previous 15-hour flight test program. A description of the items of inspection and maintenance that were accomplished prior to start of the testing follows. A configuration and change log is included as Appendix VI.

ROTOR AND HUB COMPONENTS

Rotor Blade Disassembly

The rotor blades were removed from the aircraft and disassembled to the extent of removing leading and trailing edges, spars, and retention straps. Inspection of components disclosed the following:

1. Flexures in the root end were inspected as permitted through access holes using a borescope. These flexures were in the area where cracks had occurred during the blade root-end fatigue tests (Reference 4). No cracks were found. Some corrosion was present on the flexures. Laboratory analysis showed the corrosion products to be those normally encountered during manufacturing processing and those resulting from subjection of components to the moderate corrosive atmosphere of the contractor's plant location close to the ocean.
2. Inspection of the spars showed no cracks. Each hole was scanned using a 16- to 20-power glass. Particular attention was given the edges of the laminations and the area adjacent to the holes.
3. Retention straps were removed and inspected. There was no evidence of cracks or undue fretting. No evidence of fretting was present at the bolted end, indicating that

sufficient bolt torque had been applied and maintained. The Teflon coating was partially worn off where the straps contacted the shoe, and the epoxy paint on the shoes chipped off in places on removal of the straps. No damage could be found from the forward strap inboard-rib interference encountered during the controls check on the first flights.

4. Spar-to-blade-segment attach bolt torques were measured on removal. Some bolts showed a dropoff in torque and evidence of fretting. There was no set pattern to these discrepancies.
5. Segments were inspected by looking down the ducts from the inboard end with a bright spotlight, and also from the outboard end by using a mirror to look past the cascade turning vanes. Ducts appeared to be normal. Some leakage from the segments was evident on the three outboard segments of the blue blade. A smaller amount was noted at the same stations on the other blades. Holes in segments were measured. No change in diameters was noted.
6. The leading and trailing edges were found to be in good condition.

Rotor Blade Reassembly

On reassembly, the following items were accomplished:

1. Spars were cleaned, and any scratches or discontinuities on the surface of hole bores were polished out.
2. The Armaion antifretting material was replaced.
3. All quarter-inch-diameter bolts attaching the spar to the segments were replaced. All other bolts were magnafluxed before installing.
4. Instrumentation on the blue-blade spar was replaced.
5. Retention straps were cleaned, and all scratches and discontinuities were polished out, including the hole bores.

6. Retention strap attach bolts were magnafluxed. The shoes were sanded and recoated with epoxy paint.
7. Blade tip cascade areas were reduced approximately 3.2 square inches per blade (9.6-square-inch total) by means of an adjustable restriction attached to the turning vanes.

Hub Area Inspection

Inspection of the hub area showed only one discrepancy -- chipping of the flame plating on one articulating duct where it contacts the lip seal. This chipped duct was replaced, as were all three lip seals. There was no evidence of unusual gas leakage or wear. Particular attention was given to the retention strap attach bolt holes and the area around them.

STRUCTURAL COMPONENTS

Fuselage Inspection

No evidence of overheating or overloading of fuselage structure could be found. The entire fuselage was found to be in good condition.

Power Module Inspection

A few cracks (four) were found in the power module. Most were in the area of leading- and trailing-edge fairing attachment to the fuselage and nacelle. They were regarded as minor and were stop-drilled. Other than this, the power module structure was in excellent condition.

Empennage Inspection

Inspection of the stabilizers and rudders was completed without anything abnormal being found.

Landing Gear Inspection

A check of the charge pressure on the main landing gear oleo showed the pressure to be too high (400 psi instead of 200 psi in the full extended position). The pressure was reduced to the proper value.

Miscellaneous Items Accomplished on Reassembly

1. Fairings were made for the fuselage-empennage intersection, landing gear attach fitting at the fuselage, and the nacelle stiffening strut at the fuselage.

2. Nacelle stiffening struts were installed between the nacelle and fuselage. The ballast was removed from the nacelles.
3. The rotor blade inboard rib flanges were ground to minimize the interference with the forward retention straps.
4. Additional "snap vents" were added to the fuselage to provide additional cooling for desert operation.
5. The rudder was rerigged for 2 degrees more right rudder (7-degree total) with pedals and yaw valve in neutral position. To accomplish this rerigging, it was necessary to clear a few rudder hinge interferences.
6. The stabilizer setting was lowered 1/2 degree, from 3 degrees to 2-1/2 degrees.

PROPULSION SYSTEM

The following propulsion system tasks were accomplished during the inspection:

1. An air scroll was added to each engine-mounted electrical generator to improve cooling.
2. T₂ temperature probes were installed -- three per engine inlet.
3. Engine S/N 027 was removed and shipped to the manufacturer for inspection and "zero timing".
4. Engine S/N 101 was built up and installed as engine 1.
5. The location of thermocouples was reviewed. Thermocouples were deleted, replaced, and added as required for a total of 83 revisions.
6. All hot-gas-system duct joints were checked for evidence of leakage. Instructions were issued for initial clamp torques and for periodic checks.

During initial engine runs, the idle on engine S/N 101 was set to 75-percent N_G , and the flight idle (used by the rotor overspeed system) was adjusted to 93.3-percent N_G .

FLIGHT CONTROL SYSTEM

Control Cylinder Rework

The three cylinders were removed, disassembled, and reworked to incorporate a modified piston and piston rod pin. In addition, the tail housings were instrumented.

The cylinders were proof-tested, leak-tested, and function-tested. The high-pressure relief valves were reworked to obtain the proper relief settings.

Cyclic Stick "Pulser"

A device was added in the cockpit so that the pilot may pulse the cyclic stick 1/2 inch in a repeatable manner. This device was used only for specific stability tests and is not normally attached to the cyclic stick.

Pilot Linkage Inspection

Each pilot rod bearing, bellcrank, and rod was inspected for abrasion, bends, binding, looseness, cracks, seal damage, and lubrication retention. Bearings were regreased as required. No discrepancies were noted. Swash plate bearing torque was measured (120 to 150 lb-in.) and was satisfactory. The entire power linkage was inspected. Particular attention was given to seal condition, grease retention, and grease condition. No discrepancies were found. The control pushrods inside the rotor shaft were removed, cleaned, and inspected for heat damage, bearing condition, abrasion, and straightness. The rods were magna-fluxed for cracks. Results of the inspection were satisfactory with the exception of one rod-end shank nut, which was cracked as a result of overtorque. All nuts on all rods were replaced and torqued properly. The rods were repainted and reinstalled. The control system was rerigged and checked for interferences. Collective and cyclic travels were measured. No interferences were encountered, and the travels were correct. The outboard pitch link and control cylinder strain gages were calibrated.

Yaw Control

The portion of the control cable between the cockpit bulkhead and the yaw control valve was replaced with a 1/4-inch cable. The rudders were rigged so that they were deflected 7 degrees right for the closed yaw control valve position. One push-pull rod-end fitting was extended to accommodate this rigging. The yaw control linkage bearings, push rods, pulleys, and cables were inspected. No discrepancies were found.

BRAKE SYSTEM

The brake mechanical components were inspected. All components were in a satisfactory condition. The brake hydraulic components were inspected for damage, abrasion, tube kinks, and leakage. The system was tested to 1,000 psi. No discrepancies were found. The tailwheel lock cable system was inspected for wear, binding, and damage and found to be satisfactory.

CASCADE-VALVE ACTUATION SYSTEM

The cascade-valve actuator supply tube was removed and inspected for damage. The support clips in the area of the blade root were damaged as a result of personnel mishandling. These clips were removed and replaced with heavier clips. The joint between the spar tube and flexures was rebuilt to permit flexure removal without requiring removal of the blade strap bolts.

The cascade-valve position-indicating switch wires and the cooling-air thermal switch wires were removed and replaced with a lighter bundle. A more secure attachment method was devised and used.

The cascade-valve actuating cylinders were removed and inspected and were found to have excessive leakage due to piston rod galling. The piston heat treat was modified and the piston rod was chrome-plated for buildup and reground. All rubbing surfaces were treated with Electrofilm. The cylinders were assembled with new seals, leak-tested, and proof-tested to 3,000 psi. The leakage was satisfactorily low.

The hub plumbing was inspected and found to be satisfactory. The hub flexures were removed, inspected, and subjected to Zygl examination. No discrepancies were found. The cascade-valve actuating system was reassembled and tested to 3,000 psi. Results were satisfactory. A thermal relief valve was installed on the cascade-valve actuating system supply bottles.

HYDRAULIC SYSTEMS

All high-pressure hoses were removed and replaced with factory-swaged assemblies and proof-tested to 7,000 psi. All filter elements were removed and examined for contamination accumulation. Results were satisfactory. The N_f hydraulic subsystem (rotor-speed governing) was modified to relocate the filters in the motor-case drain line and to place pressure transducers at the motor inlet and outlet ports.

The N_f pumps and motors were removed and bench-checked for case drain flow and for friction torque. Results were satisfactory.

The hydraulic system was inspected for leakage, damaged lines and components, abrasion, heat damage, kinks, cracks, signs of interference with moving items, excessive dirt, and proper fitting security. No discrepancies were noted.

The hydraulic system was filled, bled, and leak-checked. No discrepancies were noted. The system was then proof-tested to 3,750 psi to test system relief valves.

ELECTRICAL SYSTEM AND COCKPIT INSTRUMENTS

The crossflow warning system components were removed. The Y-duct sensing vane was secured in a vertical position. Engine low-speed warning switches, lights, and a disarming control were installed. A data correlation counter and "no record" lights were installed on the instrument panel in place of the crossflow indicator and the engine mismatch lights.

The voltmeter and the ammeters were removed and placed on the auxiliary cockpit instrument panel. The yaw indicator was removed and placed in the position of the unused electrical outside-air temperature indicator. (A direct-operating outside-air temperature indicator was still installed on the cockpit canopy.) The 400-cps frequency meter adjustment bridge was moved to make room for the revised radio installation.

The ARC 73 and ARC 45 controls and the radio control box were installed in the control console. The ARC 45 control and the radio control were installed immediately forward of the power levers, and the ARC 73 control was mounted alongside the console on the left-hand side. The cables to the transceiver units were run through the cockpit bulkhead. The ARC 73 and ARC 45 transceivers and the dynamotor were mounted above the forward fuel cell.

Cooling-air inlet ducts for the generators were fabricated and installed. All electrical system components and wiring were inspected for fraying, abrasion, heat damage, interferences with operating mechanisms, and general security. No discrepancies were noted.

TEST INSTRUMENTATION

See Appendix I.

APPENDIX V
ROTOR CONTROL SYSTEM ROD END FATIGUE TEST

SUBJECT

This appendix concerns an axial fatigue test of a typical XV-9A rotor control system rod end. This test was conducted in the HTC-AD structures test laboratory in May 1965.

PURPOSE

The purpose of the test was to substantiate the fatigue life of the rod end for increased flight loads.

SPECIMEN

The specimen consisted of two P/N 285-0326-7 rod ends, Shafer model YD-252.

TEST SETUP

The rod ends were installed in each end of a 4-inch-long steel rod, simulating the procedure specified in drawing 285-0307. The specimen assembly was mounted in an axial fatigue test machine. This test machine is a subresonant-type operating at 30 cycles per second, with the cycles recorded on a mechanical counter. Steady and vibratory loads were monitored from a strain-gaged load cell set up in series with the specimen assembly. This setup is shown in Figures 114 and 115.

RESULTS

The rod end successfully withstood a total of 1,264,700 cycles of the following fatigue test loadings:

2,310 \pm 5,080 pounds for 785,500 cycles
5,100 \pm 5,080 pounds for 479,200 cycles

This was equivalent to 80 hours of flight operation at the maximum loads encountered in flight. Inspection after test revealed slight brinelling felt on the bearing race when slowly rotated by hand; however, there was no evidence of incipient fatigue failure.

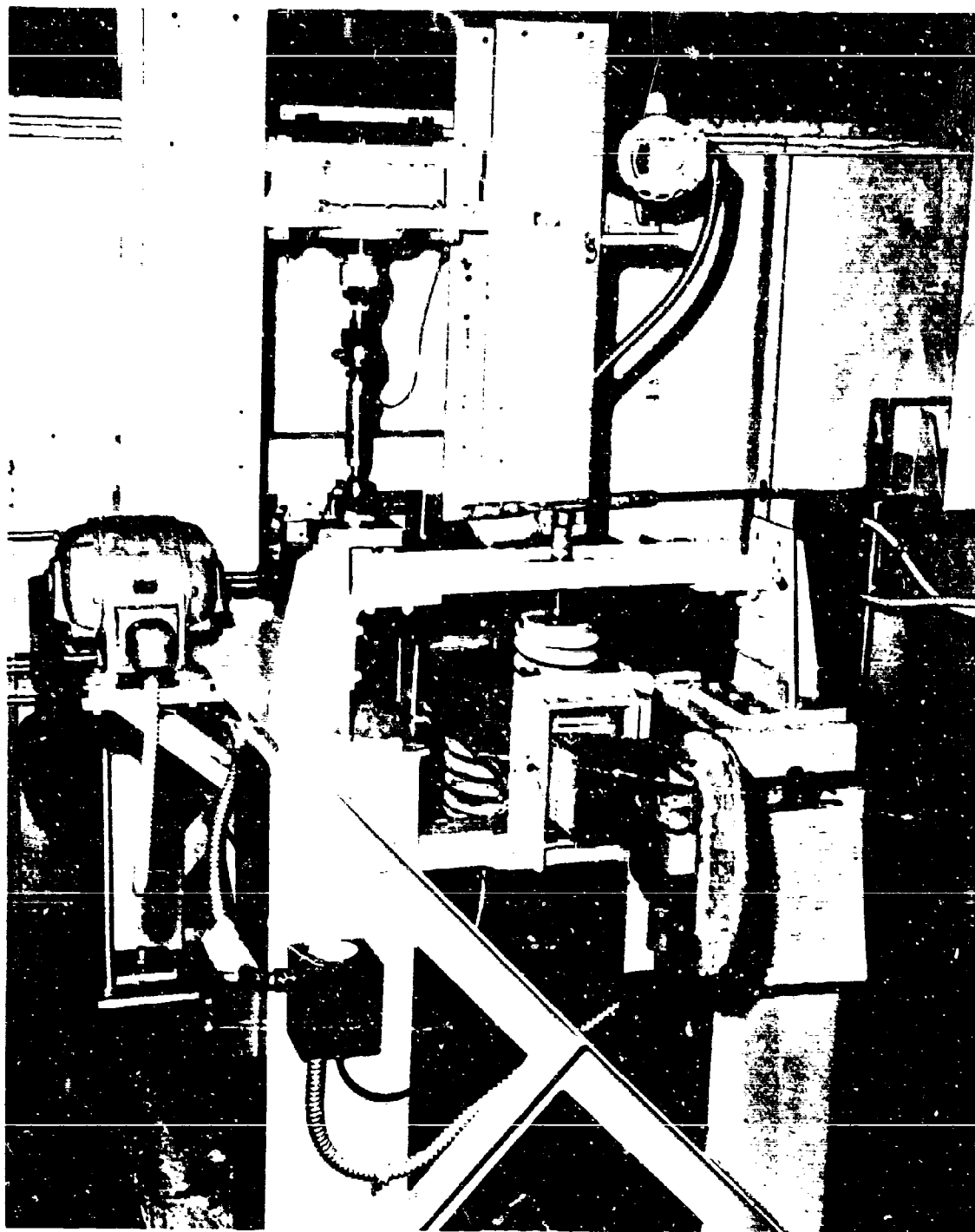


Figure 114. Rod End Specimen Installed in Fatigue Test Machine.



Figure 115. Rod End Specimen Test Setup.

APPENDIX VI
CONFIGURATION AND CHANGE LOG

<u>Item Number</u>	<u>Description</u>	<u>Accom- plish Preflight Number</u>	<u>Date</u>
1	Removed three rotor blades from hub, removed blade spars, cleaned up, inspected spars and reinstalled on blades. Replaced 1/4-inch diameter spar-to-segment attachment bolts and Armalon antifretting material. Reinstalled strain gages on blue blade and recalibrated. Reinstalled blades in hub.	22	3/22/65
2	Removed and inspected blade retention strap packs, cleaned up and polished out scratches on straps and hole bores. Magnafluxed retention-strap attach bolts. Sanded and recoated shoes with epoxy paint.	22	3/22/65
3	Replaced articulating duct lip seals on three blades.	22	3/22/65
4	Replaced one articulating duct section because of chipped flame plating.	22	3/22/65
5	Removed material from inboard rib flanges of three blades to eliminate interference with forward retention straps.	22	3/22/65
6	Reduced tip cascade area (9.6-square-inch-geometrical total) by installation of exit ramps in tip cascades.	22	3/22/65
7	Installed nacelle-to-fuselage braces, removed engine nacelle ballast.	22	3/22/65
8	Replaced rudder control cables with 1/4-inch-diameter cable; rerigged rudders to 7 degrees right with yaw valve neutral.	22	3/22/65
9	Changed stabilizer incidence from 3 degrees nose-up to 2.5 degrees nose-up.	22	3/22/65
10	Reweighed and ballasted aircraft.	22	3/22/65

<u>Item Number</u>	<u>Description</u>	<u>Accom- plish Preflight Number</u>	<u>Date</u>
11	Removed engine S/N 027-2A; installed engine S/N 101-3, L/H nacelle.	22	3/22/65
12	Installed three T ₂ probes in each engine inlet.	22	3/22/65
13	Installed ARC 73 and ARC 45 radios.	22	3/22/65
14	Installed engine low-speed warning system.	22	3/22/65
15	Installed generator cooling air scrolls. Provided cutouts and louvers in forward nacelle cowls for additional cooling.	22	3/22/65
16	Rerigged and recalibrated flight controls.	22	3/22/65
17	Installed thermal relief valve in blade-tip cascade pressure lines.	22	4/20/65
18	Installed aft fuselage overheat warning sensor and light.	22	4/27/65
19	Installed solenoid-operated bypass valves for rotor-governing deactivation capability.	22	4/27/65
20	Recalibrated all pilot's panel and test instrumentation.	22	4/1/65
21	Retracked and rebalanced rotor.	22	4/29/65
22	Removed crossflow indicating system and installed engine low-speed warning system.	22	3/22/65
23	Readjusted pitch links and balance weights on red blade.	23	5/3/65
24	Revised fuselage and tail ballast (to same as initial 15-hour program). Takeoff gross weight, 15,300 lb; initial center of gravity, sta 298.0.	23	5/3/65
25	Removed nacelle-to-fuselage braces.	24	5/5/65

<u>Item Number</u>	<u>Description</u>	<u>Accom- plish Preflight Number</u>	<u>Date</u>
26	Reinstalled nacelle ballast weights; 215 lb each nacelle.	24	5/5/65
27	Replaced engine 2 hydraulic pump.	24	5/5/65
28	Installed tip weights on stabilizers; 11 lb each tip, flights 24 B and C; 18 lb each tip, flight 24 D.	24	5/5/65
29	Removed fuel control S/N 22629 from engine S/N 101-3; installed fuel control S/N 23249; reset density adjustment to 0.69; rerigged variable geometry feed- back cable.	24	5/7/65
30	Replaced rotor-driven hydraulic pump.	24	5/11/65
31	Removed 40-lb tail ballast weight; installed 7-lb stabilizer tip weights. Takeoff gross weight, 15,314 lb; initial center of gravity, sta 298.3.	25	5/18/65
32	Removed ramp-type tip cascade exit tabs; installed vane trailing-edge exit tabs, same physical area.	26	5/20/65
33	Cleaned engine compressors with Rustlick 606 and water per GE instructions.	27	5/24/65
34	Decreased tip-cascade exit area by 3.5 square inches geometrical total.	27	5/24/65
35	Removed engine S/N 101-3A; installed engine S/N 027-2B, LH nacelle; installed fuel control S/N 23249 on engine 027-2B.	28	6/1/65
36	Added external air scoops, louvers, and cutouts to engine cowl doors for increased generator and engine oil cooling.	28	5/28/65
37	Installed full span rudder trim tabs with 1-inch chord bent up 4 degrees.	28	6/2/65
38	Installed 1/8-inch-diameter tie-cable between stabilizer tips.	28	6/4/65

<u>Item Number</u>	<u>Description</u>	<u>Accom- plish Preflight Number</u>	<u>Date</u>
39	Replaced engine primary and secondary fuel manifold lines (excessive corrosion).	30	6/15/65
40	Recalibrated flight controls and checked rigging.	31	6/17/65
41	Replaced engine 1 hydraulic pump.	32	6/23/65
42	Replaced engine 1 hydraulic fire-wall shutoff valve.	35	7/1/65
43	Repaired lateral servo dither actuators.	35	7/1/65
44	Rerigged rudder control system for rudders neutral with yaw valve neutral.	38	7/12/65
45	Removed diverter valve 2, S/N 011, RH nacelle, for repair of cracks and seal rework.	40	7/15/65
46	Removed engine S/N 026-1B; installed engine S/N 101-3A RH nacelle, fuel control S/N 22626; density set at 0.69.	40	7/15/65
47	Readjusted diverter valve actuating times from 0.5 to 1.0 sec (approximate).	40	7/20/65
48	Rerigged rudder control system for 7 degrees left rudder with yaw valve closed.	40	7/22/65
49	Removed forward fuselage ballast. Takeoff gross weight, 15,190 lb; initial center of gravity, sta 298.3.	40	7/23/65
50	Rerigged rudder control system for 7 degrees right rudder with yaw valve closed.	41	7/27/65
51	Revised fuselage and tail-gear ballast to give more aft center of gravity. Takeoff gross weight, 15,040 lb; initial center of gravity, sta 298.8.	41	7/28/65
52	Removed L/H diverter valve, S/N 012, for inspection by General Electric and replacement of rotor position switch.	42	8/2/65

<u>Item Number</u>	<u>Description</u>	<u>Accom- plish Preflight Number</u>	<u>Date</u>
53	Replaced broken spar attachment bolt, blue blade, rear spar, outboard hole in tip segment.	42	7/29/65
54	Removed, inspected, and replaced random 1/4-inch-diameter bolts in constant-section blade segments of all three blades; inspected holes in spars and segments.	43	8/6/65
55	Removed LH cockpit door for initial portion of flight.	43	8/5/65
56	Activated LH cockpit seat for crew member, removed cockpit camera.	43	8/5/65
57	Removed and replaced blue-blade tip-segment assembly because of cracked closing rib and eroded duct ends.	44	8/19/65
58	Replaced 5/16-inch-diameter bolts, tip segment, three blades with NAS 625 bolts.	44	8/18/65
59	Removed, reinstalled, and resealed tip cascade assembly, blue blade. Replaced tip segment to aft spar bolts with special A-286 high-strength bolts.	44	8/19/65
60	Reweighed aircraft at Edwards Air Force Base. Takeoff gross weight, 15,382 lbs; initial center of gravity, sta 299.2.	44	8/16/65
61	Rebalanced rotor.	44	8/26/65

APPENDIX VII
AIRCRAFT WEIGHT AND BALANCE DATA - XV-9A 15107

Weight and balance data for XV-9A aircraft S/N 15107 are presented below in Table XIV and Figure 116.

TABLE XIV
AIRPLANE WEIGHING RECORD

Reaction	Scale Reading			Tare			Net Weight			Moment		
	(1)	(2)	(3)	(1)	(2)	(3)	(1)	(2)	(3)	(1)	(2)	(3)
Left main	6,466	6,700	6,800	0	0	+8	6,466	6,700	6,808	-	-	-
Right main	6,285	6,485	6,720	0	0	+13	6,285	6,485	6,733	-	-	-
Subtotal (both main)	12,751	13,185	13,520	0	0	+21	12,751	13,185	13,541	3,266,169	3,370,745	3,550,315
Tail	2,028	2,025	1,620	0	0	-4	2,028	2,020	1,616	1,175,429	1,170,691	999,641
Total (as weighed)	14,779	15,210	15,140	0	-5	+17	14,779	15,205	15,157	4,441,598	4,541,436	4,549,956

See Figure 116.

	(1)	(2)	(3)
B = the distance from the jig point to the centerline of the main reactions. Obtain by measurement.	29.5	30.00	23.46
I = distance from reference datum to jig point of the airplane, from which a plumb bob can be dropped to the ground. Remove lower cargo access panel before weighing.	285.65	285.65	285.65
E = the distance from the reference datum to the centerline of the main reactions. E = I - B.	256.15	255.65	262.19
D = the distance from the jig point of the airplane to the centerline of the tail reaction.	293.95	293.9	332.94
F = the distance from the reference datum to the centerline of the tail reaction F = I + D.	579.60	579.55	618.59
H = calculated center of gravity as weighed.	300.53	298.68	300.19
CG = H + 0.66 (to rotate the measured cg 2 degrees in the rotor plane)	300.19	299.34	300.85
Adjusted takeoff gross weight	14,977 at sta 299.7	15,398 at sta 297.87	15,382 at sta 298.58

- (1) Weighed at bldg 15, Culver City, 29 April 1965.
(2) Weighed at bldg 15, Culver City, 8 June 1965.
(3) Weighed at Edwards Air Force Base, 16 August 1965 (fuel at 6.40 lb/gal.; temperature = 28.5 deg C).

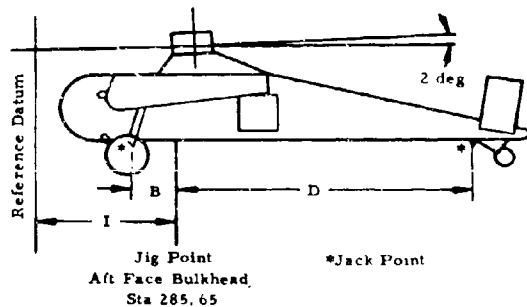


Figure 116. Weight Coordinates.

APPENDIX VIII
PILOT'S COMMENTS AND QUALITATIVE EVALUATION
OF THE XV-9A

A critique of the systems, equipment, and operational procedures is given in the following paragraphs to document operating and flight experience with the various aspects of the XV-9A.

MAINTENANCE AND OPERATIONAL EVALUATION

The basic simplicity of the Hot Cycle system was evidenced during the course of flight testing by the high availability of the aircraft for test flights, the high ratio of successfully completed flights to aborted flights, and the low maintenance requirements. Of the 15 flight operations conducted at Edwards AFB, 13 were flown as scheduled and were successfully completed, 1 flight was aborted immediately after takeoff because of a warning light malfunction, and 1 flight was discontinued because of another warning light malfunction.

The Hughes test operations crew at Edwards AFB consisted of 12 people and included the pilot, project test engineer, flight test engineer, foreman, and personnel for the maintenance of the aircraft and test instrumentation.

The primary maintenance and operational problems encountered during the program were as follows.

1. Radio

The ARC-45 radio system required considerable maintenance because of channeling problems in the RT-295 transceiver unit. As a result, 200 percent spares were required to support the flight test program. The ARC-45 output power was limited, and there was difficulty at times in maintaining good voice communications between the test airplane and the ground.

2. Warning Light Malfunctions

Malfunctions of warning lights were encountered with the rotor overheat, diverter-valve position, and tip-cascade position-indicating light systems. These malfunctions were caused by broken wiring at solder points and by defective switches.

3. Control-Servo Dither Actuators

These units were taken from available surplus stocks and were not optimum in size or force characteristics for the XV-9A control-servo actuators. An internal wiring failure occurred in one unit, and a modification was required to the eccentric mass weight of another unit to obtain proper results.

4. Blade-Tip Cascade Valve Actuation System

On one occasion, the blade-tip cascade valve on one blade failed to go to the fully open position following single-engine flight. There was no adverse effect noted on rotor operation, and postflight inspection of the rotor blade and tip cascade revealed that no damage had occurred. The malfunction could not be repeated during ground tests, and no subsequent malfunction occurred. The malfunction was attributed to mechanical hangup of the actuating linkage, which was carefully adjusted, lubricated, and checked for proper operation following the malfunction.

5. Diverter-Valve Maintenance

Because of structural failures that occurred with the GE J-85 diverter valves installed in the XV-5A airplane, the J-85 diverter valves used in the XV-9A were inspected every 5 flight hours for cracks in welds and for general condition of the doors, seals, and valve body. This inspection was accomplished by removal of fairings and engine tailpipes.

Each diverter valve was removed once during the program for weld repair, inspection, seal rework, and replacement of a defective position switch.

6. Rotor Maintenance

All leading and trailing edge sections were removed after every 5 flight hours for inspection of blade spars, attachment bolts, and blade segments. On one occasion, prior to flight 43, the 1/4-inch-diameter spar bolts in the constant-section segments were removed at random in the three blades for inspection and were found to be satisfactory; however, new bolts were installed wherever removals occurred.

The tip segment of the blue blade was replaced following flight 43 because of excessive gas leakage at the blade-duct-to-tip-cascade joint. The excessive leakage at the blade tip caused a localized over-temperature condition at the outboard end of the rear spar, and the extreme outboard

rear spar attachment bolt failed. The excessive leakage at the blade tip was caused by deterioration of a doubler-type repair to the outboard ends of the blue-blade ducts accomplished prior to the start of whirl testing in 1964.

The tip segment was replaced with a new unit, and the tip cascade was reinstalled and sealed with RTV 601 sealer. No further problems were encountered. The other two blades, which did not have the doubler-type repair on the ends of the ducts, were carefully inspected and no signs of leakage or structural failures were found.

7. Rotor-Speed Governing

The rotor-speed-governing system normally required ground adjustment prior to each flight to match engine speed, power lever position, and rotor speed properly. These adjustments were required because of excessive "drift" of the rotor-speed-governing feedback signal.

COCKPIT LAYOUT AND EQUIPMENT

General Arrangement

The XV-9A was the first vehicle to fly with the Hot Cycle propulsion system. The design utilized an OH-6A Light Observation Helicopter cockpit section, flight controls, and instrument panel. The aircraft was designed for operation by a single pilot, with minimum provisions for a second crew member.

In addition to the normal flight and engine instruments, the XV-9A cockpit included a considerable number of test instruments, switches, and counters to facilitate flight testing.

Since the OH-6A instrument panel and center console were intended for a single-engine production helicopter, the arrangement of the XV-9A instruments and switches was not optimum because of the space limitations. On future designs, a more functional grouping of engine instruments, diverter-valve and tip-cascade controls, and engine power controls is recommended. The placement of warning lights away from position- or condition-indicating lights would also be an improvement.

Operation of gas generators in the Hot Cycle system was satisfactory with standard jet-engine instruments. In a fully-developed Hot Cycle aircraft, the engine-oil pressure and temperature and rotor-oil pressure and temperature instruments may be eliminated, as these functions could be included in a master caution and warning panel.

Warning Lights

The position of the diverter valves and of the blade-tip cascade valves was displayed by indicator lights. Lights were also used to indicate fire, rotor overheating, fuselage overheating, low hydraulic pressure, low engine and rotor oil pressure, low engine speed, overheating of rotor oil, low fuel level, low fuel pressure, and open fuel crossfeed.

The use of indicator lights in a twin-engine aircraft of this type resulted in a large number of lights and presented difficulty in rapid appraisal of a particular condition. For future designs, the use of a master caution and warning panel system in lieu of warning lights is recommended.

Gas Generator Operation

The operation of gas generators in the Hot Cycle system is unique in that there is an interaction between engines that can result in exceeding engine operating limits for conditions of excessive mismatch. On future designs, an engine-matching servo system and/or a simplified engine-mismatch indicator is recommended.

Diverter Valve/Cascade Valve Operation

The operation of diverter valves and tip-cascade valves during conversion to single-engine and reconversion to twin-engine flight requires the pilot to ascertain their correct positioning for successful completion of the sequence. On future designs, a functional-type control for operation of diverter valves and tip cascades that would have a schematic arrangement such that the position of the control would display the position of all valves and the direction of the engine gas flow is recommended.

Fuel System Controls

The fuel system switches for control of boost pumps, tank shutoff valves, and firewall shutoff valves were arranged in a schematic manner with the switch position denoting the actual function of the valve or pump. The dual-needle fuel-quantity indicator originally installed was replaced with individual indicators having greater travel and improved damping. These indicators provided improved readability and more accurate quantity data.

Engine-Out Warning System

The crossflow indicating system originally installed was removed prior to the start of this program. A simplified engine low-speed warning system was installed to activate warning lights at 92-percent engine speed.

This system was an improvement; however, on future designs the incorporation of engine low-speed warning into the master caution and warning panel is recommended.

Rotor Overheat Warning System

Difficulty was encountered with the rotor-overheat switches, which were located in the cooling-air passage of the blade leading edges, giving false warnings during both ground and flight operation. These difficulties were usually the result of broken wires at the switch unit. Improvements were made that provided better support and attachment of wiring in this area. These changes greatly decreased the number of false rotor overheat warnings.

Diverter Valve/Cascade Valve Position Indication

Difficulty was also encountered with the blade-tip cascade valve position-indicating switches and the diverter-valve position-indicating switches. These problems were usually the result of switches getting out of adjustment; improvement in these items is recommended for future Hot Cycle designs.

ROTOR-SPEED GOVERNING AND OVERSPEED PROTECTION

Rotor-speed governing was operative for all flights and was generally satisfactory during twin-engine and single-engine flight. An undesirable characteristic of the system was the drift of the governed engine speed, which required pilot adjustment of the power levers to maintain matched gas generator compressor speed (N_G) and resulted in power lever mismatch of varying amounts.

The rotor-speed-governing system required frequent ground adjustment to maintain the proper governed speed range and engine speed relationship. Normally, this was accomplished by means of the N_f fine speed adjustment on the engine fuel control. The procedure used was to set both power levers at 82.5 degrees with 0-degree collective and to adjust the N_f fuel control to attain matched N_G on both engines for 98-percent N_R . The normal up-droop during takeoff to hover usually resulted in a rotor speed of 100-percent N_R after takeoff with minimum twist-grip adjustment.

Rotor-speed-governing adjustments were also performed on the bypass valves in the hydraulic rotor-speed sensing system. This technique was used when the N_f "fine" adjustment on the fuel controls became "bottomed out" in either direction. The bypass valve adjustments produced large

changes in engine speed and were carefully performed. The N_f "fine" adjustments were relatively insensitive and were more easily made. Normally, the N_G 's were matched to within 0.5 percent with the power levers set at 82.5 degree gas generator power lever angle, 0-degree collective, and 98-percent rotor speed.

The rotor-speed-governing system was instrumented to determine the cause of "drift" in the input speed signal. The N_f input speed and hydraulic motor input and output pressures were recorded for several flights. Analysis of these data showed that the torque requirements of the gas generator N_f input shaft varied from flight to flight and consequently shifted the governor reference speed, which also affected engine turbine speed and power output. The cause for the varying torque requirements of the N_f input shaft was not determined.

The rotor-speed-governing system was modified to provide the pilot with capability to deactivate governing in the event of a malfunction. Electrically operated solenoid valves were installed in the hydraulic rotor speed sensing lines for this purpose. Rotor governing could thus be deactivated by a switch on the center console.

Rotor overspeed protection was incorporated to avoid overspeeding the rotor in case of any malfunction in the power control or rotor-governing system. A rotor overspeed of 105-percent N_R tripped the limiting device and caused both engines to go to 93-percent N_G . This action was accomplished by use of the engine overspeed solenoid on the T-64 fuel control. The overspeed limiting device released the signal as rotor speed decreased to 103-percent N_R and both engines returned to the original power setting. This feature was not the most desirable, because of the power surging effect and the rapid acceleration characteristics of the XV-9A Hot Cycle rotor.

A wider range of "trip to release" would improve the protective capability of the system.

Rotor overspeed "trips" were encountered during flight on several occasions, during a maximum power climb and during hover at 103-percent N_R when rotor overspeed inadvertently increased to 105-percent N_R . On these occasions, there was no serious loss of rotor power, as the limiting device restores original power at 103-percent N_R . The overspeed system could be deactivated by the pilot, and this deactivation was performed on occasion during maximum power climb and for speed power or hover performance tests at N_R above 100 percent.

The use of rotor-speed governing and rotor-overspeed protection is definitely recommended for Hot Cycle systems. The lack of a gearbox and associated noise changes with changes in rotor speed causes difficulty in the pilot's detection of changes in rotor speed, thus making rotor overspeed protection mandatory. Improvements in rotor-speed governing to eliminate "drift" in the governed engine speed is recommended on future designs.

POWER MANAGEMENT

The XV-9A propulsion system employs twin YT-64 gas generators, with the total discharge flow of both engines combined and mixed in the rotor hub ducting and exhausted at the blade tips to produce rotor driving torque. This mode of operation for twin turbojet engines in a flight vehicle is unique to the XV-9A aircraft. Power management techniques were developed, starting with whirl testing and during subsequent tie-down and flight testing, that provided satisfactory control of rotor speed and engine operation for all helicopter flight modes.

The YT-64 gas generators in the XV-9A aircraft use the standard T-64 fuel control, which contains provisions for power turbine governing. Rotor-speed governing is provided by utilizing the N_f (power turbine) portion of the engine fuel control. A rotor speed signal for operation of the N_f governors is applied to each fuel control by means of a hydraulic speed servo system that is driven by the rotor accessory gearbox. Rotor speed governing was operative for all flights.

The primary element for power management in the XV-9A system is the pilot. The principal difference in operation of the gas generators in the Hot Cycle system is the effect of engine interaction as a result of both engines sharing a common exhaust area. The interaction effect is observed by the T_5 - N_G relationship of the engines.

Cockpit instrumentation and controls for power management are the same as for turbine shaft-driven helicopters. The primary power setting parameter was engine speed, N_G . The individual power levers are used to maintain both engines at approximately the same N_G for all conditions. Since the T-64 is a temperature-limited engine, the turbine discharge temperature, T_5 , is the limiting parameter for setting maximum power.

The normal power setting technique used was to set the collective pitch to attain the desired climb or level-flight power and to use twist-grip control to attain the desired governed rotor speed. Individual power lever changes were made, as required, during flight to maintain a nearly matched N_G condition.

The technique of setting matched engine speed was found to be the most practical means of engine operation, since the YT-64 engine is highly responsive to power lever changes at all speeds above "Flight Idle," and any change in power lever angle is immediately reflected by change in engine speed. Analysis of engine operating data indicated that with matched N_G the two engines shared very nearly the same amount of the exit area, which is highly desirable for optimum acceleration characteristics and power output, and to insure operation within the allowable temperature limits.

The engine acceleration times were improved during this program by changing the density settings on the fuel control from 0.85 to 0.69. The result was to decrease the engine acceleration times from "Idle" (75-percent N_G) to 100-percent N_G from 6- to 7-second average to 4 seconds. The effect of adjusting variable geometry feedback to obtain wider variable geometric opening was also found to improve the acceleration characteristics; however, all flights were flown with the variable geometry schedule specified by General Electric operating instructions.

The phenomenon of engine rollback was experienced in the previous program, during rotor accelerations starting from a rotor speed of 85-percent N_R or below and with the engine speeds mismatched 5-percent N_G . After improvement in engine acceleration times to 4 seconds, ground checks were run during which successful rotor accelerations were accomplished with 5-percent N_G mismatch starting from 85-percent N_R without encountering rollback. The engine-rotor acceleration characteristics were thereby improved by the improvement in engine acceleration times.

Power management during single-engine operation differs somewhat from the twin-engine case, because one engine is diverted to overboard flow through the engine tailpipe and is therefore isolated from the rotor. During single-engine operation, the rotor-speed-governing function is still operative to both engines, and the engine powering the rotor is governed in the normal manner. The power lever for the overboard engine is pulled back into the manual or nongoverning regime during single-engine flight. For single-engine operation, the engine speed may be varied widely, as there is no interaction effect.

Power control in the XV-9A aircraft was affected by the jet-reaction yaw-control valve during nonhovering flight. The effect of the yaw control valve opening was to increase the total engine exit area, which caused N_G and T_5 to vary.

Power control during minimum power descents was satisfactory, except for the condition where the available twist grip authority was not sufficient to bring the power all the way back to the desired power level. In the XV-9A power lever control system, there was frequently a 1- to 1-1/2-inch mismatch in power lever angle for this condition. This was objectionable to the pilot when making power recoveries following a minimum power descent.

Occasional rotor-governing drift would cause the pilot to mismatch power lever angle during normal twin-engine operation. This was objectionable to the pilot, in that power lever position did not consistently reflect a given N_G or power output.

The power control system was marginally adequate for the XV-9A test program. The following changes and/or improvements should be considered in future designs:

1. Increased twist-grip authority to allow a full range of power control from maximum to "Idle."
2. A twist-grip detent at the "Flight Idle" position.
3. Improved power lever angle coordination to eliminate power lever mismatch.
4. Engine speed-matching by a speed control servo system.
5. Power lever versus engine speed relationship with rotor governing operative in such a way that power lever position always represents a given N_G or power setting.
6. Improved collective-pitch control operation with a constant friction gradient.

SINGLE-ENGINE OPERATION

Single-engine flight was accomplished during flights 40 and 42 to evaluate single-engine operating characteristics, flying qualities, and performance.

Conversion from twin-engine to single-engine operation was accomplished during descent at 65-knot CAS. The pilot switching function was completely manual, in that the diverter valves and tip cascades were separately actuated to their proper position before continuing the sequence. The conversion procedure was as follows:

1. Stabilize in descent at 65-knot CAS with 90-percent N_G on both engines.

2. Actuate the selected diverter valve switch to "Overboard" position.
3. Actuate the blade tip cascade valve switch to "Closed" position.
4. Verify proper diverter valve and tip cascade positions by indicating lights.
5. Increase power on both engines.

The investigation of extended single-engine flight was hampered by the directional stability and control characteristics of the XV-9A aircraft. These characteristics were discussed in the Flight Test Results section, along with directional stability and control data that were also presented.

The directional behavior of the aircraft during single-engine flight required fairly large rudder pedal inputs and bank angles to maintain approximately straight flight, and the resultant yaw-control valve opening caused considerable difficulty in acquiring performance data.

Conversion from single-engine to twin-engine operation was basically the same as for the twin-to-single-engine operation, except for a change in sequence of events.

The conversion procedure was as follows:

1. Stabilize both engines at 90-percent N_G while in descent.
2. Actuate tip cascades to "Open" position and verify "Open" position on indicating lights.
3. Actuate overboard engine diverter valve to "Rotor" position and verify rotor position on indicating lights.
4. Increase power on both engines and resume twin-engine flight.

YAW-CONTROL VALVE CHARACTERISTICS

The operating characteristics and performance of the jet-reaction yaw-control valve in the XV-9A were more fully evaluated during the follow-on program for various flight conditions, including high-speed level flight, climb, descent, and landing.

The primary deficiency of the yaw-control valve was the power degradation resulting from rudder pedal inputs and the associated decrease in rotor lift. During hovering flight, the gas generator speed was increased

in proportion to rudder pedal inputs to supply the gas flow requirements of the yaw valve. During full-pedal hover turns, the rotor-governing system increased engine speed to supply additional gas flow for yaw control, and rotor speed remained essentially constant. Engine speed, N_G , approached or reached the topping limit of 104-percent N_G for this condition.

During climb and level flight, the XV-9A required right rudder trim, and the rudders were rigged to 7 degrees right with yaw control valve neutral (closed) to permit trimmed flight without yaw-control valve power degradation. This procedure was only partially successful, as the trim required varied with airspeed and the directional characteristics during climb required frequent pilot rudder-pedal inputs, which resulted in changing power and made the acquisition of performance data difficult.

The use of a yaw control valve operating off the main propulsive gas generator system requires that the gas generators be topped 1 to 2 percent below the maximum allowable topping speed because of the increase in total engine exit area with yaw valve opening. This condition is necessary to prevent engine overspeed during yaw-control valve inputs at high engine power.

The rudder-yaw control valve cables were changed from 3/32-inch diameter to 1/4-inch diameter prior to the start of this program to eliminate excessive cable stretch and slop in the system. Aircraft handling on the ground during taxiing turns was improved by this change, and the hover turn rates were also improved.

Where a combined yaw valve/aerodynamic rudder control system is employed as in the XV-9A, a means of deactivating the yaw valve bleed would be desirable for those flight conditions where aerodynamic control is available.

A yaw valve control becomes ineffective at low engine power conditions such as an autorotational descent and landing. During a flare and approach to hover, the XV-9A aircraft required considerable left pedal input to counteract a nose-right turning tendency. Because of this characteristic, all low-power descents were followed by run-on landings at 30- to 40-knot IAS to obtain sufficient directional control from the aerodynamic rudder surfaces.

APPENDIX IX
PROPULSION SYSTEM PERFORMANCE TEST DATA
AND CORRECTIONS

FUEL FLOW

The estimated performance of the XV-9A presented in Reference 14 was based on the expected use of hardware components that are considered to be typical of production hardware. These items involve the engine, diverter valves, and the method of oil cooling. The actual XV-9A used available components, which resulted in a higher fuel consumption than that predicted using optimum components. The fuel consumption figures in the main body of the report have been corrected where noted. This appendix presents the observed and corrected data and the method of making these corrections. Appendix IV of Reference 1 presented similar data for the initial 15-hour flight test program.

Table XV presents observed fuel flow data for all data points taken during testing. It also includes the procedure for determining corrected fuel flow on the basis of original assumptions; namely, with qualification test (QT) rather than preliminary flight rating (YT) engines, and without diverter valve leakage. The gross weights for all hover points are given; the basic gas conditions that determine rotor power and the equivalent gas power are also given.

Fuel flows have been reduced 3 percent to correct for diverter valve (2-1/2 percent) and stationary duct (1/2 percent) leakage, as measured. This XV-9A hardware is not considered to be typical of production hardware, so the data have been corrected to reflect the true system performance. Fuel flow has been corrected to reflect the better T_5 versus P_5 characteristics of the fully qualified T-64 engines as compared with the preliminary (YT-64) engines used during the tests. This correction is approximately 8 percent. The procedure for correcting fuel flow consists of first increasing airflow as the inverse square root of T_5 , then reducing fuel/air ratio in direct proportion to engine temperature rise ($T_5 - T_2$). The final correction thus varies more than the square root of T_5 , but not so much as the first power of T_5 .

TABLE XV
OBSERVED AND CORRECTED FUEL FLOW AND ROTOR AND ROTOR AND GAS HORSEPOWER

Flight Number	Record Number	TAS (mi)	Hover Weight (lb)	W ₂ (lb/sec)	T ₅ (deg R)	P ₅ (psi)	δ ₂	W ₁ (lb/hr)	P ₁ /P ₀ Ratio	RHP lb/ft ²	SFC lb/hp-hr	GHP lb/hp-hr	P ₅ psi	T ₅ (deg R)	($\frac{T_5}{\theta}$) deg R	($\frac{T_c}{\theta}$) deg R	($\frac{F_{fuel}}{W_2}$) lb/sec	(W ₂) _{OT} (lb/sec)	(W ₁) _{OT} (lb/sec)	(SFC) _{OT} (lb/hp-hr)
20	1,056	64.3	32.48	1.376	23.9	1.0198	0.8727	1.530	1.948	1.100	1.332	1.37	2.747	29.2	1.350	1.270	0.0104	31.49	1.216	1.110
21	1,156	75.5	33.14	1.396	24.5	0.9795	0.8210	1.360	1.986	1.147	1.412	1.36	2.807	29.9	1.418	1.287	0.0107	34.79	1.224	1.130
22	1,205	87.1	34.34	1.418	25.5	0.9870	0.8127	1.570	2.060	1.252	1.516	1.33	3.199	30.9	1.437	1.312	0.0110	35.94	1.381	1.100
23	1,245	99.7	35.59	1.387	25.2	0.9947	0.8127	1.570	2.060	1.084	1.191	1.41	2.746	27.6	1.374	1.230	0.0099	33.62	1.293	1.190
24	1,315	74.7	35.52	1.387	25.8	0.9911	0.8100	1.600	1.897	1.147	1.266	1.39	2.902	28.4	1.399	1.250	0.0101	37.58	1.325	1.160
25	2,018	55.7	34.62	1.346	25.4	0.9530	0.8600	1.640	1.974	1.199	1.367	1.37	3.024	29.5	1.405	1.277	0.0106	36.52	1.322	1.130
31	1,479	93.8	35.60	1.448	24.5	0.9965	0.8091	1.660	1.983	1.242	1.600	1.28	3.316	31.0	1.453	1.300	0.0108	39.31	1.483	1.150
32	1,611	106.7	37.10	1.487	25.3	0.9791	0.8169	1.860	2.032	1.418	1.745	1.31	3.699	31.7	1.503	1.320	0.0111	41.40	1.605	1.130
33	1,770	67.9	33.10	1.397	22.1	0.9770	0.7860	1.450	1.812	1.028	1.310	1.41	2.688	28.8	1.401	1.243	0.0100	36.70	1.282	1.250
34	1,197	65.6	32.57	1.381	22.3	0.9790	0.7890	1.520	1.882	1.053	1.349	1.44	2.610	28.9	1.411	1.292	0.0107	34.04	1.272	1.210
35	1,433	79.5	33.30	1.387	22.5	0.9859	0.7887	1.510	1.900	1.168	1.492	1.29	2.761	29.1	1.410	1.250	0.0101	35.37	1.247	1.070
36	1,588	90.2	34.20	1.422	25.6	0.9789	0.7805	1.600	2.046	1.297	1.580	1.23	3.160	30.8	1.452	1.295	0.0108	36.21	1.366	1.050
37	1,958	102.3	35.72	1.493	24.9	0.9798	0.7870	1.800	2.105	1.410	1.810	1.28	3.642	32.2	1.524	1.333	0.0113	38.19	1.507	1.070
38	2,441	111.6	39.67	1.507	28.4	1.0244	0.8753	2.040	2.209	1.664	1.878	1.22	4.200	33.2	1.486	1.357	0.0116	41.51	1.681	1.010
39	926	68.1	32.92	1.423	22.2	1.0250	0.7545	1.580	1.994	1.177	1.539	1.34	2.950	30.0	1.381	1.278	0.0105	34.23	1.255	1.070
40	985	80.4	33.11	1.429	22.4	1.0259	0.7574	1.580	2.019	1.222	1.409	1.29	3.023	30.3	1.372	1.283	0.0106	34.49	1.277	1.050
41	1,092	98.8	35.13	1.482	23.8	1.0136	0.7515	1.760	2.174	1.442	1.905	1.22	3.582	32.1	1.462	1.330	0.0112	36.83	1.440	1.000
42	2,265	86.1	36.35	1.402	24.6	1.0259	0.8828	1.650	1.866	1.191	1.332	1.39	2.930	28.4	1.366	1.235	0.0099	38.23	1.322	1.110
43	2,361	97.6	37.86	1.434	25.6	1.0314	0.8883	1.780	1.940	1.329	1.473	1.34	3.310	29.5	1.390	1.260	0.0103	39.77	1.430	1.080
44	2,432	108.2	40.09	1.485	27.7	1.0414	0.8910	2.000	2.073	1.570	1.727	1.27	3.938	31.8	1.426	1.320	0.0111	41.67	1.601	1.020
45	2,979	110.4	40.48	1.513	28.1	1.0547	0.8759	2.130	2.186	1.703	1.911	1.25	4.311	32.7	1.462	1.347	0.0115	42.17	1.693	0.990
46	3,131	119.1	42.65	1.543	29.5	1.0501	0.8883	2.260	2.233	1.887	2.073	1.21	4.755	33.9	1.469	1.377	0.0119	44.05	1.831	0.970
47	901	98.1	37.13	1.451	25.5	1.0368	0.8769	1.760	1.931	1.314	1.471	1.34	3.333	29.7	1.414	1.265	0.0104	39.58	1.417	1.090
48	1,050	110.2	39.93	1.512	27.8	1.0368	0.8776	2.090	2.119	1.614	1.806	1.29	4.138	32.2	1.474	1.330	0.0113	42.04	1.659	1.030
49	1,443	73.1	34.72	1.399	23.5	1.0310	0.8669	1.530	1.785	1.053	1.196	1.45	2.606	27.6	1.371	1.215	0.0096	36.88	1.236	1.170
50	1,546	79.5	35.40	1.394	23.7	1.0331	0.8710	1.560	1.802	1.070	1.206	1.46	2.757	27.7	1.364	1.216	0.0097	37.49	1.270	1.190
51	1,611	90.6	35.82	1.430	24.6	1.0336	0.8733	1.680	1.866	1.168	1.315	1.44	3.050	28.8	1.398	1.242	0.0110	38.00	1.370	1.140
52	1,866	104.5	38.56	1.497	27.0	1.0347	0.8724	1.920	2.052	1.454	1.638	1.32	3.824	31.5	1.462	1.315	0.0111	40.66	1.576	1.080
53	1,220	118.5	43.36	1.536	29.3	1.0385	0.8860	2.300	2.243	2.019	2.231	1.14	4.761	33.6	1.495	1.310	0.0118	45.30	1.857	1.080
54	1,145	54.4	37.53	1.337	24.2	1.0115	0.8593	1.640	1.901	1.210	1.348	1.36	2.869	27.5	1.315	1.215	0.0096	40.38	1.354	1.120
55	1,225	65.6	36.99	1.334	24.0	1.0155	0.8134	1.580	1.847	1.108	1.205	1.43	2.653	26.7	1.314	1.197	0.0094	38.75	1.272	1.150
56	1,300	73.3	37.51	1.370	24.9	1.0170	0.8124	1.670	1.905	1.208	1.313	1.38	2.900	27.8	1.347	1.220	0.0097	39.41	1.335	1.110
57	1,423	72.1	37.51	1.396	24.6	1.0220	0.8667	1.680	1.924	1.248	1.392	1.35	2.984	28.3	1.365	1.233	0.0101	39.48	1.392	1.120
58	1,519	97.3	38.94	1.444	25.9	1.0240	0.8823	1.660	2.033	1.444	1.617	1.29	3.490	29.9	1.410	1.273	0.0106	41.28	1.485	1.050
59	1,611	102.3	39.18	1.456	26.1	1.0230	0.8802	1.880	2.076	1.488	1.672	1.21	3.578	30.3	1.424	1.283	0.0103	41.58	1.512	1.030
60	1,669	107.1	39.65	1.475	25.8	1.0230	0.8828	1.960	2.103	1.555	1.739	1.26	3.797	31.0	1.437	1.300	0.0105	42.95	1.725	1.010
61	1,756	113.1	40.98	1,500	28.0	1.0230	0.8847	2.080	2.185	1.651	1.891	1.23	4.224	32.2	1.467	1.335	0.0115	42.95	1.725	1.010
62	2,107	70.0	31.56	1.387	20.3	0.9920	0.7190	1,480	1,939	1,050	1,464	1,41	2,581	28,9	1,396	1,248	0,0101	33,37	1,177	1,120
63	2,188	76,7	31,19	1,397	20,8	0,9930	0,7205	1,480	1,980	1,081	1,506	1,37	2,708	29,5	1,407	1,261	0,0107	33,92	1,220	1,130
64	2,344	92,4	33,25	1,434	21,7	0,9960	0,7250	1,600	2,044	1,223	1,689	1,31	3,055	30,6	1,436	1,291	0,0107	35,07	1,310	1,070
65	901	-	14,880	41,00	1,470	28,1	1,0173	0,9098	2,010	1,587	1,729	1,27	4,006	31,5	1,444	1,315	0,0110	42,57	1,650	1,040

TABLE XV (Continued)

Flight Number	Record Number	TAS (kt)	W ₂ (lb/sec)	T ₅ (deg R)	P ₅ (psia)	θ ₂	W ₁ (lb/hr)	Rotor Tip Pressure Ratio P ₅ /P ₀	RHP	SFC (lb/hr-hp)	P ₅ (psia)	T ₅ (deg R)	(T ₅ /θ) ^{0.519}	(P ₅ /T ₅) ^{0.728}	(W ₂ /T ₅) ^{0.728}	Q _T (lb/hr)	Q _T (lb/hr)	Q _T (lb/hr)	
41	957	14,530	39.41	1,499	28.1	1.0428	0.9766	2.010	1,558	1.700	1.29	3.964	32.0	1,439	1,325	41.01	1,592	1,020	
41	1,407	14,045	38.17	1,446	27.8	1.0333	0.8976	1,960	2,070	1,567	1.37	3.643	31.6	1,447	1,318	40.09	1,536	1,076	
41	1,496	13,960	39.63	1,438	27.9	1.0366	0.8976	2,000	2,086	1,513	1.636	1.32	3.804	1,439	1,318	41.41	1,591	1,050	
43	2,139	59.0	35.01	1,389	24.3	1.0352	0.9112	1,460	1,733	995	1.073	1.47	2.601	28.3	1,342	1,237	36.46	1,240	1,273
43	2,199	68.7	35.01	1,389	24.3	1.0352	0.9099	1,600	1,726	988	1.067	1.61	2.621	27.3	1,342	1,208	36.89	1,224	1,240
43	2,282	85.4	36.32	1,410	25.4	1.0352	0.9091	1,640	1,812	1,125	1.217	1.46	2.989	28.6	1,371	1,240	38.20	1,334	1,195
43	2,373	97.1	37.66	1,449	26.6	1.0352	0.9062	1,870	1,848	1,278	1.256	1.46	3.400	30.0	1,409	1,275	40.05	1,452	1,140
43	2,447	108.8	38.88	1,499	28.3	1.0380	0.9117	2,020	2,004	1,451	1.562	1.39	3.866	31.7	1,444	1,320	40.67	1,576	1,040
43	2,543	58.3	35.62	1,385	24.3	1.0360	0.9101	1,550	1,726	996	1.075	1.56	2.626	27.2	1,337	1,205	37.53	1,245	1,250
43	2,594	68.0	35.05	1,381	24.2	1.0360	0.9125	1,470	1,713	950	1.022	1.55	2.604	27.0	1,333	1,203	36.89	1,224	1,250
43	2,663	79.7	36.55	1,404	24.9	1.0360	0.9131	1,560	1,773	1,088	1.171	1.43	2.840	27.8	1,354	1,220	38.20	1,334	1,170
43	4,429	1,291	37.61	1,481	27.1	1.0487	0.9224	1,810	1,692	1,291	1.367	1.33	3.460	30.0	1,412	1,275	39.58	1,451	1,120
43	4,471	1,384	38.39	1,479	27.3	1.0386	0.9224	1,950	1,952	1,384	1.472	1.32	3.532	30.2	1,424	1,280	40.49	1,499	1,080
43	4,585	1,389	38.46	1,480	27.4	1.0380	0.9225	1,900	1,950	1,389	1.477	1.37	3.582	30.3	1,426	1,282	40.55	1,501	1,040
43	4,625	1,451	38.92	1,486	27.9	1.0366	0.9208	1,960	1,999	1,451	1.548	1.35	3.714	31.0	1,428	1,300	40.79	1,553	1,070

Single Engine Flight

1

Flight number

(0.97)(W₂ - W₁) / (C_v V₁ - V₂) V₁

2

Test point

3

True airspeed - kn

4

Hover gross weight for indicated hover points

0.97 is factor allowing 3 percent leakage through diverter valves, etc

5

Engine mass flow, total - lb/sec

V₁ = f blade tip pressure (1) and temperature (6 - 10 deg)

6

Engine discharge temperature - deg R

C_v = velocity coefficient

7

Engine discharge pressure - psia

Referred rotor horsepower

8

Engine inlet temperature ratio

Specific fuel consumption - lb/hr-hp - (10)/(12) / (9) and (5)

9

Atmospheric pressure ratio

Gas horsepower/lb/sec air W₂ - function of P₅, (7), (9), (6), and (5)

10

Total fuel flow - lb/hr

11

Rotor tip pressure ratio

12

Rotor horsepower =

(0.97)(W₂ - W₁) / (C_v V₁ - V₂) V₁

13

where:

0.97 is factor allowing 3 percent leakage through diverter valves, etc

14

V₁ = f blade tip pressure (1) and temperature (6 - 10 deg)

15

C_v = velocity coefficient

16

Referred rotor horsepower

17

Specific fuel consumption - lb/hr-hp - (10)/(12) / (9) and (5)

18

Gas horsepower/lb/sec air W₂ - function of P₅, (7), (9), (6), and (5)

19

Atmospheric pressure ratio

20

Total fuel flow - lb/hr

21

Rotor tip pressure ratio

22

QT airflow is determined by increasing YT engine

23

airflow (5) by inverse ratio of square root of T₅ that is, $\sqrt{\frac{T_5}{T_5 \theta}}$ or $\sqrt{\frac{1}{T_5 \theta}}$

24

The fuel flow is the product of fuel/air ratio \times airflow \times leakage factor, or $(20) \times (21) \times 0.97 \times 3,600$ sec/hr

25

Specific fuel consumption - lb/hr-hp = $(22)/(23)$

26

(T₅/θ)^{0.519} is referred temperature for QT engines.

27

Read from Figure 36 at given P₅/θ.

28

As indicated

29

Taken at (19) from Figure 39 for QT engines

30

QT airflow is determined by increasing YT engine

31

airflow (5) by inverse ratio of square root of T₅ that is, $\sqrt{\frac{T_5}{T_5 \theta}}$ or $\sqrt{\frac{1}{T_5 \theta}}$

32

The fuel flow is the product of fuel/air ratio \times airflow \times leakage factor, or $(20) \times (21) \times 0.97 \times 3,600$ sec/hr

33

Specific fuel consumption - lb/hr-hp = $(22)/(23)$

34

*Fuel flow gage inoperative.

35

**W₂ = mass flow through slightly open yaw - averaged 13% W₂ in hover and 1.1% W₂ in cruise.

As an expedient, the XV-9A utilizes compressor bleed to drive an aspirator system for engine oil cooling. This system imposes an unnecessarily large fuel consumption penalty but, to save time and money, was employed on the research vehicle. In order to reflect the inherent rotor system performance, the fuel flow attributable to this bleed extraction has been subtracted from the data as plotted. This correction was no more than 5 percent. The effect of the bleed is seen in Figure 39 as an increase of the test fuel/air ratio at a given engine temperature rise above the predelivery calibration. The correction of fuel flow for compressor bleed amounts to moving the fuel/air ratio points from their observed location to the General Electric calibration lines.

UNCLASSIFIED
Security Classification

DOCUMENT CONTROL DATA - R&D		
<i>(Security classification of title, body of abstract and indexing annotation must be entered when the overall report is classified)</i>		
1. ORIGINATING ACTIVITY (Corporate author) Hughes Tool Company - Aircraft Division Culver City, California		2a. REPORT SECURITY CLASSIFICATION Unclassified 2b. GROUP
3. REPORT TITLE 20-HOUR FOLLOW-ON FLIGHT TEST PROGRAM, XV-9A HOT CYCLE RESEARCH AIRCRAFT		
4. DESCRIPTIVE NOTES (Type of report and inclusive dates) Final Report, 17 March 1965 through 23 December 1965		
5. AUTHOR(S) (Last name, first name, initial) Pieper, C. W. Hirsh, N. B.		
6. REPORT DATE December 1966	7a. TOTAL NO. OF PAGES 222	7b. NO. OF REFS 14
8a. CONTRACT OR GRANT NO. DA 44-177-AMC-225(T) A. PROJECT NO. Task 1M131001D15701 c. d.	9a. ORIGINATOR'S REPORT NUMBER(S) USAAVLABS Technical Report 66-81 9b. OTHER REPORT NO(S) (Any other numbers that may be assigned this report) HTC-AD 66-4	
10. AVAILABILITY/LIMITATION NOTICES		
11. SUPPLEMENTARY NOTES	12. SPONSORING MILITARY ACTIVITY U. S. Army Aviation Materiel Laboratories Fort Eustis, Virginia	
13. ABSTRACT <p>> This report summarizes additional technical data for evaluation of Hot Cycle propulsion system performance and operating characteristics provided by a 20-hour follow-on flight test program on the XV-9A Hot Cycle Research Aircraft.</p> <p>The tests were performed from 30 April through 26 August 1965 and included an evaluation of the performance, structural qualities, and stability and control of the Hot Cycle rotor and propulsion system in greater depth than that practical during the initial 15-hour flight test. The 20 hours of flight testing involved expansion of flight envelope and included evaluation of aircraft and rotor system performance, flight loads, cooling, and flying qualities in various flight modes.</p> <p>A ground test of the tethered rotor system was performed at the conclusion of flight testing, followed by a teardown inspection of the aircraft. The teardown inspection was completed on 23 December 1965.</p>		

DD FORM 1473
1 JAN 64

UNCLASSIFIED
Security Classification

UNCLASSIFIED
Security Classification

14. KEY WORDS	LINK A		LINK B		LINK C	
	ROLE	WT	ROLE	WT	ROLE	WT
Hot Cycle Rotor System VTOL Aircraft						

INSTRUCTIONS

1. **ORIGINATING ACTIVITY:** Enter the name and address of the contractor, subcontractor, grantee, Department of Defense activity or other organization (*corporate author*) issuing the report.

2a. **REPORT SECURITY CLASSIFICATION:** Enter the overall security classification of the report. Indicate whether "Restricted Data" is included. Marking is to be in accordance with appropriate security regulations.

2b. **GROUP:** Automatic downgrading is specified in DoD Directive 5200.10 and Armed Forces Industrial Manual. Enter the group number. Also, when applicable, show that optional markings have been used for Group 3 and Group 4 as authorized.

3. **REPORT TITLE:** Enter the complete report title in all capital letters. Titles in all cases should be unclassified. If a meaningful title cannot be selected without classification, show title classification in all capitals in parenthesis immediately following the title.

4. **DESCRIPTIVE NOTES:** If appropriate, enter the type of report, e.g., interim, progress, summary, annual, or final. Give the inclusive dates when a specific reporting period is covered.

5. **AUTHOR(S):** Enter the name(s) of author(s) as shown on or in the report. Enter last name, first name, middle initial. If military, show rank and branch of service. The name of the principal author is an absolute minimum requirement.

6. **REPORT DATE:** Enter the date of the report as day, month, year; or month, year. If more than one date appears on the report, use date of publication.

7a. **TOTAL NUMBER OF PAGES:** The total page count should follow normal pagination procedures, i.e., enter the number of pages containing information.

7b. **NUMBER OF REFERENCES:** Enter the total number of references cited in the report.

8a. **CONTRACT OR GRANT NUMBER:** If appropriate, enter the applicable number of the contract or grant under which the report was written.

8b, 8c, & 8d. **PROJECT NUMBER:** Enter the appropriate military department identification, such as project number, subproject number, system numbers, task number, etc.

9a. **ORIGINATOR'S REPORT NUMBER(S):** Enter the official report number by which the document will be identified and controlled by the originating activity. This number must be unique to this report.

9b. **OTHER REPORT NUMBER(S):** If the report has been assigned any other report numbers (*either by the originator or by the sponsor*), also enter this number(s).

10. **AVAILABILITY/LIMITATION NOTICES:** Enter any limitations on further dissemination of the report, other than those imposed by security classification, using standard statements such as:

- (1) "Qualified requesters may obtain copies of this report from DDC."
- (2) "Foreign announcement and dissemination of this report by DDC is not authorized."
- (3) "U. S. Government agencies may obtain copies of this report directly from DDC. Other qualified DDC users shall request through _____."
- (4) "U. S. military agencies may obtain copies of this report directly from DDC. Other qualified users shall request through _____."
- (5) "All distribution of this report is controlled. Qualified DDC users shall request through _____."

If the report has been furnished to the Office of Technical Services, Department of Commerce, for sale to the public, indicate this fact and enter the price, if known.

11. **SUPPLEMENTARY NOTES:** Use for additional explanatory notes.

12. **SPONSORING MILITARY ACTIVITY:** Enter the name of the departmental project office or laboratory sponsoring (*paying for*) the research and development. Include address.

13. **ABSTRACT:** Enter an abstract giving a brief and factual summary of the document indicative of the report, even though it may also appear elsewhere in the body of the technical report. If additional space is required, a continuation sheet shall be attached.

It is highly desirable that the abstract of classified reports be unclassified. Each paragraph of the abstract shall end with an indication of the military security classification of the information in the paragraph, represented as (TS), (S), (C), or (U).

There is no limitation on the length of the abstract. However, the suggested length is from 150 to 225 words.

14. **KEY WORDS:** Key words are technically meaningful terms or short phrases that characterize a report and may be used as index entries for cataloging the report. Key words must be selected so that no security classification is required. Identifiers, such as equipment model designation, trade name, military project code name, geographic location, may be used as key words but will be followed by an indication of technical context. The assignment of links, rules, and weights is optional.